

Alma Mater Studiorum – Università di Bologna

Dottorato di ricerca in

Scienze biotecnologiche, biocomputazionali,  
farmaceutiche e farmacologiche

Ciclo XXXIII

**Settore concorsuale:** 03/D1

**Settore scientifico-disciplinare:** CHIM/08

Multiscale modeling of metal nanoparticles for  
biotechnological applications

**Presentata da:** Sebastian Franco Ulloa

**Coordinatore dottorato**

Prof. Maria Laura Bolognesi

**Supervisore**

Dr. Marco De Vivo

**Esame finale anno 2021**

*This thesis is dedicated to all the minorities that have been  
and continue to be oppressed because of unfounded  
prejudices and improper political interests.*

*'...This is, therefore, to say that the transformation of human consciousness through meditation is frustrated so long as we think of it as something that I by myself can bring about, by some sort of wangle, by some sort of gimmick. Because you see it leads to endless games of spiritual one-upmanship. And of guru competition. Of my guru being more effective than your guru. My yogas are faster than your yoga. I am more aware of myself than you are. I am humbler than you are. I am sorrier for my sins than you are. I love you more than you love me. There's these interminable goings on where people fight and wonder whether they are a bit more evolved than somebody else and so on.*

*All that can just fall away. And then we get this strange feeling that we've never had in our lives except occasionally by accident. Some people get a glimpse that we are no longer this poor little stranger and afraid in a world it never made. But that you are this universe. And you are creating it at every moment. Because you see it starts now. It didn't begin in the past. There was no past. If the universe began in the past, when that happened it was now. But it is still now, and the universe is still beginning now and it's trailing off like the wake of a ship from now and as the wake of the ship fades out, so does the past. You can look back there to explain things, but the explanation disappears. You will never find it there. Things are not explained by the past. They're explained by what happens now. That creates the past. And it begins here.*

*Cheer up. You can't blame anyone else for the kind of world you're in. And if you know, you see that I, in the sense of the person, the front, the ego, it really doesn't exist. Then it won't go through your head too badly if you wake up and discover that you are God.*

*That's the birth of responsibility.'*

Alan Watts

## ACKNOWLEDGEMENTS

Leaving aside the underlying assumption of causality implied by acknowledgements, there have been people in my life whose presence have nurtured my personal and professional growth, as suggested by the tail-chasing illusion of my own consciousness. Regardless of the motivation behind their actions, these people have fostered my path in a way that fills me with what I experience as gratitude.

I thank Víctor Hugo, Patricia, Juan Pablo, Laura, Myriam, and Dalila, a family whose members, while imperfect, have always supported one another in the best way they know how to. I thank María Paula and Hugo Ernesto with whom we have made a family of our own. I also thank Eirik Amundsen for teaching me how to flourish and work hard for my goals always remaining true to myself. I thank him for teaching me how to critically inspect sociopolitical discourses and stand up for myself.

I thank Fabio, Santiago Roa Sierra, Remi, Ángela, and Julie, unmatched dialectic companions that offer me fresh perspectives when I need them the most. I thank Maria Camila, Juan Diego, Chepe, Dirk, and Nicolás Ruiz for their love and support on everything I do. I also thank Jacopo, Elisa, Adam, Manuel, Maria Antonietta, and Sigbjørn, the people with whom I have shared laughter, frustration, and carbonara during these singular three years in Europe.

I thank Laura and Josephine, two incredibly strong women that I will always consider my mentors and friends. I thank Fabrizio, Piero, and Michele for serving as scientific role models. I also thank Lucía Morillas-Becerril, Federico Rimembrana, Mattia Pini, Giuseppina Tatulli, Daniela Guarnieri, Mauro Moglianetti, Ilaria Fortunati, Roberto Marotta, Xiaohuan Sun, and Giordano Zanoni for their technical contributions to this work and Stuart Holland for all his thoughtful feedback.

Lastly, I thank Marco, my supervisor, for seeing the potential he saw in me and for giving me as many opportunities and freedoms as he possibly could. The experience he allowed me to have at the Italian Institute of Technology has significantly impacted my perspectives on scientific research, Academia, and my own life.

# TABLE OF CONTENTS

<u>ACKNOWLEDGEMENTS</u>	<u>III</u>
<u>TABLE OF CONTENTS</u>	<u>IV</u>
<u>PREFACE</u>	<u>VII</u>
<u>ABSTRACT</u>	<u>VIII</u>
<b><u>CHAPTER I. METAL NANOPARTICLES IN BIOMEDICINE</u></b>	<b><u>1</u></b>
A. Modern relevance of nanoparticles	1
B. Monolayer-protected gold nanoparticles	2
1. Structure of gold nanoparticles	2
2. Function and applications	4
3. Synthesis	9
C. Experimental techniques for studying metal nanoparticles	11
D. Computational methods for studying metal nanoparticles	14
E. Scope of the present thesis	17
<b><u>CHAPTER II. THEORY AND PRINCIPLES</u></b>	<b><u>19</u></b>
A. Molecular mechanics	19
1. Force field functionals	20
2. Coarse-grained force fields	25
3. Parametrization	27
B. Molecular dynamics simulations	28
1. Time integration	30
2. Thermostats and barostats	31
3. Nonbonded interactions	38
4. Coarse-grained simulations	40
C. Free energy calculations	41
1. Potential of mean force and umbrella sampling	41
2. Thermodynamic integration	44
<b><u>CHAPTER III. NANOMODELER: A WEBSERVER FOR MOLECULAR SIMULATIONS AND ENGINEERING OF NANOPARTICLES</u></b>	<b><u>48</u></b>
Abstract	48
A. Introduction	49
B. Results and discussion	50
1. Building a 3D model of gold nanoparticles	50
2. Building topologies for molecular dynamics simulations of gold nanoparticles	54
3. Molecular dynamics simulations and test cases	57
C. Webserver building	59
1. Structure of the webserver	59
2. Preparation of cores and coatings	60
3. 3D modeling of gold nanoparticles	61
4. Molecular dynamics simulations	63
D. Conclusions	64

<b><u>CHAPTER IV. ARGININE MAGIC WITH GOLD NANOPARTICLES: SELECTIVE AND NON-</u></b>	
<b><u>DISRUPTIVE TARGETING OF NEUTRAL PHOSPHOLIPID BILAYERS</u></b>	<b>67</b>
Abstract	67
A. Introduction	68
B. Results	69
1. Gold nanoparticle functionalization and characterization	69
2. Liposome permeabilization assays	69
3. Liposomes' structural integrity	71
4. The nature of the gold nanoparticle-liposome interaction	74
5. The role of electrostatic attraction	75
6. Resolution of atomically detailed pairing between gold nanoparticles and liposomes	77
C. Discussion	83
D. Methods	85
1. General	85
2. Nanoparticle preparation	86
3. Liposome preparation	87
4. Molecular dynamics simulations	87
<b><u>CHAPTER V. MOLECULAR-DYNAMICS-BASED THROUGHPUT SCREENING OF GOLD</u></b>	
<b><u>NANOPARTICLES FOR CHEMOSENSING</u></b>	<b>91</b>
Abstract	91
A. Introduction	92
B. Method development	93
1. System preparation	93
2. Steered unbinding simulations	95
3. Training dataset and protocol benchmarking	96
C. Chemosensor screening	99
D. Perspectives	103
<b><u>CHAPTER VI. NANOMODELER CG: A TOOL FOR MODELING AND ENGINEERING FUNCTIONAL</u></b>	
<b><u>NANOPARTICLES AT A COARSE-GRAINED RESOLUTION</u></b>	<b>106</b>
Abstract	106
A. Introduction	107
B. Results and discussion	108
1. Modeling nanoparticle structures	109
2. Building user-tailored topologies for nanoparticles	111
3. Molecular dynamics simulations and case study	113
C. Webserver building	117
1. Construction and parametrization of packed cores	117
2. 3D modeling of nanoparticles	120
3. Molecular dynamics simulations	121
D. Conclusions	123
<b><u>CHAPTER VII. DISPERSION STATE PHASE DIAGRAM OF CITRATE-COATED METAL</u></b>	
<b><u>NANOPARTICLES IN SALINE SOLUTIONS</u></b>	<b>126</b>
Abstract	126
A. Introduction	127
B. Results	129
1. Stoichiometry of citrate chemisorbed onto metal nanoparticles	129
2. Effect of ionic strength and nanoparticle charge on the $\zeta$ -potential	132

3. Role of inter-particle interactions for nanoparticle dimerization	135
4. Linking nanoparticle dimerization with colloidal stability	139
C. Methods	142
1. Development of the theoretical model	142
2. Nanoparticle modeling and $\zeta$ -potential calculations	143
3. Free energy calculations	144
4. Nanoparticle synthesis, absorbance experiments, and imaging	145
<b><u>CHAPTER VIII. MEMBRANOTROPIC NANOPARTICLES HARVEST CHOLESTEROL TO PROMOTE THEIR PASSIVE CELLULAR UPTAKE</u></b>	<b>147</b>
Abstract	147
A. Introduction	148
B. Methods	149
1. Our methodological approach	149
2. System preparation	150
3. Molecular dynamics simulations and free energy calculations	151
4. Trajectory analysis	153
5. Cell culture and transmission electron microscopy	154
C. Results	154
1. Functionalized peptide-coated nanoparticles adopt a biphasic binding mode at lipid membranes	154
2. Membrane binding of primitive peptides suggests a unique binding mechanism for peptide-coated nanoparticles	156
3. Functionalized peptide-coated nanoparticles harvest cholesterol molecules and lipid tails, aiding passive diffusion	159
D. Discussion	163
E. Conclusions	166
<b><u>CHAPTER IX. FINAL REMARKS AND PERSPECTIVES</u></b>	<b>168</b>
<b><u>APPENDIX A. NANOMODELER USER MANUAL</u></b>	<b>170</b>
<b><u>APPENDIX B. SYNTHESIS, CHARACTERIZATION, AND SUPPLEMENTARY SIMULATIONS OF CATIONIC NANOPARTICLES</u></b>	<b>180</b>
<b><u>APPENDIX C. CHEMOSENSOR-ANALYTE DATASET, CATECHOLAMINES IN THE HUMAN BRAIN, AND VIRTUAL SCREENING RESULTS</u></b>	<b>190</b>
<b><u>APPENDIX D. THEORETICAL AND COARSE-GRAINED MODELING OF ION-CAPPED METAL NANOPARTICLES</u></b>	<b>201</b>
<b><u>APPENDIX E. SUPPLEMENTARY SIMULATIONS OF PEPTIDE-COATED METAL NANOPARTICLES</u></b>	<b>214</b>
<b><u>ABBREVIATIONS</u></b>	<b>217</b>
<b><u>BIBLIOGRAPHY</u></b>	<b>220</b>

## PREFACE

In 2015, an article published in *Nature* reported a collection of sharp-edged stones found at the shore of Lake Turkana in modern Kenya. The somewhat mundane pieces of rock date back to the Piacenzian Age, the last stage before the Quaternary glaciations in which the survival skills of all species would be pushed to their limits. Archaeologists hypothesize that Hominini, the ape ancestors to modern humans, built these stone artifacts by battering rocks against plant foods and bones. Our simian forbearers would then use the knapped stones for hunting and protection. Inadvertently, Hominini left their crafts for us to find 3.3 million years later and recognize as the oldest technological tools ever uncovered.

Nowadays, we have moved on from battering stones to adopt – some would say – more sophisticated techniques and raw materials. We stand proud of the faculty for building tools that we have honed throughout our own evolution. Interestingly, our species consistently elevates this one skill to justify holding itself superior to all other forms of life. Today, 3.3 million years have passed, and we are still driven by the same biological instincts that drove our simian ancestors into building tools that increased their chances of survival.

This work is a manifestation of the self-preservation instincts inherent to the human species. This work is the fruit of my own blind faith. This work is a personal battle against the unbearable lightness of being. This work is my ode to modern sharp-edged stones.



## ABSTRACT

Functionalized metal nanoparticles are supramolecular assemblies that are gaining increasing attention in biomedicine due to their broad-spectrum applicability. In this context, understanding the nano-biointerface is critical for implementing nanoparticles into medical practices, yet the structure-function relation of functionalized metal nanoparticles remains puzzling. This work discusses the design of metal nanoparticles with targeted applications from three focal points: structural modeling, method development, and biomolecular interactions. First, the NanoModeler webserver is introduced for the standardized building and parametrizing of metal nanoparticles for simulations at atomistic and coarse-grained resolutions. Second, a theoretical model is formulated to characterize the surface of charged nanoparticles, which, when combined with mesoscale simulations, clarifies the fundamental principles that enable colloidal stability at physiological conditions. Third, atomistic and coarse-grained simulations were combined to describe, at the molecular level, the non-disruptive cellular permeabilization induced by membranotropic nanoparticles to facilitate intracellular cargo delivery. The multilayered work presented here comprehends new online tools, physics-based methods, and molecular insights that expand our understanding of the structure-function relation in metal nanoparticles and contribute to the design of safe and effective nanoparticle-based therapeutic agents.

# CHAPTER I. METAL NANOPARTICLES IN BIOMEDICINE

## A. Modern relevance of nanoparticles

Nanotechnology is the science of synthetic materials with dimensions in the nanometer ( $10^{-9}$  meter) range. It is revolutionizing the way we understand matter. Continuous advances in synthetic chemistry are granting us control over ever smaller molecular entities, enabling the assembly and functionalization of nanometric architectures. At nanoscale, materials display unique physicochemical and optical properties that can differ dramatically from those of coarser bulk materials. A nanoparticle (NP) is defined as a material with at least one dimension measuring between 1 and 100 nm. NPs are promising platforms in many fields, including biomedicine, polymer science, and electronics.<sup>1</sup>

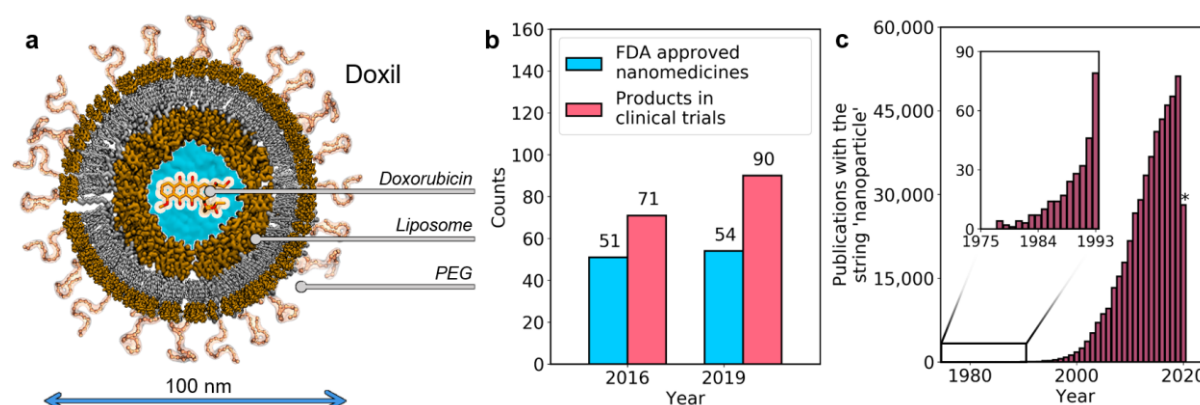


**Figure 1.** Current landscape of nanomedicines. **a.** Schematic representation of Doxil, the first nanomedicine approved by the FDA. The image shows the biologically active compound doxorubicin (orange) inside a 100 nm liposome (brown and gray), which is in turn passivated by a shell of PEG (light pink). **b.** Number of nanomedicines approved by the FDA or in clinical trials in 2016 and 2019.<sup>8,9</sup> **c.** Number of citations including the term ‘nanoparticle’ from 1975 to 2020 according to the Scopus database. The starred (\*) entry is the value on July 2, 2020.

Nanotechnology is a nascent discipline with many open questions, yet NP-based formulations already play an active role in medical treatments. The prescription of NPs in medicine dates back to 1995, when the Food and Drug Administration (FDA) approved Doxil.<sup>2</sup> Doxil comprises 100 nm liposomes encapsulating doxorubicin, which is used to treat Kaposi’s sarcoma (**Figure 1a**).<sup>3</sup> The lipid shuttle changes doxorubicin’s toxicological profile by

increasing its half-life and promoting the local and specific delivery of the active compound into malignant cells.<sup>4,5</sup>

Nanomedicines are medicines that incorporate NPs into their formulation. They are the subject of growing interest and popularity.<sup>6</sup> By 2016, there were already 51 FDA-approved nanomedicines and 71 products in clinical trials.<sup>7</sup> In the last three years, three more nanomedicines were approved and 90 more entered clinical trials (**Figure 1b** and **Figure 1c**).<sup>8,9</sup> In addition to the engineered nanomaterials explicitly introduced into the market, synthetic NPs are increasingly present in commercial products like food and cosmetics.<sup>10</sup> Hence, understanding how these materials interact with biological macromolecules is pivotal to accurately assessing their safety and environmental impact.<sup>11</sup>

## **B. Monolayer-protected gold nanoparticles**

### *1. Structure of gold nanoparticles*

In the last 40 years, NPs have been synthesized from many materials, including dendrimers, metal-organic frameworks, quantum dots, and lipids.<sup>12</sup> Of these, metal NPs hold promise as tunable and transferable platforms for many applications. Monolayer-protected metal NPs are hybrid materials comprising an inner metallic core surrounded by an adlayer of molecules known as ligands (**Figure 2a**).<sup>13</sup> The most commonly used metals include platinum, silver, iron, and titanium oxide,<sup>14</sup> but gold stands out due to its biocompatibility, photostability, and ease of functionalization.<sup>15</sup> There are few restrictions on the type of molecules that can be used in the monolayer to protect the gold nanoparticles (AuNPs). Research has been carried out with coatings such as peptides,<sup>16</sup> nucleic acids,<sup>17</sup> antibodies,<sup>18</sup> and carbohydrates.<sup>19</sup> The conjugation of these molecules onto gold cores typically takes place by means of a thiolate group (**Figure 2b**). The structure of AuNPs can thus be divided into three parts: i) the inner gold core, ii) the gold-sulfur interface, and iii) the organic ligands (**Figure 2c**).

The inner gold core defines the mass distribution and (an)isotropy of the AuNP.<sup>20</sup> The atomic arrangement of the inner gold core can change considerably as the size of the AuNP increases. Gold nanoclusters (AuNCs) with a diameter of less than 3 nm display highly symmetrical non-periodical organizations that in some cases confers them with an intrinsic chirality.<sup>21</sup> For AuNCs with a diameter greater than 3 nm, the gold bodies adopt a bulk FCC lattice that, according to the experimental conditions, can be sculpted into shapes like cubes, rods, and

pyramids as well as nearly spherical shapes like icosahedra, truncated decahedra, and cuboctahedra.<sup>22,23</sup> The structure of AuNPs is dynamic, so the core can present polymorphisms even at a constant stoichiometric ratio.<sup>24</sup>

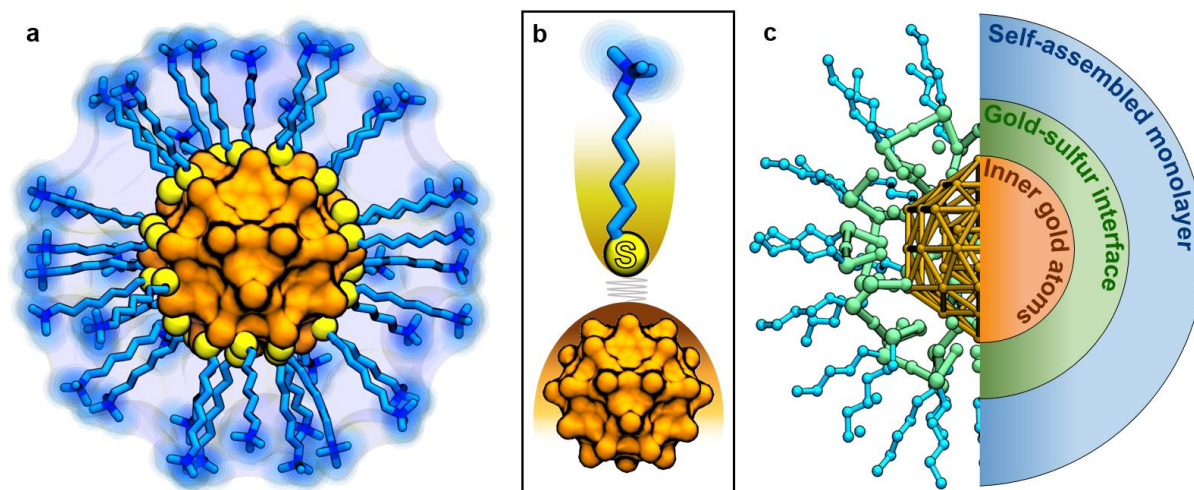


**Figure 2.** Structure of functionalized AuNPs. **a.** Conceptual illustration of a typical functionalized AuNP with chemical formula  $\text{Au}_{144}(\text{SR})_{60}$ . An internal gold core, in orange, is coated by an organic monolayer displayed in blue (sulfur atoms in yellow). **b.** The chemical bond between thiolates and gold surface atoms enables the functionalization of AuNPs. **c.** The three structural features that characterize functionalized AuNPs, namely, the internal quasi-static gold atoms (orange), the gold-sulfur interface (green), and the flexible self-assembled monolayer (blue).

The gold-sulfur interface also varies significantly from system to system. For small AuNCs, the interface comprises gold-sulfur staple-like motifs. These motifs add a second type of chirality to the AuNPs because, in general, the staples adopt sided arrangements (Chapter III).<sup>25</sup> As the core size increases, the length of these motifs decreases, steaming the plasticity of the interface. In the bulk limit, the stability granted by the formation of the staples is overcome by the entropically preferred ligand migration, allowing the coating compounds to sail on the surface of the gold core.<sup>26</sup> Although mobile, the interface can be stabilized by ligand-ligand interactions that favor specific configurations.<sup>27</sup>

The ligands protecting the metallic cores determine the surface chemistry of AuNPs and thus their interaction with their environment. The ligands themselves can also contain stereogenic centers, which confer AuNPs with an additional source of chirality. Depending on the physicochemical descriptors of the ligands (e.g. net charge, hydrophobicity, and flexibility) the coating monolayer can adopt a complex and dynamic packing analogous to the 3D folding of proteins. The most commonly studied AuNPs have homogeneous morphologies, that is,

monolayers comprising identical copies of a single compound. However, AuNPs can also be coated with mixed monolayers comprising two or more types of molecules.

Under controlled conditions, the structure of AuNPs is limited to the three segments described above. The structure of AuNPs extends to bigger agglomerates in physiological media. When AuNPs are immersed in a biological fluid such as blood, matrix proteins immediately cover the AuNPs in a supramolecular architecture known as the protein corona.<sup>28</sup> The protein corona is characterized by peptides with low dissociation kinetics stably bound to the nanomaterial. The protein corona is exceptionally detrimental in medical applications because it screens the monolayer's ligands, hijacking the functional response of AuNPs.<sup>29</sup> The formation of this shell also triggers an immune response that promotes the clearance of the particles from the organism.<sup>30</sup>

Rationally modifying the ligands of the coating monolayer may prevent protein chemisorption. The two most common alternatives are the introduction of polyethylene glycol (PEG) chains and zwitterionic ligands. Capping the ligands with PEG chains (as done for Doxil) results in a stealth layer that reduces the opsonization by serum proteins,<sup>31</sup> favors solubility in water,<sup>32,33</sup> and increases the bloodstream circulation times.<sup>34</sup> Nonetheless, PEGylation often implies non-biodegradability, immunogenicity, and accumulation in membrane-bound organelles, caveats that can be overcome by zwitterionic ligands (e.g. ligands terminated in a sulfonate choline group).<sup>35,36</sup>

## *2. Function and applications*

The metallic core and the coating monolayer of AuNPs can be exploited individually or synergistically to enable a wide variety of applications. These components are intertwined, and they govern the overall response of an AuNP to an external stimulus. However, in general terms, the metallic core is mainly responsible for the optical and electronic properties of AuNPs, whereas the chemical groups in the coating monolayer drive the interaction with external molecules.

Nanometer-sized metallic bodies display remarkable optical properties because of their unique response to electromagnetic radiation. The cloud of electrons malleably bound to the metallic core can be excited by incident photons to induce a spatial displacement between the electronic cloud and the heavy cationic nuclei. The constant excitation/relaxation of the electrons results in an oscillatory motion that can synchronize with the frequency of the incident light in a

phenomenon known as surface plasmon resonance (SPR).<sup>37</sup> For gold, the frequency of the light emitted by SPR falls into the infrared (IR)/near-infrared (NIR)/visible (Vis) spectrum. SPR is the same effect responsible for the fluorescence observed in AuNCs.

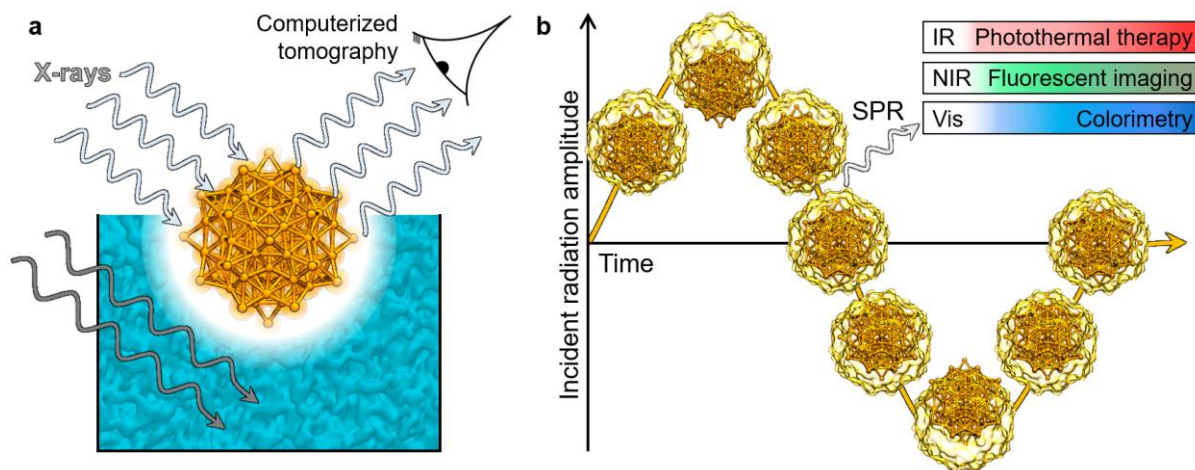


**Figure 3.** Optical response of AuNCs. **a.** In computerized tomography, X-rays are blasted onto a biological sample. Due to their voluminous electronic cloud, gold atoms diffract the beams, thus serving as a contrasting agent. **b.** Numerous applications of AuNPs are based on the SPR effect. The oscillation of the sea of electrons (yellow) around the cationic nuclei (orange) enables the emission of light upon photoexcitation. AuNPs typically emit in the IR, NIR, or Vis spectrums, making them promising candidates for photothermal therapies, fluorescent imaging, and colorimetric assays.

The SPR of functionalized AuNPs makes them promising candidates for imaging, sensing, and thermal therapies. AuNPs have been used in the fluorescent imaging of tumor cells. In addition, the high atomic number of gold makes AuNPs easily traceable through X-ray spectroscopy, for which they have found applications in computerized tomography scanning (**Figure 3a**).<sup>38,39</sup> In regard to sensing, the fluorescent/colorimetric profiles of AuNPs can be deactivated in the presence of specific analytes or targets. For example, the emission spectra of certain AuNPs can be redshifted upon encountering recognizable nucleotide sequences or cancer-related enzymes like kinases, caspases, and metalloproteinases.<sup>40-42</sup> Interestingly, AuNPs can also be designed with an opposite response mechanism, in which their fluorescence is ignited when bound to analytes like arginine.<sup>43,44</sup>

In contrast to imaging and sensing, photothermal therapies benefit from AuNPs with emission peaks in the NIR region (**Figure 3b**). This is because the chromophores that naturally occur in human cells display a low absorbance to NIR radiation, preventing any impacting photons from damaging healthy tissues.<sup>45</sup> In thermal therapies, the radiation emitted by AuNPs heats up their local environment. Increasing the temperature of a cancerous cell to 42°C can induce cytotoxic

effects, and the apoptotic pathway is triggered at 45°C. If temperatures reach 70-80°C, hyperthermic effects start to appear, these include changes in the cytoskeletal structure, cell membrane rupture, protein denaturation, and impairment of nucleotide synthesis.<sup>46</sup> Thus, if the excited AuNPs are concentrated at a cancerous tissue, photothermal therapy can cause the progressive death of the tumor. Currently, the gold-silica nanoshells known as AuroShell are undergoing human clinical trials for the treatment of prostate, head, and neck cancer.<sup>47,48</sup>

In addition to SPR, noble metals like gold can adopt various oxidation states (0/I/III), granting them intrinsic catalytic properties. The reactivity of gold can be harnessed in oxidation reactions. A typical case for studying the catalyzing efficiency of gold surfaces is the oxidation of carbon monoxide, but other cases include epoxidation, aldehyde hydrogenation, and activation of alkyne C-C bonds.<sup>49-51</sup> The same affinity for oxygenated species make gold particles act as antioxidant agents in the scavenging of reactive oxygen species.<sup>52,53</sup> Importantly, the gold cores can be digested at an acidic pH (e.g. the one in lysosomes), releasing a low concentration of metallic ions that, in turn, are the main cause of toxicity during AuNP endocytosis.<sup>54</sup>

The coating monolayer of AuNPs supports a broad variety of functionalizing chemical groups. The strength of the gold-sulfur bond is comparable to that of the gold-gold bond (ca. 40 kcal mol<sup>-1</sup>), and it is responsible for the ease of functionalization in AuNPs.<sup>55</sup> In this way, the surface chemistry of the particles can be tailored to achieve a target function. Given that the dimensions of AuNPs are in the same size range as those of biomacromolecules, several research efforts have focused on mimicking the evolutionary functions of proteins, lipid bilayers, deoxyribonucleic acid, and ribonucleic acid. Thus, by fine-tuning the composition of the coating monolayer, AuNPs have found applications as cargo-carriers, chemosensors, and nanozymes.<sup>56,57</sup>

The in vivo applications of AuNPs depend on them reaching their target destination. Whether the site of interest is the surface of the cell membrane (e.g. in photothermal therapy), the cytosolic space (e.g. in drug delivery), or the nuclear envelope (e.g. in imaging and chemosensing), the surface chemistry of AuNPs must be designed to overcome the biological barriers.<sup>58</sup> Depending on their size, AuNPs can be internalized into cells by phagocytosis, pinocytosis, receptor-mediated endocytosis (caveolin or clathrin), or even passive endocytosis.<sup>59</sup> However, all these mechanisms result in the isolation and eventual excretion of the AuNPs, hampering their performance.<sup>60</sup> Subsequently, much scientific research has

considered the interactions between functionalized AuNPs and cell membranes in order to design monolayers that promote passive translocation through cell membranes (**Figure 4**).<sup>61,62</sup>

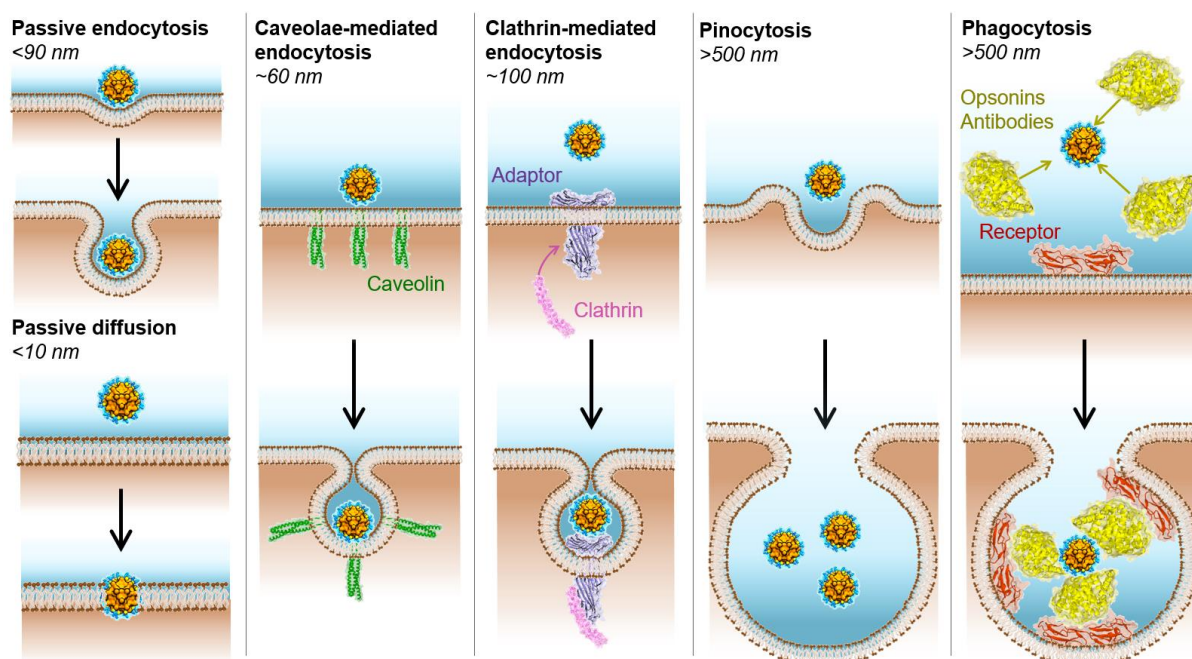


**Figure 4.** The most common internalization mechanisms encountered for AuNPs. The pathways are divided as passive or energy-dependent. Passive diffusion is a rare mechanism observed in cases like small anionic particles with patterned mixed monolayers. In passive endocytosis, the membrane (brown) wraps the particles (cyan and orange) until it pinches off a loaded liposome. The bilayer then bends due to the AuNP-membrane affinity. Caveolae (green) and clathrin (purple)-mediated endocytosis are triggered by the binding of AuNPs to superficial receptors on the membrane. Larger AuNPs can be internalized via pinocytosis or phagocytosis. During pinocytosis, the AuNPs are trapped in micrometer-long invaginations filled with water. During phagocytosis, the gold xenobiotics are first passivated by opsonins and antibodies (yellow), which are later recognized by membrane receptors that induce the encapsulation of the particles.

The interaction between AuNPs and lipid bilayers is extremely system-dependent; however, numerous studies have reached a consensus on certain aspects. The passive translocation of AuNPs results from a complex interplay between adsorption kinetics on the membrane's surface and the affinity for the apolar core of the bilayer. The former is mainly driven by electrostatic pairing, whereas the latter is mediated by the hydrophobic matching between the AuNP and the lipid tails.<sup>63,64</sup> Cationic AuNPs are associated with a high cytotoxicity because they consistently disrupt eukaryotic, partially anionic membranes (Chapter IV).<sup>65,66</sup> In contrast, negatively charged AuNPs interact weakly with cell membranes, limiting their internalization rates.<sup>67,68</sup> In addition to charge, several other physicochemical parameters have been considered, including volume,<sup>69,70</sup> shape,<sup>71,72</sup> hydrophobicity,<sup>73–75</sup> curvature,<sup>76–78</sup> elasticity,<sup>79,80</sup>



and ligand density.<sup>81–83</sup> To date, the most effective strategies for promoting passive penetration are lipidic coatings,<sup>84,85</sup> zwitterionic ligands,<sup>36,86</sup> conjugation to membranotropic peptides,<sup>87,88</sup> mixed monolayers with patterned arrangements,<sup>89–92</sup> and host-guest triggering mechanisms.<sup>93</sup>

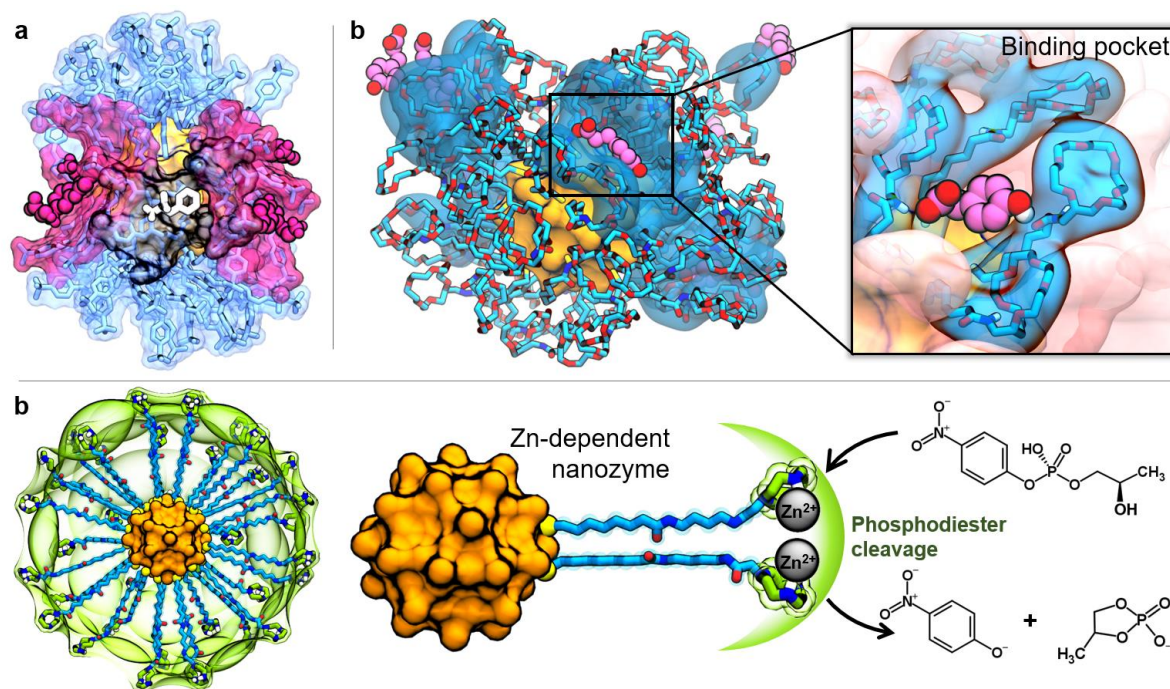


**Figure 5.** Applications of functionalized AuNPs mediated by the coating monolayer. **a.** Four copies of a small organic analyte binding to the monolayer of a gold nanoreceptor. The analytes display two different binding modes (in purple and gray). The coating ligands are shown in light blue, and the gold core in orange. **b.** Five copies of an organic analyte (pink) interacting with an AuNP (cyan and orange). The inset zooms into the binding pocket of one of the molecules, emphasizing the H-bonds formed between the analyte and the ligands. **c.** A Zn-dependent nanozyme whose ligands (blue and green) cooperatively cleave the phosphodiester bond of 2-hydroxypropyl-p-nitrophenyl phosphate.

The coating monolayer has an innate plasticity that allows it to fold and form chemical microenvironments, or pockets, as it occurs with proteins.<sup>57</sup> Although transient and short-lasting, the cavities formed within the packed monolayer can recognize chemically complementary molecules or analytes that bind in distinguishable orientations (**Figure 5a** and **Figure 5b**).<sup>94</sup> Notably, the subtlest of changes in the ligands' structure (e.g. inverting an amide moiety) can reduce or completely inhibit the recognition activity.<sup>95</sup> Nonetheless, these kinds of nanoreceptors hold potential for identifying and quantifying the presence of small analytes in complex matrices (e.g. biomarkers, Chapter V). This technology has already proven valuable in detecting illicit psychotropic substances<sup>96</sup> and other drugs like salicylic acid.<sup>97</sup>

Monolayer-protected AuNPs have also been prepared with organic thiols to mimic the catalytic activity of enzymes, and they are often referred to as ‘nanozymes.’<sup>98</sup> As with naturally occurring enzymes, the neighboring functional groups in the binding site cooperate during the chemical reaction.<sup>99</sup> Nanozymes are a stable and efficient alternative for the catalysis of specific reactions because the preparation of AuNPs avoids extensive efforts otherwise present in protein expression and purification.<sup>100</sup> Some examples of nanozymes include AuNPs coated with 1,4,7-triazacyclononane derivatives that, in the presence of Zn (II) ions, can form a chelated complex that cleaves phosphodiester bonds as with nucleases (**Figure 5c**).<sup>101</sup> In addition, peptide-conjugated AuNPs can imitate the activity of esterases by catalyzing, for example, the hydrolysis of 2,4-dinitrophenyl butyrate.<sup>102</sup>

### 3. *Synthesis*

Functionalized AuNPs can be prepared following diverse synthetic pathways. In general, such pathways can be classified as i) physical, ii) bio-assisted, and iii) wet-chemical-reduction methods according to the experimental conditions and the reagents that they use (**Figure 6**).

For physical methods, pulsed laser ablation (PLA) is a frequently encountered method for preparing supported ligand-free metal NCs and, more recently, synthesizing functionalized AuNPs in solution (**Figure 6a**). Gas-phase PLA uses a localized light source (laser) targeted at a metallic surface to vaporize a portion of atoms that condense back into stable clusters as they quickly cool.<sup>103</sup> Gas-phase PLA can be applied to monometallic clusters (e.g. Au, Ag, Cu, and Ni), and used to prepare alloyed NPs (e.g. Au/Ag, Au/Cu, and Au/Ni).<sup>104</sup> After their formation, the clusters move around the isolated container until they find a surface (e.g. amorphous carbon) for their support and eventual collection. The principles of gas-phase PLA can be extended to the on-site synthesis of AuNPs.<sup>105</sup> Here, the primordial metallic surface is immersed in an aqueous solution that contains a surfactant such as sodium dodecyl sulfate (SDS).<sup>106</sup> After the ultra-fast evaporation of the metals (picosecond scale), the clusters are formed in solution, and the surfactant forms a stabilizing layer that obstructs cascaded aggregation (nanosecond scale).<sup>107</sup>

Bio-assisted methods are an alternative to the physical synthesis of AuNPs. In this category, gold-containing acid salts (most typically chloroauric acid, HAuCl<sub>4</sub>) are spontaneously reduced to metallic gold in the presence of cells (**Figure 6b**).<sup>108</sup> In bio-assisted methods, naturally occurring oxido-reductases transform the free gold ions into neutral metallic atoms that

agglomerate into larger bodies.<sup>109</sup> As these structures coarsen, proteins bearing free cysteines or amino groups corral them to form a coating monolayer.<sup>110</sup> Experimental evidence suggests that this process can occur intra- and extracellularly depending on the selected cell lines. Moreover, these pathways have been tested with a variety of organisms from the bacterial, fungi, and plant kingdoms. Bio-assisted methods facilitate the preparation of protein-functionalized, biocompatible AuNPs, and they are gaining increasing attention as a ‘green’ choice.<sup>111</sup> Nonetheless, these synthetic routes require a thorough benchmarking of the experimental conditions in order to guarantee reliable control over the shape and size of the final AuNPs.<sup>112</sup>

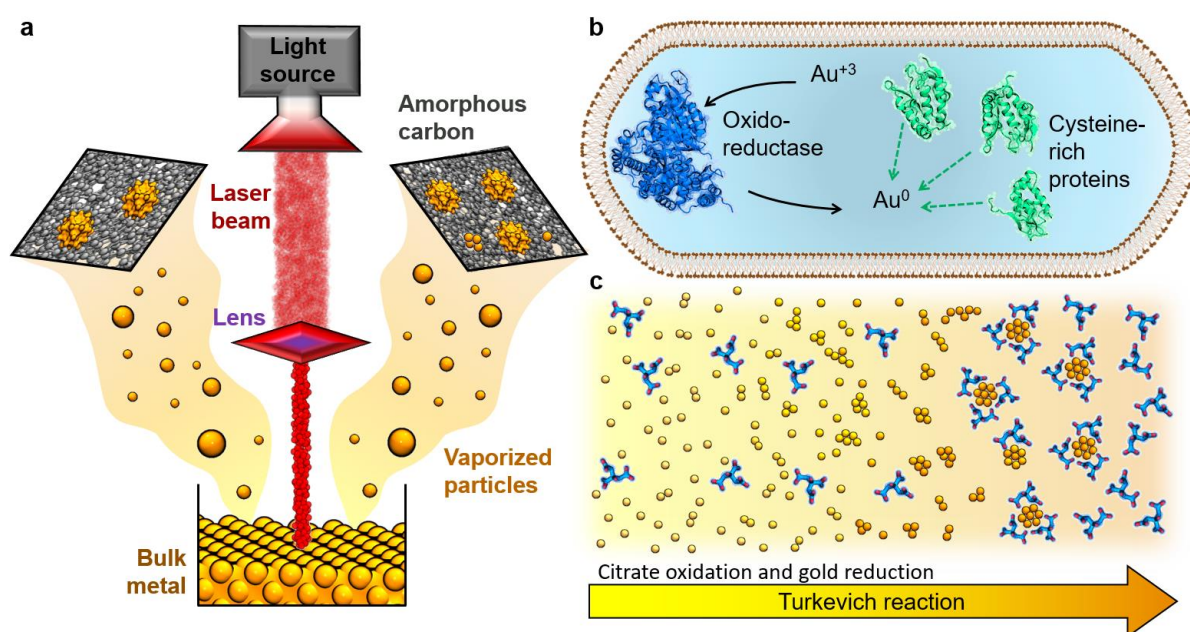


**Figure 6.** Methods for the synthesis of AuNPs. **a.** In PLA, a focalized laser beam evaporates adatoms from a metallic surface that are later deposited onto amorphous carbon. **b.** Bio-assisted methods exploit the oxido-reductases available in living cells to produce clusters of metallic gold. Then, cysteine-rich proteins conjugate onto the clusters to form a stable soluble complex. **c.** In wet-chemical-reduction methods, gold salts react with a reducing agent to form metallic gold. In the Turkevich reaction, an excess of citrate is used to immediately coat the formed neutral clusters in order to avoid a cascading aggregation process.

Wet-chemical-reduction methods are the most popular option for preparing stable AuNP suspensions because they offer good control over the size and shape of the particles. Moreover, wet-chemical reduction methods require relatively low-cost technologies.<sup>112</sup> Of these techniques, the most common are the Turkevich reaction and the Brust-Schiffrin method (**Figure 6c**). The Turkevich method was developed in 1951 and has been revised since then.<sup>113</sup> As with most synthetic routes for obtaining colloidal NPs, this reaction’s mechanism has not

been fully elucidated because it is difficult to collect data during NP growth. Nevertheless, exhaustive research on the experimental conditions have granted good control over the final product.<sup>114</sup> In Turkevich synthesis, tetrachloroauric acid is reduced by sodium citrate in an aqueous solution. As the metal atoms gain electrons, the excess citrate molecules cap the agglomerates and prevent them from aggregating (Chapter VII).<sup>115</sup> Citrate-capped gold colloids can then be subject to associative 1:1 ligand exchange reactions to purposely functionalize the AuNPs.<sup>116</sup>

The Brust-Schiffrin method is a two-phase reaction originally proposed in 1994.<sup>117</sup> This synthetic route is preferred for the synthesis of small AuNPs (size less than 5 nm) and AuNCs because the product has a narrow polydispersity, while retaining a facile synthesis in ambient conditions, high thermal and air stability, and ease of surface functionalization.<sup>118</sup> This procedure is the preferred option when synthesizing thiol-stabilized AuNPs.<sup>119</sup> In the original Brust-Schiffrin method, an aqueous solution of chloroauric acid is mixed with a solution of tetraoctylammonium bromide (TOAB) in toluene. TOAB acts as a phase-transfer catalyst that drags gold ions into the organic phase. The aqueous layer is then discarded, and a thiol (e.g. dodecanethiol) is added to remove TOAB from the gold complexation (through the formation of gold-sulfur bonds). Lastly, a solution of sodium borohydride ( $\text{NaBH}_4$ ) reduces the unbound ions to metallic gold, resulting in the final AuNP.<sup>120</sup>

### C. Experimental techniques for studying metal nanoparticles

Experimental techniques can shed light on the structural and dynamical features of AuNPs. The most common techniques can be divided into four categories i) those that offer direct information about the structure of stable metal clusters, ii) those that describe the average structural features and dynamics of the monolayer, iii) those that measure in-solution or mesoscopic properties of a colloid, and iv) those that reveal information about the interaction patterns with other macromolecules or even identical NPs in a dispersed solution (**Figure 7**).

X-ray crystallography is the most reliable method for elucidating NPs. This technique has been successfully applied to several ultra-stable systems, and it has provided atomically detailed descriptions of functionalized AuNPs and AuNCs (Chapter III).<sup>121,122</sup> By tracking the diffraction of X-rays impacting a monocrystal, it is possible to deduce the average structure of the unit cell of the periodic lattice. The use of single crystal X-ray diffraction has so far been limited to small AuNPs (size less than 3 nm) strongly stabilized by the inter-ligand interactions

between neighboring periodic images. Scanning transmission electron microscopy (STEM) has emerged as an accurate and more economical alternative, which, coupled to computational optimization algorithms, can also shed light on the atomic arrangement of gold atoms in bigger cores.<sup>123</sup> The structural features of the metallic core can also be indirectly inferred with techniques like IR spectroscopy and vibrational circular dichroism (VCD), which provide a unique profile for distinct enantiomers.<sup>124,125</sup>

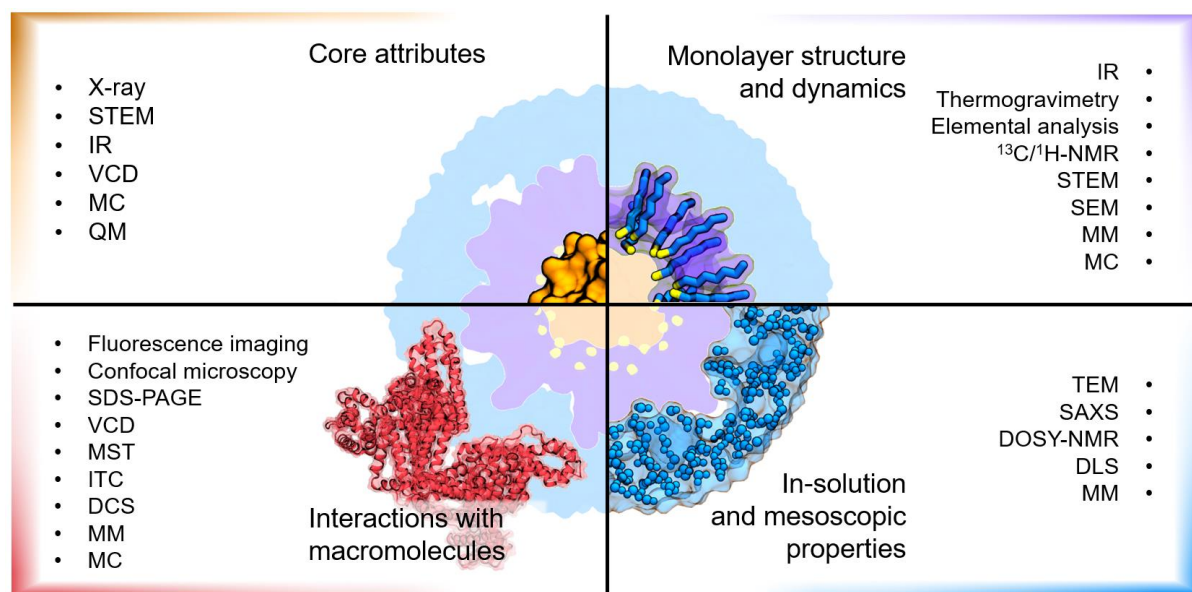


**Figure 7.** Experimental and computational techniques commonly used to study AuNPs. The techniques listed in the top left panel are useful for resolving the internal structure of the metallic core and the gold-sulfur interface. The techniques in the top right panel can provide dynamic and average structural features of the monolayer. The techniques in the bottom right panel provide mesoscopic information of colloidal AuNPs like their propensity to aggregate through the mainstream metric  $\zeta$ -potential. The techniques in the bottom left panel shed light on the interactions between AuNPs and other macromolecules. The acronyms in the figure stand for scanning transmission electron microscopy (STEM), infrared (IR) spectroscopy, vibrational circular dichroism (VCD), nuclear magnetic resonance (NMR) spectroscopy, scanning electron microscopy (SEM), transmission electron microscopy (TEM), small angle X-ray scattering spectroscopy, diffusion ordered (DOSY)-NMR spectroscopy, dynamic light scattering (DLS), sodium dodecyl sulfate (SDS)-polyacrylamide gel electrophoresis (PAGE), microscale thermophoresis (MST), isothermal titration calorimetry (ITC), differential centrifugal sedimentation (DCS), quantum mechanical (QM) simulations, molecular mechanical (MM) simulations, and Monte Carlo (MC) simulations.

Zooming out from the metallic core, there are several techniques that can shed light on the composition and arrangement of the coating monolayer. For example, shifts in the IR spectra of gold colloids can indicate the conjugation of the thiols on the surface.<sup>126</sup> Thermogravimetry and elemental analysis can be used to derive the stoichiometric formula of the coating

monolayer and deduce its purity.<sup>127</sup> Furthermore, despite the intrinsic flexibility of the coating ligands, the average structural features are still accessible. The shifts in <sup>13</sup>C-nuclear magnetic resonance (NMR) spectroscopy signals can reveal the mean distance between the metallic core and the different types of carbon atoms, as well as their bending angles (i.e. order parameters).<sup>128</sup> For mixed monolayers, the ligands' grafting pattern (i.e. monolayer morphology) can be inferred from <sup>1</sup>H-NMR,<sup>129</sup> high-resolution STEM,<sup>130</sup> or scanning electron microscopy (SEM).<sup>131</sup>

One can also investigate the protein corona formed on AuNPs upon their introduction to biological matrices. Upon protein conjugation, VCD can reveal modifications in the secondary structure of the peptides, and methods like microscale thermophoresis (MST) and isothermal titration calorimetry (ITC) can be used to quantify the binding energy between macromolecules.<sup>132,133</sup> In other approaches, the numerous components of the corona can be separated and characterized according to their molecular weight through SDS-polyacrylamide gel electrophoresis (PAGE). Similarly, differential centrifugal sedimentation (DCS) can recognize the complexation of proteins on AuNPs by measuring the agglomerate's size-dependent sedimentation time.

Size is poorly defined for NPs because diverse experimental techniques provide equally valid, yet different interpretations. Specifically, transmission electron microscopy (TEM) maps the electronic density of unilamellar samples, thus providing the marginal size of the gold core.<sup>134</sup> Other methods, like small-angle X-ray scattering (SAXS), can provide the radially weighted center of mass, or radius of gyration, which better indicates the mass distribution within the AuNP.<sup>128</sup> The hydrodynamic radius of AuNPs can also be estimated from diffusion ordered (DOSY)-NMR spectroscopy. DOSY-NMR measures the diffusion coefficient of a hydrogen-containing species, which can then be related to the hydrodynamics radius of AuNPs by the Stokes-Einstein equation (Chapter III).<sup>135</sup> Lastly, the electrophoretic ratio of AuNPs is another variable related to the diffusion of the massive body in the presence of an external electrical field. More importantly, the electrophoretic radius is the distance at which the electrostatic potential of the AuNPs becomes the  $\zeta$ -potential (Chapter VII). The electrophoretic radius, and therefore the  $\zeta$ -potential, can be quantified with dynamic light scattering (DLS).<sup>136</sup>

The  $\zeta$ -potential is in many cases the go-to metric to determine the colloidal stability of AuNPs, but it is insufficient for studying their interactions with neighboring molecules. The self-aggregation of AuNPs can be further monitored by changes in the ultraviolet (UV)-Vis

electromagnetic range (Chapter VII). Another test of biomedical relevance is the use of inductively coupled plasma (ICP)-atomic emission spectroscopy (AES) to measure the particles' tendency to releasing heavy metal ions and therefore the AuNPs' stability and toxicity in acidic media.<sup>137</sup> The reactivity of AuNPs can also be explored by absorbance changes during quenching experiments in the presence of a substrate (e.g. hydrogen peroxide).<sup>138</sup> Where AuNPs act as sensors rather than catalysts, the recognition of an analyte is ascertained by slower relaxation times in protons as measured in <sup>1</sup>H-NMR magnetization transfer experiments.<sup>57</sup>

Cellular assays are critical to assessing AuNPs as potential biomedical devices. There are several procedures to label and monitor AuNPs in biological media. The movement of AuNPs inside cells can be monitored with confocal microscopy<sup>139</sup> and TEM,<sup>140</sup> but also with fluorescence spectroscopy due to their SPR bands.<sup>141</sup> These techniques allow the counting of AuNPs, which can then be used to quantify the cytosolic uptake. Fluorescent confocal microscopy can also be used with leakage experiments to study the permeabilization of liposomes loaded with fluorescent dyes (e.g. calcein).<sup>142</sup>

#### **D. Computational methods for studying metal nanoparticles**

Numerous computational methods have been developed and adapted to study the dynamics of AuNP-biomacromolecule interactions. The choice of a particular computational approach depends on two factors. The first factor is the length scale of the process of interest. This factor determines the size of the system to be modeled, which is directly related to the number of interaction sites needed to accurately describe the physicochemical transformation involved. The second factor is the timescale of the process of interest. As the duration of a process increases, so does the amount of resources needed to execute the corresponding calculations. Different methods account for different atomic and molecular features, and the computational scientist must balance the complex interplay between physical accuracy and computational cost.

In molecular simulations, computational scientists study a controlled number of particles in a finite volume. Here, 'particles' refers to the basic chemical unit adopted in the simulations. This can mean subatomic entities (e.g. nuclei and electrons), entire atoms, or even segments of molecules. The chosen unit, in turn, determines the resolution of the simulation, thus capturing a specific set of processes. For example, describing molecular polarization, charge transfer,

and aromaticity requires the explicit description of electrons, while other phenomena like self-diffusion, physical adsorption, and non-covalent binding can be studied at coarser resolutions. In this sense, computational methods can be classified according to their resolution in one of three categories: quantum mechanical, atomistic, and mesoscopic.

Quantum mechanics (QM)-based models numerically solve Schrödinger's equation. In this way, quantum-based methods offer a framework to accurately describe the molecular orbitals of a given system. The shape of the orbitals (i.e. their atomic coefficients) provides an in-depth understanding of the distribution of the electrons around a molecule.<sup>143</sup> Because the electronic cloud of molecules ultimately dictates their physicochemical properties, QM methods are particularly useful for rationalizing electron-based phenomena. In nanotechnology, this methods can be used to model the photoexcitation of AuNPs,<sup>144</sup> compute absorbance spectra in fluorescent AuNCs,<sup>145</sup> estimate SPR frequencies,<sup>146</sup> and unravel the reaction path followed by nanozymes. QM is currently the most accurate framework available. However, QM methods demand the iterative solution of self-consistent equations whose complexity increases exponentially with the number of electrons in the system. QM calculations require long computing times and large amounts of processing units compared to other methods presented in this chapter. Consequently, the accuracy of these methods is often overshadowed by their cost, and thus they are mainly used for systems comprising up to hundreds of atoms.<sup>147</sup>

Atomistic approaches are based on the molecular mechanical (MM) framework, and they describe each atom as a single interaction site. In contrast to QM methods (based on Schrödinger's equation), MM methods are based on classical mechanics (Newton's second law). Atomistic models are more computationally efficient than their QM counterparts because the electrons of the system (i.e. the molecular orbitals) are not described individually. Instead, each atom is assigned a collection of parameters that are fitted to reproduce experimental or QM data.<sup>148</sup> A force field (FF) is formed by the collection of all the assigned parameters as well as the mathematical functions that link it to the potential energy of a system (Chapter II).

The reduced number of equations to solve in atomistic simulations makes them a viable alternative for studying nanometer-long systems with up to millions of atoms for several microseconds. In this sense, atomistic methods have become a go-to approach when studying detailed, nonbonded interactions between biomacromolecules, polymers, and NPs.<sup>149</sup> For NPs, atomistic models have been used, for example, to characterize the Michaelis-Menten complex of nanozymes catalyzing the cleavage of phosphodiester bonds.<sup>56</sup> Similar simulations have



been used in chemosensing to determine the dynamics and energetics of small analytes binding to NP monolayers.<sup>57</sup> Atomistic approaches can also be used to dissect the interaction patterns between multiple macromolecules. These methods can shed light on how functionalized NPs translocate across lipid bilayers<sup>150</sup> or associate to matrix proteins, which are two critical processes for NP biocompatibility.<sup>151</sup>

The last category, mesoscale approaches, includes a wide range of methodologies in which each interaction site (bead) represents a group of atoms. The most commonly encountered mesoscale methods in nanotechnology are coarse-grain (CG) simulations and dissipative particle dynamics (DPD). CG is inspired by atomistic approaches and are thus subject to the same mathematical treatment. However, CG methods group several atoms into an individual interaction site, providing a coarser molecular resolution (Chapter II).<sup>152</sup> In contrast, DPD is based on Langevin's equation, in which each bead is subject to three forces: i) an external conservative force, ii) a dissipative force, and iii) a random force.<sup>153</sup> Due to its formulation, DPD is meant to simulate microscopic hydrodynamic phenomena.<sup>154</sup> Importantly, in mesoscale methods, the length, time, and energy scales cannot be immediately derived from the number of beads or their parameters. In fact, their physical correspondences are obtained by estimating an observable such as the diffusion coefficient of water or the thickness of a lipid bilayer.<sup>155</sup>

Mesoscale methods are a valuable alternative for simulating systems of hundreds of nanometers in size for up to a couple of milliseconds. These methods achieve semi-quantitative agreement with experiments in systems where the dynamics are mainly governed by dispersive forces. CG and DPD approaches have been extensively used to study NPs interacting with lipid bilayers. Specifically, they can be used to describe the collision of NPs with vesicles,<sup>78</sup> receptor-mediated endocytosis,<sup>155,156</sup> and cooperative cellular internalization.<sup>76,157</sup> Due to the dimensions of the protein corona, mesoscale methods are also useful for understanding the complexation of NPs to multiple human serum albumin molecules.<sup>158,159</sup> Recently, CG models have also been used to rationalize how a medium's ionic strength affects the aggregation of metal NPs (Chapter VII).<sup>160</sup>

In addition to the three above-mentioned methodologies, other strategies have provided valuable insights about AuNPs. For example, Monte Carlo (MC) simulations, which allow the sampling of out-of-equilibrium states, have revealed the snorkeling configuration that charged AuNPs adopt once embedded in a membrane.<sup>161,162</sup> Similar techniques have been used to study ligand migration on the surface of AuNPs.<sup>163</sup> Another example is hybrid particle-field

dynamics, which fuses the molecular resolution of CG approaches with the computational efficiency of coarser mean-field methods and which has been used to study the aggregation of functionalized NPs.<sup>164,165</sup> Lastly, a variety of theoretical models, such as the Helfrich Hamiltonian,<sup>166</sup> have been used to study the interaction between adhesive NPs and cell membranes.<sup>167,168</sup>

## **E. Scope of the present thesis**

The present work has four aims. The first aim is to develop informatics tools to build realistic models of NPs. Until recently, preparing 3D models of metal NPs required the efforts of the interested researchers. Motivated by this lack of accessibility, this thesis aims to facilitate the atomistic and CG modeling of functionalized metal NPs. The second aim is to support the rational design of metal NPs, after standardizing a setup for molecular simulations, by developing a computational method to screen AuNPs for their ability to recognize specific organic analytes. The third aim is to use theoretical, atomistic, and CG approaches to understand the physical principles that govern NP aggregation in physiological conditions. The fourth aim is related to the interaction between functionalized metal NPs and cell membranes, which is a biological barrier that therapeutic agents must overcome for optimal performance. Here, the aim is to understand the singular non-disruptive translocation of metal NPs that bear charged membranotropic ligands in their coating.

In sum, this work deals with multiple aspects of metal NPs in biomedicine, covering a broad range of topics including molecular modeling, method development, first principles in colloid science, and concrete biomedical applicability. The document is organized as follows:

- Chapter II discusses the theoretical foundations behind the methods implemented in the rest of the work. This chapter focuses on the physical and mathematical principles behind molecular mechanics, molecular dynamics, and free energy calculations.
- Chapter III discusses the NanoModeler webserver. This novel technological tool facilitates the atomistic modeling and engineering of functionalized AuNPs and AuNCs.
- Chapter IV discusses models generated with NanoModeler to study the interaction between various cationic AuNPs and lipid bilayers. In particular, this chapter discusses the extension of ‘arginine magic’ to AuNPs in order to enhance their translocation rates

across cellular membranes, without jeopardizing the biocompatibility of the metal assemblies.

- Chapter V discusses a molecular-dynamics-based method to screen libraries of AuNPs to identify structures that can recognize organic analytes. The methodology is applied to a library of amino acid-coated AuNPs that could aid the early diagnosis and prognosis of neuroblastoma.
- Chapter VI discusses NanoModeler CG, the second release of the original webserver that now supports the modeling of functionalized metal NPs at a CG resolution.
- Chapter VII discusses models generated with NanoModeler CG to study the dispersion state of citrate-stabilized gold colloids. Here, a new theoretical model is combined with multiscale simulations and UV-Vis spectroscopy experiments to rationalize the effect of the ionic strength on the dispersivity of gold nanosuspensions.
- Chapter VIII discusses the interactions between peptide-coated metal NPs and lipid bilayers. This chapter discusses the use of models generated with NanoModeler CG to explain the enhanced cellular uptake of NPs in the presence of a membranotropic coating.
- Chapter IX summarizes the key findings and comments on the impact and perspectives of the projects.

## CHAPTER II. THEORY AND PRINCIPLES

### A. Molecular mechanics

Molecular mechanics (MM) is a computational method that calculates the total energy of a chemical system based on classical mechanics. MM comprises a large family of computational methods employed for studying a microscopic portion (simulation box) of macroscopic systems (**Figure 8a**). Molecules are represented as collections of interaction sites (i.e. particles), described by a partial charge and an atom type, with an immutable connectivity that represents the chemical bonds in the system (**Figure 8b**). In MM-based methods, the total energy of a system ( $E$ ) is the sum of its classical kinetic energy ( $K$ ) and the potential energy ( $U$ , Equation 1). Moreover, the potential energy is expressed as a function of the masses, ( $\{m\}$ ), the partial charges ( $\{q\}$ ), the atom types ( $\{\aleph\}$ ), the system's connectivity ( $\Omega$ ), and the positions ( $\{\mathbf{r}\}$ ) and linear momenta ( $\{\mathbf{p}\}$ ) of all the atoms (Equation 2). Note that for a system with  $N$  particles, the corresponding phase space has  $6N$  dimensions, that is,  $3N$  position coordinates and  $3N$  velocity coordinates (**Figure 8c**,  $\Gamma = \Gamma(\{\mathbf{r}\}, \{\mathbf{p}\})$ ).<sup>169</sup> In this way, a molecular simulation is the collection of all the parameters above (i.e.  $\{m\}$ ,  $\{q\}$ ,  $\{\aleph\}$ ,  $\Omega$ ) at multiple points of a system's phase space.

$$E = K + U = \sum_i^N \frac{p_i^2}{2m_i} + U \quad (1)$$

$$U = U(\Gamma, \{q\}, \{\aleph\}, \Omega) \quad (2)$$

The atomic partial charges reflect the heterogeneity of the electron distribution along a system. In this way, particles with a dense electronic cloud are assigned negative charges, whereas sites deficient in electrons are assigned positive values. Electron density differences arise from differences in electronegativity (e.g. polar bonds or hydrogen bonds), polarizing sources (e.g. external electric fields or ion gradients), and resonant moieties (e.g. aromatic rings or amides). Notably, the sum of all the partial charges adds up to the net charge of the system.<sup>170</sup> Furthermore, the atom type is a categorical variable characteristic of the specific chemical environment of each atom. The atom type defines how an atom interacts with the rest of sites in a system.<sup>171</sup> In principle, each atom in a system (without any molecular symmetry) should

have a unique atom type because it is exposed to a unique chemical environment. However, this would lead to an innate non-transferability of MM methods because new atom types would have to be formulated for each system. In practice, the atom types are generic labels for atoms with similar chemical environments and connectivity, e.g. the oxygen atom of aliphatic ketones is always assigned the same atom type for any aliphatic ketone.

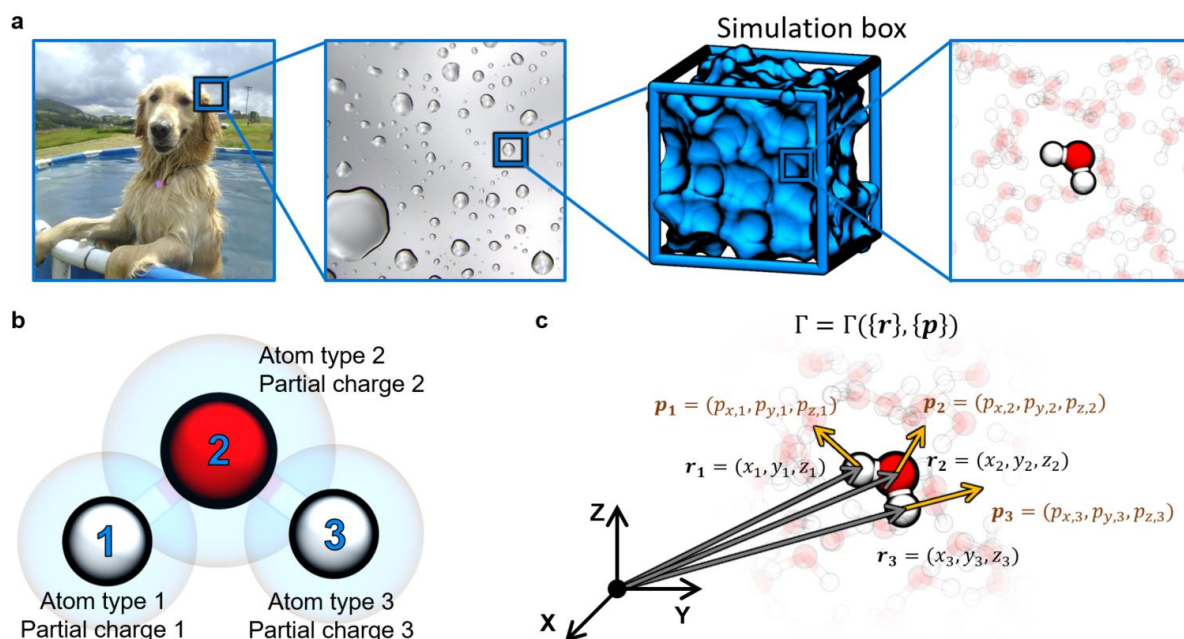


**Figure 8.** Description of a water droplet in MM. **a.** Simulation box containing the particles to be simulated computationally. **b.** Representation of a water molecule in MM. Each particle (atom) is identified by a partial charge and an atom type. **c.** Phase space of a system composed by water molecules. The vectors illustrate the three position and three momentum coordinates for one of the molecules. Bulk water is shown in blue, oxygen atoms in red and hydrogen in white.

### 1. Force field functionals

In MM-based methods, molecules are modeled as a series of point charges connected by bonded interactions described by individual contributions to the total potential energy  $U$  (**Figure 9a**). A force field (FF) is defined by a functional for the potential energy ( $U$  in Equation 2) and a collection of atom types.<sup>172</sup> FFs separate the potential energy of a system in two components: the bonded ( $U_b$ ) and nonbonded energy ( $U_{nb}$ , Equation 3). The bonded term accounts for the energy associated with intramolecular geometrical deformations, while the nonbonded term accounts for inter-particle pair potentials.<sup>149</sup>

$$U = U_b + U_{nb} \quad (3)$$

Biomolecular FFs decompose  $U_b$  into four terms (Equation 4): i) bond stretching, ii) angle bending, iii) proper dihedral torsion, and iv) out-of-plane torsion. The first of these contributions,  $U_{stretch}$ , is modeled by a Morse potential, which is repulsive at short bond lengths, attractive at bond lengths close to an equilibrium value, and zero at long distances. However, when the bond lengths are not expected to deviate significantly from their equilibrium values, the Morse potential is often replaced by a Taylor expansion, which is also more computationally efficient. For a system comprising  $N_{bonds}$  bonds, the bonded energy  $U_b$  is given by Equation 5, where  $l_i$  is the length of the  $i$ -th bond,  $l_{0,i}$  its equilibrium value, and  $k_{b,i}$  its force constant (**Figure 9b**).<sup>148</sup>

$$U_b = U_{stretch} + U_{bend} + U_{torsion} + U_{out-of-plane} \quad (4)$$

$$U_{stretch} = \sum_i^{N_{bonds}} k_{b,i} (l_i - l_{0,i})^2 \quad (5)$$

As with the stretching term, angle bending can be described as a second-order Taylor series, and the accuracy of the modeling can be improved by including higher order terms in the expansion. In general, for a system comprising  $N_{angles}$  angles, the bending energy is given by Equation 6, where  $\theta_i$  is the value of the  $i$ -th angle,  $\theta_{0,i}$  its equilibrium value, and  $k_{\theta,i}$  its force constant (**Figure 9c**).<sup>148</sup>

$$U_{bend} = \sum_i^{N_{angles}} k_{\theta,i} (\theta_i - \theta_{0,i})^2 \quad (6)$$

In contrast to the previous two terms, the proper dihedral torsion energy cannot be expressed as a truncated Taylor expansion because it must oscillate in order to reproduce the periodicity of proper dihedral rotation. Furthermore, the maxima in the periodic potential should have different amplitudes according to the substituents at both ends of the dihedral, and it should also depend on the nature of the rotating bond. Based on these considerations, the torsion potential is expressed as a sum of cosine (or sine) functions, where the number of functions to add ( $N_{cosine}$ ) depends on the FF. For a system comprising  $N_{dihedrals}$  dihedral angles, the torsion energy is given by Equation 7, where  $\phi_i$  is the value of the  $i$ -th dihedral, and  $\phi_{0,j,i}$ ,  $V_{\phi,j}$ , and  $n_j$  are the phase, magnitude, and multiplicity of the  $j$ -th function, respectively (**Figure 9d**).<sup>148</sup>

$$U_{torsion} = \sum_i^{N_{dihedrals}} \sum_j^{N_{cosine}} \frac{V_{\phi,j}}{2} [1 + \cos(n_j \phi_i - \phi_{0,j,i})] \quad (7)$$

The three aforementioned potentials are adjusted to obtain realistic 3D geometries at a molecule's potential energy minima. Nonetheless, they turn out to be insufficient at reproducing the structural changes of cyclic molecules since they underestimate the strain among the enclosed atoms. As a response to this caveat, most FFs include an out-of-plane or improper torsion term  $U_{out-of-plane}$ . This interaction takes place between four atoms belonging to the same molecule not necessarily bonded consecutively. Mathematically, the function adopted for improper torsions can be the same as for proper torsions (Equation 7), but some FFs also implement harmonic potentials (**Figure 9e**).<sup>148</sup>

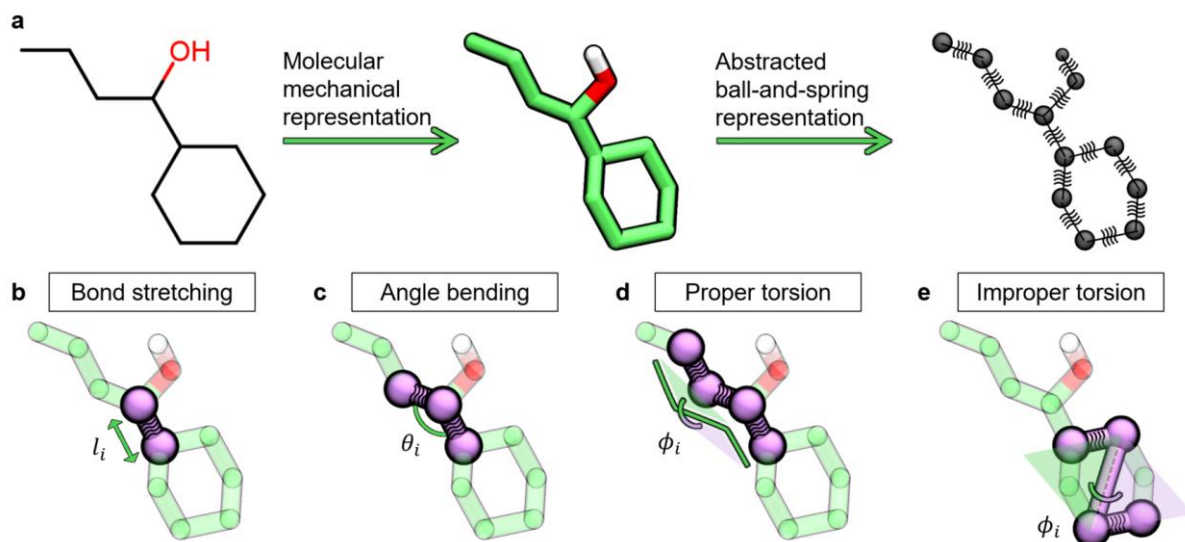


**Figure 9.** Bonded energy terms contributing to a conventional FF. **a.** Computational modeling of 1-cyclohexyl 1-butanol in a classical FF. A molecule is described as a series of points (atoms) with a predetermined connectivity. From a physical perspective, the atoms are bound to each other by springs. The internal potential energy of the molecule is calculated as the sum of the bond stretching (**b**), angle bending (**c**), dihedral torsion (**d**), and out-of-plane bending (**e**) terms.

In addition to the four bonded interactions described above, FFs may also include cross-terms that account for the coupling between different internal coordinates. For example, stretch-stretch terms are potential energy functions that include the length of two bonds. The most frequently encountered cross-terms are stretch-stretch, stretch-bend, bend-bend, stretch-torsion, and bend-bend-torsion. The use of cross-terms can be useful at reproducing specific crystallographic or spectroscopic data at the expense of a reduced simulation performance (i.e.

simulated time per unit of running time). However, the work presented here employs FFs that do not include cross-terms.<sup>148</sup>

The nonbonded interactions ( $U_{nb}$ ) included in classical mechanical FFs arise from electrostatic ( $U_{elec}$ ) and van der Waals forces ( $U_{vdW}$ , Equation 8). As stated above, classical mechanics represent molecules as a collection of point charges. Consequently, the electrostatic energy of a system consisting of  $N$  particles is given by Coulomb's formulation (Equation 9), where  $q_i$  is the partial charge of the  $i$ -th particle,  $r_{ij}$  is the distance between particles  $i$  and  $j$ ,  $\epsilon_0$  is the vacuum permittivity (**Figure 10** left panel). Importantly, the condition at the bottom of the second sum in Equation 9 ensures that each pairwise interaction is only counted once.<sup>148</sup>

$$U_{nb} = U_{elec} + U_{vdW} \quad (8)$$

$$U_{elec} = \sum_i^N \sum_{j>i}^N \frac{q_i q_j}{4\pi\epsilon_0 r_{ij}} \quad (9)$$

If electrostatics alone were considered by FFs, molecules would not have any volume, and charges of opposite sign would annihilate each other. FFs also account for van der Waals forces, specifically, London dispersion forces and exchange-correlation forces, two interactions of quantum mechanical origin. On the one hand, London dispersion forces arise from instantaneous dipole moments within molecules that induce a dipole in neighboring molecules, leading to an attractive inductive effect. On the other hand, exchange forces arise from the inability of electrons to share the same quantum numbers (i.e. the Pauli exclusion principle), which, regulates the overlap of electron densities belonging to different molecules. In MM, London forces are typically modeled as functions that scale with  $r^{-6}$  and exchange forces with a scaling of  $r^{-12}$ , thus, the former dominates at long inter-particle distances whereas the latter at short distances. In sum, van der Waals interactions are expressed as a 6-12 Lennard-Jones potential (Equation 10), where  $\epsilon_{ij}$  is the well depth, and  $\sigma_{ij}$  is the distance at which the London and exchange contributions cancel out for the  $i$ - $j$  pair (**Figure 10** right panel).<sup>148</sup>

$$U_{vdW} = \sum_i^N \sum_{j>i}^N 4\epsilon_{ij} \left[ \left( \frac{\sigma_{ij}}{r_{ij}} \right)^{12} - \left( \frac{\sigma_{ij}}{r_{ij}} \right)^6 \right] \quad (10)$$



Note that the  $\epsilon_{ij}$  and  $\sigma_{ij}$  parameters should be unique for each pair of atoms in the system. Therefore, the number of parameters should increase quadratically with the number of atom types (i.e.  $\sim N^2$ ). This would again limit the transferability of FFs since it would quickly result in an unmanageable number of free parameters. Instead of explicitly defining all possible permutations, combination rules are employed to derive the parameters for each atom pair based on self-interacting attributes denoted as  $\epsilon_{ii}$  and  $\sigma_{ii}$  from the individual atom types involved. One set of rules commonly employed are the Lorentz-Berthelot rules (Equations 11 and 12).<sup>173</sup>

$$\sigma_{ij} = \frac{1}{2}(\sigma_{ii} + \sigma_{jj}) \quad (11)$$

$$\epsilon_{ij} = (\epsilon_{ii}\epsilon_{jj})^{\frac{1}{2}} \quad (12)$$

Different FFs can employ expressions mathematically equivalent to Equation 10 to describe van der Waals interactions for the sake of computational efficiency and/or consistency in the parametrization schemes. In the present work, the function in Equation 13 is particularly relevant. The relation between Equations 10 and 13 is given by Equations 14 and 15. The combination rules associated to Equation 13 are shown as Equations 16 and 17.<sup>174</sup>

$$U_{vdW} = \sum_i^N \sum_{j>i}^N \left( \frac{A_{ij}}{r_{ij}^{12}} - \frac{B_{ij}}{r_{ij}^6} \right) \quad (13)$$

$$A_{ij} = 4\epsilon_{ij}\sigma_{ij}^{12} \quad (14)$$

$$B_{ij} = 4\epsilon_{ij}\sigma_{ij}^6 \quad (15)$$

$$A_{ij} = (A_{ii}A_{jj})^{\frac{1}{2}} \quad (16)$$

$$B_{ij} = (B_{ii}B_{jj})^{\frac{1}{2}} \quad (17)$$

The electrostatic and van der Waals interactions are both pair potentials that are summed for all atom pairs in the system. Nonetheless, atoms within the same molecule can be reasonably found at very short distances from one another due to the bonded interactions ( $U_b$ ). In order to avoid the divergence of the repulsive forces between such atoms, FFs exclude certain pairs

from nonbonded calculations. In detail, atom pairs in a molecule separated by  $N_{excl}$  bonds or less are skipped during the computation of  $U_{nb}$ . Values for  $N_{excl}$  typically range between 1 and 3 depending on the FF.<sup>175</sup>

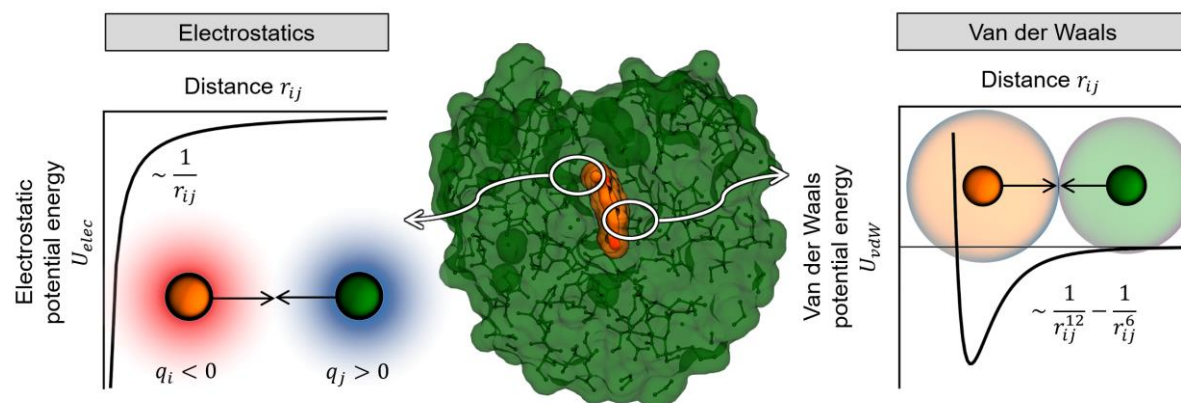


**Figure 10.** The interaction between two different molecules (in orange and green in the middle panel) is driven by electrostatic and van der Waals interactions. Electrostatics (left panel) are described by Coulomb’s law; thus, the potential is always attractive for partial charges of opposite sign and repulsive for partial charges equally signed. Van der Waals interactions (right panel) confer molecules their volume and prevent the annihilation of charges of opposite sign as promoted by electrostatics. The van der Waals interactions are described by a Lennard-Jones potential that displays a global minimum at the distance where the molecular surfaces contact each other.

## 2. Coarse-grained force fields

FFs offer a mathematical framework for calculating the potential energy of a system of particles. In the previous section, the terms ‘particle’ and ‘atom’ were interchangeable. However, the classical mechanical framework can be generalized to coarser interaction sites. In coarse-grained (CG) systems, multiple atoms are grouped into an individual particle – or bead – that represents the indivisible chemical units of the system (**Figure 11**).<sup>176</sup> Similar to atoms in atomistic simulations, beads are identified with a bead type and a partial charge. The bead types are associated with a set of bonded and van der Waals parameters, while the partial charges are employed for the calculation of the electrostatic potential energy. Importantly, in CG FFs, the mass of each bead must be adjusted to equal the mass of the atoms that the bead represents.<sup>177</sup>

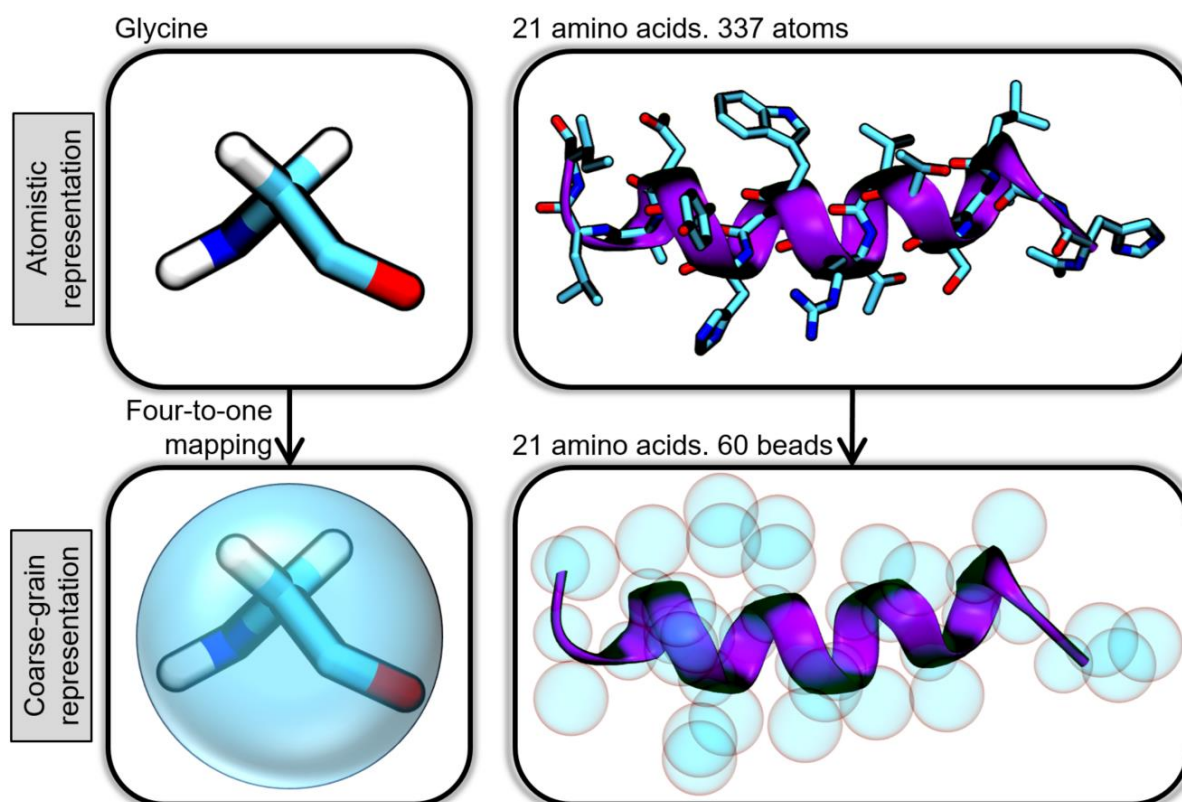


**Figure 11.** Conceptual principles behind CG representations. Various atoms are grouped into a single interaction site known as bead. Glycine, an amino acid composed by four heavy (i.e. non-hydrogen) atoms, is mapped into a single bead following the four-to-one scheme of the Martini FF. Similarly, the number of interaction sites in the gH625 oligopeptide (21 amino acids long), is reduced from 337 in its atomistic representation to 60 after coarse-graining. CG beads and carbon atoms are shown in cyan, nitrogen in blue, oxygen in red, and the secondary structure of gH625 in purple.

CG methods reduce the number of degrees of freedom in the system (i.e.  $N$  decreases), making it more computationally efficient than its atomistic counterpart at the expense of reduced resolution. The reduction in degrees of freedom depends on the mapping scheme adopted, that is, the number of atoms that are packed into one bead. Therefore, the mapping scheme dictates the gain in computational performance and loss of spatial resolution.<sup>178</sup> In CG methods, since atomic detail is lost, some interactions are jeopardized. For example, the H-bond networks responsible for the secondary structure in proteins are limited. For this reason, when modeling biomacromolecules, it is a common practice to implement elastic networks that bias the geometry of the system toward a known, reliable state.<sup>179,180</sup> At their core, elastic networks are a series of bonds that are added to the potential energy function of the force field.

The most commonly employed CG FF for biomacromolecular simulations is Martini.<sup>181,182</sup> This FF uses a four-to-one mapping scheme, meaning that, in average, four heavy (i.e. non-

hydrogen) atoms are mapped into one bead. It is important to note that the mapping scheme of an FF is a guide as for how to parametrize a system, rather than a rule. The CG mapping is not absolute even within the same FF. Equivalently, there are many ways to map the same molecule into a CG FF.<sup>183</sup>

### 3. *Parametrization*

Atomistic and CG FFs comprise a mathematical function for the calculation of the potential energy of a system as well as the free parameters present in such function, yet there is not a unique protocol for deriving the free parameters. Every FF adopts a different parametrization procedure, which determines the FF's reach and applicability. The parameters are typically fitted to reproduce experimental measurements or, when unavailable, quantum mechanics (QM) data.<sup>184</sup> The OPLS-UA FF, for example, was originally parametrized to reproduce heats of vaporization and densities of organic liquids.<sup>185</sup> Other FFs, like the Gromos series, have been parametrized against partition coefficients of organic molecules.<sup>186,187</sup> Subsequently, the choice of the FF to employ is not always trivial, and it must be tailored to the system and properties of interest. A clear example of this is the multiple FFs available for water, each with its strengths and caveats. For example, force fields like SPC/FW,<sup>188</sup> TIP4P-EW,<sup>189</sup> and TIP7P<sup>190</sup> are successful at reproducing the self-diffusion coefficient of liquid water, but they all underestimate dramatically its dipole moment (errors ca. 20%).

The choice of the FF must be based on three factors: i) accuracy, ii) computational cost, and iii) compatibility. Regarding the first factor, FFs including more potential energy functions generally display an improved accuracy over those with less terms. However, including more functions in the expression for the potential energy can significantly increase the computational cost associated with the calculation. In the case of water, for example, the TIP3P model<sup>191</sup> contains one interaction site centered at each atom's nucleus, making it a computationally efficient alternative compared to more complex representations of water like TIP4P,<sup>191</sup> TIP5P,<sup>192</sup> and TIP7P.<sup>190</sup> Lastly, when considering a multi-component system (e.g. a lipid bilayer in water), it is also important to consider the compatibility between FFs. If the combined use of FFs is not benchmarked prior to their use, unphysical artifacts may arise during a simulation. Using FFs belonging to the same family grants compatibility in the assigned parameters.<sup>193</sup> In the present work, two families of FFs are employed: AMBER for the atomistic and Martini for the CG simulations.

The AMBER series includes FFs for the simulation of various biomacromolecules and related compounds. The FF14SB FF is used for simulating proteins, and it is parametrized against conformational energies derived from QM calculations.<sup>194</sup> The Parmbsc1 FF, fitted to reproduce hydration free energies, is used for nucleic acids.<sup>195,196</sup> The Generalized Amber Force Field (GAFF) is a transferable FF used for simulating small organic molecules that is fit to crystallized and QM-derived structures.<sup>197</sup> Lipids are also supported through the LIPID17 FF parametrized against experimental structural features of phospholipid bilayers.<sup>198,199</sup> In regard to nanoparticles (NPs), functionalized gold nanoparticles and nanoclusters were first contemplated by Pohjolainen and co-workers, who, in 2016, fitted an AMBER-compatible FF to QM vibrational spectra.<sup>200</sup> As for aqueous solvents, the AMBER family of FFs is compatible with the TIP3P water model.<sup>191</sup> This model is particularly useful as it reproduces the dielectric constant of liquid water (error of 5%), enabling it to accurately propagate electrostatic forces exerted by solvated species.<sup>201</sup> Importantly, the AMBER FFs also offer a standardized protocol for the parametrization of new residues. In this workflow, the atom types are assigned to the molecule by analogy to those already implemented in GAFF.<sup>202</sup> Moreover, the atomic partial charges of the molecule are fitted to reproduce the QM electrostatic potential at the Hartree-Fock/6-31G\* level of theory.<sup>203–206</sup>

The Martini family of FFs is a collection of FFs commonly employed for polymeric systems at a CG resolution. Its initial release was intended for the simulation of proteins, nucleic acids, and lipids; however, its parameters database has been successfully transferred to the simulation of functionalized metal NPs.<sup>207</sup> Over time, this family of FFs has also been adapted to polymers like polyethylene glycol,<sup>208,209</sup> polystyrene sulfonate, and polydiallyldimethylammonium.<sup>210</sup> In contrast to the AMBER series, the Martini FFs are parametrized to reproduce the partition coefficients of small organic molecules.<sup>181,211,212</sup> The Martini FF also counts with its own water models like refPol, which accurately reproduces the dielectric constant of water.<sup>213–216</sup>

## B. Molecular dynamics simulations

Molecular dynamics (MD) is a computational method that generates a succession of temporally correlated structures. An MD run thus samples a system's phase space for a time  $T_{max}$ . In fact, an MD trajectory consists of  $N_{frames}$  frames each corresponding to a different point in the  $6N$ -dimensional phase space. The temporal correlation between the  $N_{frames}$  snapshots allows estimating the expected value of an experimentally measurable property as a time ( $t$ ) average.

Equation 18 describes an experimental observable property  $O$  as the approximation made by MD simulations.<sup>217</sup>

$$\langle O \rangle = \frac{1}{T_{max}} \int_0^{T_{max}} O(\Gamma, t) dt \cong \frac{1}{N_{frames}} \sum_i^{N_{frames}} O(\Gamma, t) \quad (18)$$

Classical MD is a computational method that combines MD algorithms with Lagrangian mechanics, a formalism in which the Lagrangian  $\mathcal{L}$  is the fundamental quantity of a system. The Lagrangian is given by Equation 19 for a system of particles, and the dynamics of the particles is described by the Euler-Lagrange equation (Equation 20), with  $\nabla_i$  and  $\nabla_{v_i}$  as the vector differential operators with respect to the position (Equation 21) and velocity (Equation 22) coordinates of particle  $i$ , respectively.<sup>218</sup>

$$\mathcal{L}(\Gamma, t) = K(\Gamma, t) - U(\Gamma, t) \quad (19)$$

$$\nabla_i \mathcal{L}(\Gamma, t) - \frac{d}{dt} (\nabla_{v_i} \mathcal{L}(\Gamma, t)) = 0 \quad (20)$$

$$\nabla_i = \left( \frac{\partial}{\partial x_i}, \frac{\partial}{\partial y_i}, \frac{\partial}{\partial z_i} \right) \quad (21)$$

$$\nabla_{v_i} = \left( \frac{\partial}{\partial v_{x,i}}, \frac{\partial}{\partial v_{y,i}}, \frac{\partial}{\partial v_{z,i}} \right) \quad (22)$$

If the kinetic energy is independent of the particles' position (as in Equation 1) and the potential energy is independent of the particles' velocity (as in Equation 2), Equation 20 is simplified to Equation 23.<sup>218</sup>

$$-\nabla_i U(\{\mathbf{r}\}, t) = \frac{d}{dt} (\nabla_{v_i} K(\{\mathbf{p}\}, t)) \quad (23)$$

Then, using the definition of a conservative force (Equation 24) in Equation 23 leads to Equation 25. Note that Equation 25 is Newton's second law of motion for particle  $i$ , with  $\mathbf{F}_i$  the net force acting over the particle,  $\mathbf{a}_i$  the particle's acceleration, and  $m_i$  the particle's mass. Lastly, the trajectory of particle  $i$  is obtained by solving its associated equation of motion (Equation 25).<sup>219</sup>

$$\mathbf{F}_i(\{\mathbf{r}\}, t) = -\nabla_i U(\{\mathbf{r}\}, t) \quad (24)$$

$$\mathbf{F}_i(\{\mathbf{r}\}, t) = m_i \frac{d^2 \mathbf{r}_i(t)}{dt^2} = m_i \mathbf{a}_i(t) \quad (25)$$

Equation 25 can be written for every particle in a system, which results in  $3N$  partial differential equations. Moreover, since the potential energy depends on the position of all the particles in the system, Equation 25 implies  $3N$  coupled differential equations that, in general, cannot be solved analytically, so they are approximated through numerical integration methods.<sup>217</sup>

### 1. Time integration

MD is based on solving  $\mathbf{r}_i$  in Equation 25 for all the particles in a system. In general, it is not possible to solve Equation 25 analytically, so the function  $\mathbf{r}_i(t)$  is iteratively computed for discrete times  $t + n_t \Delta t$ , where  $n_t$  is a positive integer. In order to update the position of a particle, it is necessary to know its prior velocity, which, in turn, depends on its prior acceleration. Thus, the goal of time integration is to determine the next phase space configuration in time given the present and past states. The functions  $\mathbf{r}_i(t + \Delta t)$ ,  $\mathbf{v}_i(t + \Delta t)$ , and  $\mathbf{a}_i(t + \Delta t)$  are expanded as a Taylor series about  $t$  (Equation 26).<sup>148</sup> The accuracy of the integration scheme is given by the highest power of  $\Delta t$  considered in the expansion, i.e.  $\sigma(\Delta t^n)$ . The accuracy of the integration scheme increases as more terms are included by Equation 26.<sup>148</sup>

$$\begin{aligned} \mathbf{r}_i(t + \Delta t) &= \mathbf{r}_i(t) + \Delta t \mathbf{v}_i(t) + \frac{1}{2} \Delta t^2 \mathbf{a}_i(t) + \dots \\ \mathbf{v}_i(t + \Delta t) &= \mathbf{v}_i(t) + \Delta t \mathbf{a}_i(t) + \dots \\ \mathbf{a}_i(t + \Delta t) &= \mathbf{a}_i(t) + \dots \end{aligned} \quad (26)$$

Note that, if the expansion in Equation 26 is truncated at  $\sigma(\Delta t^2)$ , the kinetic equations of motion are recovered. In this case,  $\Delta t$  can be interpreted as the duration for which the forces acting on the particles are constant, and this value should be chosen so that the fastest motions are still included in the trajectory. When choosing the timestep of the simulation the interplay between accuracy and computational cost must be considered. In general, the computational performance of a simulation increases linearly as  $\Delta t$  decreases. However, if  $\Delta t$  is too large, numerical integration will result in an inaccurate (unphysical) trajectory, or a numerical

instability leading to the eventual crash of the simulation. On the other hand, if  $\Delta t$  is too small, the simulation becomes computationally demanding without necessarily providing additional accuracy.<sup>217</sup>

In spite of there being several approaches for determining the accelerations, velocities, and positions of the particles, MD requires integration schemes that conserve the total energy of the system. Algorithms satisfying the latter condition are classified as symplectic integrators. One of the most commonly employed symplectic integrators is the leap-frog algorithm. This is a second-order,  $\mathcal{O}(\Delta t^2)$ , algorithm that iteratively updates the position and velocity vectors with a displacement of  $\Delta t/2$  (Equation 27). As with any integrator, solutions of the leap-frog scheme approach the analytical solution as  $\Delta t$  decreases.<sup>217</sup> This work utilizes the leap-frog integration scheme for all the MD simulations reported.

$$\begin{aligned} \mathbf{r}_i(t + \Delta t) &= \mathbf{r}_i(t) + \Delta t \mathbf{v}_i\left(t + \frac{1}{2} \Delta t\right) \\ \mathbf{v}_i\left(t + \frac{1}{2} \Delta t\right) &= \mathbf{v}_i\left(t - \frac{1}{2} \Delta t\right) + \Delta t \mathbf{a}_i(t) \end{aligned} \tag{27}$$

In atomistic biomacromolecular simulations, the fastest vibrational modes usually correspond to the stretching of the C-H bonds, which have a period of ca. 10 fs. A timestep of 0.5 or 1 fs should be employed to grasp these vibrations. Nonetheless, when C-H stretching plays a negligible role in the conformational changes of interest, it is a common practice to constrain the C-H bond lengths to their equilibrium value and increase the timestep to 2 fs.<sup>148</sup>

## 2. *Thermostats and barostats*

The formulation of MD described this far, allows systems to evolve in time by keeping the number of particles, volume, and total energy constant, so a microcanonical (NVE) statistical ensemble is sampled as the equations of motion are integrated.<sup>220</sup> This setup can turn out useful for studying phenomena like thermal photoporation of membranes;<sup>221</sup> however, MD simulations are typically benchmarked against experiments carried at constant temperature. Retaining a constant temperature along an MD simulation is particularly important when studying biological systems, as these can be exceptionally sensitive to overheating and/or overcooling.



From a physical standpoint, thermostats modify Newton's equations of motion. The addition of this term imposes a thermodynamic boundary condition that allows sampling a statistical ensemble at a constant temperature.<sup>220</sup> The temperature is related to the velocity of particles through the theorem of equipartition of energy (Equation 28). This theorem connects properties of a microstate ( $\{\mathbf{v}_i\}$ ) with a thermodynamic variable, in this case, the temperature. Thus, to regulate temperature thermostats modify the velocity of the particles (**Figure 12a** and **Figure 12b**). Indeed, at each timestep thermostats scale the velocities of all particles by a factor  $\lambda$  shown in Equation 29.<sup>220</sup>

$$\langle K \rangle(t) = \left\langle \sum_i^N \frac{m_i v_i(t)^2}{2} \right\rangle = \frac{3}{2} N k_B T(t) \quad (28)$$

$$\mathbf{v}_i(t + \Delta t) = \lambda(t) \mathbf{v}_i(t) \quad (29)$$

Differentiating Equation 28 with respect to the temperature, Equation 30 is obtained for  $dT$ . In parallel, using Equation 29 in the classical definition of kinetic energy for two consecutive states results in Equation 31.

$$dT(t) \cong \Delta T(t) = \frac{2}{3Nk_B} \Delta \langle K \rangle(t) \quad (30)$$

$$\begin{aligned} \Delta \langle K \rangle(t) &= \frac{1}{N} \sum_i \frac{m_i \lambda(t)^2 v_i(t)^2}{2} - \frac{1}{N} \sum_i \frac{m_i v_i(t)^2}{2} \\ &= (\lambda(t)^2 - 1) \frac{1}{N} \sum_i \frac{m_i v_i(t)^2}{2} \end{aligned} \quad (31)$$

Lastly, solving Equation 31, an expression for the change in temperature as a function of the scaling parameter  $\lambda$  can be derived (Equation 32).

$$\Delta T(t) = (\lambda(t)^2 - 1) T(t) \quad (32)$$

Thermostats use different algorithms for defining the scaling parameter  $\lambda$  so that the kinetic energy is restrained, and the temperature of the system fluctuates around a reference value  $T_0$ . For example, the Berendsen algorithm is a weak-coupling thermostat in which the system is assumed to be in contact with a fictitious thermal bath at nominal temperature  $T_0$ . With this thermostat, the rate of change of the temperature of the system is proportional to the

temperature's deviation from  $T_0$  (Equation 33).<sup>220</sup> The outcome of substituting Equation 32 into 33 is an expression for the scaling factor  $\lambda$  in terms of the instantaneous temperature and user-defined parameters ( $\tau_B$  and  $\Delta t$ , Equation 34).

$$\frac{dT(t)}{dt} \cong \frac{\Delta T(t)}{\Delta t} = \frac{1}{\tau_B} [T_0 - T(t)] \quad (33)$$

$$\lambda(t) = \left[ 1 + \frac{\Delta t}{\tau_B} \left( \frac{T_0}{T(t)} - 1 \right) \right]^{\frac{1}{2}} \quad (34)$$

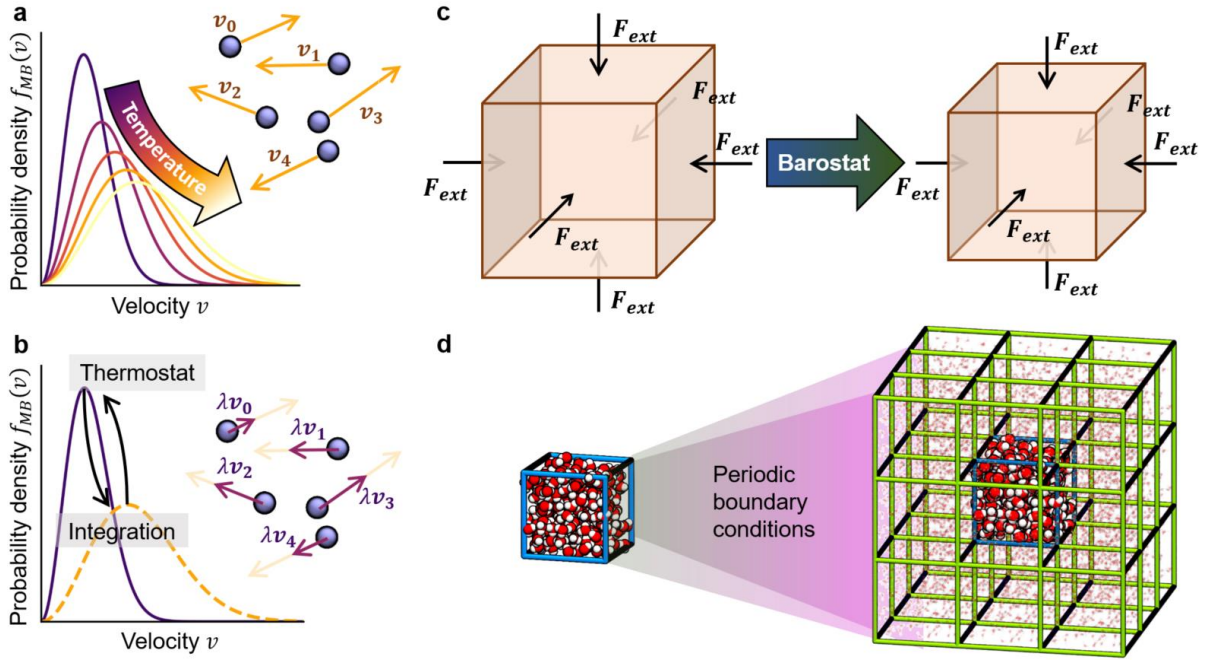


**Figure 12.** Thermostats, barostats, and PBC. **a.** Maxwell-Boltzmann probability distribution as a function of the norm of the velocity vector. **b.** A canonical thermostat scaling the velocity of the particles (purple) at each timestep toward a Maxwell-Boltzmann distribution correspondent with the target temperature. **c.** Barostats rescale the volume of the simulation box (brown) for the instantaneous pressure to drift toward the target pressure. **d.** When PBC are applied, the simulation box (blue) is virtually replicated in all three dimensions (green) to simulate a continuum.

The analytical solution of Equation 33 suggests that the temperature of the system decays exponentially with time toward the target temperature. The speed at which it decays is determined by the coupling parameter  $\tau_B$ . The optimal value for  $\tau_B$  should be determined for each system based on how successful the thermostat is at reproducing the nominal temperature and its fluctuations. In general, as  $\tau_B$  increases, the thermostat is progressively deactivated, leading to thermal fluctuations beyond what is physically reasonable. Instead, if  $\tau_B$  is too short,

the temperature fluctuations can become unrealistically small. In fact, as  $\tau_B$  approaches zero, the temperature becomes constrained at the target temperature.<sup>220</sup>

Thermostats are commonly used to simulate closed systems in an NVT statistical ensemble (i.e. constant number of particles, volume, and temperature). However, realistic NVT systems are also canonical. In canonical NVT ensembles, the probability ( $p$ ) of a state  $s$  is proportional to the Boltzmann factor (Equation 35), with  $E_s$  the total energy of state  $s$ ,  $T$  the system's absolute temperature, and  $k_B$  the Boltzmann constant. The proportionality between the probability  $p$  and the Boltzmann weighting factor is denoted by  $Z^{-1}$ , with  $Z$  as the canonical partition function of the system. The partition function  $Z$  is the sum of the Boltzmann factors associated with each microstate accessible by the system. Since the total energy depends on the (continuous) phase space, the accessible states are summed over by a  $6N$ -dimensional integral in Equation 36.<sup>222</sup>

$$p = p(N, V, T, s) = Z^{-1} e^{-\frac{E_s}{k_B T}} \quad (35)$$

$$Z = Z(N, V, T) = \frac{1}{h^3} \int e^{-\frac{E(\Gamma)}{k_B T}} d\Gamma \quad (36)$$

The velocity of the particles in canonical statistical ensembles follow a Maxwell-Boltzmann distribution (Equation 37 and **Figure 12a**). Interestingly, the Berendsen thermostat allows sampling states at constant temperature (i.e. mean kinetic energy) but with particle velocities that do not obey a Maxwell-Boltzmann distribution. Consequently, this thermostat does not actually sample a canonical ensemble.<sup>220</sup>

$$f_{MB}(v) = \left( \frac{m_i}{2\pi k_B T} \right)^{\frac{3}{2}} 4\pi v^2 e^{-\frac{mv^2}{2k_B T}} \quad (37)$$

The velocity-rescale (v-rescale) thermostat is adopted in the present work. The v-rescale thermostat uses the same weak-coupling term of the Berendsen thermostat and a stochastic term that ensures the proper velocity distribution at each timestep (Equation 38). Substituting Equation 32 into 38 results in an expression for the scaling factor  $\lambda$ , where the function  $W_W$  is a Wiener noise term. The Wiener noise function generates pseudo-random numbers that are temporally correlated (i.e.  $W_W$  is smooth).<sup>223</sup>

$$\frac{\Delta T(t)}{\Delta t} = \frac{1}{\tau_B} [T_0 - T(t)] + 2 \left( \frac{T_0 T(t)}{N \tau_B} \right)^{\frac{1}{2}} \frac{\Delta W_W(t)}{\Delta t} \quad (38)$$

$$\lambda(t) = \left\{ 1 + \frac{\Delta t}{\tau_B} \left[ \frac{T_0}{T(t)} - 1 \right] + 2 \left( \frac{T_0}{T(t) N \tau_B} \right)^{\frac{1}{2}} \Delta W_W(t) \right\}^{\frac{1}{2}} \quad (39)$$

In many cases, the NVT ensemble does not fully reproduce experimental (e.g. physiological) conditions, which are often performed at constant pressure. In the NPT ensemble, the number of particles, pressure, and temperature remain constant, while the volume is allowed to variations that contribute to the total energy of the system. The proper isobaric-isothermal statistical ensemble is captured when the probability ( $p$ ) of sampling a state  $s$  is given by Equation 40, with  $P$  and  $V$  the pressure and volume of the system, respectively. Similar to before, the proportionality constant  $\mathcal{E}$  is the isobaric-isothermal partition function that now integrates for all possible volumes (Equation 41).<sup>222</sup>

$$p(N, P, T, s) = \mathcal{E}^{-1} e^{-\frac{E_s + PV}{k_B T}} \quad (40)$$

$$\mathcal{E} = \mathcal{E}(N, P, T) = \frac{1}{h^3} \int \int e^{-\frac{E_s(\Gamma)}{k_B T}} d\Gamma dV = \int Z e^{-\frac{PV}{k_B T}} dV \quad (41)$$

A practical way of deriving an expression for the pressure in terms of microscopic variables is through the ensemble average proposed in the left-hand side of Equation 42. The expression can be expanded by differentiating with the chain rule, according to Newton's second law (Equation 25) and the equipartition of energy (Equation 28). Note that, in an isolated, unperturbed system, the velocity vector of the particles does not have a preferred orientation, i.e. it is randomly distributed. Subsequently, the ensemble average on the left-hand side of Equation 42 is zero. The first term on the right-hand side of Equation 42 is known as the virial, and it can be further simplified (Equation 42 bottom).<sup>224</sup>

$$\begin{aligned} \left\langle \sum_i \frac{d}{dt} [\mathbf{r}_i(t) \cdot m_i \mathbf{v}_i(t)] \right\rangle &= \left\langle \sum_i \mathbf{r}_i(t) \cdot m_i \mathbf{a}_i(t) \right\rangle + \left\langle \sum_i m_i v_i(t)^2 \right\rangle \\ &= \left\langle \sum_i \mathbf{r}_i(t) \cdot \mathbf{F}'_i(t) \right\rangle + \left\langle \sum_i 2K_i(t) \right\rangle \end{aligned} \quad (42)$$

$$\begin{aligned}
&= \left\langle \sum_i \mathbf{r}_i(t) \cdot \mathbf{F}'_i(t) \right\rangle + 2\langle K \rangle(t) \\
&= \left\langle \sum_i \mathbf{r}_i(t) \cdot \mathbf{F}'_i(t) \right\rangle + 3Nk_B T(t)
\end{aligned}$$

In pressure coupling, the system is subject to an external force that (de)compresses the simulation box, so the system reaches a target pressure (**Figure 12c**). In this way, the total force acting over the  $i$ -th particle ( $\mathbf{F}'_i$ ) can be separated into the force implied by the FF and the thermostat ( $\mathbf{F}_i$ ), and the force due to the external piston ( $\mathbf{F}_i^{ext}$ ). In a cubic simulation box of edge-length  $L$ , the external force at one of the faces relates to the pressure by Equation 43.<sup>224</sup>

$$F_i^{ext} = PL^2 \quad (43)$$

The force  $\mathbf{F}_i^{ext}$  will always act inwards, and it is only applied on atoms exactly at the box's faces, so the sum over all particles in Equation 42 will only be non-zero for atoms exactly at the surfaces. If the origin of coordinates is placed at one of the cube's edges, the surfaces will be located at  $x = (0, L)$ ,  $y = (0, L)$ , and  $z = (0, L)$ . Subsequently, in three of the faces, the remaining dot product in Equation 42 will collapse to zero. Applying these arguments to Equation 42, one obtains Equation 44. Equation 45 is reached by solving for the instantaneous pressure.

$$0 = \langle -3PLL^2 \rangle + \left\langle \sum_i \mathbf{r}_i(t) \cdot \mathbf{F}_i(t) \right\rangle + 3Nk_B T(t) \quad (44)$$

$$P = \frac{1}{3V} \left[ \left\langle \sum_i \mathbf{r}_i(t) \cdot \mathbf{F}_i(t) \right\rangle + 3Nk_B T(t) \right] \quad (45)$$

It is important to highlight that the instantaneous pressure of a system will depend on how much the expected value  $\langle \sum_i \mathbf{r}_i(t) \cdot \mathbf{F}_i(t) \rangle$  deviates from  $-3PV$ , which in turn depends on the number of atoms being subject to the external force. Thus, for systems with thousands of atoms or more, the instantaneous pressure is misrepresentative of the system's behavior. Indeed, the moving average of the pressure is the metric that actually represents the thermodynamic pressure of the system during MD simulations.<sup>148</sup>

Barostats are modifications to Newton's equations of motion with the purpose of generating a statistical ensemble at constant pressure. Barostats can apply the same compressive force in all

directions (isotropic barostats), or they may use different ones for each coordinate (anisotropic barostats). Indirectly, barostats update the volume by scaling the edge-lengths of the simulation box by a factor  $\mu_P$ , as shown in Equation 46 for a rectangular box of edge-lengths  $\mathbf{L} = (L_x, L_y, L_z)$ . As such, the volume of the system is updated by the matrix product of the scaling factor  $\mu_P$  (transposed, Equation 47). Note that a modification on the volume also implies a modification on the position of the particles (Equation 48).<sup>225</sup>

$$\mathbf{L}'(t + \Delta t) = \mu_P(t)^\top \cdot \mathbf{L}(t) \quad (46)$$

$$V'(t + \Delta t) = \prod_{i=1}^3 \mu_{P,i}(t) L_i(t) \quad (47)$$

$$\mathbf{r}_i(t + \Delta t) = \mu_P(t)^\top \cdot \mathbf{r}_i(t) \quad (48)$$

In the present work two barostats were employed, the Berendsen and the Parrinello-Rahman barostats. In the Berendsen barostat all scaling factors are equal ( $\mu_{P,1} = \mu_{P,2} = \mu_{P,3} = \mu_P$ ) and based on the weak-coupling principle of the thermostat of same name. In this case, the pressure of the system is coupled to a ‘pressure bath’ at pressure  $P_0$ , with the rate of change given by Equation 49.<sup>225</sup>

$$\frac{dP(t)}{dt} = \frac{1}{\tau_P} (P_0 - P(t)) \quad (49)$$

In addition, it is also possible to obtain an expression that relates the rate of change of the pressure and volume by differentiating the definition of isothermal compressibility with respect to time (Equation 50). The scaling factor is found by substituting 47 and 49 into 50 and solving for  $\mu_P$  (Equation 51). In Equation 51, the isothermal compressibility  $\kappa$  is the resistance offered by the system against being compressed. This value is typically set to that of the solvent (e.g.  $4.5 \times 10^{-5} \text{ bar}^{-1}$  for water).<sup>225</sup>

$$\frac{dP(t)}{dt} = - \frac{1}{\kappa V(t)} \frac{dV(t)}{dt} \quad (50)$$

$$\mu = \left[ 1 - \Delta t \frac{\kappa}{\tau_P} (P_0 - P(t)) \right]^{\frac{1}{3}} \quad (51)$$

In contrast to the Berendsen barostat, the scaling factor  $\mu_P$  does not have to be uniform in the three dimensions when a Parrinello-Rahman barostat is implemented, which enables the system to change its shape during the simulation. In the case of liquid-state modeling, the simulation box will not deviate significantly from its original shape, although this is particularly useful for studying phase transitions in solid phase dynamics.<sup>226,227</sup>

### 3. *Nonbonded interactions*

The simulation of a realistic dissolution should allow the diffusion of the solute through a solvent extended infinitely. Due to the finite memory and work capacity of processing units, it is unfeasible to perform this task explicitly. Instead, MD considers a selected portion of space known as the simulation box. There are multiple alternatives on how to deal with particles that reach the frontiers of such box. A common practice is to use periodic boundary conditions (PBC), a scheme in which the simulation box is treated as a unit cell that repeats itself infinitely in all three dimensions (**Figure 12d**). Therefore, when an atom exits through one of the simulation box's faces, another identical atom enters the box through the opposite face. Under these conditions, any point in space can be described by what happens inside the simulation box. Nonetheless, if the simulation box is too small, a molecule's motion can be affected by its mirror image. Indeed, the appearance of self-correlated motions results in artifacts misrepresentative of the system's dynamics.<sup>148</sup>

PBC allows describing an infinitely big space in terms of a reduced, selected portion. This implies that, in principle, nonbonded interactions (i.e. van der Waals and electrostatics) should be summed over an impossible (infinite) number of atoms. Advantageously, the sums in Equations 9 and 10 are conditionally convergent, so the series can be truncated for atom pairs within a certain threshold distance from each other. The threshold distance depends on the scaling law of the pairwise potential. In practice, it is feasible to explicitly evaluate the sums when the scaling law ( $r^{-N_{law}}$ ) decays fast enough ( $N_{law} \geq 3$ ). Since the 6-12 Lennard-Jones potential satisfies this condition, the van der Waals interactions are treated by truncating the sum. The Coulomb potential, instead, would take too long to converge (because  $N_{law} = 1$ ).<sup>148</sup>

Electrostatics are treated with the Ewald summation method, in which the potential is modified to make the series converge faster.<sup>228</sup> In this method, for each (partial) charge in the system  $q_i$ , a Gaussian charge density  $\rho_i$  of opposite sign and centered at the particle's position is added (Equation 52). Integrating  $\rho_i$  in spherical coordinates over the entire space, one can reach a

modified expression for the electric potential energy ( $U_{elec}^{real}$  in Equation 53), where  $\alpha_e$  is a free parameter that determines the width of the Gaussian distribution,  $\mathbf{n}_{xyz}$  is a vector of integers indicating the periodic image ( $\mathbf{n}_{xyz} = \mathbf{0}$  is the simulation box), and  $erfc$  is the complementary error function (Equation 54). The star (\*) on the third sum indicates that the case  $i = j$  should be excluded for  $\mathbf{n}_{xyz} = \mathbf{0}$ .<sup>148</sup>

$$\rho_i(r) = -\frac{q_i \alpha_e^3}{\pi^{3/2}} e^{-\alpha_e^2 |r-r_i|^2} \quad (52)$$

$$U_{elec}^{real} = \frac{1}{2} \sum_i \sum_j \sum_{\mathbf{n}_{xyz}=\mathbf{0}}^* \frac{q_i q_j}{4\pi\epsilon_0} \frac{erfc(\alpha_e |\mathbf{r} + \mathbf{n}_{xyz}|)}{|\mathbf{r} + \mathbf{n}_{xyz}|} \quad (53)$$

$$erfc(x) = \frac{2}{\pi^{1/2}} \int_x^\infty e^{-y^2} dy \quad (54)$$

The modified electric potential energy  $U_{elec}^{real}$  converges faster than Equation 9, so a cutoff distance is imposed for its truncation. Then, a set of oppositely charged densities  $\{-\rho\}$  is added to correct for the first set of charge densities  $\{\rho\}$ .<sup>148</sup> The corresponding electrostatic potential  $\psi$  is computed by solving Poisson's equation (Equation 55) in the Fourier space. The Fourier transformation of a function  $f$  is given by Equation 56, where  $k$  is the wave number ( $2\pi n_x L_x^{-1}$  for a 1D system).<sup>229,230</sup>

$$\nabla^2 \psi = -\frac{\rho}{\epsilon_0} \quad (55)$$

$$\hat{f}(k) = \frac{1}{(2\pi)^{1/2}} \int_{-\infty}^{\infty} f(x) e^{-2\pi i k x} dx \quad (56)$$

The Ewald summation transforms Poisson's equation into the reciprocal space  $k$ , and solves for the reciprocal electrostatic potential  $\hat{\psi}$ , and translates it to the real space  $r$ . The resulting expression for the electrostatic potential energy is shown as Equation 57. The Gaussian decay of this function in reciprocal space makes it converge faster than the original Coulomb potential. In practice, the inclusion of 100-200 reciprocal vectors  $\mathbf{k}$  provides enough numerical accuracy.<sup>148</sup>



$$U_{elec}^{recip} = \frac{1}{2} \sum_i \sum_j \sum_{k \neq 0} \frac{1}{\pi L_x L_y L_z} \frac{q_i q_j}{4\pi\epsilon_0} \frac{4\pi^2}{k^2} e^{-\frac{k^2}{4\alpha_e^2}} \cos(\mathbf{k} \cdot \mathbf{r}_{ij}) \quad (57)$$

Note that, in Equations 53 and 57, each pair of charges is included twice, and the energy is then halved at the beginning of the formula to normalize the double counting. Moreover, in the cases where  $i = j$ , the contribution of the Gaussian densities is non-zero, so a final correction term for their self-interaction must be included (Equation 58).<sup>148</sup>

$$U_{elec}^{corr} = -\frac{\alpha_e}{\pi^{1/2}} \sum_i \frac{q_i^2}{4\pi\epsilon_0} \quad (58)$$

Finally, the total electrostatic potential energy of the system (Equation 59) results from adding Equations 53, 57, and 58.

$$U_{elec} = U_{elec}^{real} + U_{elec}^{recip} + U_{elec}^{corr} \quad (59)$$

The time required for evaluating Equation 59 scales as  $\sim N^2$ , making it computationally expensive for simulations with thousands of atoms. Particle-mesh Ewald is a method that evaluates the Ewald summation for electrostatic energy that scales as  $\sim N \log N$ . This algorithm evaluates the energy for a 3D grid with a charge in each interstice that is calculated by interpolating the vicinal charges of the system.<sup>231</sup>

#### 4. Coarse-grained simulations

The setup of CG MD simulations is almost identical to that of their atomistic counterparts. Nonetheless, the reduction in degrees of freedom implied in CG FFs have consequences in the interpretability of the input parameters and output trajectories. The coarsening of the simulation allows a bead representation of molecules that uses a reduced number of interaction sites, allowing a larger simulation scale. With atomistic MD simulations, state of the art studies use boxes tens of nanometers long, whereas, with the Martini CG FF, boxes hundreds-of-nanometers-long are accessible.<sup>232,233</sup>

In addition to increasing the length-scale at reach, CG methods hide fast vibrations. In CG MD, the bonded energy terms do not have the same physical meaning as the bonds, angles, and dihedrals of an atomistic FF, so they are not fitted to reproduce vibrational or rotational frequencies. Rather, bonded parameters in CG FFs are parametrized to maintain the structural

integrity of macromolecules, leading to the usage of smaller force constants.<sup>181</sup> Therefore, the movements that before set the upper threshold for the timestep are no longer present. In the particular case of the Martini FF, timesteps in the range of 10-20 fs are typically used. For a fixed amount of computing resources, this also results in longer time-scales compared to atomistic MD.<sup>232,233</sup>

The reduced number of degrees of freedom and weaker force constants in CG simulations also smooth the potential and thus the free energy surfaces of the system. Consequently, the kinetic energy of the particles is enough to explore more energy basins than they would in an atomistic simulation. Thus, the simulation time has a variable correspondence to the real physical time.<sup>181,212</sup> For example, Martini water beads are known to diffuse four times faster than in experiments, so some studies claim that the simulated time in Martini MD is a fourth of the physical time actually sampled.<sup>180</sup> Nonetheless, this factor has found to be system-dependent and to vary between three and eight.<sup>152</sup> In other words, grouping atoms into beads leads to an underestimation of the conformational entropy that is balanced by overcompensating the enthalpic contribution through the FF parameters.<sup>234</sup>

## C. Free energy calculations

Free energy calculations are theoretical frameworks that can be combined with MD simulations to compute variations in the free energy of a system as a particular process takes place.<sup>235,236</sup> The present work utilizes two methods: potential of mean force and thermodynamic integration, both of which calculate the energy along a collective variable (CV). A CV is a parameter (often geometrical) that describes the evolution of a process (**Figure 13a**). The probability of sampling a CV,  $\xi$ , depends on the free energy of a system at a particular state. Depending on the free energy along  $\xi$ , the simulation time needed to sample the path of interest may be unfeasible.<sup>237</sup> For this reason, free energy calculations are typically coupled to enhanced-sampling techniques, which bias the dynamics of the system in order to promote the population of otherwise unexplored regions of the system's phase space.<sup>238</sup>

### 1. Potential of mean force and umbrella sampling

Potential of mean force (PMF) calculations compute the free energy along a CV from the probability of sampling each value of  $\xi$  along the path of interest.<sup>239</sup> In order to exhaustively sample  $\xi$ , a biasing term  $U_{bias}$  is added to the total energy of the system as shown in Equation

60, where  $E_b$  represents the total energy of the biased system (**Figure 13b**). The probability of sampling a value  $\xi_i$  in the perturbed system is the sum of all the probabilities where  $\xi = \xi_i$ , which is shown as Equation 61 for a canonical ensemble. The biased probability  $p_b$  in Equation 61 can also be written in terms of the unperturbed energy  $E$  and the known biasing potential  $U_{bias}$  using Equation 60. In Equation 61,  $Z_b$  is the canonical partition function of the biased system,  $\Gamma_{\xi_i}$  the phase space configurations where  $\xi = \xi_i$ , and  $Z_i$  is the unbiased partition function at calculated over  $\Gamma_{\xi_i}$ .<sup>240</sup>

$$E_b(\Gamma, \xi) = E(\Gamma) + U_{bias}(\xi) \quad (60)$$

$$\begin{aligned} p_b(\xi(\Gamma) = \xi_i) &= \frac{1}{Z_b} \int e^{-\frac{E_b(\Gamma, \xi)}{k_B T}} \delta(\xi(\Gamma) - \xi_i) d\Gamma \\ &= \frac{1}{Z_b} \int e^{-\frac{E(\Gamma)}{k_B T}} e^{-\frac{U_{bias}(\xi(\Gamma)=\xi_i)}{k_B T}} d\Gamma_{\xi_i} \\ &= \frac{1}{Z_b} e^{-\frac{U_{bias}(\xi(\Gamma)=\xi_i)}{k_B T}} \int e^{-\frac{E(\Gamma)}{k_B T}} d\Gamma_{\xi_i} \\ &= \frac{Z_i}{Z_b} e^{-\frac{U_{bias}(\xi(\Gamma)=\xi_i)}{k_B T}} \end{aligned} \quad (61)$$

Applying a Boltzmann inversion to the definition of the Helmholtz free energy  $A$  (Equation 62) and using Equation 61 returns an expression for the PMF at  $\xi_i$ . Note that Equation 63 relates the unbiased free energy  $A$  with the known biasing potential  $U_{bias}$  and the probability sampled from the biased simulation  $p_b$ . The last term in Equation 63 is a constant that cancels out when calculating relative free energies (i.e. difference between states). Note that Equations 61, 62, and 63 apply only to canonical ensembles, but they can be generalized for the isobaric-isothermal ensemble by integrating over the volume as in Equation 41. The PMF profile obtained from an NPT ensemble corresponds to the Gibbs free energy  $G$ .<sup>241</sup>

$$A(\xi(\Gamma) = \xi_i) = -k_B T \log Z(\xi(\Gamma) = \xi_i) \quad (62)$$

$$A(\xi(\Gamma) = \xi_i) = -k_B T \log p_b(\xi(\Gamma) = \xi_i) - U_{bias}(\xi(\Gamma) = \xi_i) - k_B T \log Z_b \quad (63)$$

In the specific case in which the biasing potential is harmonic (Equation 64) around a reference value  $\xi_{ref}$ , the sampling method is called umbrella sampling (US, **Figure 13b**).<sup>242</sup>

$$U_{bias}(\xi) = \frac{k_{bias}}{2} (\xi - \xi_{ref})^2 \quad (64)$$

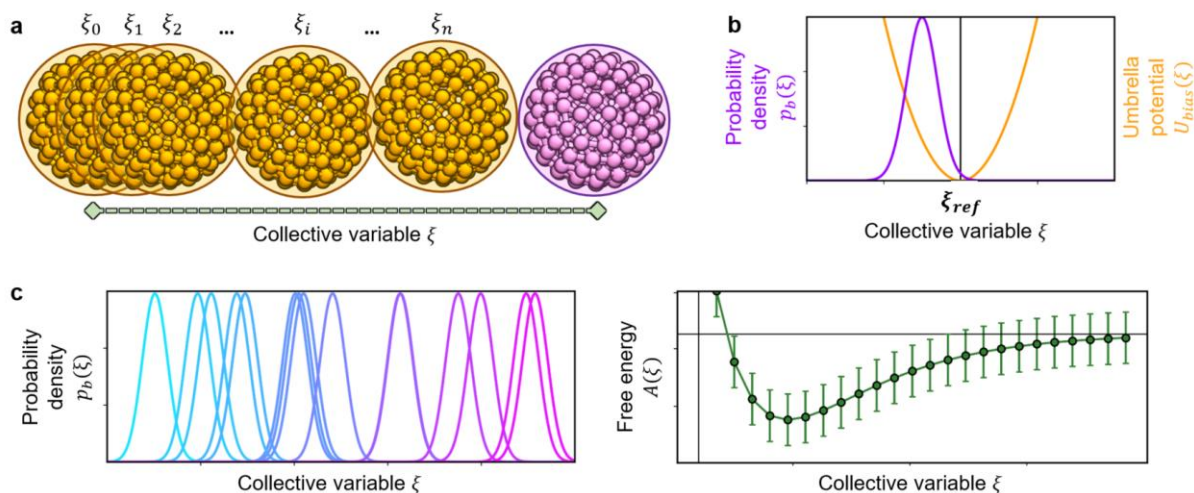


**Figure 13.** Example illustrating the workflow behind PMF calculations. **a.** The collective variable  $\xi$  is defined as the distance between the center of mass of two spherical molecules (orange and pink). Calculating a PMF profile requires the exhaustive sampling of the system's degrees of freedom in the  $\xi$  range of interest. **b.** For the sampling, several windows are simulated in which a biasing potential (harmonic in US) is applied at a reference value  $\xi_{ref}$ . **c.** The free energy profile can then be constructed by measuring the biased probability  $p_b(\xi)$  and applying the Boltzmann inversion in Equation 63.

One US sampling MD simulation is usually not enough to sample the whole range of interest of  $\xi$ . In practice, the range of interest is stratified into  $n_{win}$  window simulations, each with a biasing potential centered at a different reference point ( $\{\xi_j\}$ ). Each simulation provides a free energy curve for a small range of  $\xi$ . Curves from consecutive windows are then fitted at their overlapping regions to recover the complete free energy profile (**Figure 13c**). The most commonly employed numeric method to perform this fitting is the weighted histogram analysis method (WHAM).<sup>243,244</sup> This method calculates the constant  $Z_b$  from Equation 63 for all the window simulations. To do so, WHAM creates a histogram of  $\xi$  with  $n_{bin}$  bins for the whole range of  $\xi$  and uses it to iteratively solve Equations 65 and 66 to self-consistency. In Equations 65 and 66,  $\xi_i$  is the  $i$ -th histogram bin,  $\chi_{T,j}$  is the total number of points sampled in the  $j$ -th simulation,  $\chi_{j,i}$  is the number of points in the  $i$ -th histogram sampled by the  $j$ -th simulation,  $U_{bias,j}$  is the biasing potential in the  $j$ -th simulation, and  $Z_{b,j}$  is the partition function of the  $j$ -th simulation.

$$Z_{b,j} = \sum_i^{n_{bin}} p(\xi(\Gamma) = \xi_i) e^{-\frac{U_{bias,j}(\xi(\Gamma)=\xi_i)}{k_B T}} \quad (65)$$

$$p(\xi(\Gamma) = \xi_i) = \frac{\sum_j^{n_{win}} \chi_{j,i}(\xi(\Gamma) = \xi_i)}{\sum_j^{n_{win}} \chi_{T,j} Z_{b,j}^{-1} e^{-\frac{U_{bias,j}(\xi(\Gamma)=\xi_i)}{k_B T}}} \quad (66)$$

## 2. Thermodynamic integration

Thermodynamic integration (TI) is another free energy calculation method that computes the free energy of a process through an alternative approach to Equation 63.<sup>238</sup> Similar as in PMF, in TI, the range for  $\xi$  is stratified into a discrete set of windows  $\{\xi_j\}$ . In TI, however the free energy is computed by first sampling the instantaneous force required to constrain the system at  $\xi = \xi_j$  (Equation 67). This sampling allows computing the expected value of the constraining force at each window. Finally, the constraining forces are numerically integrated over the range of  $\xi$  to obtain the change in the free energy between two states  $s_0$  and  $s_1$  (Equation 68). The convergence of the free energy depends on the number of windows simulated.<sup>245</sup>

$$\begin{aligned} \left. \frac{\partial A(\xi)}{\partial \xi} \right|_{\xi=\xi_j} &= \left. -k_B T \frac{1}{Z} \frac{\partial Z}{\partial \xi} \right|_{\xi=\xi_j} \\ &= \left. -k_B T \frac{1}{Z} \frac{\partial}{\partial \xi} \left[ \int e^{-\frac{E(\Gamma, \xi)}{k_B T}} d\Gamma \right] \right|_{\xi=\xi_j} \\ &= \left. \frac{1}{Z} \int e^{-\frac{E(\Gamma, \xi)}{k_B T}} \frac{\partial E(\Gamma, \xi)}{\partial \xi} d\Gamma \right|_{\xi=\xi_j} \\ &= \left\langle \frac{\partial E(\Gamma, \xi)}{\partial \xi} \right\rangle_{\xi=\xi_j} \end{aligned} \quad (67)$$

$$A(\xi_{s_0}) - A(\xi_{s_1}) = \int_{\xi_{s_0}}^{\xi_{s_1}} \left\langle \frac{\partial E(\Gamma, \xi)}{\partial \xi} \right\rangle_{\xi=\xi_j} d\xi \cong \sum_j \left\langle \frac{\partial E(\Gamma, \xi)}{\partial \xi} \right\rangle_{\xi=\xi_j} \Delta \xi \quad (68)$$

The scheme introduced above is generic for any modified potential  $E(\Gamma, \xi)$ , hence,  $\xi$  does not necessarily represent a geometrical CV. In this case,  $\xi$  is interpreted as a coupling parameter

that shifts the system from state  $s_0$  and  $s_1$  (**Figure 14**). TI allows studying alchemical transformations, in which particles are created/annihilated. In these transformations, the total energy difference between states  $s_0$  and  $s_1$  is the potential energy associated with the molecules being created/annihilated. In other words, the total energy of the system is given by  $E_{s_0}(\Gamma)$  and  $E_{s_1}(\Gamma)$  when  $\xi = 0$  and  $\xi = 1$ , respectively.<sup>246</sup> At any other value of  $\xi$ , the simulation does not model a physical system, in fact, the intermediate states are mathematical constructs that enable calculating the free energy difference between the initial and final states.<sup>247</sup> In analogy to the WHAM algorithm that reconstructs the free energy surface in PMF calculations, TI uses the Bennett's acceptance ratio to weight and average the free energy contribution at each window.<sup>248</sup>

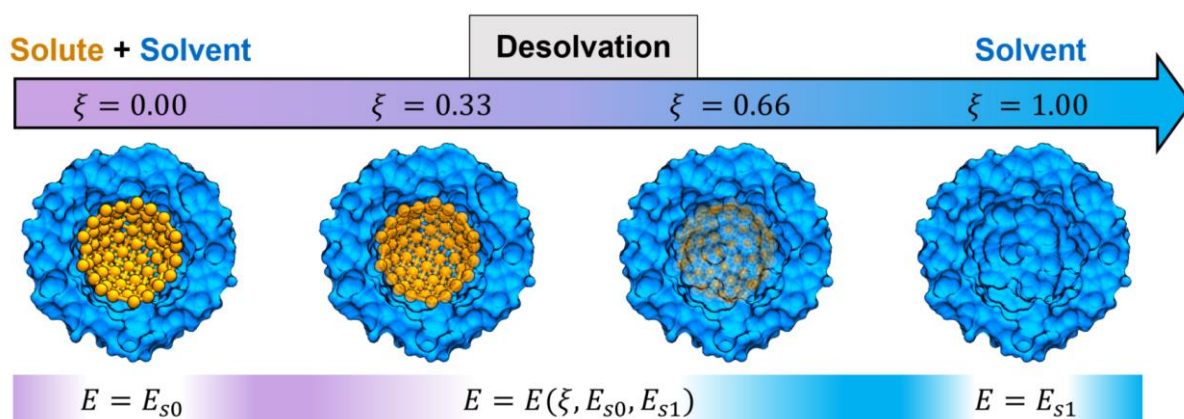


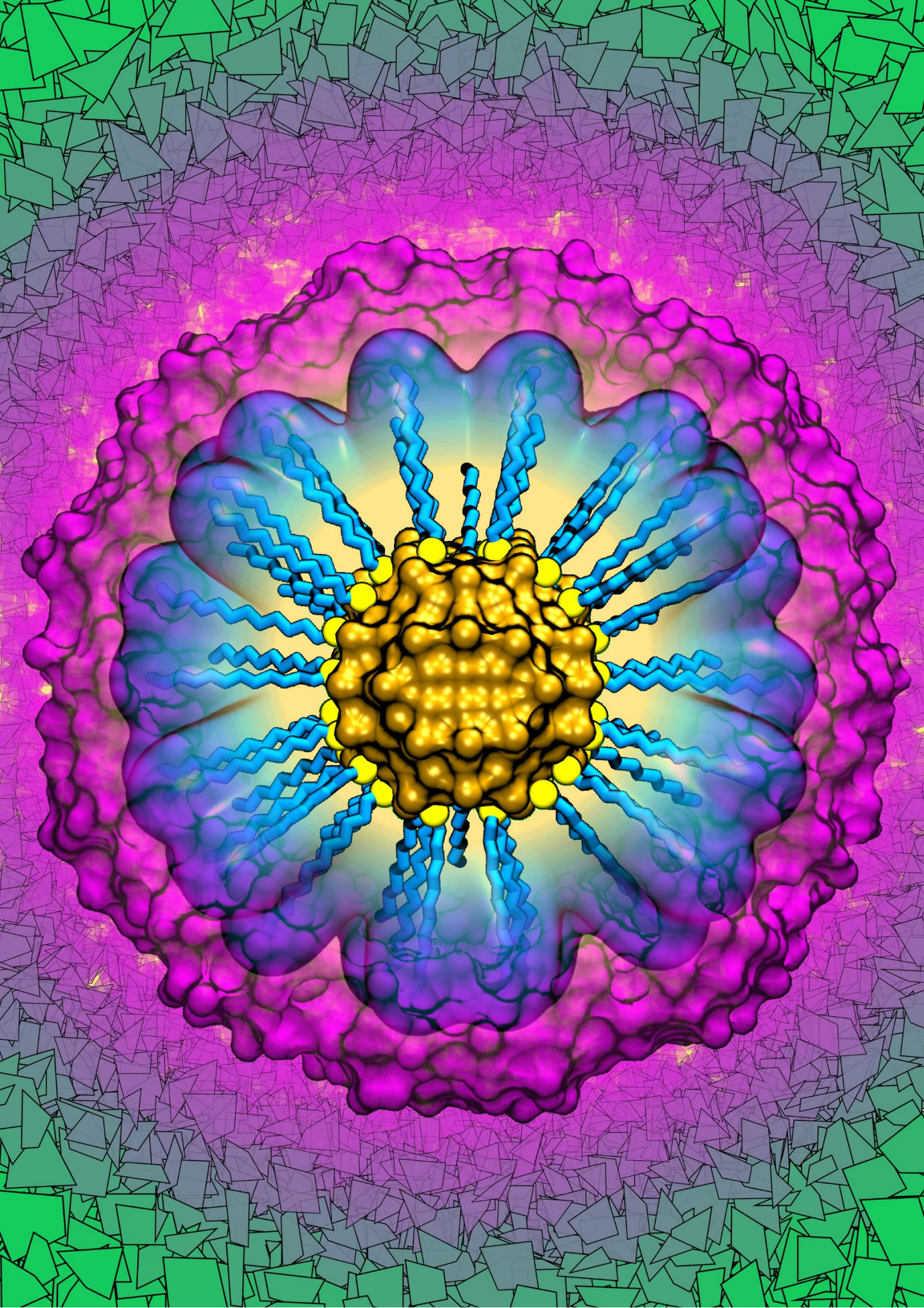
**Figure 14.** Example illustrating the workflow behind TI when calculating the (de)solvation energy of a spherical molecule (orange). The total energy of the system changes as a function of the coupling parameter  $\xi$  in such a way that  $E(\Gamma, \xi = 0) = E_{s_0}(\Gamma)$  and  $E(\Gamma, \xi = 1) = E_{s_1}(\Gamma)$ . The difference in free energy between states  $s_0$  and  $s_1$  is then computed by tracking the changes in the energy between sampling windows. States where  $0 < \xi < 1$  are fictitious systems with no physical counterpart.

When calculating the solvation energy of a molecule comprising  $N_{mol}$  atoms, the potential energy (van der Waals and electrostatic interactions) of the  $N_{mol}$  atoms are gradually turned off through the  $\xi$  parameter. Intuitively, the Lennard-Jones and Coulomb potentials could depend linearly on  $\xi$  (Equation 69).<sup>249</sup> However, as the potential energy smoothens, it becomes more likely for an atom pair to fall into a singularity ( $r_{ij} = 0$ ) at which the potential energy diverges. To circumvent this instability, the Lennard-Jones and Coulomb potentials in  $E$  are replaced by ‘soft-core’ versions, as shown in Equations 70 and 71, where the  $\alpha_{LJ}$  and  $\alpha_C$  factors are empirical parameters often set to 0.5. Note that the original form of the potentials is recovered at  $\xi = 0$ .<sup>250</sup>

$$E(\Gamma, \xi) = (1 - \xi)E_{s0}(\Gamma, \xi) + \xi E_{s1}(\Gamma, \xi) \quad (69)$$

$$U_{vdW}^{soft-core} = \sum_i^{N_{mol}} \sum_j 4\epsilon_{ij} \sigma_{ij}^6 \left[ \frac{\sigma_{ij}^6}{(r_{ij}^6 + \xi^2 \alpha_{LJ} \sigma_{ij}^6)^2} - \frac{1}{(r_{ij}^6 + \xi^2 \alpha_{LJ} \sigma_{ij}^6)} \right] \quad (70)$$

$$U_{elec}^{soft-core} = \sum_i^{N_{mol}} \sum_j \frac{q_i q_j}{4\pi(r_{ij}^2 + \xi^2 \alpha_C)} \quad (71)$$





# CHAPTER III. NANOMODELER: A WEBSERVER FOR MOLECULAR SIMULATIONS AND ENGINEERING OF NANOPARTICLES

## Abstract

Functionalized nanoparticles (NPs) are at the frontier of nanoscience. They hold the promise of innovative applications for human health and technology. In this context, molecular dynamics (MD) simulations of NPs are increasingly employed to understand the fundamental structural and dynamical features of NPs. While informative, such simulations demand a laborious two-step process for their setup. In-house scripts are required to: i) construct complex 3D models of the inner metal core and outer layer of organic ligands, and ii) correctly assign force field parameters to these composite systems. Here, we present NanoModeler ([www.nanomodeler.eu](http://www.nanomodeler.eu)), the first webserver designed to automatically generate and parameterize model systems of monolayer-protected gold NPs (AuNPs) and gold nanoclusters (AuNCs). The only required input is a structure file of one or two ligand(s) to be grafted onto the gold core, with the option of specifying homogeneous or heterogeneous NP morphologies. NanoModeler then generates 3D models of the nanosystem and the associated topology files. These files are ready for use with the Gromacs MD engine, and they are compatible with the AMBER family of force fields. We illustrate NanoModeler's capabilities with MD simulations of selected representative NP model systems. NanoModeler is the first platform to automate and standardize the construction and parameterization of realistic models for atomistic simulations of AuNPs and AuNCs.

## A. Introduction

Monolayer-protected metal nanoparticles (NPs) are nanosized molecules comprising a metallic inner core covered by an organic layer with a varying number of coating ligands. These ligands shield the NP core and dictate the supramolecular chemistry at the NP surface. They can be functionalized in different ways, generating NPs with diverse structural and physicochemical properties. For example, functionalized NPs can recognize selected substrates with programmed specificity and affinity,<sup>57</sup> and can catalyze chemical transformations (i.e. nanozymes).<sup>98,99,101</sup> Functionalized NPs have thus found application in bioimaging,<sup>251</sup> photothermal therapy,<sup>48,221,252</sup> drug delivery,<sup>178,253,254</sup> and other fields.<sup>97,255–257</sup>

Due to their flexible chemical structure, it is difficult to examine the organization and dynamics of the coating ligands in functionalized NPs. However, understanding the fundamental dynamical behavior of the ligands is necessary to rationally design functionalized NPs with programmed abilities.<sup>57,258</sup> In this context, atomistic molecular dynamics (MD) simulations can significantly improve our understanding of the ligand dynamics and interactions at the basis of NP applications, including nuclear magnetic resonance (NMR)-based chemosensing<sup>57,259</sup> and nanocatalysis.<sup>98,138</sup> For example, MD simulations take full account of the molecule's flexibility in explicit solvents.<sup>172,260</sup> They are thus suitable for elucidating NP dynamics and flexibility.<sup>261</sup> As a result, the literature contains a growing number of studies that combine MD simulations with experiments to investigate NPs involved in complex phenomena, including penetration of lipid bilayers,<sup>89,262–267</sup> protein/lipid corona formation,<sup>29,268,269</sup> and particle aggregation.<sup>270,271</sup>

It is not easy to construct realistic 3D models of NPs and their parameterization for MD simulations.<sup>272</sup> There are many tools for building and parametrizing macromolecules such as proteins,<sup>171,202,273,274</sup> nucleic acids,<sup>275–277</sup> and lipids.<sup>278–280</sup> However, there are no standardized tools for building and parametrizing complex NP models for MD simulations. Computational researchers must develop in-house software to build such models, and prepare ad hoc protocols to create the NP topology, which includes all the force field parameters for MD simulations (i.e. bonded and nonbonded parameters). This process can be quite complex, and it is certainly laborious.

Here, we present NanoModeler ([www.nanomodeler.eu](http://www.nanomodeler.eu)), the first webserver for the automatic and standardized construction and parameterization of realistic models for use in atomistic MD simulations of gold nanoparticles (AuNPs) and nanoclusters (AuNCs). This tool facilitates the

investigation and engineering of AuNPs and AuNCs, onto which molecular composites can be grafted to form a functionalized monolayer.

Many AuNPs and AuNCs structures have become available in experimental and theoretical studies.<sup>24,37,281,282</sup> This growing body of data has prompted the parameterization of these NPs for MD simulations. Based on these data, NanoModeler generates 3D models and topologies for homogeneous and mixed-monolayer-protected AuNPs and AuNCs. These models are ready to be investigated via MD simulations. One or two ligand types can be considered when building a 3D model of the NPs, which are then assembled to produce a topology file that is compatible with the AMBER family of force fields.

In summary, NanoModeler allows the automatic set-up of atomistic MD simulations of multifaceted mixtures of functionalized AuNPs. This novel tool will help researchers study and engineer functionalized AuNPs and nanoclusters, while serving as a technological platform for future software developments related to MD simulations of AuNPs.

## **B. Results and discussion**

The NanoModeler webserver ([www.nanomodeler.eu](http://www.nanomodeler.eu)) is a free service, which the scientific community can use to prepare the necessary files for MD simulations of monolayer-protected AuNPs and AuNCs. The backend of the tool is coded in Python. The frontend graphical user interface (GUI) uses a mixture of Hypertext Markup Language (HTML), Cascading Style Sheets (CSS), and JavaScript. The NanoModeler website includes documentation and tutorials, which describe the overall process for setting up the system of interest, and the available options. This material is featured both in the server's website and Appendix A. Below, we explain how NanoModeler operates, step by step, as per the workflow in **Figure 15a**.

### *1. Building a 3D model of gold nanoparticles*

When using MD simulations to obtain an atomistic understanding of AuNPs, the user must build a reliable 3D model of the AuNP of interest. The structure of AuNPs can be divided into three characteristic building blocks: i) The inner quasi-static gold atoms; ii) the gold-sulfur staple-like motifs positioned on the surface of the core, and iii) the coating ligands linked to the staple-like motifs. NanoModeler uses these three building blocks to construct and assemble the final AuNP model.

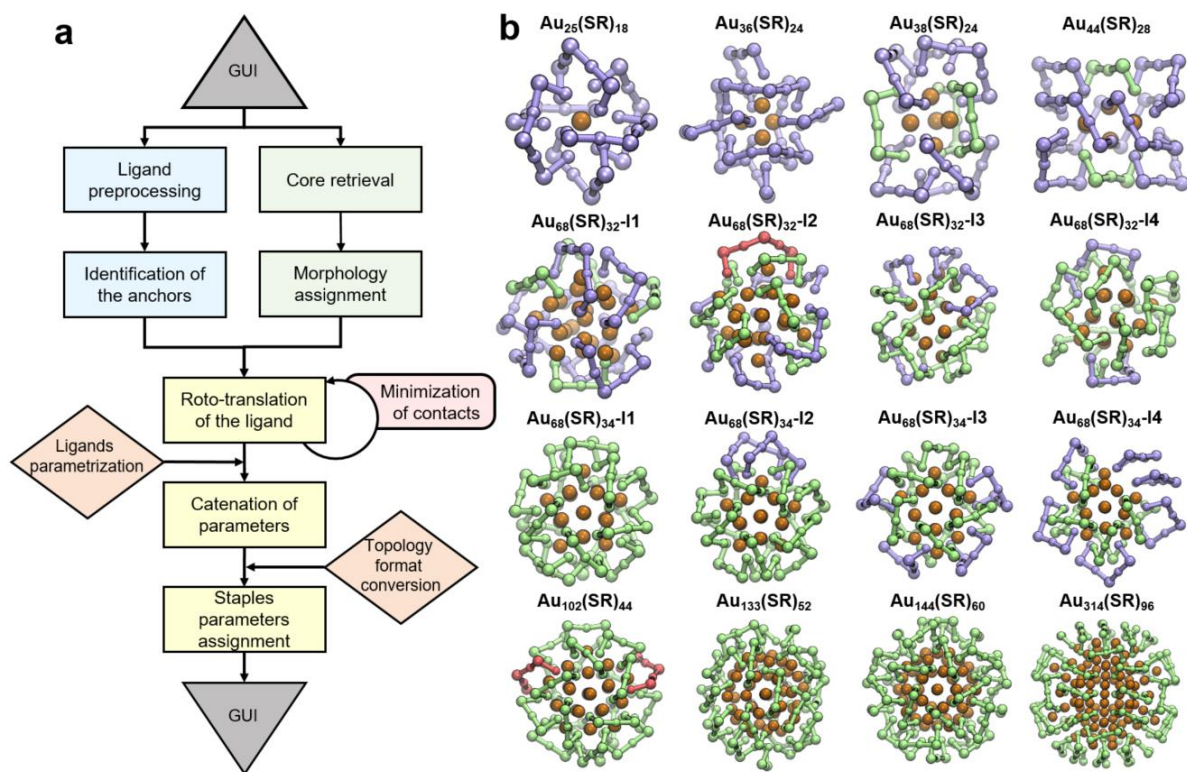


**Figure 15.** Operation scheme of NanoModeler and its supported gold cores. **a.** Workflow of NanoModeler upon job submission. Steps involving only the ligand are in blue, those involving the core are in green, and those involving both the core and the ligands are in yellow. The GUI is in gray, external software dependencies are in orange, and additional steps are in red. **b.** Structure of the available cores that can be used to build functionalized AuNPs. In each core supported by NanoModeler, staples – the anchoring sites to which the coating ligands are coupled – are displayed in green, purple, and red. In more detail, staples of type STR are in green, STC in purple, and STV in red. For a detailed definition of the staple types (STR, STC, and STV), as well as of their associated atom types, please refer to **Figure 16**.

Importantly, the key properties and interaction patterns of AuNPs also depend on the size of the metal core.<sup>3,283</sup> In recent years, experimental and theoretical studies have elucidated several structures of AuNPs and AuNCs. The cores from these studies are incorporated into NanoModeler (**Table 1**). NanoModeler offers 16 different cores ranging in diameter from 0.9 (Au<sub>25</sub>(SR)<sub>18</sub>) to 2.1 nm (Au<sub>314</sub>(SR)<sub>96</sub>, **Figure 15b**). Each core structure can be used as the supporting body to assemble the final AuNP. We define the core as the coordinates of the gold atoms and the 3D disposition of the sulfur atoms, including the first carbon of the ligands, as originally placed in the template AuNP structure (**Figure 16a**).

Each specific core also defines the structure and disposition of the gold-sulfur interface ‘staples’,<sup>25,55</sup> which are depicted in **Figure 16**. These motifs act as anchoring sites, to which the coating ligands are coupled. NanoModeler supports three staple types, hereafter named

STR, STC, and STV, with differing connectivity and angle parameters (**Figure 16**). Each one includes two or three sulfur atoms. In all three staple types, each sulfur atom is bound to two gold atoms and one carbon atom. Notably, certain cores exist in different isoforms, that is, as the same chemical formula with a different number of staples organized in distinctive arrangements. For example, the Au<sub>68</sub>(SR)<sub>32</sub> and Au<sub>68</sub>(SR)<sub>34</sub> cores in NanoModeler result in four isoforms of comparable dimensions, which differ in the type and location of the staples.

**Table 1.** List of the 16 cores supported by NanoModeler, identified by their gold-to-sulfur ratio. The table also reports the average diameter as well as the number and type of staples present on each core. Staples are the anchoring sites to which the coating ligands are coupled, and are here named as STR, STC, and STV based on their chemical structure and atomic connectivity. For a detailed definition of staple types, as classified in NanoModeler, please refer to **Figure 16**. The ligand with which the system was originally elucidated (if present) and the respective reference are also shown.

Core	Size (nm)	STR	STC	STV	Original ligand	Remarks
AU <sub>25</sub> (SR) <sub>18</sub>	0.9	-	6	-	Phenylethane thiol	Ref <sup>284</sup>
AU <sub>36</sub> (SR) <sub>24</sub>	1.1	-	8	-	Cyclopentane thiol	Ref <sup>121</sup>
AU <sub>38</sub> (SR) <sub>24</sub>	1.1	3	6	-	Phenylethane thiol	Ref <sup>285</sup>
AU <sub>44</sub> (SR) <sub>28</sub>	1.1	2	8	-	Methane thiol	Ref <sup>286</sup>
AU <sub>68</sub> (SR) <sub>32</sub>	1.3	4	8	-	None	Isoform 1. Ref <sup>287</sup>
AU <sub>68</sub> (SR) <sub>32</sub>	1.3	7	5	1	None	Isoform 2. Ref <sup>287</sup>
AU <sub>68</sub> (SR) <sub>32</sub>	1.3	10	4	-	None	Isoform 3. Ref <sup>287</sup>
AU <sub>68</sub> (SR) <sub>32</sub>	1.3	13	2	-	None	Isoform 4. Ref <sup>287</sup>
AU <sub>68</sub> (SR) <sub>34</sub>	1.2	17	-	-	None	Isoform 1. Ref <sup>288</sup>
AU <sub>68</sub> (SR) <sub>34</sub>	1.3	14	2	-	None	Isoform 2. Ref <sup>288</sup>
AU <sub>68</sub> (SR) <sub>34</sub>	1.3	11	4	-	None	Isoform 3. Ref <sup>288</sup>
AU <sub>68</sub> (SR) <sub>34</sub>	1.4	8	6	-	None	Isoform 4. Ref <sup>288</sup>
AU <sub>102</sub> (SR) <sub>44</sub>	1.5	19	-	2	<i>p</i> -mercaptobenzoic acid	Ref <sup>289</sup>
AU <sub>133</sub> (SR) <sub>52</sub>	1.7	26	-	-	<i>p</i> - <i>tert</i> -butylbenzene thiol	Ref <sup>290</sup>
AU <sub>144</sub> (SR) <sub>60</sub>	1.7	30	-	-	<i>p</i> -mercaptobenzoic acid	Ref <sup>291</sup>
AU <sub>314</sub> (SR) <sub>96</sub>	2.1	48	-	-	None	Ref <sup>37</sup>

The staples of a given core have a static arrangement that, in turn, fixes the total number of ligands to be placed on each of the cores. Moreover, due to the chiral nature of the ligands' sulfur atom, the ligands can be located on different sides with respect to the staples' plane, leading to *cis-trans* isomers.<sup>55,124,292</sup> The number of isomers depends on the size and number of staples, and can quickly become unmanageably high. For example, the 1.1 nm Au<sub>38</sub>(SR)<sub>24</sub> nanocluster already admits 2<sup>24</sup> *cis-trans* stereoisomers.<sup>125</sup> As a result, NanoModeler allows the

user to treat *cis-trans* isomerism in two ways. First, NanoModeler can keep the isomerism with which the core was originally elucidated. Second, the first carbon atom of each ligand can be placed along the vector formed between the system's centroid and the sulfur atoms. The latter method produces an out-of-equilibrium structure, which attempts to be equidistant from all possible isomers.

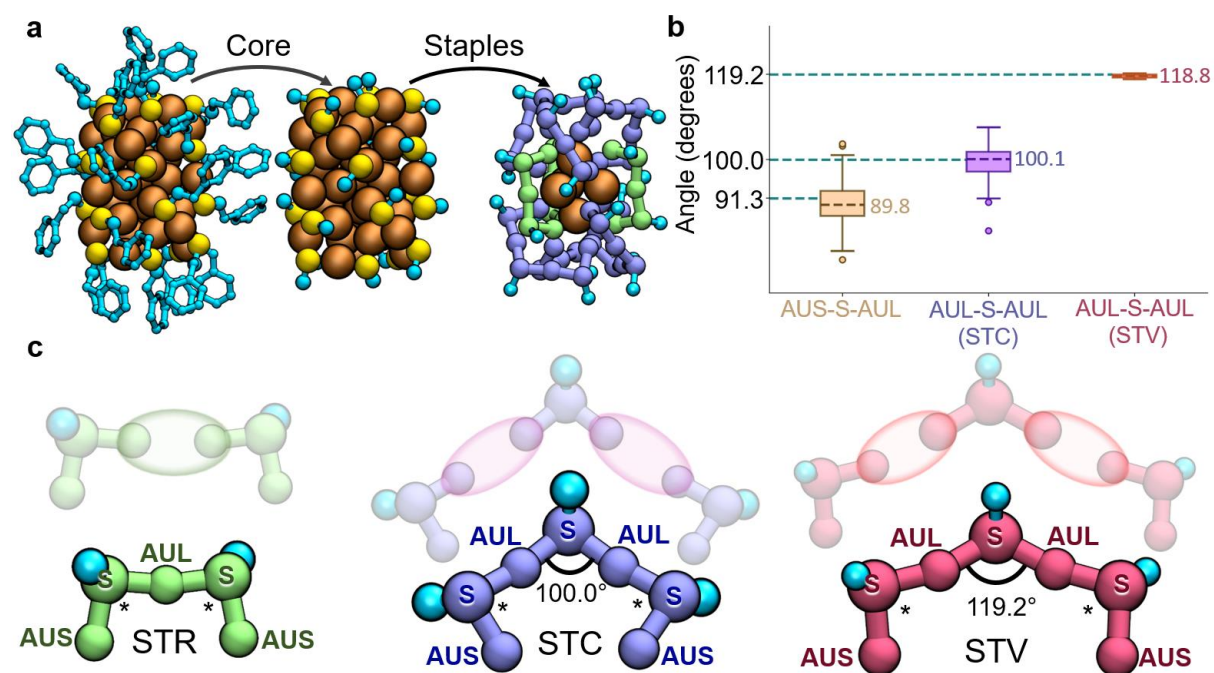


**Figure 16.** Staple motifs in gold cores. **a.** X-ray-derived structure for Au<sub>38</sub>(phenylethane thiol)<sub>24</sub>, its core as incorporated in NanoModeler, and its staple-type classification. Gold atoms are in orange, sulfur in yellow, and carbon in cyan. **b.** Boxplot for the different types of gold-sulfur-gold angles in the staples, in all the 16 cores. The colored numbers represent the median of each distribution, whereas the aquamarine lines indicate the equilibrium values as derived by Pohjolainen and co-workers.<sup>72</sup> **c.** The three staple types considered in NanoModeler are shown. Staples are the anchoring sites used to couple the coating ligands to the core of the AuNP. The staple named STR comprises two intersecting subunits, while staples named STC and STV comprise three subunits. Each subunit includes one sulfur atom, plus the nearest two gold atoms and one carbon atom. Subunits are shown in transparency on top of each staple. AUL and AUS are atom types used by NanoModeler to classify gold atoms that belong to staples. AUL or AUS indicate a gold atom's position in the respective staple. The atom type S indicates thiolate sulfur atoms. Notably, STC and STV differ only in the AUL – S – AUL angle. The AUS – S – AUL angles are indicated with a star (\*). STR residues are in green, STC in purple, and STV in red.

In addition to all the possible sizes, staple distributions, and *cis-trans* isomers considered in NanoModeler, AuNPs allow the user to implement thiols with great chemical diversity. The thiols' chemical structure (as a .mol2 file) is the only input required by NanoModeler. In this way, AuNPs and AuNCs can be coated by functionalized thiols, with the structure specified by the user. These thiols can also be placed to form homogeneous or mixed monolayers. For

homogeneous monolayers, a unique ligand uniformly covers the metallic core's surface. For heterogeneous monolayers, two coating ligands can be arranged in different ways over the NP's surface to give rise to various morphologies.<sup>293</sup> These morphologies include random,<sup>294,295</sup> Janus-like,<sup>296,297</sup> and striped<sup>259,298–300</sup> distributions, all of which are accessible by NanoModeler (**Figure 17**). These distributions are a key factor in the overall behavior of AuNPs.<sup>131,259,301–303</sup>

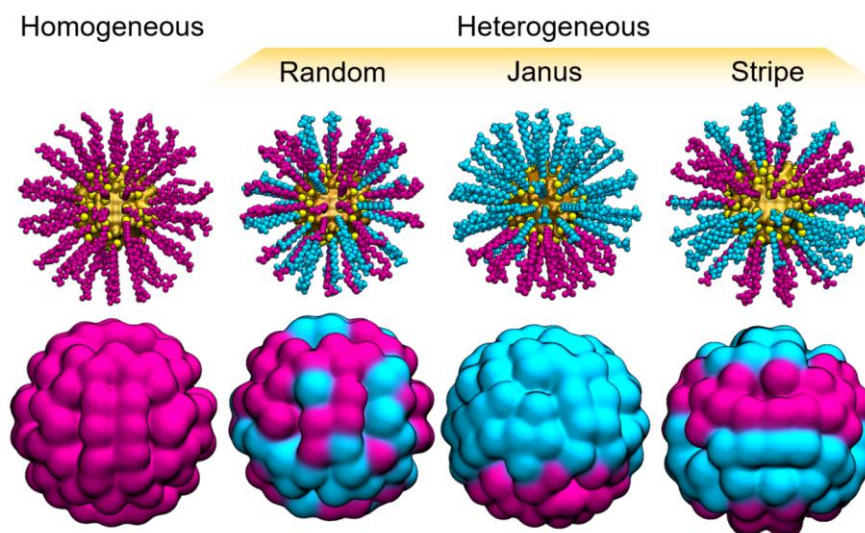


**Figure 17.** Graphical representation of the four morphologies supported by NanoModeler. If only one coating ligand is provided, the outcome is a homogeneous-monolayer-protected AuNP. If two coating ligands (pink and cyan) are provided, the other three morphologies become available. These morphologies correspond to random, Janus-like, and striped distributions. Gold atoms are shown in orange and sulfur in yellow.

Thus, NanoModeler can assemble monolayer-protected AuNPs, each defined by a given size, geometry, 3D shape, and functionalization. It can output these AuNPs in common file formats (.pdb and .gro). The building and assembly operations can implement a variety of different cores, from sub-nanometer-sized AuNCs up to 2 nm AuNPs. The available cores also consider diverse staple arrangements, accounting for possible conformers. Furthermore, NanoModeler allows the assembly of both homogeneous and heterogeneous monolayers, with random, Janus-like, or striped distributions of the grafted thiols.

## 2. Building topologies for molecular dynamics simulations of gold nanoparticles

In order to run MD simulations, each AuNP's 3D model requires bonded and nonbonded parameters, such as force constants, equilibrium values, atomic partial charges, and Lennard-Jones coefficients (Chapter II). These are eventually used to build the topology of a given

AuNP, which is used to compute the forces and evolve the system according to Newton's equations of motion in MD simulations. Over the years, several groups have developed parameters for simulating selected functionalized gold cores.<sup>200,304,305</sup> Here, after collecting all the available parameters, we have automated the creation of topology files for each given AuNP of interest. In NanoModeler, the parameters file is written in a Gromacs-compatible format (.top).

NanoModeler builds the topology file in a similar way to building the 3D model, from the inside to the outside of the structure. Starting from the inner metallic core, NanoModeler uses the nonbonded parameters of gold generated by Heinz and co-workers.<sup>304</sup> For this implementation, gold atoms are categorized as AUL or AUS if they belong to staples. AUL and AUS differ in their specific position in the respective staple (**Figure 16**). All the remaining gold atoms of the system are assigned the AU atom type. Notably, AU atom types are not subject to any bonded forces. Instead, they are only treated using the van der Waals term.<sup>200</sup> All the gold atoms in a given AuNP are assigned a charge of zero. Considering partially charged gold atoms does not increase the accuracy of MD simulations because the electrostatic potential quickly goes to zero on the core's surface.<sup>200,263,305</sup>

NanoModeler implements bonded and nonbonded parameters for the staple motifs, which are taken from Pohjolainen et al. (**Table 2**).<sup>200</sup> The classification of staples used in ref<sup>200</sup> to derive the bonded parameters is also appropriate for the extended dataset implemented in our webserver. Thus, NanoModeler classifies the type of staples (i.e. STR, STC, STV, **Figure 16c**) on any given core, and assigns the corresponding bonded parameters from ref<sup>200</sup>. To this end, NanoModeler first divides the staples into subunits comprising one sulfur atom, one carbon atom, and two gold atoms. In total, NanoModeler stores as many subunits as sulfur atoms in the core. Thus, each subunit includes one sulfur atom, plus the nearest two gold atoms and one carbon atom. The staple is then classified as STR, STC, or STV, based on the number of consecutive intersecting subunits and the AUL – S – AUL angle formed in the central subunit. It is important to note that there are two non-overlapping distributions for the AUL – S – AUL angle (i.e. STC distribution does not overlap with STV distribution in the plot in **Figure 16b**). Indeed, these distributions correspond to the two different staple types STC and STV, which have a median AUL – S – AUL angle of 100.1° and 118.8°, respectively. Notably, in **Figure 16b**, the distribution on the angles associated to the STV staple is narrower than that for STC and for the AUS – S – AUL angle. However, this may be due to a varying number of samples



for the three sets used to calculate the distribution for each of the angles in the staples. In detail, the AUS – S – AUL angle is present 548 times among the implemented cores and the AUL – S – AUL (STC) angle is present 59 times, while the AUL – S – AUL (STV) angle is present only 3 times in our dataset (**Table 1**). Thus, the narrower distribution of the AUL – S – AUL (STV) angle is due to the limited number of values for the AUL – S – AUL (STV) angle reported in the literature for the considered cores. Once the staple type is identified, the respective bonded parameters are assigned for each subunit (**Table 2**).<sup>304,200</sup> Finally, NanoModeler assigns parameters to the functionalized coating thiols. Partial atomic charges of the thiol must be present in the input .mol2 file. The server assigns the bonded and Lennard-Jones parameters, calculated with the ‘parmchk2’ tool in AmberTools18,<sup>202,273</sup> and derived from the Generalized Amber Force Field (GAFF) force field.<sup>197</sup> In this way, a single topology file is generated, then the *acpype.py* script<sup>306</sup> is used to convert the topology file to a Gromacs-compatible format. The user also has the option of uploading a parameters file (.frcmod file format) to overwrite or complete those provided by default.

**Table 2.** Compilation of all the bonded and nonbonded parameters implemented in NanoModeler. Bonded parameters are taken from Pohjolainen et al.,<sup>200</sup> whereas nonbonded parameters are adapted from Heinz et al.<sup>304</sup>

<b>Bond</b>	$k_b$ (kJ mol <sup>-1</sup> nm <sup>-2</sup> )	$l_0$ (nm)
AUS – S	62,730.0	0.241
AUL – S	62,730.0	0.233
CA – S	198,321.6	0.175
CT – S	99,113.0	0.184
<b>Angle</b>	$k_\theta$ (kJ mol <sup>-1</sup> rad <sup>-2</sup> )	$\theta_0$ (degrees)
AUS – S – AUL	460.24	91.3
S – AUL – S	460.24	172.4
AUL – S – AUL (STC)	460.24	100.0
AUL – S – AUL (STV)	1,460.24	119.2
AUS – S – C*	146.37	111.6
AUL – S – C*	146.37	106.8
CA – C – OH	585.76	112.0
CA – C – O	585.76	126.0
CA – CA – S	418.40	120.0
S – CT – HC	418.40	107.0
H1 – CT – CA	418.40	109.0
<b>Dihedral</b>	$V_\phi$ (kJ mol <sup>-1</sup> )	$\phi_0$ (degrees)
X – X – CA – S	4.6024	180.0
C – CA – CA – CA	4.6024	180.0
<b>Nonbonded</b>	$\sigma_{ii}$ (nm)	$\epsilon_{ii}$ (kJ mol <sup>-1</sup> )
AU / AUL / AUS	0.2629	22.133
S	0.3563	1.046

As output, NanoModeler provides the structure of the input ligands (.mol2 file format), the structure of the assembled AuNP (.pdb and .gro file format), and the parameters of the functionalized AuNP (.top file format). The structure (.gro) and topology (.top) files are ready to use with the Gromacs MD engine. NanoModeler currently supports 16 cores containing up to three different staple types (STR, STC, and STV), and with specified coating ligands arranged in four possible morphologies (homogeneous, random, Janus, and striped). The resulting topology files are ready for use in atomistic MD simulations. All parameters are compatible with the AMBER family of force fields, so the parametrized AuNPs can be simulated in complex mixtures containing biologically relevant macromolecules, such as proteins,<sup>194,307</sup> nucleic acids,<sup>195,196,308–310</sup> lipids,<sup>198,199,311</sup> and carbohydrates.<sup>312</sup>

### 3. *Molecular dynamics simulations and test cases*

To demonstrate NanoModeler's capabilities and potential for studying and engineering AuNPs and AuNCs, we built three different model systems and validated them by performing 200-ns-long MD simulations, comparing different observables to experimental data. The first system (NP1) was based on the Au<sub>314</sub>(SR)<sub>96</sub> core, coated with a homogeneous monolayer of octanethiol. The second system (NP2) was based on the Au<sub>144</sub>(SR)<sub>60</sub> core, passivated with decanethiol. The third system (NP3) was based on the Au<sub>314</sub>(SR)<sub>96</sub> core, covered with dodecanethiol. We used NanoModeler to generate the topology of each model system. Each model was simulated in a different organic solvent, as used in the experiments (Chapter III-C).

Considering that the simulated systems differ in the chemical structure of the coating thiols as well as in the core size and the surrounding solvent, we first verified the stability of the metallic cores. For this, we calculated the root mean squared displacement (RMSD) of the staples in NP1, NP2, and NP3, as well as the RMSD of the atoms with type AU (i.e. inner core atoms). As it can be seen from **Figure 18a**, the staples present and AU atoms are highly stable, with deviations smaller than 0.1 nm as compared to the starting model, in all the simulated AuNPs. The low RMSD of the AU atoms alone (0.013 nm) verifies that the exclusive-van der Waals term suffices to restrain the shape of the metallic substructure.<sup>200</sup>

For NP1, we first calculated the average distance between the core's surface and each carbon atom of the alkyl chains in chloroform. As depicted in **Figure 18b**, the simulated and experimental<sup>128,313</sup> results are in excellent agreement. Moreover, the linear ascent of the curves indicates that the alkyl chains around the metallic core are extended toward the organic solvent,

as already reported for similar systems.<sup>57</sup> The nearly-spherical conformation of NP1 is also supported by its average eccentricity of  $0.014 \pm 0.001$  calculated from our MD simulations.

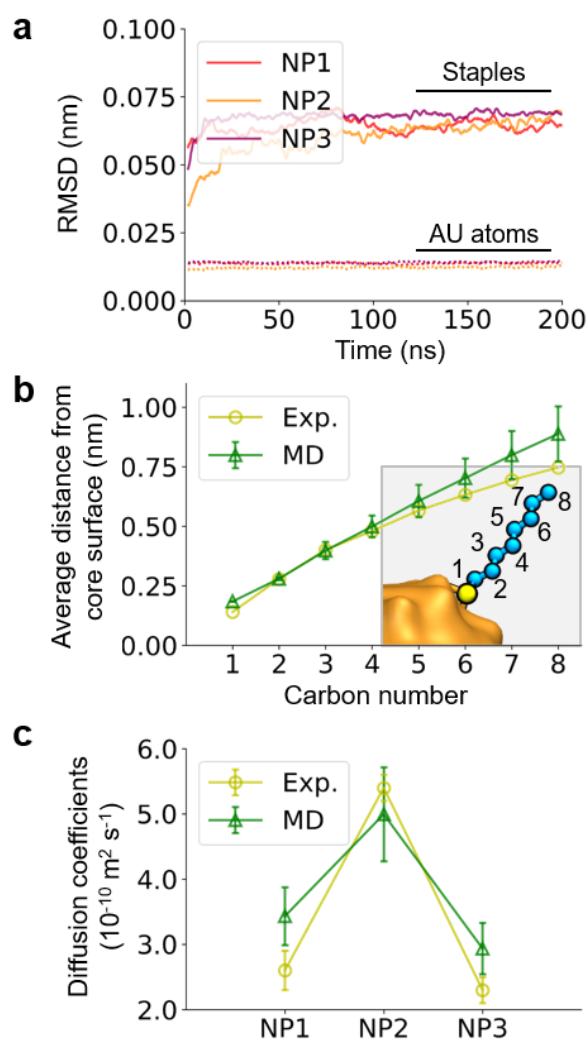


**Figure 18.** Model benchmarking against experimental data. **a.** Moving averages calculated from the RMSD of the staples and the AU atom types for NP1, NP2, and NP3. The moving averages were calculated with a window size of 20 frames (i.e. 200 ps). **b.** The average distance between the metallic core and the carbon atoms of the alkyl chains coating NP1. The average distances from the core's surface are computed as expectation values (and their associated standard deviation) from the RDF of the carbon atoms, as explained in detail in Chapter III-C. The values calculated from our MD simulations are shown in green, whereas the experimental values are in yellow. **c.** Calculated and experimental values for the translational diffusion coefficients of the three systems under study. The diffusion coefficients of NP1 and NP3 were measured in chloroform, while the diffusion coefficient for NP2 was measured in dichloromethane.

We then calculated the translational diffusion coefficient for NP1, NP2, and NP3 using the Stokes-Einstein relation (Chapter III-C). Here too, the computed coefficients are in qualitative agreement with the experimental values (**Figure 18c**).<sup>128,314</sup> In the experiments and

simulations, the coefficients for NP1 and NP3 were assessed by dissolving them in chloroform, whereas NP2 was solvated in dichloromethane. The elevated diffusion coefficient of NP2 is thus a consequence of the decreased viscosity of dichloromethane with respect to that of chloroform. Moreover, the approach used to calculate the diffusion coefficients has already been applied to similar systems in dichloromethane by Piserchia and co-workers.<sup>314</sup> In line with their work, an overestimation of the hydrodynamic radius leads to an apparent decrease in the diffusion coefficient, as with NP2 in our simulations.

Finally, we further characterized NP3 by estimating its radius of gyration. Our simulations returned a value of  $1.160 \pm 0.003$  nm, which is in reasonable agreement with the experimental value of  $0.924 \pm 0.005$  nm. The discrepancy might be due to the rigidity of the gold-sulfur interface in NP3, and possible dynamic processes such as diffusion and/or exchange of thiolates on the coating monolayer of AuNPs.<sup>55</sup>

Taken altogether, these test cases demonstrate that NanoModeler can be used for the appropriate set up of MD simulations to eventually analyze structural dynamics and calculate physicochemical properties of AuNPs and AuNCs, leading to a deeper understanding of the solubility, effective radii, diffusion profiles, and NMR spectra.

## **C. Webserver building**

### *1. Structure of the webserver*

The NanoModeler webserver ([www.nanomodeler.eu](http://www.nanomodeler.eu)) has two main components: the frontend and the backend. The frontend is a single-page application that uses the Angular 6 framework, a TypeScript-based web application platform that dynamically rewrites the page for an enhanced user experience. In addition, the graphical interface incorporates the Bootstrap framework, allowing the application to be accessible from various devices (e.g. smartphones, tablets, and laptops) without compromising its functionalities. The backend is an aggregation of Microservices that run in Docker containers. Some containers, like the orchestrator and data persistence layer, are built on top of NodeJS, whereas the code to assemble nanosystems and their topology is written in Python. Below, the assembly of the 3D models and topologies are discussed in detail.

## 2. Preparation of cores and coatings

Here, we outline NanoModeler's operating steps, as shown in **Figure 15a**. The assembly of the 3D model of a given AuNP is based on the initial arrangement of the gold and sulfur atoms, as reported in the literature (**Table 1**). Thanks to the wealth of atomically detailed data on AuNPs, NanoModeler implements 16 different cores, ranging from 0.9 to 2.1 nm in diameter. Each core is listed in **Table 1**, together with its respective size (average diameter) and the name of the coating thiol with which it was first elucidated.

Prior to their implementation, the cores' files were processed with in-house scripts that classify the gold and sulfur atoms based on their relative structural arrangement. In general, the gold-sulfur interface comprises staple-like motifs where each sulfur atom is bound to two gold atoms.<sup>25,314</sup> All staples in the cores are assigned to one of three classes, i.e. STR, STC, and STV (**Figure 16**). The staples are identified and classified based on their Au – S distances and S – Au – S angles. Notably, three types of gold atoms are also differentiated, i.e. AUL, AUS, and AU. The AUL and AUS gold atoms are classified based on the position in their respective staple (**Figure 16**). The remaining gold atoms are classified as AU. All three gold atom types are assigned the same nonbonded parameters; the AU/AUL/AUS differentiation is structural only and is necessary for the assignment of bonded parameters. All core structures in NanoModeler contain the gold atoms, the sulfur atoms in the staples, and the first carbon of the ligand with which they were originally elucidated (when present, **Figure 19a**). However, some structures were reported without any bound ligand, that is, without a *cis-trans* isomerism known a priori. For these cases, vectors were drawn from the centroid of the systems to the sulfur atoms, and a methyl group was positioned away from each sulfur atom at the characteristic thiol carbon-sulfur distance (0.18 nm).<sup>315</sup> After their methylation, the systems were parametrized following the workflow presented below, and minimized using the steepest descent method until the forces were smaller than 250 kJ mol<sup>-1</sup> nm<sup>-1</sup> (500 steps). Then, the hydrogen atoms of the methyl groups were deleted, and the structure of the core was stored as the rest.

To create the functionalized AuNP, the user must provide the structure of one or two ligands in .mol2 file format. To perform MD simulations, the input files must contain the partial charges of all atoms. In this case, charges may be calculated with the restrained electrostatic potential (RESP)<sup>203,316</sup> approach through the R.E.D. Server.<sup>317</sup> The provided ligand structures may have an open valence on the atom that serves as the anchor point to connect the thiol to

the core. If so, this will be used to link the ligands to the core. If the ligand contains a capping group (e.g. the hydrogen on the thiol's S – H group), this must be specified. The atoms and bonds belonging to this group are then removed from the structure to allow linking to the core. Special care should be taken here because the charge of the capping group is equally distributed by NanoModeler across the other atoms in the molecule (**Figure 19b**).

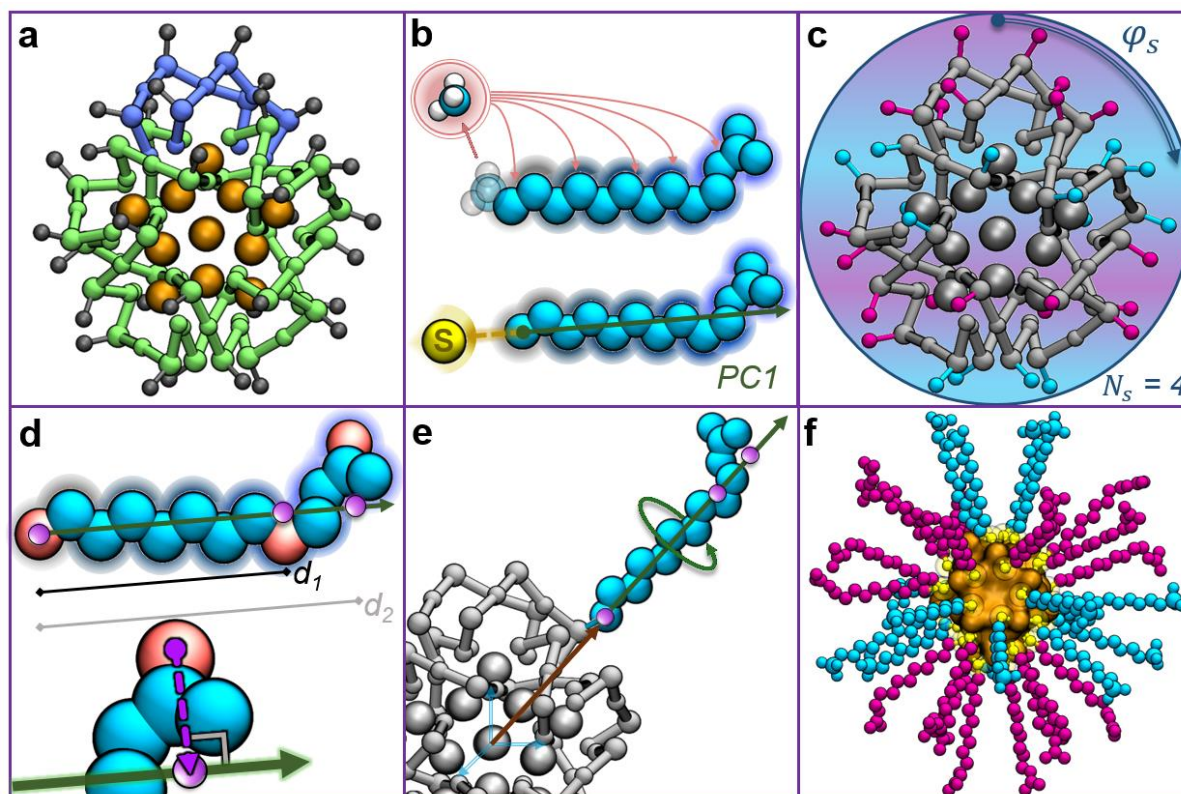


**Figure 19.** Graphical description of how NanoModeler operates. **a.** Generic structure of a core. **b.** Initial treatment of coating ligands. The charge of an eventual capping group is distributed across the other atoms in the ligand. If atom *S* is absent, NanoModeler places it along the compound's *PC1* axis. **c.** Assignment of a morphology and, in particular, the assignment of a striped distribution of the thiols. **d.** Determination of  $d_1$  and  $d_2$  as the distances between *C* and the projection along *PC1* of two randomly chosen atoms. **e.** Roto-translation of one ligand into its respective site. **f.** Final model obtained for an AuNP with a striped conformation. Inner gold atoms are shown in orange, STR staples in green, STC staples in light purple, two arbitrary ligands are in pink and cyan, randomly chosen atoms for the roto-translation of a ligand are in red, and virtual sites are in dark purple.

### 3. 3D modeling of gold nanoparticles

When building a nanostructure in NanoModeler, the user must specify the core. The server then assigns a morphology by giving each carbon atom from the core a particular label, which defines the ligand to be placed in that position. If only one ligand is uploaded, all labels are the same. If two ligands are uploaded, the labels are assigned depending on the specified

morphology type. Currently, three mixed morphologies are supported, namely ‘Random,’ ‘Janus,’ and ‘Stripe.’ When the morphology is set to ‘Random’ or ‘Janus,’ the user may specify the fraction (between 0 and 1) of sites to be labeled with the first ligand. The remaining sites are assigned to the second ligand. When the morphology is set to ‘Stripe,’ the azimuthal angle  $\varphi_s$  is divided into  $N_s$  equidistant intervals, where  $N_s$  is the number of stripes specified by the user (**Figure 19c**). The carbon atoms are then labeled in an intercalating fashion depending on the interval into which they fall.

After the morphology is assigned to the core, the structure file of the ligands is read. Regardless of the presence of a capping group in the ligands, the structure may or may not contain the thiol’s sulfur atom (namely the  $S$  atom), through which it is bound to the metallic core. If  $S$  is absent, the user must indicate the carbon atom of the coating molecule (namely the  $C$  atom), which should be covalently bound to  $S$  (**Figure 19b**). In this case,  $S$  is placed 0.18 nm from  $C$  along the principal axis of the molecule. To calculate the principal axis of a ligand ( $PCI$ ), the molecule is translated so that  $C$  is the origin of coordinates.  $PCI$  corresponds to the eigenvector associated with the largest eigenvalue of the covariance matrix. The covariance matrix  $\Sigma$  is constructed with Equation 72 from the Cartesian coordinates of all the atoms:

$$\Sigma_{ij} = \frac{\sum_{k=1}^{N_{mol}} (X_i^k - \bar{X}_i)(X_j^k - \bar{X}_j)}{N_{mol} - 1} \quad (72)$$

where  $N_{mol}$  is the number of atoms in the (ligand) molecule,  $X_i^k$  is the  $i$ -th coordinate of the  $k$ -th atom, and  $\bar{X}_i$  is the mean of the  $i$ -th coordinates from all the atoms. The server then identifies three characteristic points of each ligand for further anchoring. The first point is  $C$ . For the other two points, two atoms of each ligand, excluding  $S$  and  $C$ , are chosen and projected along  $PCI$ . The selection of the latter two points is performed pseudo-randomly, so that the results are reproducible given the same input files. The distances  $d_1$  and  $d_2$  between these two points and  $C$  are calculated and stored for later use (**Figure 19d**).

Each carbon atom of the core is then treated sequentially. First, a vector is drawn from the centroid of the core to the carbon atom. The morphology label on-site is read, and the values of  $d_1$  and  $d_2$  of the respective ligand are retrieved. The vector is then scaled to reach a distance  $d_1$  from the carbon atom, and a virtual site is saved at this position. The same procedure is carried out for  $d_2$  (**Figure 19e**). A quaternion transformation matrix is fitted so that the three aforementioned points of the ligand match the carbon atom and the two virtual sites. At this

point, the transformation is applied to the ligand to obtain the roto-translated structure. Note that the coordinates of *S* must be modified to match those of the closest sulfur atom present in the core. The method is thus invariant to the original position of *S* in the ligands' structure. Since the fitting points are collinear, the roto-translation is arbitrary, and it may result in clashes with the rest of the system. To overcome this, the ligand is rotated along the vector between the centroid of the core and *C* iteratively. The coordinate is scanned through 100 iterations. For each iteration, the minimum distance between the ligand and the rest of the system is stored. The final orientation results in the largest minimum distance after the entire scanning. The structure of the NP is obtained after repeating this procedure for all ligands (**Figure 19f**).

#### 4. *Molecular dynamics simulations*

To validate the topologies built with NanoModeler, we simulated three AuNPs, each with different coatings. The three coating thiols were octanethiol (NP1), decanethiol (NP2), and dodecanethiol (NP3). The partial charges of the thiols were calculated with the RESP fitting procedure as implemented in the R.E.D. Server.<sup>203,316,317</sup> The initial conformation and the parameters files were generated with NanoModeler.

For the MD runs, a dodecahedral simulation box was built to ensure a minimum distance of 1.0 nm between the AuNP and the box edge. The box was then filled with chloroform molecules, whose parameters are reported elsewhere.<sup>318</sup> To relax the solvent around the particle, a minimization was carried out using the steepest descent method. The system was heated for 500 ps with the velocity-rescale thermostat ( $\tau_B = 0.1$  ps) in the NVT ensemble to 295 K, a temperature chosen to match the experimental conditions used by Terrill et al.<sup>128</sup> We then pressurized the system to 1 bar with a 500-ps-long simulation in the NPT ensemble with the isotropic Parrinello-Rahman barostat ( $\tau_P = 2.0$  ps,  $\kappa = 10^{-4}$  bar<sup>-1</sup>).<sup>227</sup> Once the system had reached the intended temperature and pressure, the system was simulated for 200 ns, discarding the first 25 ns as equilibration. All bonds were constrained using the linear constraints solver algorithm<sup>319</sup> and a timestep of 2 fs was used. Short-range nonbonded interactions were calculated within a radius of 1.2 nm of each atom, whereas long-range electrostatic interactions were considered using the fourth-ordered particle-mesh Ewald method.<sup>231</sup> The simulations for NP2 were performed in dichloromethane,<sup>318</sup> following the same protocol at 300 K to match the respective experimental conditions.<sup>314</sup> All simulations were conducted with Gromacs-v5.1.4.<sup>320–322</sup>



For the trajectory analysis, we used a mixture of Gromacs tools and in-house scripts. To calculate the average distances between the gold's surface and the carbon atoms, we used Equation 73:

$$\langle r_i \rangle = \int_0^{D_{max}} \rho_{c,i}(r) r dr \quad (73)$$

where  $\langle r_i \rangle$  is the mean distance between the gold's surface and the  $i$ -th carbon of the alkyl chain,  $D_{max}$  is half of the shortest box vector and  $\rho_{c,i}$  is the normalized radial distribution function (RDF) of the  $i$ -th carbon. The RDF was originally calculated with Gromacs and then normalized to 1.0. To calculate the translational diffusion coefficients, we used the Stokes-Einstein relation (Equation 74), following the workflow presented by Piserchia et al.:<sup>314</sup>

$$D_{transl} = \frac{k_B T}{8\pi\eta_{solv} R_{hydrodynamic}^3} \quad (74)$$

where  $k_B$  is the Boltzmann constant,  $T$  is the temperature,  $\eta_{solv}$  is the experimental viscosity of the solvent, and  $R_{hydrodynamic}$  is the hydrodynamic radius of the AuNP calculated as the average distance to the AuNPs centroid from the most exposed atom of the thiols. The standard deviations shown in **Figure 18** were estimated by propagating the uncertainty associated with the probability density function following Equation 75.

$$\sigma_{r_i} = [\langle r_i^2 \rangle - \langle r_i \rangle^2]^{\frac{1}{2}} \quad (75)$$

The radius of gyration  $R_g$  was calculated with Equation 76, where  $N_{NP}$  is the number of atoms in the AuNP, using the 'gyrate' tool available in Gromacs. All the aforementioned properties were calculated from snapshots saved every 10 ps.

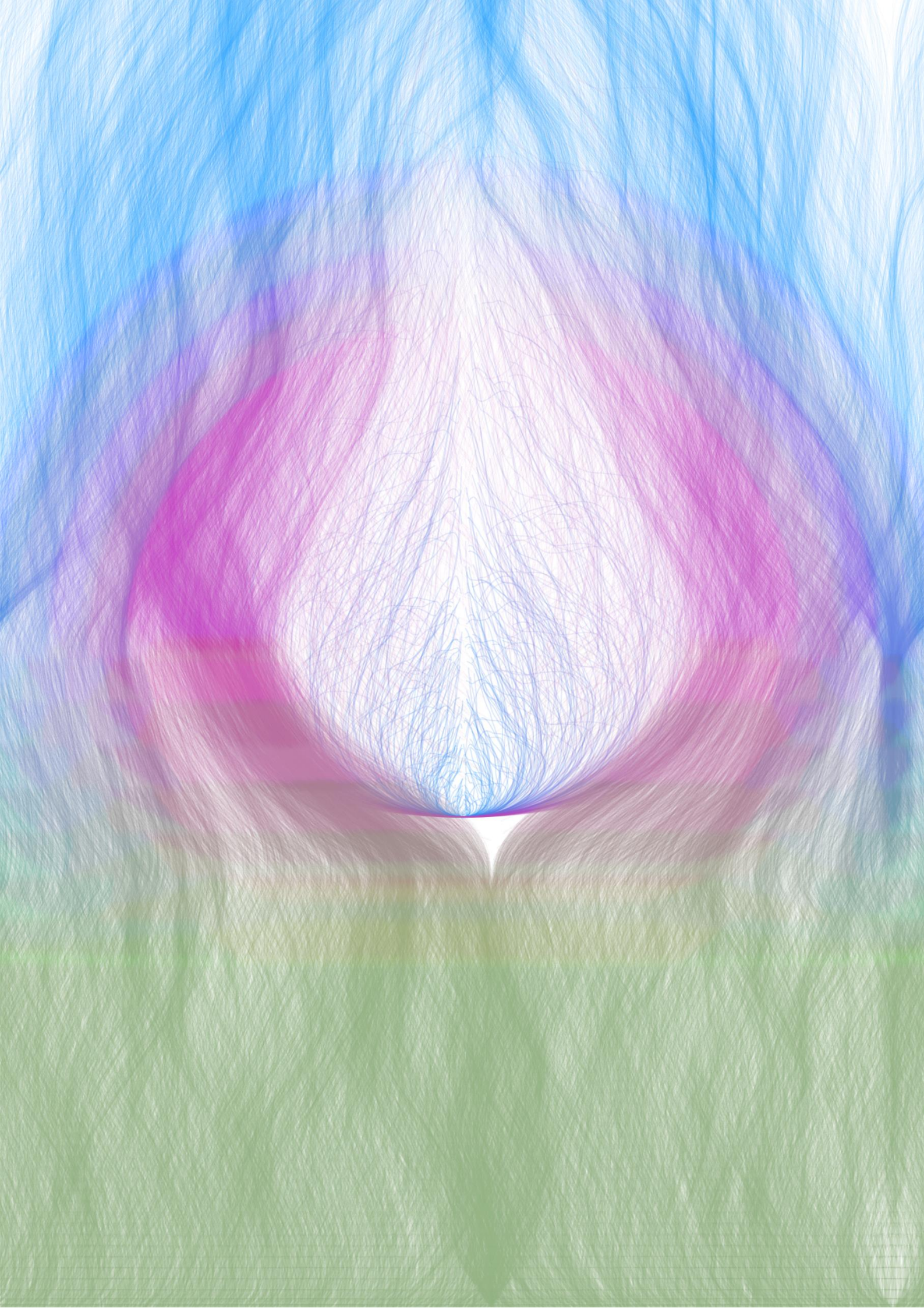
$$R_g = \frac{\sum_i^{N_{NP}} m_i r_i^2}{\sum_i^{N_{NP}} m_i} \quad (76)$$

## D. Conclusions

In this work, we present the first release of NanoModeler, the first web-based platform for building 3D models of AuNPs and AuNCs and the topology setup needed for atomistic MD simulations. These models are generated from three building blocks, namely, i) the inner quasi-

static gold atoms, ii) the gold-sulfur interface, and iii) the coating ligands. The former two building blocks are retrieved from experimental and high-level computational studies (**Table 1** and **Table 2**). The third building block must be provided by the user and allows the construction of specific functionalized thiols for grafting onto the AuNP of interest. Moreover, NanoModeler allows the assembly of AuNPs with different types of coating thiols, thus forming mixed-monolayer-protected AuNPs and AuNCs. Finally, these models are used to generate topology files for MD simulations, as demonstrated here with selected representative test cases that validate our models and setup procedure (**Figure 18**). These topology parameters are compatible with the AMBER family of force fields, allowing the simulation of the nanosystems in conjunction with other biologically relevant macromolecules, such as proteins, nucleic acids, lipids, and carbohydrates.

Upcoming features of NanoModeler may include a fragment-based library for the on-site building of the coating thiols, and partial charges estimation. Future versions of NanoModeler will also offer coarse-grained representation of NPs, allowing the automatic assembly and setup of very large systems for MD simulations (Chapter VI).<sup>294,323</sup> We intend to patch these features to the current server in future releases. This webserver is free for use by experimental and computational scientists working on functionalized NPs. We trust that NanoModeler will accelerate new developments in the emerging field of computational nanodesign and simulations in order to engineer functionalized NPs.<sup>324</sup>



# **CHAPTER IV. ARGININE MAGIC WITH GOLD NANOPARTICLES: SELECTIVE AND NON-DISRUPTIVE TARGETING OF NEUTRAL PHOSPHOLIPID BILAYERS**

## **Abstract**

Understanding and controlling the interaction between nanoparticles and biological entities is fundamental to the development of nanomedicines. In particular, the possibility to develop nanoparticles capable of targeting directly lipid membranes, even if devoid of a net charge, would open the way to numerous applications. Here, we combined experimental and computational methodologies to analyze the interaction between liposomes and cationic gold nanoparticles (AuNPs). Our results highlight the peculiar properties of nanoparticles that feature guanidinium headgroups in their protecting monolayer. In contrast to nanoparticles decorated with other positively charged headgroups, we found that guanidinium-coated AuNPs can bind to neutral phosphatidylcholine liposomes, inducing non-disruptive membrane permeabilization. Atomistic molecular simulations revealed that this ability is due to the multivalent H-bond interaction between the phosphate residues of the liposome's phospholipids and the guanidinium groups. Our results demonstrate that the peculiar properties of 'arginine magic,' an effect responsible for the membranotropic properties of some naturally occurring peptides, are also displayed by guanidinium-bearing functionalized AuNPs.

## A. Introduction

The ability of nanoparticles (NPs) to interact with the surfaces of cells, microorganism, and viruses plays a key role in their biological activity. Cationic NPs generally show higher affinity for lipid membranes and better internalization rates.<sup>325–328</sup> These properties are usually ascribed to the electrostatic attraction between the NPs and the negatively charged membranes.<sup>90,162,302,329–331</sup> Among the different existing categories, small (less than 5 nm in size) gold nanoparticles (AuNPs) coated with monolayers of cationic ligands (usually trialkylammonium headgroups) are particularly interesting. These AuNPs were reported to be taken up by cells via an energy independent (passive) mechanism.<sup>332</sup> Studies with model membranes suggest that AuNPs can induce disruption of the lipid bilayer, which might also explain the observed cytotoxicity.<sup>333–340</sup>

On the other hand, Stellacci and others showed in the last decade that also anionic alkylsulfonate-coated AuNPs can passively penetrate cell membranes, embed within synthetic bilayers, or induce hemifusion between vesicles, depending on the particle size and ligand shell conformation.<sup>90,162,302,329,330</sup> These studies shifted the focus onto the role of the entire chemical structure of the NP's coating monolayer, and suggested that hydrophobic contacts between the inner portions of the phospholipid bilayer and the NP coating molecules might be important in regulating the AuNP-membrane interaction.

Properties similar to those of cationic NPs are shared by other polycationic entities, such as antimicrobial peptides, cell-penetrating peptides (CPPs), polymers, and dendrimers.<sup>341,342</sup> These macromolecules can bind to cells and spontaneously pass through plasma/endosomal membranes. To do so, they use different mechanisms that range from pore formation, as with most antimicrobial peptides,<sup>343</sup> to transient bilayer disruption, as with several CPPs.<sup>344,345</sup> Remarkably, the chemical structure of the positively charged monomers plays a critical role in the molecule's effectiveness in translocating across membranes. The best internalization rates are usually achieved by guanidinium functionalization, so that the ability of arginine residues to increase the cell-penetration capacities of macromolecules was named 'arginine magic.'<sup>339</sup> The origins of this effect are still debated and have been ascribed to different factors including the high pKa of the guanidinium group and, more likely, its H-bonding ability, its unique hydration, and its like-charged pairing properties.

The conceptual similarity between cell-penetrating polymers and cationic AuNPs was recognized early on<sup>337</sup> and one should expect that guanidinium-functionalized AuNPs have peculiar properties in interacting with biological membranes. To date, however, AuNPs coated with guanidinium groups have only been investigated as artificial phosphodiesterases and macromolecular receptors.<sup>97,346–348</sup> Here, we report the results of a comparative study revealing that small AuNPs coated with guanidinium ligands can interact non-disruptively with neutral phospholipid bilayers. Our experiments demonstrate that electrostatic interactions are not the main factor affecting the binding of AuNPs to membranes. Using experiments and molecular dynamics (MD) simulations, we show that the distinctive features of guanidinium-coated AuNPs are due to the selective ability of this functional group to recognize the phosphate group of the lipids at the membrane.

## B. Results

### 1. Gold nanoparticle functionalization and characterization

The main goal of this study was to evaluate the interaction between lipid bilayers and cationic AuNPs and to elucidate the structure-activity relationship at play. We therefore selected a small library of cationic AuNPs coated with Lig1-6 (**Figure 20a**).

The ligands featured alkyl linkers of different lengths and either guanidinium (Lig1 and 2) or trimethylammonium (Lig3-6) headgroups. Notably, the oxygen atoms in Lig4 and 5 were introduced to modulate the monolayer's polarity. Synthesis of Lig1-6 and AuNP1-6 followed standard procedures (Appendix B.1). The size of the gold cores in AuNP1-6 ranged from 1.5 to 2.4 nm, according to transmission electron microscopy (TEM) measurements (**Figure 20b**). The  $\zeta$ -potential values in a phosphate-buffered saline (PBS) solution ranged from +10.3 to +15.0 mV, confirming the cationic coating of the particles (**Figure B-1**). All the AuNPs were well soluble in water and in the buffered solutions used in this study. In the rest of the chapter, AuNP concentrations will be expressed as total concentrations of the coating ligands ([ligand]) to account for the small differences in size of AuNP1-6.

### 2. Liposome permeabilization assays

To initially evaluate the interaction between neutral liposomes and AuNPs, we performed the fluorescein release assay (**Figure 20c**), which is typically used for this purpose.<sup>349–356</sup> In this assay, the escape and consequent dilution of a fluorescein dye from the inner water pool of

liposomes is revealed by an increase in fluorescence emission intensity, due to the dilution-induced reduction of self-quenching. Hence, an increase in the sample's emission indicates that the added agents can interact with the lipid bilayer and perturb its structure. For several polycationic species, this ability correlates with a cell-penetrating ability.<sup>353,354,356</sup> We used phosphatidylcholine (PC, **Figure 20d**) liposomes encapsulating calcein, a polyanionic fluorescein derivative (**Figure B-2**). Liposomes were prepared by extrusion with 100 nm polycarbonate filters, and they displayed an average hydrodynamic diameter of 90 nm and a  $\zeta$ -potential close to zero (-1.7 mV), as expected for neutral lipids like PC (**Table B-1**).

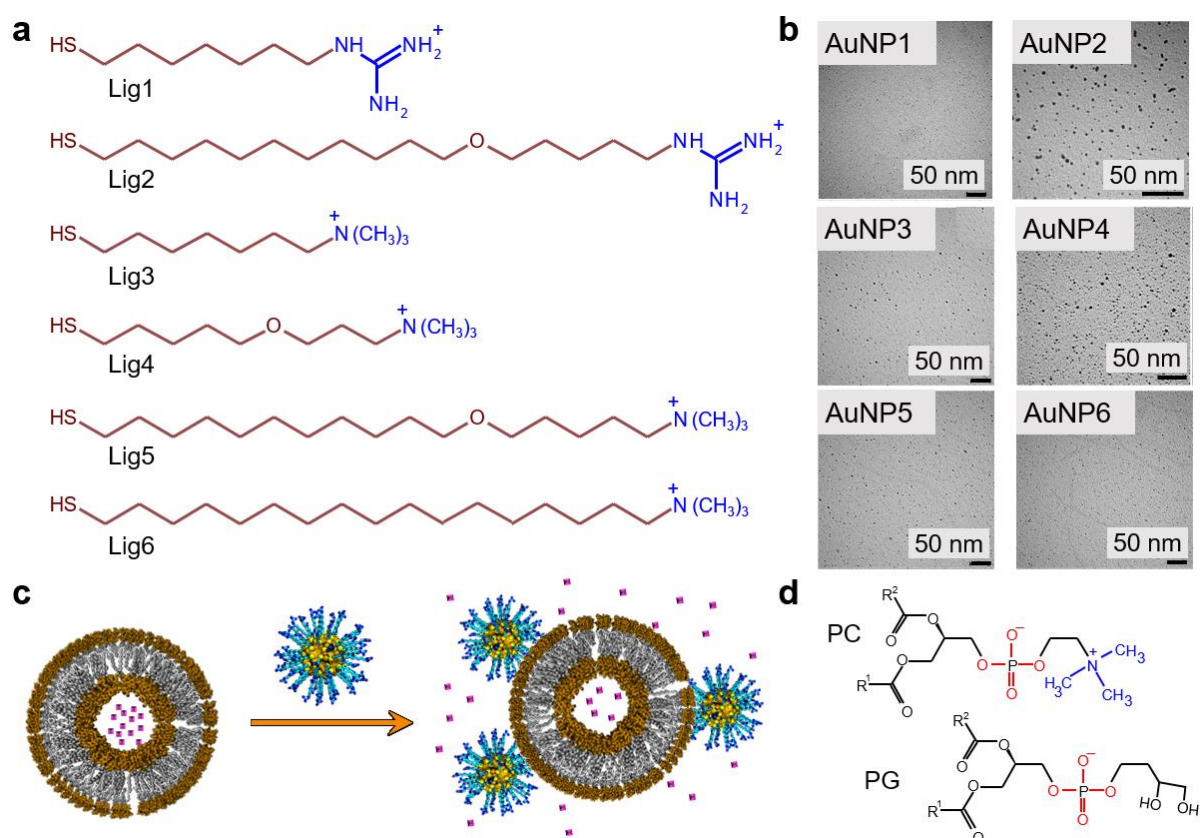


**Figure 20.** Ligands, lipids, and AuNPs investigated. **a.** Structure of the coating thiols Lig1-6. **b.** Representative TEM images of AuNP1-6 (scale bars: 50 nm). **c.** Graphical illustration of calcein release experiments. Gold atoms are shown in orange, ligands in cyan, lipid headgroups in brown, lipid tails in gray, and calcein in pink. **d.** Phospholipids used in this study.

We performed preliminary fluorescence experiments by incubating calcein-loaded liposomes with AuNP1 in a 4-(2-Hydroxyethyl)-1-piperazineethanesulfonic acid (HEPES) buffer solution. These experiments showed a clear increase in emission, revealing the particles' ability to induce dye release. The final emission values observed in each experiment increased with the concentration of AuNPs to eventually level off at a ligand-to-lipid ratio of ca. 2 (**Figure B-**

3), roughly corresponding to one AuNP for every 30-35 phospholipids. The fluorescein release process was very fast, concluding a few minutes after the AuNP addition. Based on these results, we set the ligand-to-lipid ratio to 3 for the subsequent experiments and we systematically investigated the membrane perturbation ability of AuNP1-6.

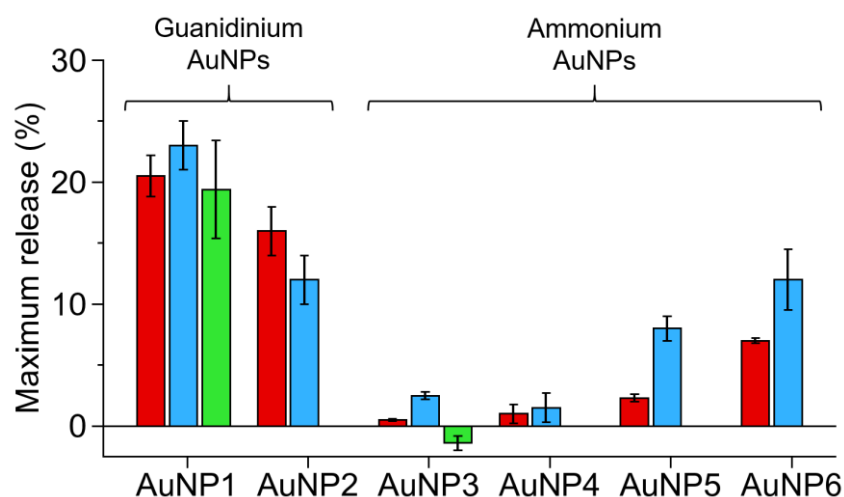


**Figure 21.** Maximum release of calcein from PC (red), PC:PG (blue), and PC:CHOL (green) liposomes after addition of each of the six AuNPs. Experimental conditions: [HEPES] = 10 mM, [NaCl] = 100 mM, [PC]/[PC:PG]/[PC:CHOL] = 22  $\mu$ M, [ligand] = 66  $\mu$ M, pH 7.0, 25°C,  $\lambda_{exc}$  = 495 nm,  $\lambda_{em}$  = 515 nm.

Remarkably, the results (**Figure 21**) clearly show that guanidinium-bearing AuNPs always led to the escape of a larger amount of calcein than their trimethylammonium counterparts. Specifically, AuNP1 and AuNP2 induced emission recoveries close to 20% (with respect to the emission increase obtained by disassembling the liposomes with the Triton-X100 surfactant), whereas the emission increase was negligible (less than 2%) for AuNP3-5, and only slightly greater (about 7%) for AuNP6. Since all the AuNPs had a similar charge, these results revealed that the interaction between cationic AuNPs and neutral lipid bilayers is governed by factors other than the coating molecules' charge. Namely, the AuNPs' membrane perturbation activity is modulated by variations in the chemical structure, including the nature of the cationic headgroups in equally charged ligands and the features of the underlying chains.

### 3. Liposomes' structural integrity

To get more information on the nature of the permeabilization process, we investigated the structural integrity of the liposomes in the presence of the AuNPs. First, to ensure that the effects observed were not due to leaky or unstable liposomes, we investigated the effect of



adding cholesterol (CHOL) to the bilayers. CHOL is present in a relevant amount (about 25-30% mol) in mammalian cell membranes and helps increase their stability and barrier ability.<sup>357,358</sup> We repeated the release experiments using PC:CHOL 10:3 liposomes (97 nm diameter, -0.7 mV  $\zeta$ -potential) and AuNP1 and AuNP3 as representative cases. The results (**Figure 21**) for the CHOL-loaded liposomes showed emission recoveries similar to those measured in the absence of CHOL, revealing that the ability of guanidinium AuNPs to induce calcein escape persisted even on less fluid bilayers.

After verifying that the calcein release induced by AuNP1 was conserved in CHOL-containing liposomes, we analyzed the samples with dynamic light scattering (DLS) to ensure that the liposomes maintained their structural integrity upon AuNP addition. In all our samples, the PC liposomes retained a nearly constant hydrodynamic size and dispersion index (PDI) when incubated with AuNP1-6 at the concentrations used in the calcein release experiments (**Figure B-4**). Thus, the DLS measurements endorsed the structural stability of the liposomes upon AuNP addition. As a further control, the effect of increasing the AuNP concentration was investigated for AuNP1 (**Figure B-5**). Here too, the hydrodynamic size and PDI were unaffected for AuNP concentrations (expressed as total concentration of coating ligands) of up to 500  $\mu$ M, i.e. 10-fold the concentration used in the calcein release experiments.

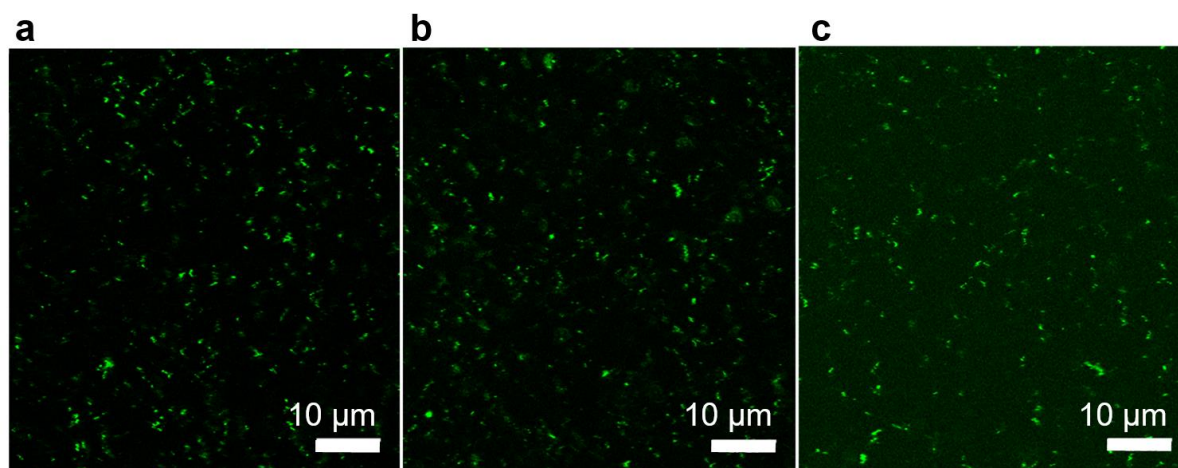


**Figure 22.** Confocal microscopy images. **a.** Calcein-loaded PC liposomes. **b.** Same sample as in **a** after the addition of AuNP3. **c.** Same sample as in **a** after the addition of AuNP1. Scale bar: 10  $\mu$ m. Experimental conditions: [HEPES] = 10 mM, [NaCl] = 100 mM, [PC] = 22  $\mu$ M, [ligand] = 66  $\mu$ M, pH 7.0, 25°C,  $\lambda_{exc}$  = 488 nm,  $\lambda_{em}$  > 510 nm.

The release of calcein from liposomes was also monitored with fluorescence confocal microscopy. Images recorded from samples of calcein-loaded PC liposomes showed the presence of scattered green dots, corresponding to the residual emission of individual

liposomes (**Figure 22a**). The addition of AuNP3 (**Figure 22b**) did not produce any significant changes, consistent with the results of the previous experiments. However, for AuNP1 (**Figure 22c**), a relevant increase in the green background emission was clearly detected, while the dotted emission from the liposome remained. We ascribed this effect to the release of calcein into the bulk solution. According to confocal images, this occurred without affecting the integrity of the liposomes.

The results from steady state fluorescence experiments and confocal microscopy were confirmed by fluorescence lifetime measurements on the same samples under 440 nm pulsed excitation. In all cases (**Figure 23**), we detected two emission decay processes. The first process had a longer lifetime ( $\tau_1$ , 4 ns), and it was assigned to residual unquenched calcein (indeed, the same lifetime was measured for a dilute calcein solution). The second process had a shorter lifetime ( $\tau_2$ , 0.3 ns), and it was assigned to the self-quenched dye molecules entrapped within liposomes. Support for these assignments comes from measurements of the lifetimes of the most intense emission spikes recorded during intensity trace measurements (**Figure B-6**). These spikes corresponded to events where several liposomes were simultaneously illuminated by the laser beam, leading to a steep increase in the light emitted. As such, they provided information on the state of the entrapped dyes. During the spikes, the lifetimes' composition substantially changed with the fraction of the short-living species, substantially increasing and reaching up to 90%. This confirmed the identification of the short-living species as quenched entrapped dyes.

Upon addition of AuNPs, the ratio of lifetime populations in liposome samples underwent no significant modifications with AuNP3 (**Figure 23**), confirming that liposomes are unaffected by the presence of these AuNPs. However, the addition of AuNP1 resulted in a clear increase in the fraction of unquenched dyes, as expected in the case of a release of entrapped calcein.

Taken together, fluorescence emission experiments, DLS measurements, and confocal microscopy point to a permeabilization mechanism where the interaction of the AuNPs with the liposomes induces a local destabilization of the double layer. This causes the release of the entrapped dye molecules without affecting the overall structural integrity of the liposomes.

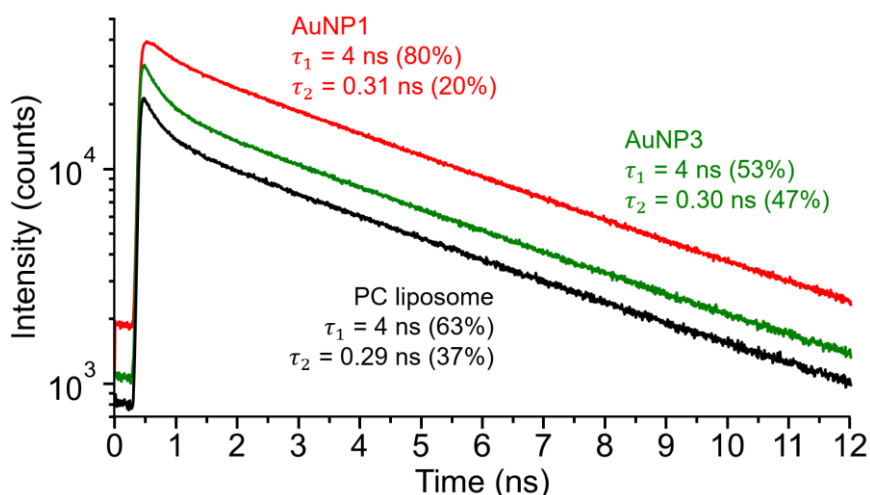


**Figure 23.** Fluorescence decay curves of calcein-loaded PC liposomes alone (black), after the addition of AuNP1 (red), and after the addition of AuNP3 (green) under the same excitation power. The relative amplitude of each component is in parentheses. Experimental conditions: [HEPES] = 10 mM, [NaCl] = 100 mM, [PC] = 22  $\mu$ M, [ligand] = 66  $\mu$ M, pH 7.0, 25°C.

#### 4. The nature of the gold nanoparticle-liposome interaction

To shed light on the supramolecular structure of the AuNP-liposome complex, we investigated our samples with cryogenic electron microscopy (cryo-EM, **Figure 24a-f**). Samples were first vitrified in liquid ethane, to preserve their structural integrity. They were then analyzed with transmission electron microscopy at cryogenic temperature (i.e. below -170°C). Micrographs of PC liposomes revealed the presence of subspherical liposomes in all samples. The average diameter of the PC liposomes was  $79 \pm 27$  nm ( $N_{obs} = 492$ ), in agreement with the dimensions measured with DLS experiments (**Figure 24g**). In addition to the expected unilamellar vesicles, we observed the presence of more complex structures, such as nested multilamellar vesicles. Such structures were present in all the samples and therefore could not be due to the presence of the AuNPs.

When the cryo-EM analysis was performed on samples containing PC liposomes and AuNPs, we found that the addition of AuNPs did not significantly modify the shape and size of the liposomes (**Figure 24g**). Interestingly, for AuNP1 but not for AuNP3, we detected regions where small clusters of 2 nm AuNPs laid near the liposomal membrane (**Figure 24a-c**). To avoid the ambiguity of projection images, we performed cryo-electron tomography to investigate whether these pictures showed an interaction between AuNP1 and liposomal membranes (**Figure 24d-f**). This analysis confirmed the presence of AuNPs mainly adsorbed

on the external liposome membrane (**Figure 24d-f**). In addition, the regions of the membrane that were interacting with the AuNPs were partially broken or perturbed (**Figure 24f**).

Cryo-EM results thus confirmed that the presence of AuNPs did not substantially affect the structural integrity of the liposomes. However, the preferential adhesion of AuNP1 to liposomes suggests a greater affinity of these particles for PC membranes.

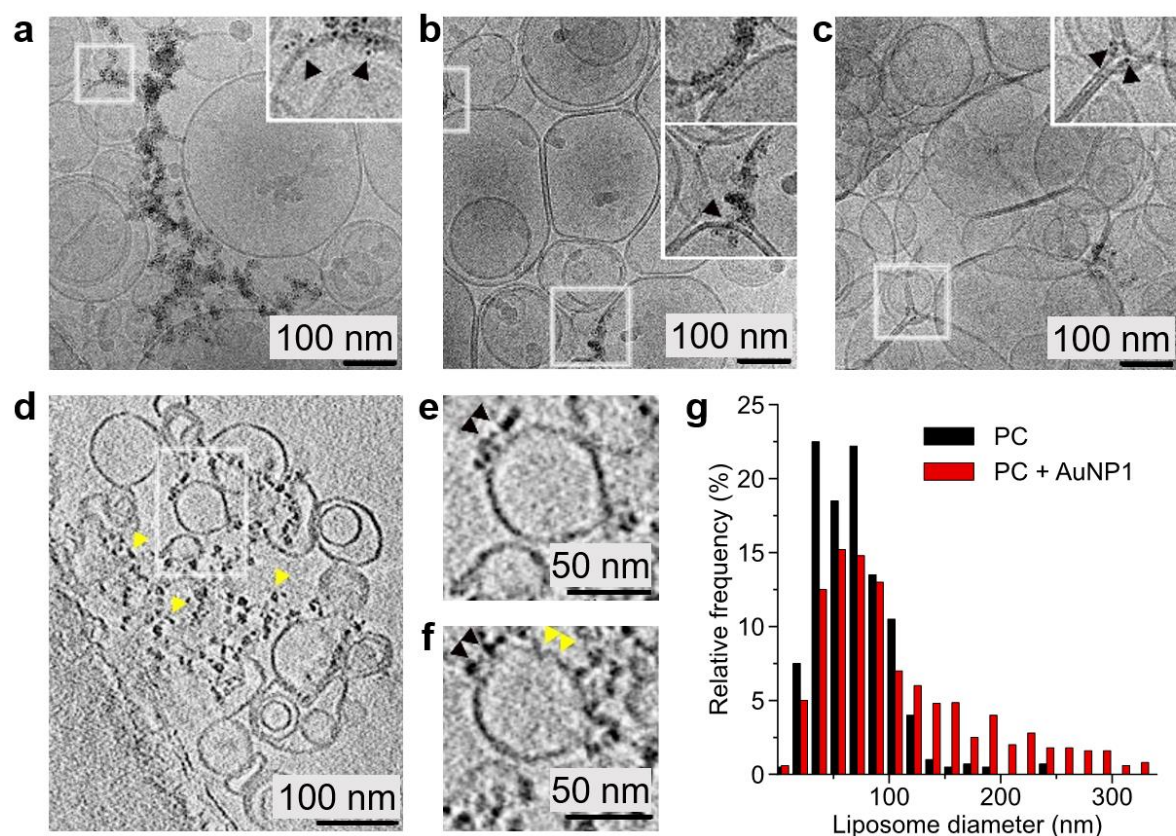


**Figure 24.** Cryo-EM and cryo-electron tomography analysis of PC liposomes with AuNP1. **a-c.** Cryo-EM projection images showing the presence of AuNPs associated with the liposomes. The insets are higher magnifications of the corresponding boxed regions. Note the presence of AuNPs interacting with the liposome membranes (black arrowheads). **d.** Cryo-electron tomography averaged image (10 adjacent slices) of liposomes interacting with several AuNPs (yellow arrowheads). **e** and **f** are high magnification images (average of 10 adjacent slices) of the boxed region in **d** at different levels inside the tomogram. Note in **e** and **f**, respectively, the presence of AuNPs interacting with the liposome membrane (black arrowheads) and the liposome membrane partially perturbed (yellow arrowheads). **g.** Size distribution of unloaded PC liposomes (black) and PC liposomes incubated with AuNP1 (red).

### 5. The role of electrostatic attraction

Based on these results, we decided to inspect the role of electrostatics in the particles' ability to interact with liposomes. We repeated the calcein release experiments with liposomes

comprising negatively charged phosphatidylglycerol (PG, **Figure 20d**) and PC in a 1:9 PG-to-PC ratio. These liposomes had an average hydrodynamic diameter of 100 nm and, as expected, a negative  $\zeta$ -potential of -7.7 mV (in PBS buffer, pH 7.0). Introducing a net negative charge into the liposomes would, in principle, enhance the electrostatic attraction to cationic AuNPs. Indeed, for CPPs, the presence of PG in the liposomes has been reported to increase their interaction with the bilayer and thus their double-layer perturbation activity.<sup>342–344</sup> Interestingly, release experiments (**Figure 21**) revealed negligible differences between PC and PG liposomes for guanidinium AuNP1 and AuNP2. However, the long-chain ammonium-bearing AuNP5 and AuNP6 induced a greater calcein release from PG-containing liposomes, when compared to the pure PC vesicles. Finally, very small effects were observed for the short-chain AuNP3 and AuNP4.

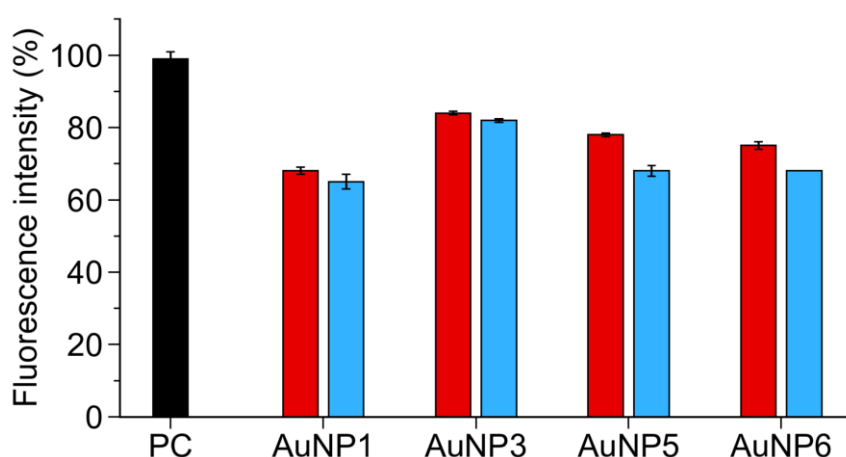


**Figure 25.** Fluorescence intensity relative to Nile-red-loaded PC liposomes. PC liposomes alone (black, set to 100%), PC (red), and PC:PG liposomes (blue) after the addition of AuNP1, AuNP3, AuNP5, and AuNP6. Experimental conditions: [HEPES] = 10 mM, [NaCl] = 100 mM, [PC]/[PC:PG] = 22  $\mu$ M, [ligand] = 66  $\mu$ M, pH 7.0, 25°C,  $\lambda_{exc}$  = 534 nm,  $\lambda_{em}$  = 629 nm.

The interaction of AuNPs with liposomes was further investigated by measuring the fluorescence emission of PC and PC:PG liposomes, loaded with Nile red (**Figure B-2**), a hydrophobic dye that locates within the bilayer and cannot be released. AuNPs can effectively quench the emission of dyes that are sufficiently close (within 3 nm) to the gold core. Binding of the AuNPs to the liposomes should therefore decrease the sample emission. The results (**Figure 25**) closely paralleled those of the calcein release experiments. Indeed, the addition of AuNP1 to Nile-red-loaded PC liposomes (**Figure 25**) resulted in a 30% quenching of emissions, while AuNP3 produced only a 13% quenching, and AuNP5 and AuNP6 produced a 20% decrease. For PC:PG liposomes (**Figure 25**), the net charge present on the liposomes

had no effect on AuNP1 and AuNP3, which continued to produce relevant and marginal quenching of emission, respectively. However, quenching clearly increased for AuNP5 and AuNP6, reaching the level observed for AuNP1. Hence, this experiment indicated that the guanidinium AuNPs bind to neutral and negatively charged liposomes, the long-chain ammonium AuNPs bind to negatively charged liposomes only, and that the short-chain ammonium AuNPs do not bind to any liposome.

This experimental evidence provides key insights into the interactions that govern the AuNP-membrane association. Evidently, AuNPs must bind to the liposomal membrane to produce the permeabilization effects. DLS, confocal microscopy, and cryo-EM experiments confirm that this binding does not affect the liposome integrity, and likely involves the adhesion of the AuNP to the outer surface. One would therefore expect that positively charged AuNPs would not interact with neutral liposomes but would bind to negatively charged liposomes. However, we observed that guanidinium AuNPs bind to and permeabilize neutral liposomes. Moreover, this activity is not enhanced by additional net charge attraction. Ammonium AuNPs positively interact with negatively charged liposomes only, and only when coated with long-chain thiols. This suggests that guanidinium AuNPs can bind to neutral bilayers via interactions other than Coulomb pairing. These interactions provide an affinity so great that the additional attractions with PC:PG liposomes do not lead to increased permeabilization activity. Ammonium AuNPs do not bind to neutral liposomes, but they should bind to PC:PG liposomes. Under our experimental conditions, charge attraction is not sufficient, and the additional presence of long-chain thiols is required. This indicates that effective binding of AuNPs to liposomes requires stronger interactions, such as those provided by combining headgroup electrostatic attractions with hydrophobic interactions, formed between the ligand alkyl linker and the inner region of the double layer.

#### *6. Resolution of atomically detailed pairing between gold nanoparticles and liposomes*

To investigate the molecular origin of the interactions between our cationic AuNPs and lipid membranes, we performed equilibrium atomistic MD simulations. Starting from atomistic models,<sup>359</sup> we resolved the temporal evolution of the AuNP-membrane association to rationalize the exceptional behavior of guanidinium-bearing AuNPs. We considered AuNP1, AuNP3, and three additional models (**Figure 26a**) with intermediate capacities for H-bonding. In detail, in the latter three models, we replaced the trimethylammonium headgroup of AuNP3 with dimethylamine (AuNP3a), monomethylamine (AuNP3b), and ammonium (AuNP3c).

This allowed us to investigate the properties of protonated amines as cationic AuNP headgroups, which are present in CPPs and related species, but are experimentally inaccessible in AuNPs.

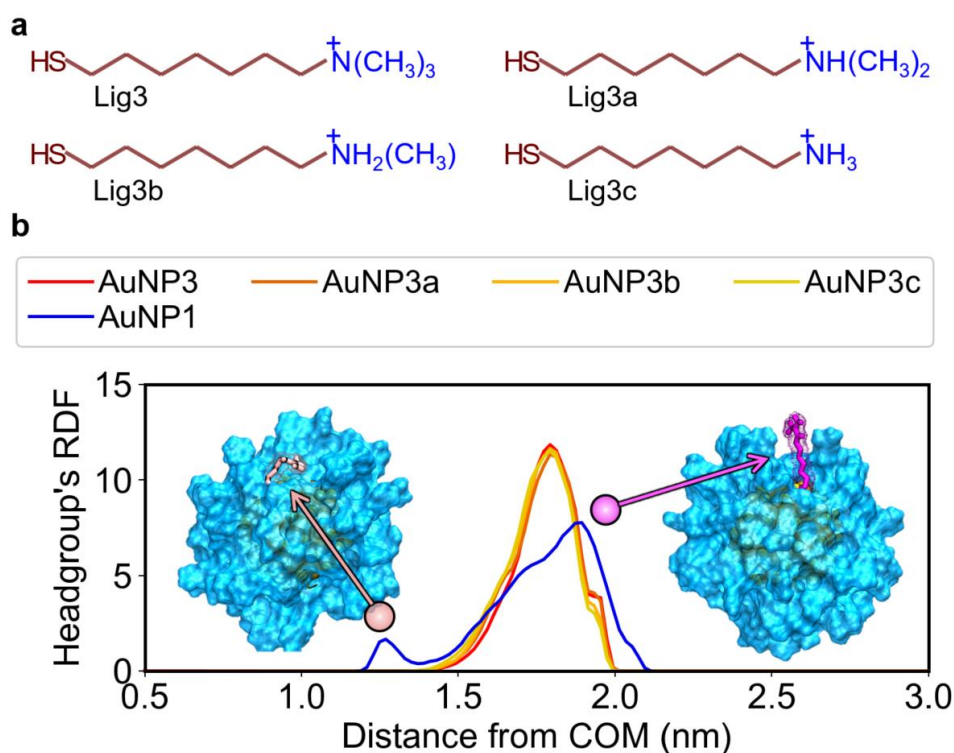


**Figure 26.** Computational models and ligand packing. **a.** Chemical structure of the thiols forming the monolayer of the simulated AuNPs. **b.** RDF of the AuNPs' headgroups as a function of the distance from the gold core COM. The ammonium derivatives (red to yellow lines) display a single peak corresponding to an extended conformation (purple), while the guanidinium-bearing AuNP1 (blue line) also presents a coiled configuration (pink). Gold atoms are shown in orange and the coating monolayer as a cyan molecular surface.

We first performed MD simulations of AuNPs alone in water (100 ns for each of the five systems) in order to equilibrate their structures and properties. The convergence of the AuNPs structure was determined by the stabilization of the root-mean-squared displacement (RMSD, **Figure B-7**).<sup>57,95</sup> The cationic headgroups of all the ligands caused a reciprocal repulsion. Indeed, by computing the radial distribution function (RDF) of the headgroups with respect to the gold core's center of mass (COM), we found that the ligand shell of all five AuNPs displayed a predominantly extended conformation with a maximum at 1.8 nm (**Figure 26b**). However, for AuNP1, the headgroups' RDF profile was significantly different. In this case, the maximum was located at 1.9 nm, which is expected because guanidinium is larger than ammonium. However, the distance distribution was significantly broader, with a shoulder at 1.6-1.7 nm and a second maximum at 1.3 nm.

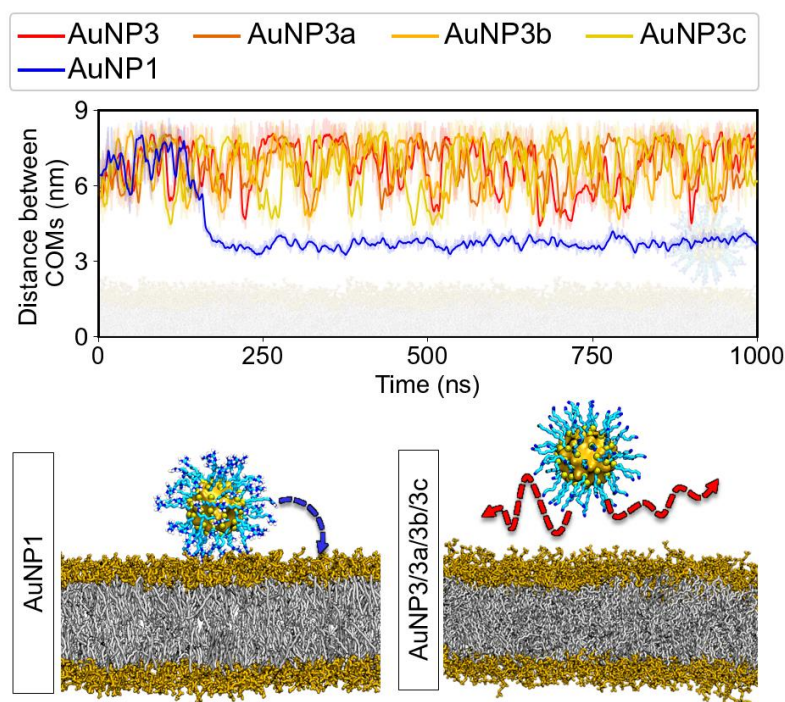


**Figure 27.** Distance between the COM of the membrane and the COM of the gold atoms. AuNP1 is the only particle to spontaneously bind to the PC bilayer even though they all explore states of sufficient proximity to the bilayer. Gold atoms are displayed in orange, sulfur in yellow, carbon in cyan, nitrogen in blue, hydrogen in white, PC headgroups in brown, and hydrophobic lipid tails in gray.

These differences suggest a coiled arrangement of the thiols. Indeed, some ligands adopted a bent conformation, with the headgroup embedded within the hydrophobic core of the monolayer. On average, this configuration appeared for around 3% of the sampled structures, which corresponds to 2 ligands (out of 60) per frame. The appearance of this coiled conformation, albeit with low frequency, is likely due to the amphiphilic nature of guanidinium, which acts as a H-bond donor along its molecular plane and as a hydrophobic patch at the plane's faces.<sup>360</sup> At the same time, the presence of folded ligands enhances the amphiphilic nature of AuNP1 by inducing the exposition of the inner alkyl linkers to the bulk solution.

Subsequently, equilibrated AuNPs were allowed to freely interact with a 1-palmitoyl-2-oleoyl-sn-glycero-3-phosphocholine (POPC) in 1- $\mu$ s-long MD simulations for each system. Notably, no external forces or potential gradients were applied in these experiments. Remarkably, and in line with the experimental evidence, only AuNP1 spontaneously associated with the membranes during our simulations (**Figure 27**). In detail, the south pole (here defined as the AuNPs' region closest to the membrane's surface) of AuNP1 came into close contact with the membrane's headgroups 165 ns after the simulation started, and it remained stably bound to



the bilayer for the rest of the simulation. In three additional replica simulations, we observed the same phenomenon taking place at 25, 420, and 555 ns. AuNP binding to the membrane was always irreversible in the time span of our MD simulations. Simulations of the other model AuNPs (i.e. AuNP3/3a/3b/3c) showed no spontaneous binding with the membrane within the sampled timescale, suggesting a less favorable association. Tracking the distance between the AuNPs and the membrane in their respective simulations (**Figure 27**) revealed that all AuNPs explored states of similar proximity when they were freely diffusing in the solvent. This confirms that all the AuNPs can get close enough to the bilayer surface to initiate binding. Nevertheless, the actual anchoring only occurs for AuNP1.

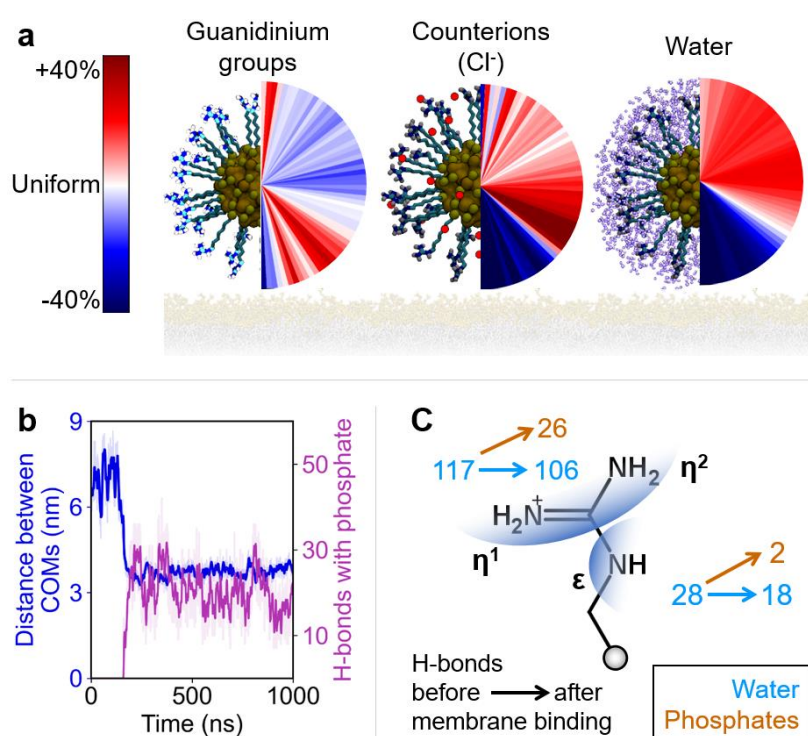


**Figure 28.** Effect of membrane binding on the monolayer of AuNP1. **a.** Angular (polar) number density relative to a perfectly homogeneous distribution. In the color bar, white is a perfectly uniform distribution in the spherical slice, red are highly populated regions, and blue are the least populated regions. Headgroups are shown in cyan carbons, chloride ions in red, and water molecules in purple. **b.** Distance between the bilayer's COM and the COM of the gold atoms (blue line), as well as the H-bonds between AuNP1 and the lipid bilayer (violet line). The approach of AuNP1 triggers an H-bond network that stabilizes the bound complex. **c.** Change in the number of H-bonds before and after membrane binding for both distinct donor positions in the guanidinium group.

Our results agree well with previously reported computational studies of similar systems, none of which found a spontaneous interaction of ammonium AuNPs with neutral PC bilayers. Heikkilä and co-workers performed united-atom simulations of AuNP3c interacting with a

bicompartmental asymmetric PC:PG bilayer in the presence of an ionic imbalance.<sup>361</sup> Their simulations quantified a barrier of 5 k<sub>B</sub>T during the AuNP's adsorption on the zwitterionic leaflet of the bilayer, making the binding unfeasible by thermal motion alone. In addition, Alexander-Katz and co-workers performed coarse-grained simulations of NPs analogous to AuNP3/3a/3b/3c.<sup>338</sup> These and other simulations<sup>313,362</sup> demonstrated the need for a transmembrane potential to induce the binding of cationic AuNP and their eventual translocation through pore formation.

The binding of AuNP1 to the double layer is expected to induce a substantial reorganization of the species that are forming, or strongly interacting with, the AuNPs monolayer, namely the guanidinium headgroups, the chloride counterions, and the water molecules. To get more detail on this point, we computed the number density of each component with respect to the AuNPs polar angle and quantified their deviation from a perfectly uniform distribution (**Figure 28a**). These calculations revealed that the southernmost part of the monolayer (but not the south pole) became more populated with guanidinium groups upon binding. Hence, the ligand shell reorganized to maximize the number of guanidinium-phosphate interactions. Several H-bonds with the lipid headgroups were rapidly formed as soon as AuNP1 was adsorbed onto the bilayer (**Figure 28b**), confirming the establishment of a multivalent interaction. The gathering of guanidinium groups led to a high positive charge density at the south pole of the AuNP. This charge accumulation was stabilized by the chloride counterions that agglomerated in the neighboring subequatorial region. Consequently, the pairing between the ligands and the chloride ions ushered the water molecules toward the north pole of the monolayer. Notably, upon binding, the composition of the monolayer remained unchanged, including the number of embedded chloride ions and water molecules.

As noted, the contact between AuNP1 and the lipid bilayer triggered the formation of several H-bonds between the guanidinium-terminated ligands and the phosphate groups of PC (**Figure 28b**). We quantified the persistency of such H-bonds when AuNP1 passed from being fully solvated to being adsorbed on the membrane. Interestingly, the total number of H-bonds formed by the guanidinium groups when in solution or bound at the membrane was similar ( $145 \pm 8$  vs.  $152 \pm 10$ , respectively). Hence, H-bonding with membrane headgroups nicely compensated the loss of AuNP solvation. Still, there was a subtle repartitioning between the different ligand H-bond donors in the two states. In solution, the  $\eta^1$  and  $\eta^2$  nitrogen atoms of guanidinium formed a total of  $117 \pm 7$  H-bonds with water, whereas the  $\epsilon$  nitrogen atom formed

$28 \pm 4$  H-bonds (**Figure 28c**). When bound to the membrane, the  $\eta$  positions formed  $106 \pm 8$  and  $26 \pm 4$  H-bonds with the solvent and the phosphate groups, respectively. The  $\epsilon$  position formed  $18 \pm 2$  and  $2 \pm 1$  H-bonds with water and phosphates, respectively. Therefore, the total number of H-bonds involving the  $\eta$  positions slightly increased to  $132 \pm 8$  (vs  $117 \pm 7$ ). Moreover, H-bonds for the  $\epsilon$  positions slightly decreased to  $20 \pm 2$  (vs  $28 \pm 4$ ). This difference is mainly due to the  $\epsilon$  atoms at the south pole. These did not penetrate the bilayer sufficiently to form H-bonds with the phosphates, and they were distant from the water molecules displaced toward the opposite pole. The increase in H-bonds at the  $\eta$  positions is likely the driving force of the binding to the membrane, since charge-assisted and cooperative phosphate-guanidinium H-bonds are stronger than solvation interactions of phosphate-guanidinium groups.

In line with experiments, the membrane integrity was preserved during our simulations. The membrane thickness (**Figure B-8**) and the lipid order parameter (**Figure B-9**) remained within the expected thermal fluctuations. However, upon AuNP1 binding, the membrane suffered slight distortions. These may foreshadow the enhanced permeation that leads to substantial calcein release at longer timescales.

We could demonstrate these distortions by monitoring two angles,  $\alpha_{PC}$  and  $\beta_{PC}$ , when AuNP1 was adsorbed on the lipid bilayer. The first angle,  $\alpha_{PC}$ , measures the orientation of the PC groups with respect to the membrane's normal (Z-) axis (**Figure 29a**), as routinely implemented in such analyses.<sup>363</sup> In our unperturbed membrane, this angle adopted an equilibrium value of  $67^\circ$  (**Figure 29b**). When AuNP1 sat on the bilayer, the  $\alpha_{PC}$  angle increased by around  $10^\circ$  to  $77^\circ$ , indicating that the AuNP fished the phosphate groups out of the bilayer to optimize the H-bond network (**Figure 29c**). The angle  $\beta_{PC}$  was defined to track the orientation of the PC group with respect to the XY projection of the gold atom's COM (**Figure 29d**). In this case, we observed a local decrease of around  $30^\circ$  with respect to the  $90^\circ$  angle expected for a random distribution of an unperturbed membrane (**Figure 29e**). The reduction in  $\beta_{PC}$  suggests that the phosphate groups lean inwards to the AuNP's contact region, and that the ammonium groups point outwards (**Figure 29f**). Thus, the PC group of the lipids adopts an arrangement reminiscent of the electrical double layer formed by electrolytic solvents around charged bodies.<sup>364</sup> The affinity between the guanidinium and phosphate groups causes a partial polarization at the contact region, despite the membrane having a neutral net charge. Notably, this effect can only be captured when the AuNPs and the lipids are modeled at an atomistic resolution.<sup>313,338,362,364</sup>

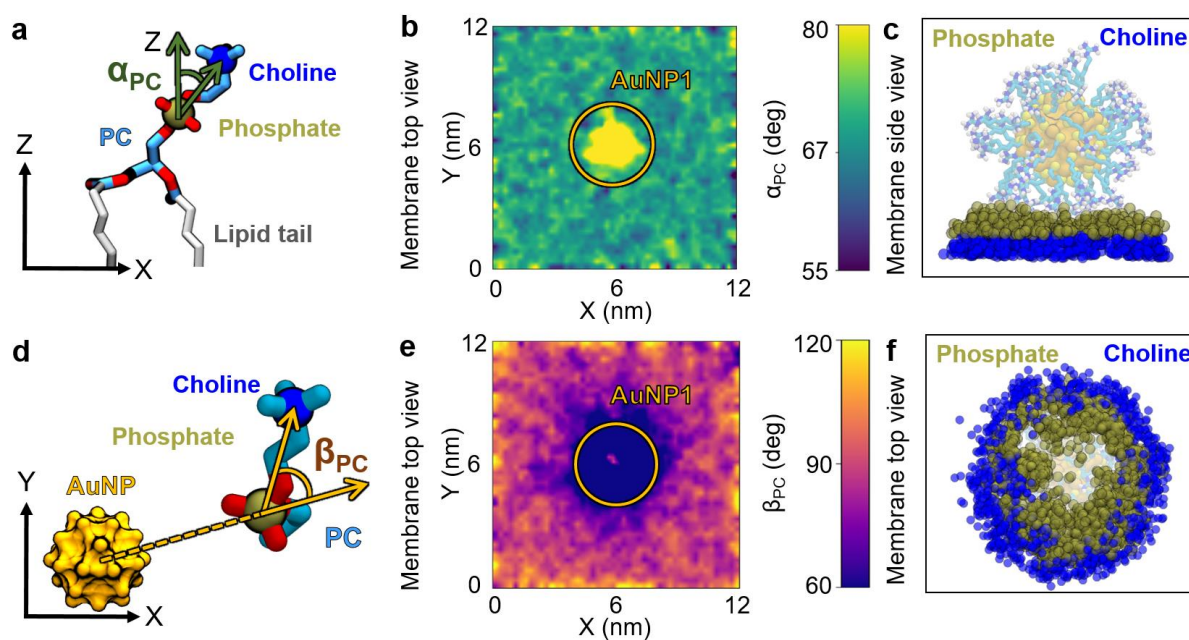


**Figure 29.** Membrane deformations upon binding of AuNP1. **a.** Definition of  $\alpha_{PC}$  as the angle between the PC group and the direction normal to the bilayer (Z-axis). **b.** Map of  $\alpha_{PC}$  upon AuNP binding, as seen from the top (X and Y are the dimensions of the simulation box, as in **e**). There is a local decrease of  $\alpha_{PC}$  in the contact region. **c.** Conceptual illustration of the phosphate fishing made by superimposing 300 trajectory frames. **d.** Definition of  $\beta_{PC}$  as the angle between the XY projection of the vector between the AuNP COM and the phosphate group, and the vector between the phosphorus and nitrogen atoms of the PC group. **e.** Map of  $\beta_{PC}$  upon AuNP1 binding from the top. There is a local decrease of  $\beta_{PC}$  around the contact region. **f.** Conceptual illustration of the membrane polarization near the AuNP1 binding spot.

Taken together, our experimental and computational results endorse the importance of local atomically detailed structural features in AuNP-membrane interactions, which cannot be ascribed to electrostatics only.

### C. Discussion

Our results provide a better understanding of the interaction of AuNPs with phospholipid bilayers. The first finding is that the binding of cationic AuNPs to liposomes resulted in their permeabilization in all the cases. This behavior is explained by MD simulations that suggest that the adhesion of an AuNP to the outer surface of a phospholipid bilayer causes local distortions that could trigger the permeabilization.

Second, and more important, we showed that AuNPs coated with a monolayer of guanidinium-bearing ligands are highly efficient in interacting with neutral phospholipid bilayers and inducing their non-disruptive permeabilization. This activity is substantially greater than that

of other cationic AuNPs and, notably, occurs irrespective of the bilayer's charge. Hence, guanidinium AuNPs, in contrast to other cationic AuNPs, are capable of binding to neutral bilayers. MD simulations indicate that the driving force could be the ability of these AuNPs to establish a multivalent interaction with the liposome's phosphate moieties. They also suggest that the H-bond donor arrangement of guanidinium, which is perfectly fit for the interaction with phosphate, is crucial in allowing the AuNP to bind to the membrane. Hence, as in the case of CPPs and polymers, the 'arginine magic' is at play with AuNPs too, and the guanidinium headgroup has a fundamental role as a phosphate-recognizing unit. This feature is particularly relevant because it favors the interaction with biological membranes even in the absence of other attractive forces.

The third finding is the relevance of different intermolecular interactions in controlling the binding of AuNPs to biological membranes. H-bonding appears to be very efficient for guanidinium but, according to MD simulations, is not so effective for protonated amines. This is likely because this group's pre-organization is not optimal for interacting with phosphates. Ion pairing is another interaction that has often been invoked to explain how NPs bind to membranes. However, the outer surface of mammalian cells mostly comprises neutral lipids, and this reduces the significance of this interaction.<sup>363</sup> Indeed, we found that, even for bilayers comprising 10% anionic lipids, ion pairing is not sufficient to drive AuNP binding, as for AuNP3 and AuNP4, and must be accompanied by additional interactions. Remarkably, our results suggest that hydrophobic interactions provided by the alkyl chains of the inner portion of the ligand shell play an important role. This is supported by the fact that, for trimethylammonium AuNPs, effective binding and permeabilization occurred only with long-chain ligands, as with AuNP5 and AuNP6. Indeed, this apparently segregated region of the ligand shell has already been shown to interact with the inner hydrophobic regions of other biomacromolecular entities. The first evidence came from the pioneering studies of Rotello and co-workers,<sup>365,366</sup> who demonstrated the ability of the inner alkyl portion of the ligand shell to induce protein denaturation upon AuNPs binding. Later on, Katz and Stellacci suggested that the 'snorkeling' of the alkyl portion of the coating ligands is the key step of the interaction between anionic AuNPs and phospholipid bilayers.<sup>162,302,329,338</sup> Finally, Stellacci recently reported the ability of anionic AuNPs to induce virus degradation upon binding, thanks to the effect of the ligand shell's inner hydrophobic region.<sup>367,368</sup>

In the landscape of NPs for biological applications, ligand-protected noble metal nanoparticles emerge as the only entities capable of featuring precise headgroup functionalization and a flexible inner hydrophobic shell. In addition, the use of ‘arginine magic’ can provide other unique abilities in the interaction with biological membranes. Implications in nanoparticles targeting cells, microorganisms, and viruses may be relevant.

## **D. Methods**

### *1. General*

Chemical reagents were bought from Aldrich at highest quality and used without further purification. Water was purified using a Milli-Q and water purification system. Reactions were monitored by thin-layer chromatography on 0.25 mm Merck silica gel plates (60 F254) using ultraviolet (UV) light as visualizing agent and/or heating after spraying ninhydrin. Solvents were of analytical reagent grade, laboratory reagent grade or high-performance liquid chromatography grade. Nuclear magnetic resonance (NMR) spectra in the solution state were recorded on an AVIII 500 spectrometer (500 MHz for <sup>1</sup>H frequency). Electrospray ionization-mass spectrometry (ESI-MS) was performed with an Agilent Technologies 1100 Series system equipped with a binary pump (G1312A) and MSD SL Trap mass spectrometer (G2445D SL). The synthesis and characterization of the ligands is described in Appendix B.1.

The hydrodynamic particle size and  $\zeta$ -potential were measured with a Malvern Zetasizer Nano-S equipped with a HeNe laser (633 nm) and a Peltier thermostatic system. Measurements were performed at 25°C in water, HEPES 10 mM, or HEPES 10mM with NaCl 100 mM buffers at pH 7.0. The images were registered with an OSIS Veleta 4K camera.

Thermogravimetric analysis was run on 0.4 mg AuNP samples using a Q5000 infrared instrument from 25 to 1,000°C under a continuous air flow. Heating the AuNP samples until 890°C led to a weight loss of 56.28, 25.55, 51.32, and 44.09% for AuNP1, AuNP2, AuNP4, and AuNP6, respectively. AuNP3 and 4 had been characterized elsewhere.<sup>97,369</sup>

Fluorescence spectra and emission recovery experiment were performed in HEPES 10 mM or HEPES 10mM with NaCl 100 mM buffers at pH 7.0 on a Varian Cary Eclipse fluorescence spectrophotometer. Both the spectrophotometers were equipped with thermalized cell holders. Confocal images were taken using a laser scanning confocal microscope (BX51WI-FV300, Olympus) coupled to an Argon laser (IMA-101040ALS, Melles Griot) emitting laser light at

488 nm. The laser beam was scanned on 512×512 pixel sample area using a 60× water immersion objective (UPLSAPO60×W-Olympus). Fluorescence emission was collected through the same objective, separated from excitation light through a 490 nm long-pass dichroic mirror, and recorded by the photomultiplier tube with a 510 nm long-pass filter. For fluorescence lifetime experiments, the sample was excited using a frequency doubled Titanium/Sapphire femtosecond laser at 440 nm, 76 MHz (VerdiV5-Mira900-F Coherent), coupled with the BX51WI-FV300 confocal microscope. The emission signal was sent to a single-photon avalanche photodiode (SPAD). Before the light entered the photodiode, it passed through a 525/50 band-pass filter. The laser sync and the output of the SPAD were fed to a time-correlated single photon counting electronics (PicoHarp 300, PicoQuant, Germany) for the calculation of the emission decay curve. The fitting of decay curve was performed with the Symphotime software (PicoQuant, Germany), using a two-component exponential model.

TEM was recorded on a FEI Tecnai G12 microscope operating at 100 kV. For cryo-EM, vitrification of samples was performed in liquid ethane cooled at liquid nitrogen temperature using the FEI Vitrobot Mark IV semi-automatic autoplunger. Bright field cryo-EM was run at -176°C in a FEI Tecnai G2 F20 transmission electron microscope, working at an acceleration voltage of 200 kV and equipped, relevant for this project, with a field emission gun and an automatic cryo-box. The images have been acquired in low dose modality with a GATAN Ultrascan 1000 2k×2k CCD.

## 2. *Nanoparticle preparation*

Tetraoctylammonium bromide (TOAB, 2.5 eq) was dissolved in toluene and the solution was degassed for 40 minutes. This solution was used to wash three times an aqueous solution of gold (III) chloride trihydrate ( $\text{HAuCl}_4 \cdot 3\text{H}_2\text{O}$ , 1 eq). The combined organic phases were collected in a round-bottom flask along with the remaining solution of TOAB. This mixture was left to stir for about 20 minutes under an inert atmosphere. Afterwards dioctylamine (20 eq) was added all at once. After 1.5 hours the solution was put in an ice bath, then sodium borohydride ( $\text{NaBH}_4$ , dissolved in milli-Q water,  $0.048 \text{ mg } \mu\text{L}^{-1}$ , 10 eq) was added all at once. After 2 hours, the drop of water (which had been used to dissolve  $\text{NaBH}_4$ ) was removed from the reaction mixture, and the desired thiol dissolved in methanol (MeOH) was added. After the formation of the AuNPs was observed, the mixture was usually stirred for another hour. They were purified by trituration with various organic solvents (each trituration entails the

suspension of the AuNPs in the solvent of choice, sonication, centrifugation, and then removal of the supernatant), then they were dried and characterized.

### 3. *Liposome preparation*

Dichloromethane solutions of PC and, when present PG, CHOL, or Nile red, were dried for 4 hours under vacuum and then hydrated with a buffered solution of the fluorophore (1 mL, calcein 50 mM, HEPES 10 mM, NaCl 100 mM, pH 7.0) under rotation at 42°C for 40 minutes. Then, 6 freeze/thaw cycles were performed, followed by 15 extrusion filtrations with a polycarbonate membrane (0.1  $\mu\text{m}$ , 19 mm) using an Avanti Polar syringe extruder. Size extrusion chromatography (G75) with buffer solution (HEPES 10 mM, NaCl 100 mM, pH 7.0) was used to remove the extravesicular fluorophore. The liposome samples were stored at 4°C.

Fluorescence recovery experiments were initiated by the addition of an AuNPs stock solution to 2 mL buffered solution (HEPES 10 mM, NaCl 100 mM, pH 7.0) containing liposomes (22  $\mu\text{M}$  phospholipid concentration) in a quartz cell. Sample emission at 25°C was measured followed until no further variations were detected (usually within 5 minutes). The maximum fluorophore emission was measured after addition of Triton X100 in the cell.

### 4. *Molecular dynamics simulations*

For this project, we performed MD simulations pertaining five AuNPs in an aqueous solution and in the presence of a POPC bilayer. In line with wet-lab experiments, the core size of our AuNPs models was 1.8 nm. The core was functionalized by 60 organic thiols. The thiols consisted of a 7-carbon alkyl chain followed by a cationic capping group. The investigated headgroups were: Guanidinium (AuNP1), trimethylammonium (AuNP3), dimethylamine (AuNP3a), monomethylamine (AuNP3b), and ammonium (AuNP3c). The initial geometry of the AuNPs was generated with the NanoModeler webserver.<sup>359</sup> The parameters employed for the internal quasi-static gold atoms were those derived by Heinz et al.,<sup>304</sup> and those used for the gold-sulfur interface were obtained by Pohjolainen et al.<sup>200</sup> elsewhere. For the coating thiols, the partial charges of all the atoms were calculated with the restrained electrostatic potential approach<sup>204,316</sup> by means of the R.E.D. Server<sup>317</sup> whereas the bonded parameters belong to the Generalized Amber Force Field.<sup>197</sup>

We first equilibrated the aforementioned AuNPs in a saline solution. For this, the AuNPs were individually solvated in a dodecahedral box of water (TIP3P parameters<sup>191</sup>) such that the



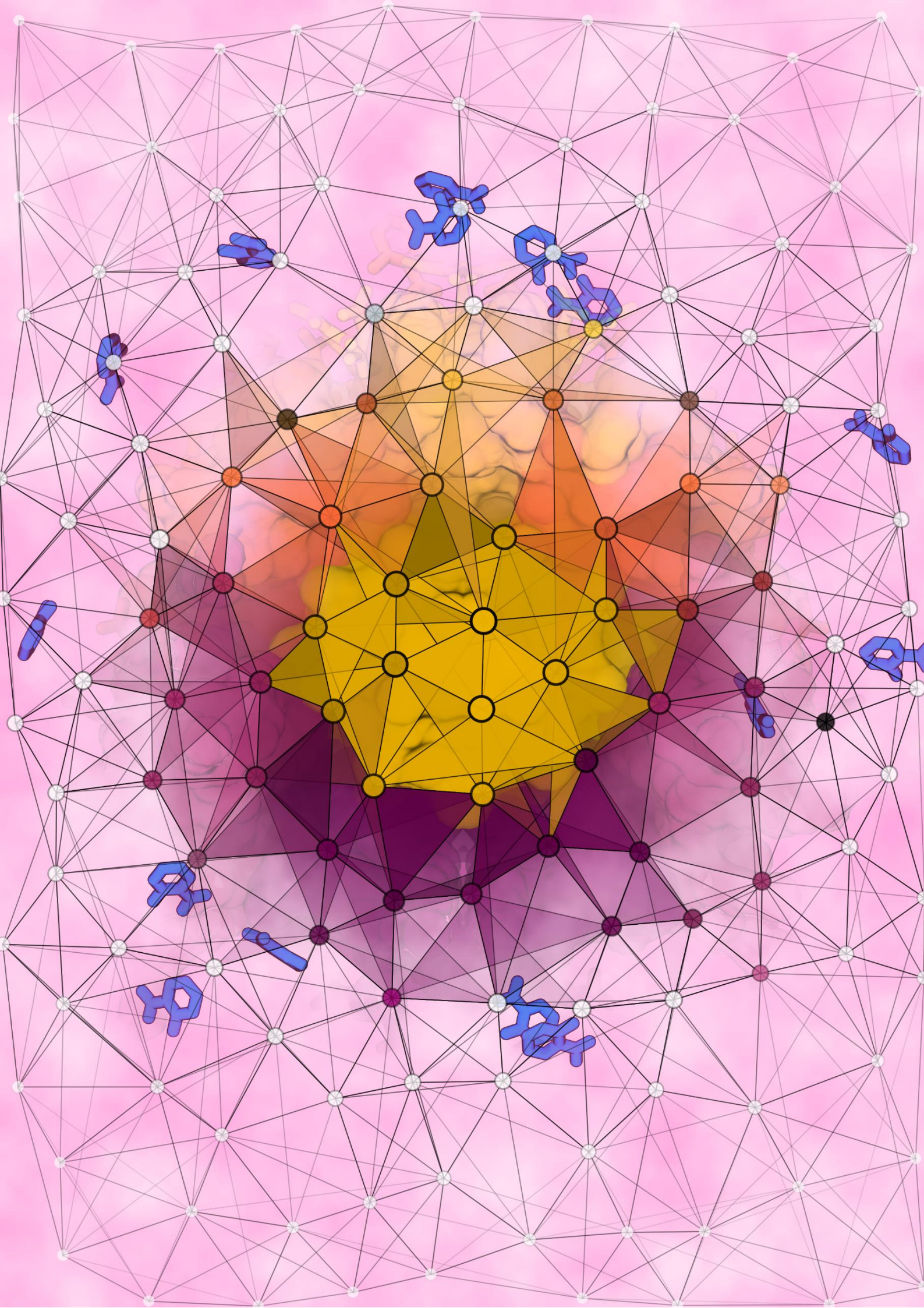
minimum distance between the solute and the edges of the box was 1.0 nm. Then, sodium chloride was added to the system, so that the system reached its electroneutrality plus 150 mM ionic strength. We proceeded to minimize the solvent around the AuNPs with the steepest descent method for a maximum of 50,000 steps. Once the system lied in an energetic minimum, it was thermalized to 310 K by a 500-ps-long simulation in the canonical ensemble using the velocity-rescale thermostat ( $\tau_B = 0.1$  ps). Posterior to the thermalization, the system was pressurized to 1 bar with a second 500-ps-long simulation this time in the isothermal-isobaric ensemble and applying the Berendsen barostat ( $\tau_P = 2.0$  ps,  $\kappa = 4.5 \times 10^{-5}$  bar<sup>-1</sup>). Finally, a production run of 100 ns was performed exchanging the Berendsen barostat for its Parrinello-Rahman counterpart.<sup>227</sup> The analysis of the trajectories was done discarding the first 25 ns of simulation for equilibration purposes.

In parallel, we equilibrated the structure of a POPC membrane. For this, a bilayer of POPC lipids with XY dimensions of 13×13 nm was generated with the CHARMM-GUI server.<sup>278</sup> The phospholipids were then parametrized with the Lipid17 force field<sup>198,199</sup> to ensure compatibility with those employed for the AuNPs in future stages. The bilayer was then solvated guaranteeing approximately 40 TIP3P water molecules per lipid. This system was minimized, thermalized, and pressurized like the AuNPs in saline solutions. For the production run, we implemented the semi-isotropic Parrinello-Rahman barostat. In this case, the production run also lasted 100 ns, and the first 25 ns were discarded for equilibration purposes during the analysis.

After having equilibrated the structures of the AuNPs and the membrane, we proceeded to merge them into single systems. In order to do this, the structure of each AuNP and the membrane were extracted from the last frame of their respective simulations and placed 2 nm away from each other. In accordance with the rest of our simulations, we performed a solvation, minimization, thermalization, pressurization, and production runs. In these cases, the production runs lasted 1  $\mu$ s, each.

All our simulations constrained the bonds with the linear constraints solver algorithm<sup>319</sup> and utilized a timestep of 2 fs. The short-range nonbonded interactions were explicitly calculated for pairs within a distance of 1.2 nm, and the long-range interactions were accounted for with the particle-mesh Ewald method of fourth order.<sup>231</sup> Periodic boundary conditions were imposed, and the geometry of the systems was saved every 10 ps. The simulations were performed with Gromacs-v2019.2.<sup>320,321</sup> The analysis of the trajectories was done with a

mixture of tools already implemented in Gromacs and with a series of in-house scripts using the MDAnalysis-v1.0 Python open library.<sup>370</sup>



# CHAPTER V. MOLECULAR-DYNAMICS-BASED THROUGHPUT SCREENING OF GOLD NANOPARTICLES FOR CHEMOSENSING

## Abstract

Nanoparticle-assisted chemosensing is a non-covalent recognition process that allows tracking chemical and biological markers with applications in biomedical, environmental, and substance control, among many others. Here a computational protocol is introduced employing molecular dynamics simulations and enhanced sampling techniques for high-throughput screening of gold nanoparticle (AuNP) libraries. The approach was benchmarked with a training set of AuNP-analyte dyads with binding free energies previously measured by fluorometric titration. Our method classified known binding dyads with accuracies, sensitivities, and specificities of 0.77, 0.77, and 0.78, respectively. We applied this protocol on a library of 100 thiolate-protected AuNPs to design chemosensors of 3-methoxytyramine (3MT), a prognostic marker of asymptomatic neuroblastoma. We propose ten 2 nm AuNPs for affinity testing to 3MT in aqueous solutions, which is scheduled for the third trimester of 2020. Experimental validation of these results would enable a time and cost-efficient protocol for the identification of sensitive AuNP-based chemosensors.

## A. Introduction

Chemosensors, or molecular sensors, are defined as molecules of abiotic origin that signal the presence of matter or energy.<sup>371</sup> The receptor involved in the sensing process is a supramolecular structure that binds reversibly to a target analyte through non-covalent interactions.<sup>372</sup> When the target analyte binds to a chemosensor, a transduction mechanism outputs an observable signal cascaded by a change in the physicochemical properties of either the receptor or the analyte.<sup>94</sup> In practice, the signal expressed is a measurable variation in the luminescence,<sup>373</sup> absorbance,<sup>374</sup> redox potential,<sup>375</sup> or relaxation<sup>376</sup> of the overall system. The amplitude of the signal depends on the dyad's binding affinity and association rate that are governed by stabilizing interactions between complementary chemical moieties of both molecules.<sup>377,378</sup>

Gold nanoparticles (AuNPs) are excellent platforms for designing chemosensors due to their optical and electrical properties that can be modulated by their local chemical environment.<sup>379</sup> Moreover, spherical AuNPs display a high surface-to-volume ratio and relative ease of functionalization that facilitate their synthesis.<sup>118,380</sup> Gold-based chemosensors have proven compatible with multiple transduction strategies, enabling the development of fluorometric and naked-eye colorimetric sensors.<sup>381,382</sup> Nonetheless, these strategies are based on the quenching (or triggering) of infrared and visible absorption bands, a mechanism that is hardly analyte-specific.<sup>94</sup> Conversely, nuclear magnetic resonance (NMR) spectroscopy allows analyte-specific detection because each organic analyte manifests a distinctive resonance frequency profile.<sup>96,376</sup> Specifically, in saturation transfer difference (STD) NMR experiments, the recognition of the analyte is characterized by a spin population transfer process only visible when the coating monolayer of the AuNP tightly interacts with analyte molecules.<sup>383</sup>

Analyte-specific recognition is pivotal for using chemosensors in complex matrices. NMR STD experiments allow distinguishing of compounds bound to the monolayer of an AuNP, yet the rational design of chemosensors requires a detailed understanding of the monolayer's folding dynamics and the specific interactions that lead to analyte recognition.<sup>21,97</sup> In this regard, molecular dynamics (MD) simulations are a valuable technique for elucidating surface interactions between AuNPs and analytes at atomistic resolution.<sup>56</sup> So far, MD simulations have been used to explain AuNP-analyte affinity in terms of the coating monolayer's plasticity.<sup>57,95</sup> Nonetheless, these studies use lengthy microsecond-long simulations with a limited transferability to the high-throughput screening of nanoreceptors.

In this work, we introduce an MD-based method for the high-throughput of AuNPs for chemosensing applications. The newly developed method uses enhanced sampling techniques to calculate the free energy of binding a small molecule (analyte) into the organic monolayer of an AuNP. We used our protocol to design receptors of 3-methoxytyramine (3MT), which is a prognostic biomarker of asymptomatic neuroblastoma, an extracranial solid tumor responsible for 15% of pediatric cancer-related deaths.<sup>384–386</sup> Our method is a highly parallelizable approach that requires a short 10-ns-long simulation for each AuNP-analyte system, allowing the screening of thousands of AuNP-analyte dyads. Thus, the method proposed here is a time and cost-efficient strategy for designing gold-supported chemosensors.

## B. Method development

Here, we propose a computational method for the screening of functionalized AuNPs as chemosensors. The proposed protocol uses on-the-fly potential of mean force (PMF) calculations to compute the free energy of binding ( $\Delta G_{bind}$ ) a small molecule (analyte) into the monolayer of a functionalized AuNP. In our methodology, multiple copies of an analyte are initially embedded into the monolayer of an AuNP. Then, the analyte molecules are simultaneously pulled away from the AuNP using steered MD simulations. Interestingly, our framework exploits the symmetry of spherical AuNPs by considering the pulling of each analyte as an independent replica simulation. In the end, the free energy  $\Delta G_{bind}$  is reconstructed from the mean force exerted on the analyte molecules at each step of the steered unbinding.

### 1. System preparation

The developed methodology starts from structure files in which, for each AuNP-analyte dyad, the analyte is inserted into the coating monolayer of the AuNP. The NanoModeler webserver<sup>359</sup> generates the initial conformation of the AuNPs (**Figure 30a**). This server produces 3D structures with the coating ligands in an extended conformation. In this study, we used 2 nm AuNPs coated by 60 thiols (i.e. Au<sub>144</sub>(SR)<sub>60</sub>). NanoModeler also produces the corresponding parameters files for the AuNPs. The inner quasi-static gold atoms of the AuNPs are modeled as neutral spheres with van der Waals parameters taken from Heinz et al.,<sup>304</sup> and the staple-like motifs at the gold-sulfur interface are modeled with the AMBER-compatible parameters derived by Pohjolainen et al.<sup>200</sup> For the outer monolayer, PROPKA-v3.1<sup>387</sup> is used to determine the most probable protonation state of a single stretched ligand at a neutral pH. The atomic partial charges are derived with the restrained electrostatic potential (RESP) method<sup>204,316</sup> at

the ligand's fully extended conformation, and the bonded parameters are taken from the Generalized Amber Force Field (GAFF).<sup>197</sup>

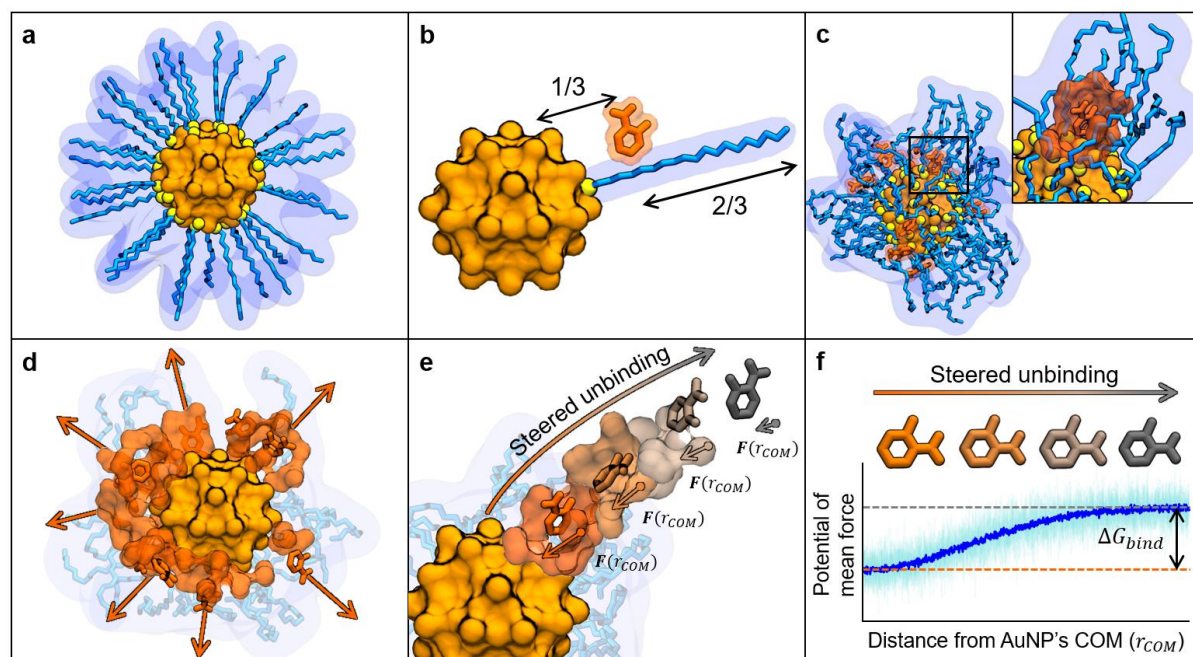


**Figure 30.** Conceptual illustration of the MD-based screening method. **a.** Generation of a spherically symmetrical AuNP with coating thiols in elongated conformations. **b.** Placement of the analytes two thirds into the monolayer (only one ligand and one analyte are shown for clarity). **c.** Equilibration of the coating ligands around the ten analyte molecules embedded within the monolayer. **d.** Binding pose of the ten analyte molecules after the relaxation of the monolayer. **e.** Pulling of the analytes away from the COM of the gold core. Only one analyte is shown for clarity. The ten analyte molecules are pulled simultaneously. **f.** Change in the free energy as a function of the distance between the COM of an analyte and the gold core ( $r_{COM}$ ). The binding free energy  $\Delta G_{bind}$  of one analyte molecule is approximated from the PMF along the collective variable  $r_{COM}$ . The gold core is shown in orange, the coating monolayer in blue, sulfur atoms in yellow, and analyte molecules (and their binding sites) in shades of copper.

The starting structure of each AuNP-analyte dyad includes ten copies of the analyte. Previous fluorometric titration experiments showed that 2 nm AuNPs can bind up to 30 analyte molecules, each.<sup>96</sup> Thus, using ten analyte molecules in our simulations ensures that the monolayer remains undersaturated. The analytes are initially placed two thirds into the monolayer using in-house scripts written in Python (**Figure 30b**). That is, the distance between the center of mass (COM) of each analyte and the gold core's surface is one third of the total length of the coating ligands. The initial orientation of the analytes is determined pseudo-randomly and ensures a minimum distance of 0.15 nm between atoms to avoid intermolecular clashes. The analytes are parametrized as the coating thiols, using PROPKA-v3.1,<sup>387</sup> the RESP

method,<sup>204,316</sup> and the GAFF force field<sup>197</sup> to obtain the protonation state, partial charges, and bonded parameters, respectively.

After generating models for the AuNPs and the analytes, their structure (and parameters) files are merged into a single system. A dodecahedral simulation box is defined around the system leaving a minimum distance of 1.6 nm between the AuNP and the box's faces. Then, the box is solvated with TIP3P water molecules.<sup>191</sup> Sodium chloride is added to reach electroneutrality and a salt concentration of 150 mM, a typical ionic strength in biological fluids.<sup>388</sup> The fully solvated system is minimized with the steepest descent method for a maximum of 50,000 steps. All the simulations in this study employ periodic boundary conditions, an integration timestep of 2 fs, linear constraints on all bonds involving hydrogen atoms,<sup>319</sup> and a cutoff radius of 1.2 nm for short-ranged nonbonded interactions. The simulations also account for long-ranged electrostatic interactions using the fourth-ordered particle-mesh Ewald method.<sup>231</sup> The simulations in this study were run in Gromacs-v2019.4,<sup>320,321</sup> and the trajectory files were analyzed with in-house scripts using the MDAnalysis-v1.0 Python open library.<sup>370</sup>

## 2. *Steered unbinding simulations*

Following system minimization, the coating monolayers are allowed to equilibrate around the embedded analyte molecules (**Figure 30c**). To this end, the systems are thermalized and pressurized while restraining each analytes' atoms with a harmonic potential ( $k_b = 10,000 \text{ kJ mol}^{-1} \text{ nm}^{-2}$ ). The thermalization step consists of a 500-ps-long simulation in the NVT statistical ensemble that heats the system to 300 K, at a constant rate, using a velocity-rescale thermostat ( $\tau_B = 0.1 \text{ ps}$ ). The pressurization is another 500-ps-long simulation in the NPT statistical ensemble that equilibrates the pressure to 1 bar using a Berendsen barostat ( $\tau_P = 2.0 \text{ ps}$ ,  $\kappa = 4.5 \times 10^{-5} \text{ bar}^{-1}$ ).

Once the systems reach the target temperature and pressure, they are subject to a steered MD simulation in which each analyte is simultaneously pulled away from the AuNP's COM (**Figure 30d**). A harmonic potential ( $k_{bias} = 2,000 \text{ kJ mol}^{-1} \text{ nm}^{-2}$ ) couples the COM of each analyte to the COM of the AuNP (i.e.  $r_{COM}$ ). The equilibrium value of the steering potential increases at a rate of  $0.4 \text{ nm ns}^{-1}$ . This increase rate allows the unbinding to occur within 10 ns (for ligands 2-nm-long when extended). Notably, for spherical AuNPs, each analyte molecule serves as an individual replica of the overall unbinding process (**Figure 30e**). During the steered MD simulation, the force acting on the collective variable  $r_{COM}$  is stored every 4 ps and



used to reconstruct the PMF profile along  $r_{COM}$  (**Figure 30f**). Finally, the binding free energy  $\Delta G_{bind}$  is estimated using Equation 77, where  $\langle F(r_{COM}) \rangle$  is the force along the collective variable  $r_{COM}$  (averaged over the ten analyte molecules), and  $r_{COM}^{best}$  is the distance at which the analyte is the most stable inside the bilayer ( $F$  closes to zero). In practice, the integral in Equation 77 extends until half the length of the shortest box edge. Throughout this study, we discuss the absolute value of the binding free energy for clarity of the discussion.

$$\Delta G_{bind} = \left| \int_{r_{COM}^{best}}^{\infty} \langle F(r_{COM}) \rangle dr_{COM} \right| \quad (77)$$

**Table 3.** Number of charged AuNPs and analytes in the 31 AuNP-analyte dyads of the training dataset. The columns account for anionic (-1 e per thiol), neutral, and cationic (1 e per thiol) AuNPs, and the rows account for anionic (-1 e per analyte), zwitterionic (phenylalanine), and cationic (1 e per analyte) analytes.

		Nanoparticle			Total
		Anionic	Neutral	Cationic	
Analyte	Anionic	1	8	1	10
	Zwitterionic	1	0	0	1
	Cationic	20	0	0	20
	Total	22	8	1	31

### 3. Training dataset and protocol benchmarking

The free energy  $\Delta G_{bind}$  serves as a scoring function that ranks multiple AuNP-analyte dyads (i.e. pairs comprised by one analyte interacting with one thiol-protected AuNP) according to their binding strength. In this sense, our method introduces a threshold parameter  $\Delta G_{bind}^{ref}$  to separate dyads in which the analyte binds strongly to the AuNP's monolayer, namely 'active' dyads ( $\Delta G_{bind} > \Delta G_{bind}^{ref}$ ), from those in which the analyte interacts weakly with the AuNP, namely 'inactive' dyads ( $\Delta G_{bind} < \Delta G_{bind}^{ref}$ ). To determine  $\Delta G_{bind}^{ref}$ , we applied our method to a training dataset containing AuNP-analyte dyads with known affinity constants ( $K_{bind}^{exp}$ ). The dataset comprised 31 dyads (**Table C-1**, **Table C-2**, and **Table C-3**) whose affinities were previously measured by fluorometric titration experiments.<sup>95–97,376,383</sup> The experimental binding free energies ranged between 2.8 and 8.7 kcal mol<sup>-1</sup> in 22 of the training dyads. We labeled these dyads as 'active' entries. Instead, the affinities of the remaining 9 dyads were

below the experimental detection limit, suggesting a significantly weak binding. These weakly interacting systems were labeled as ‘inactive’ entries.

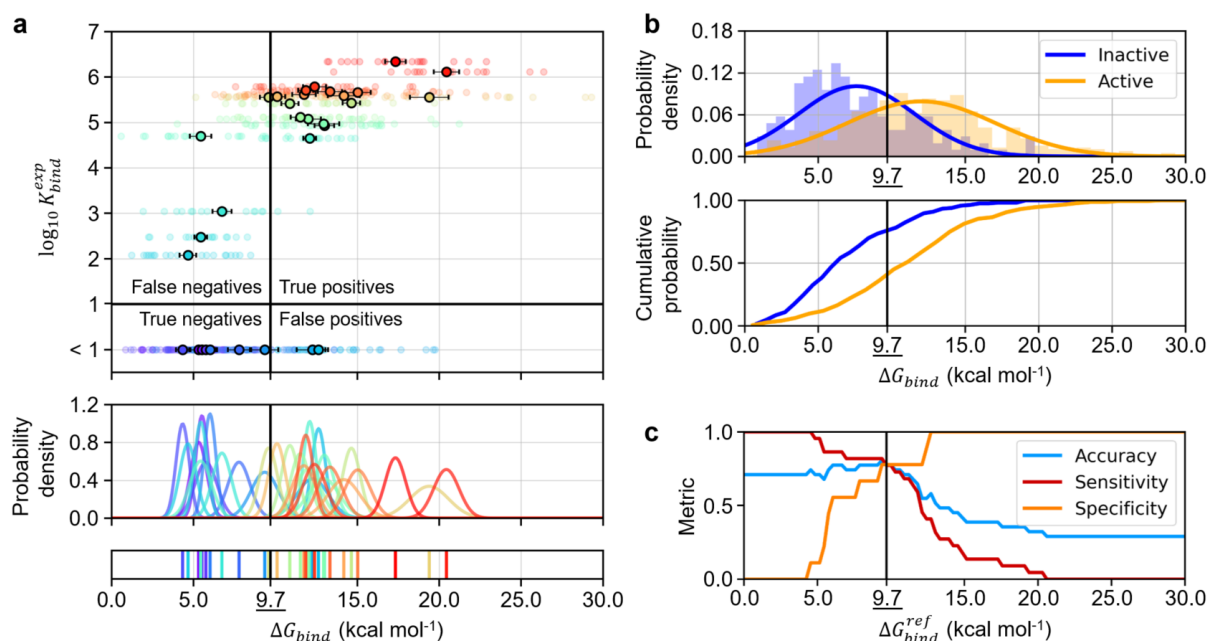


**Figure 31.** Performance of the MD-based screening protocol. **a.** Computed ( $\Delta G_{bind}$ ) and experimental ( $\log_{10} K_{bind}^{exp}$ ) affinity for each AuNP-analyte dyad. Each dyad is colored according to its experimental affinity, which increases from purple to red. The transparent points in the top panel indicate the binding free energy computed for each of the ten analyte copies. The error bars indicate the standard error of the obtained distributions. The middle panel shows Gaussian distributions fitted to the binding free energies predicted for each dyad (Gaussian width set to the standard error of each population). The bottom panel shows the mean of each distribution. **b.** Probability distribution function (top panel) and cumulative probability normalized to 1.0 (bottom panel) of the computed binding energies for the known active (yellow) and inactive (blue) dyads. **c.** Accuracy, sensitivity, and specificity of the method as a function of the threshold binding energy,  $\Delta G_{bind}^{ref}$ , used to classify dyads as active and inactive. The best performance was reached at a reference binding energy of 9.7 kcal mol<sup>-1</sup>, which is marked with a vertical black line throughout all the plots.

The dyads of the training set displayed different charges (**Table 3**). The AuNPs had a charge of -1 e per thiol, zero, or 1 e per thiol, and the analytes had a charge of -1 e, zwitterionic (phenylalanine), or 1 e. Out of the 31 dyads, 21 displayed AuNPs and analytes with complementary charges, 8 had neutral AuNPs with anionic analytes, 1 had an anionic AuNP with a neutral (zwitterionic) analyte, and 1 had an anionic AuNP with an anionic analyte. The dyads in the training set contained 11 unique AuNPs (**Table C-1**). All the AuNPs had 2 nm spherical cores coated by linear ligands 2 nm in length at elongated conformations. Specifically, the coating ligands were comprised of a 7-carbon hydrophobic linker and a (charged) capping group. The capping group bore a negative charge in 3 of the thiols, a cationic

charge in 1 thiol, and a neutral polyethylene glycol moiety in 7 thiols (**Table 3** and **Table C-2**). Conversely, the dyads in the training set contained 17 unique analytes (**Table C-3**), 13 of which were (cationic) phenethylamine derivatives, 1 was the zwitterionic form of phenylalanine, and 3 were (anionic) salicylate derivatives.

Applying our computational protocol to the training dyads resulted in binding free energies  $\Delta G_{bind}$  ranging from  $4.3 \pm 0.5$  to  $20.4 \pm 0.8$  kcal mol<sup>-1</sup> (mean  $\pm$  standard error, **Figure 31a**). The obtained results showed a visible distinction between the free energy of active (red, yellow, green, and cyan points in **Figure 31a**) and inactive dyads (blue and purple points in **Figure 31a**). Moreover, we grouped the binding energies of the active and inactive systems to compute the probability distribution of  $\Delta G_{bind}$  for the active and inactive classes (**Figure 31b**). Even though both distributions overlapped, the binding energies of the active dyads were shifted toward higher energy values. We assessed the difference between both distributions by applying a two-tailed Kolmogorov-Smirnov test.<sup>389</sup> This test demonstrated that, indeed, neither of the distributions can be recovered from sampling each other ( $p$ -value < 0.001). Thus, our method differentiates active from inactive dyads.

The optimal threshold parameter  $\Delta G_{bind}^{ref}$  was determined by testing the method's enrichment at various values (**Figure 31c**). We classified the dyads as active ( $\Delta G_{bind} > \Delta G_{bind}^{ref}$ ) or inactive ( $\Delta G_{bind} < \Delta G_{bind}^{ref}$ ) using values of  $\Delta G_{bind}^{ref}$  ranging from 0.0 to 30.0 kcal mol<sup>-1</sup>. For each value of  $\Delta G_{bind}^{ref}$ , the accuracy (Equation 78), sensitivity (Equation 79), and specificity (Equation 80) were calculated based on the number of true active (TP), true inactive (TN), false active (FP), and false inactive (FN) dyads. The most accurate classification was obtained with a threshold energy of 9.7 kcal mol<sup>-1</sup>. As a comparison, in the context of proteins, a competitive inhibitor with a binding affinity of 9.7 kcal mol<sup>-1</sup> has an inhibition constant of roughly 9 nM, which would be considered a 'potent' inhibitor.<sup>390</sup> Moreover, the threshold of 9.7 kcal mol<sup>-1</sup> resulted in an accuracy, sensitivity, and specificity of 0.77, 0.77, and 0.78, respectively. Importantly, the ratio between active and inactive dyads in the training set was 0.41, which is also the accuracy of a random classifier applied to the same dataset. Thus, the proposed protocol recognizes active dyads with twice the accuracy of a random classifier.

$$Accuracy = \frac{TP + TN}{TP + TN + FP + FN} \quad (78)$$

$$\text{Sensitivity} = \frac{TP}{TP + FN} \quad (79)$$

$$\text{Specificity} = \frac{TN}{TN + FP} \quad (80)$$

Using the threshold of 9.7 kcal mol<sup>-1</sup>, the protocol correctly classified 17 dyads as active (TP) and 7 as inactive (TN), and it mistakenly classified 2 dyads as active (FP) and 5 as inactive (FN). Interestingly, 4 out of the 5 false negatives used neutral AuNPs with salicylate (i.e. an anionic analyte), which suggested a systemic underperformance in dyads that were electrostatically impaired. Nonetheless, parametrizing the protocol excluding neutral AuNPs increased the accuracy only slightly to 0.83, showing that the performance of the protocol is independent of the dyads' charge. Admittedly, understanding the protocol's limitations requires further experimental evidence on dyads covering a wider chemical space. Importantly, our protocol, in its current state, successfully sieves active chemosensors from libraries of dyads, as discussed above.

### C. Chemosensor screening

The reach of the newly developed protocol was exemplified by designing AuNPs that detect 3MT, a catecholamine monitored in the diagnosis and prognosis of neuroblastoma (**Figure 32a**).<sup>384-386</sup> To this end, we built a library of 100 coating thiols that were synthetically accessible (**Figure 32b**). The thiols consisted of a 7-carbon aliphatic spacer followed by three amino acids. The two inner residues (*AA1* and *AA2*) iterated over ten essential amino acids: alanine (Ala), glutamine (Gln), glycine (Gly), isoleucine (Ile), leucine (Leu), phenylalanine (Phe), proline (Pro), serine (Ser), tryptophan (Trp), and tyrosine (Tyr). Instead, the outermost amino acid (*AA3*) was always an aspartate (Asp) in order for the thiols to resemble those in our training set (i.e. mostly aliphatic chains capped by an anionic headgroup). Throughout this work, we refer to each thiol according to its two internal residues using the *AA1-AA2* notation (e.g. Ala-Tyr). Note that the charged amino acids Asp, glutamate (Glu), and histidine (His) were excluded from the *AA1* and *AA2* positions to ensure a net charge of -1 e per thiol and to avoid zwitterionic species. Asparagine (Asn), methionine (Met), threonine (Thr), and valine (Val) were also dropped, since they were considered chemically redundant given the inclusion of Ala, Gln, Leu, and Ser. Lastly, cysteine (Cys) was excluded since it would have led to dual thiolates difficult to selectively graft onto gold cores.

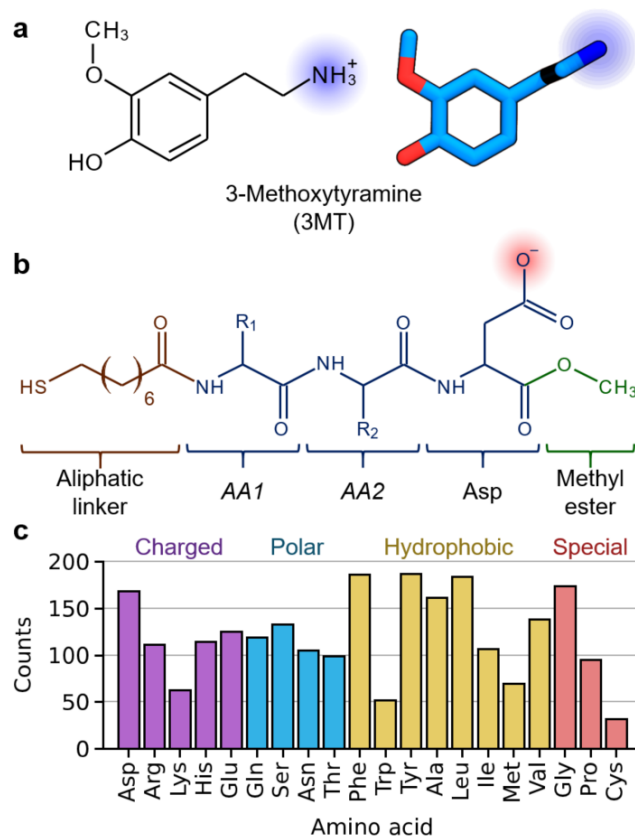


**Figure 32.** Chemical structure of the target analyte and the built thiols, and the amino acids present in the binding pockets of catecholamines. **a.** Chemical structure (left panel) and 3D geometry (right panel) of 3MT. **b.** Scaffold of the thiols in our built library. The ligands' structure consists of an aliphatic linker (brown), three amino acids (blue), and a methyl ester capping (green). The outermost amino acid is Asp, whereas the two innermost AA1 and AA2 iterate over Ala, Gln, Gly, Ile, Leu, Phe, Pro, Ser, Trp, and Tyr. **c.** Frequency of the 20 essential amino acids in the binding sites of catecholamines. The binding pockets are extracted from proteins bound to any of the 13 molecules in the biosynthetic pathways for catecholamines and trace amines (171 structures in total). The amino acids included have at least one atom within 0.5 nm of the ligands (**Figure C-1** and **Table C-4**). Amino acids with charged, polar, hydrophobic, and special side chains are shown in purple, blue, yellow, and red, respectively.

We also considered the chemical similarity between the thiols and the naturally occurring binding pockets of catecholamines. The Protein Data Bank (PDB) database contained 171 proteins bound to catecholamine derivatives, specifically, the 13 catecholamines and trace amines produced in the human brain (**Figure C-1**). We defined a binding site as the collection of amino acids with heavy (i.e. non-hydrogen) atoms within 0.5 nm of the catecholamines. The binding sites showed a different persistence for each of the 20 essential amino acids (**Figure 32c**). Based on this information, each thiol was assigned a similarity index  $\eta_P$  calculated from the frequency ( $\nu_{AA}$ ) of AA1 and AA2 in the naturally occurring binding sites of catecholamines (Equation 81). The similarity index  $\eta_P$  lied between 0.28 (for Trp-Trp) and 1.00 (for Tyr-Tyr).

$$\eta_P = \frac{v_{AA1} + v_{AA2}}{2} \quad (81)$$

The thiol database built was screened against 3MT using our MD-based protocol to calculate the dyads' binding free energy (**Figure 33a**). The binding free energies ranged from  $3.1 \pm 0.1$  (Leu-Gln) to  $17.3 \pm 0.6$  kcal mol<sup>-1</sup> (Pro-Leu), a similar interval as the one obtained for the training dataset (i.e.  $4.3 \pm 0.5$  to  $20.4 \pm 0.8$  kcal mol<sup>-1</sup>). Out of the 100 thiols, 34 presented a binding energy greater than the threshold value of 9.7 kcal mol<sup>-1</sup>. Thus, these 34 AuNPs were predicted to recognize 3MT in aqueous solutions. The thiol that bound the strongest to 3MT was Pro-Leu ( $17.3 \pm 0.6$  kcal mol<sup>-1</sup>), followed by Phe-Gln ( $16.1 \pm 0.4$  kcal mol<sup>-1</sup>), Phe-Ser ( $14.5 \pm 0.4$  kcal mol<sup>-1</sup>), Ile-Gln ( $14.3 \pm 0.5$  kcal mol<sup>-1</sup>), and Ile-Trp ( $13.0 \pm 0.3$  kcal mol<sup>-1</sup>). In contrast, the thiols that bound the weakest to 3MT were Leu-Gln ( $3.1 \pm 0.1$  kcal mol<sup>-1</sup>), Trp-Ser ( $3.4 \pm 0.3$  kcal mol<sup>-1</sup>), Gly-Pro ( $4.4 \pm 0.1$  kcal mol<sup>-1</sup>), Phe-Phe ( $4.8 \pm 0.1$  kcal mol<sup>-1</sup>), and Tyr-Trp ( $5.1 \pm 0.2$  kcal mol<sup>-1</sup>). Notably, the asymmetry of the matrix shown in **Figure 33a** suggested that, similar to proteins, inverting the AA1-AA2 amino acid sequence changed the binding energy of the dyad and the 3D folding of the monolayer.

To determine if certain amino acids were conserved along the active AuNPs, we examined the binding free energy distributions of thiols with the AA1 and AA2 residues, separately (**Figure 33b**). Notably, placing a Leu residue in the AA2 position led to a binding energy distribution with a first quartile of 9.4 kcal mol<sup>-1</sup> and a median of 10.6 kcal mol<sup>-1</sup>. This situation displayed the highest first quartile and the only median above the 9.7 kcal mol<sup>-1</sup> free energy threshold. As a matter of fact, 10 out of the 34 active thiols bore a Leu residue in their structure, consistent with the fact that Leu was the second most abundant amino acid in naturally occurring binding pockets of catecholamines. Except for Leu in AA2, neither of the AA1 and AA2 positions had a preferred amino acid. These results indicate that the binding pockets carved into the monolayers vary with the thiol's chemistry, and that the binding of 3MT can be stabilized by different interactions in AuNPs with different functional groups.

We visually inspected the PDB structures that had been crystallized with catecholamines similar to 3MT (since there were not any structures available with 3MT). In detail, we retrieved the 3 structures bound to p-tyramine (AEF), which lacks the methoxy group of 3MT, and the 13 structures bound to L-dopamine (LDP), which replaces the methoxy group of 3MT for a hydroxyl group (**Figure C-1** and **Table C-4**). Surprisingly, despite Phe being highly abundant in the binding pockets of AEF and LDP (**Figure 32c**), Phe residues were never found forming

specific  $\pi$ -stacking interactions with the aromatic ring of catecholamines. Out of the 16 structures analyzed, only 1 showed a T-shaped  $\pi$ -stacking interaction (PDB code: 6DYO). In the rest of the cases, the hydrophobic segment of the catecholamines was stabilized by non-specific dispersive interactions. These observations are in line with the high content of Leu that we saw in our (predictively) active AuNPs because Leu has a flexible, hydrophobic sidechain that can easily reorganize around 3MT. It also rationalizes the surprisingly low content of aromatic residues (Trp and Tyr) among the active AuNPs.

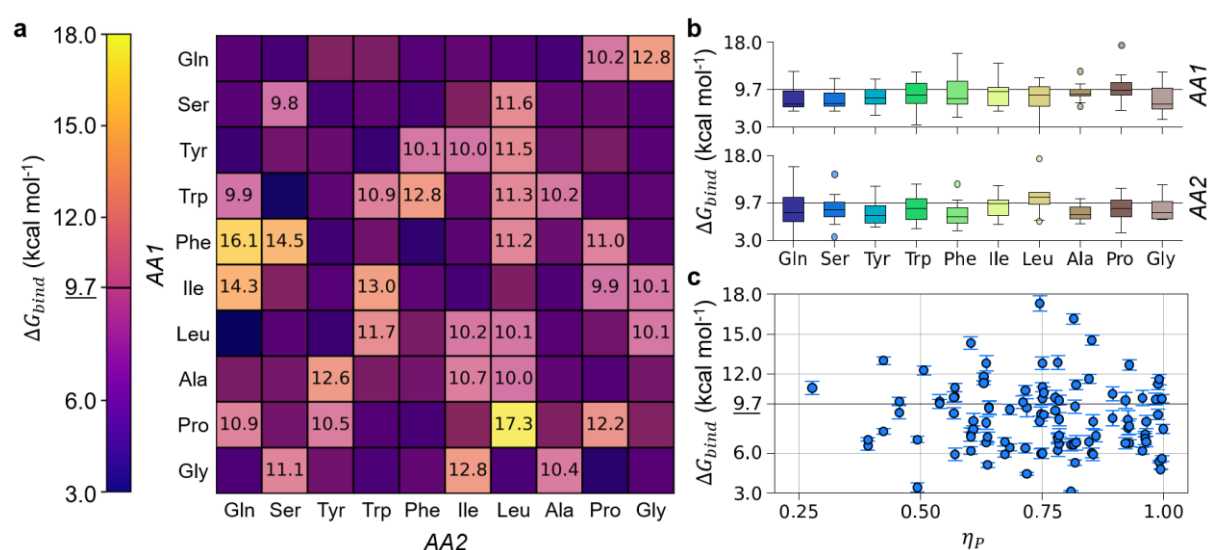


**Figure 33.** Results from the MD-based screening protocol. **a.** Binding free energies for the 100 thiols of the built library. Only the values greater than  $9.7 \text{ kcal mol}^{-1}$  (i.e.  $\Delta G_{bind}^{ref}$ ) are written explicitly for clarity. **b.** Distribution of the binding free energies grouped by the AA1 (top panel) and AA2 (bottom panel) positions. Each amino acid is assigned a unique color. **c.** Scatter plot of the binding free energy as a function of the similarity coefficient  $\eta_P$  for all the screened thiols. The error bars indicate the standard error for each AuNP-analyte dyad.

We further dissected the chemical similarity between active thiols and protein binding pockets by inspecting the binding free energy as a function of the  $\eta_P$  coefficient (**Figure 33c**). Our analysis showed that the binding free energy was uncorrelated to the similarity index  $\eta_P$ , corroborating that AuNPs can trap 3MT in chemical environments alternative to those found in proteins. It is noteworthy that the amino acids in the active thiols were not preferentially polar (i.e. Gln and Ser) nor bulky (i.e. Phe, Trp, and Tyr), suggesting that the binding of 3MT required the formation of well-organized local environments, and it is not only governed by the net number of favorable polar or dispersive contacts accessible.

**Table 4.** Binding free energy and pocket similarity index for the ten best and ten worst scored coating thiols for the detection of 3MT.

<i>AA1</i>	<i>AA2</i>	$\Delta G_{bind}$ (kcal mol <sup>-1</sup> )	$SE_G^a$ (kcal mol <sup>-1</sup> )	$\eta_P$
Pro	Leu	17.3	0.6	0.75
Phe	Gln	16.1	0.4	0.82
Phe	Ser	14.5	0.4	0.85
Ile	Gln	14.3	0.5	0.60
Ile	Trp	13.0	0.3	0.43
Gln	Gly	12.8	0.5	0.78
Gly	Ile	12.8	0.5	0.75
Trp	Phe	12.8	0.6	0.64
Ala	Tyr	12.6	0.4	0.93
Pro	Pro	12.2	0.3	0.51
...	...	...	...	...
Ile	Ile	5.9	0.5	0.57
Ser	Tyr	5.9	0.5	0.86
Phe	Tyr	5.5	0.2	1.00
Leu	Tyr	5.3	0.1	0.99
Tyr	Gln	5.3	0.2	0.82
Tyr	Trp	5.1	0.2	0.64
Phe	Phe	4.8	0.1	0.99
Gly	Pro	4.4	0.1	0.72
Trp	Ser	3.4	0.3	0.49
Leu	Gln	3.1	0.1	0.81

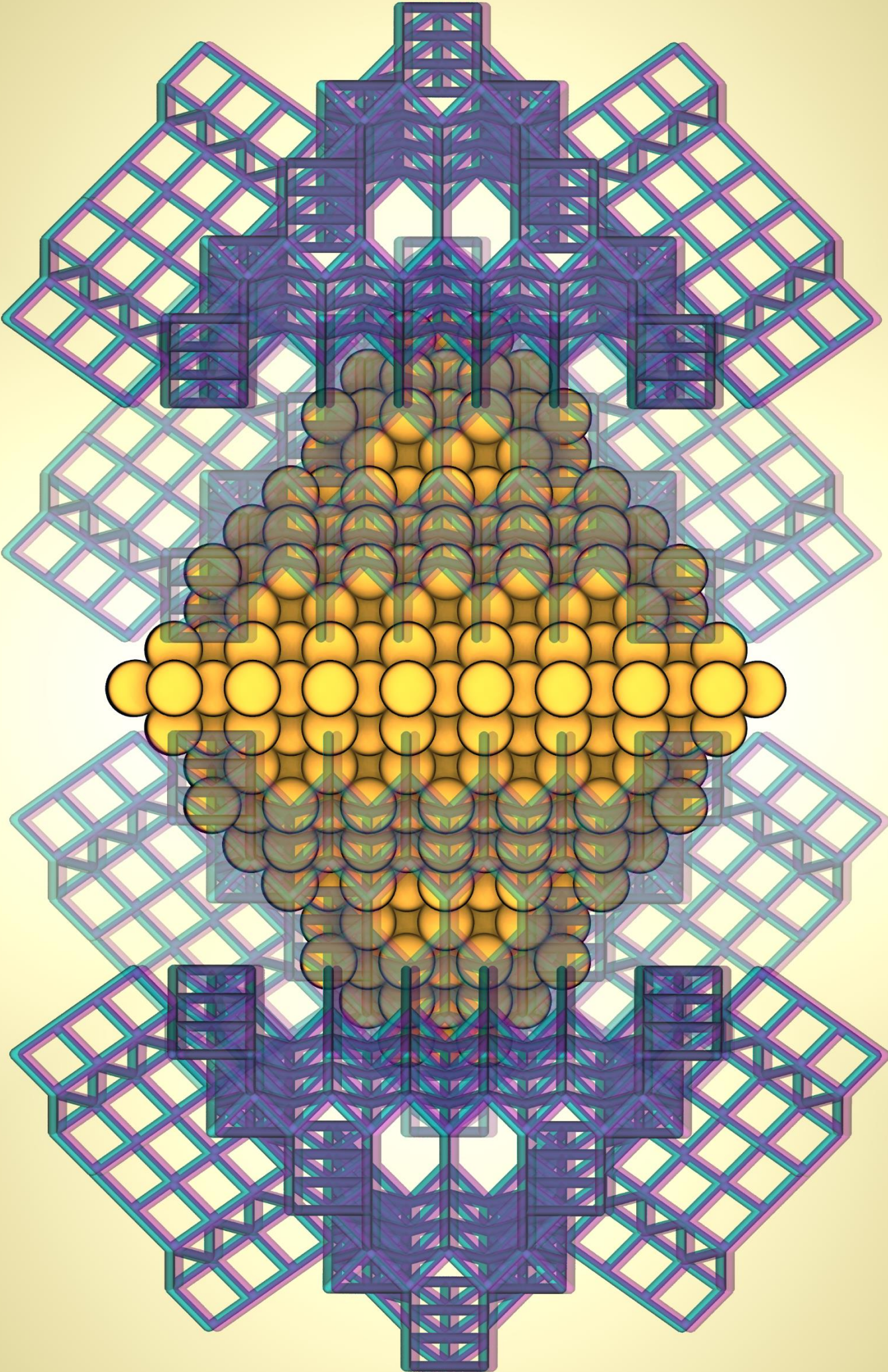
<sup>a</sup> $SE_G$ : Standard error of the computed binding free energies.

## D. Perspectives

Gold-supported NMR nanoreceptors first appeared in 2013<sup>376</sup> and offer a new paradigm for detecting small molecules. In this context, the computational protocol introduced here enables the quick screening of gold nanoreceptors, significantly reducing the time and cost barriers that are currently involved in the design of gold-supported chemosensors. The computational protocol introduced here has allowed us to propose ten candidate thiols that are expected to bind to 3MT. We also selected the ten thiols with the weakest binding energy as negative controls (**Table 4** and **Table C-5**). Fluorometric titration experiments will be carried out to determine the affinity of 3MT for each of these 20 AuNPs proposed. The experimental assays are scheduled for the third trimester of 2020, and they will be performed in collaboration with Prof. Fabrizio Mancin from the University of Padova. Measurable affinity constants in the top



ten thiols and undetectable binding in the weakest ten thiols would confirm that the newly developed method can effectively scan libraries of AuNPs for active nanoreceptors. Validating the protocol introduced here would set the foundations for the high-throughput virtual screening of AuNPs, ultimately boosting the design of gold-supported chemosensors.



# CHAPTER VI. NANOMODELER CG: A TOOL FOR MODELING AND ENGINEERING FUNCTIONAL NANOPARTICLES AT A COARSE-GRAINED RESOLUTION

## Abstract

Functionalized metal nanoparticles (NPs) are macromolecular assemblies with a tunable physicochemical profile that makes them interesting for biotechnology, materials science, and energy conversion. In this regard, molecular simulations offer a way to scrutinize the structural and dynamical features of monolayer-protected NPs and their interactions with relevant matrices. Previously, we developed NanoModeler, a webserver that automated the preparation of functionalized gold NPs for atomistic molecular dynamics (MD) simulations. Here, we present NanoModeler CG ([www.nanomodeler.eu](http://www.nanomodeler.eu)), a new release of NanoModeler that now allows building and parametrizing monolayer-protected metal NPs at a coarse-grained (CG) resolution. This new version extends our original methodology to NPs of eight different core shapes, up to 50 nm in size, and coated by eight different monolayer morphologies. The resulting topologies are compatible with the Martini force field but are easily extendible to any other set of parameters parsed by the user. Finally, we demonstrate NanoModeler CG's capabilities by reproducing experimental structural features of alkylthiolated NPs and rationalizing the brush-to-mushroom phase transition of polyethylene-glycol-coated anionic NPs. By automating the construction and parametrization of functionalized NPs, the NanoModeler series offers a standardized way to computationally model monolayer-protected nanosized systems.

## A. Introduction

Metal nanoparticles (NPs) are attracting interest because rapid advances in synthetic chemistry offer greater control over their structural and chemical features.<sup>391</sup> Metal NPs have electronic and optical properties that are specific to their size, being absent in bulks of the same materials.<sup>380</sup> Furthermore, their high area-to-volume ratio and ease of surface functionalization make metal NPs appealing candidates for many of applications.<sup>102</sup> Tailored metal NPs are now used in materials sciences,<sup>392</sup> catalysis,<sup>98,100,101</sup> drug delivery,<sup>253,393,394</sup> and bioimaging,<sup>395–397</sup> to name a few.

Metal NPs comprise an inner metallic core to which a functionalizing monolayer is attached. The protecting monolayer is a supramolecular body comprising a collection of molecules, known as ligands. These ligands are typically bound to the core by thiols and amines (for noble metals), phosphine oxides and phosphonates (for semi-conducting quantum dots), or carboxyls and hydroxyls (for transition metal oxides).<sup>25,398</sup> By modifying the surface chemistry of the naked cores, the functionalizing ligands confer the NPs a characteristic charge distribution and hydrophobicity.<sup>302</sup> These ultimately dictate the NPs' solubility, chemical stability, and interaction patterns with external entities.<sup>399</sup> In other words, the protecting monolayer governs the physicochemical properties of metal NPs, thus influencing their effectiveness and transferability to applications in biomedicine, materials science, and energy conversion/storage.<sup>12,146</sup>

The knowledge-based design of functionalized metal NPs for custom applications requires an in-depth understanding of their structural and dynamical characteristics.<sup>21,264,400</sup> Computational methods, in particular molecular dynamics (MD) simulations, are a versatile approach to this problem. MD simulations are especially useful as they allow researchers to study a controlled set of particles at a molecular scale for time intervals in the order of microseconds.<sup>172,270,305,400,401</sup> MD simulations have been used to dissect the membrane translocation mechanism of mixed monolayer gold NPs (AuNPs),<sup>89,150,323,338</sup> identify diverse binding modes of analytes in flexible monolayers,<sup>57,95</sup> and characterize binding complexes with nucleic acids.<sup>56</sup>

Previously, we introduced NanoModeler, a webserver that allows its users to prepare the structure and topology files required for atomistic MD simulations of AuNPs and nanoclusters.<sup>359</sup> NanoModeler enabled an automatic and standardized protocol for the

molecular modeling of AuNPs. However, the generated atomistic representations were limited by the reduced number of experimentally elucidated gold cores. The available crystallographic information restrains the original atomistic approach to 16 AuNPs of under 2.1 nm in diameter, leaving unaddressed the modeling of bigger NPs made of metals other than gold.

In this context, coarse-grained (CG) MD is a computational strategy for simulating large systems by grouping a collection of atoms into an individual bead.<sup>211</sup> Reducing the total number of degrees of freedom in a system thus allows the modeling of larger spatial dimensions with a constant number of interaction sites. According to the force field used, each bead type is assigned a set of parameters to compute the system's potential energy.<sup>207</sup> Of the available CG force fields, Martini is one of the most benchmarked and widely used for simulating biomacromolecules and functionalized metal NPs.<sup>182,234</sup> Some tools currently allow CG simulations of macromolecules like proteins,<sup>306,402</sup> nucleic acids,<sup>403,404</sup> and lipids;<sup>280</sup> however, functionalized NPs must still be prepared through in-house scripting and the efforts of the interested researcher.

Here, we present NanoModeler CG, a new release in the NanoModeler series that allows the building and parametrizing of functionalized metal NPs at a CG resolution. This new version incorporates the principles of CG mapping to address the need for reliable models of metal NPs over 2 nm in size. Indeed, NanoModeler CG supports NPs with cores shaped in eight different geometries (up to 50 nm in size) coated by monolayers with eight different morphologies. Moreover, this tool produces structure and parameters files of NPs that are compatible with the Gromacs MD engine and the Martini force field by default. In this way, the automatic generation of NP models is brought in line with experimental advances that offer growing synthetic control over metal NPs.

## **B. Results and discussion**

NanoModeler CG is the second version of the NanoModeler webserver ([www.nanomodeler.eu](http://www.nanomodeler.eu)).<sup>359</sup> This version extends the automatic modeling of monolayer-protected metal NPs to CG representations, allowing users to prepare the necessary files for MD simulations. This version upgrades the previous interface. The backend is written in Python, and the new frontend is written in HTML, CSS, and JavaScript. **Figure 34a** shows NanoModeler CG's general workflow.

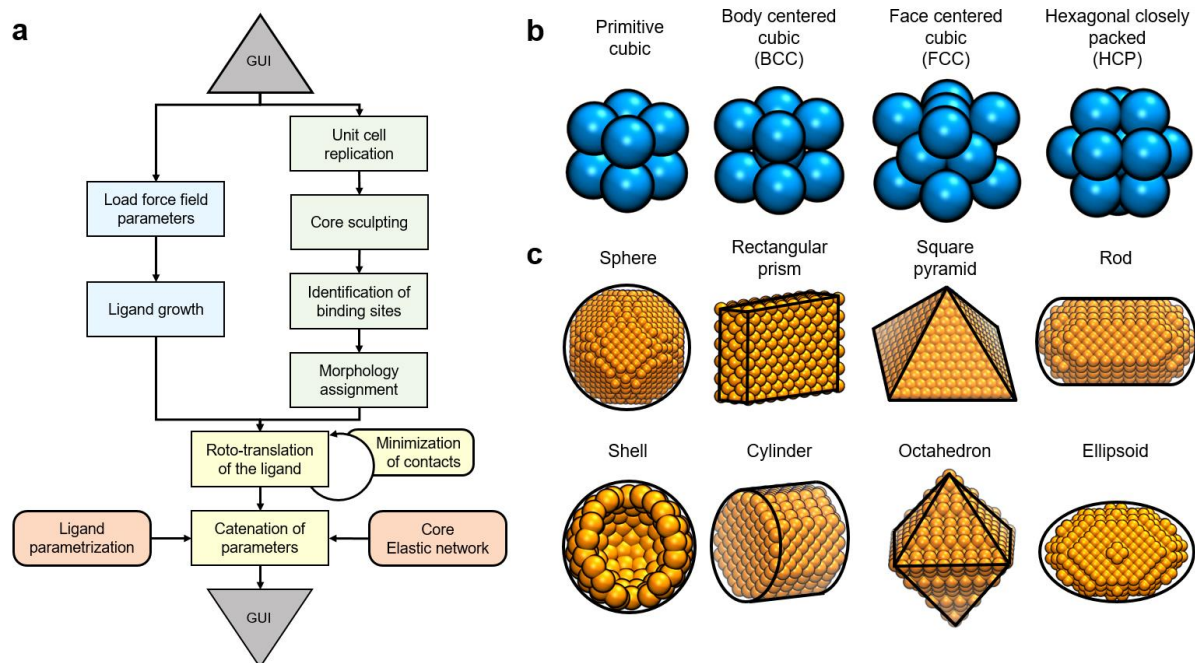


**Figure 34.** NanoModeler CG's operations and scope. **a.** NanoModeler CG's general workflow when processing a new job. Steps involving core beads only are in green, steps involving ligands only are in blue, and steps involving core beads and ligands are in yellow. The GUI is in gray and referrals to force field parameters are in orange. **b.** The four unitary cells supported during the core constructions. **c.** The eight shapes in which the webserver can sculpt cores.

### 1. Modeling nanoparticle structures

In CG MD simulations, the mapping scheme is critical stage for properly preparing a system. The mapping scheme is a method for encasing multiple atoms into individual interaction sites i.e. beads. Based on this consideration, NanoModeler CG is designed to generate highly customizable 3D models of monolayer-protected metal NPs. The structure of the metal NPs is divided into two components: an inner rigid core and a functionalizing monolayer. NanoModeler CG sequentially assembles these building blocks to construct the target NP.

The building of the inner core is key for the modeling of metal NPs because it fixes features that are decisive for many nanotechnological applications such as imaging or drug delivery.<sup>6,42</sup> Specifically, the core modulates the size, shape, curvature, and mass distribution of the resulting nanoarchitecture.<sup>123,405</sup> In this regard, NanoModeler CG can generate cores of up to 50 nm. Moreover, because the arrangement of the core beads is material-dependent and a priori unknown, the server supports the construction of these cores from the four crystal lattices most commonly encountered in bulk metals (**Figure 34b**), namely primitive cubic, body-centered cubic (BCC), face-centered cubic (FCC), and hexagonal closely packed (HCP). The new

platform also allows tuning of the core beads' radius. This allows the use of output models with CG force fields that support any bead mapping strategy.

The synthesis of shaped metal NPs is now accessible thanks to recent advances in synthetic chemistry. Due to the appearance of anisotropy in their geometry, shaped NPs can display properties that their spherical counterparts cannot. Accordingly, computational methods, in particular MD simulations, are increasingly important ancillary techniques for studying anisotropic metal NPs.<sup>406</sup> NanoModeler CG can sculpt the crystal lattice into seven different shapes that are experimentally available (**Figure 34c**), namely sphere, ellipsoid, octahedron, cylinder, rod, rectangular prism, and square pyramid.<sup>407,408</sup> In addition, the server can build spherical hollow shells. Shells may be preferred over solid spheres because shells display a smoother surface, and the absence of inner beads results in a better performance during the computation of nonbonded energetics.

The total number of beads at the core's surface depends on the size and shape of the NP and on the bead radius parsed. These superficial beads are available for the grafting of the protecting monolayer. The server flags some of these beads as 'anchors' and stores them as attachment points for the functionalizing ligands (Chapter VI-C). The number of anchors to select (i.e. the number of ligands to bind to the core) is determined based on the user-specified grafting density (also known as 'ligand footprint'), another experimentally tunable variable over which NanoModeler CG offers full control. While detecting the anchors, the server also saves the vector normal to the NP's surface at those specific locations. This information is later read to generate a monolayer as voluminous and sterically available as possible, which minimizes the chances of clashes in the final model.

Unlike the initial release of our webserver,<sup>359</sup> NanoModeler CG does not require an input structure file of the coating ligand(s). Instead, the new CG module builds on-site minimized structures of the ligand(s) based on directives parsed by the user through the graphical user interface (GUI). The server reads a bead sequence to assemble a copy of the ligand(s) in an extended conformation that meets the bonded parameters' equilibrium values. Therefore, the final model downloaded from the server will lie at a local energy minimum, making the model more robust and less prone to diverging potential energies during MD simulations (and minimizations). Furthermore, mixed monolayers are gaining attention in the nanotechnology because they can combine coatings with diverse physicochemical attributes into supramolecular structures with novel properties.<sup>129,409</sup> To account for this, the coating ligand(s)

in NanoModeler CG can be grafted onto the NPs in many patterns. The server facilitates the modeling of these systems by supporting seven customizable mixed monolayer morphologies in addition to the standard single-ligand homogeneous arrangement. These are: random, Janus-X (along the X-axis), Janus-Y, Janus-Z, stripe-X, stripe-Y, and stripe-Z (**Figure 35**).

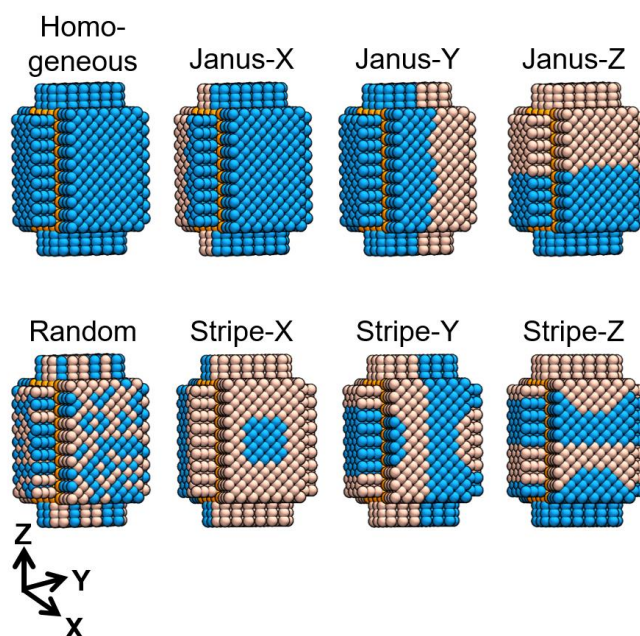


**Figure 35.** The eight monolayer morphologies supported by NanoModeler CG: Homogeneous, random, Janus-X, Janus-Y, Janus-Z, stripe-X, stripe-Y, and stripe-Z. Core beads are in orange, and two example 3-bead-long ligands are in blue and pink.

In summary, NanoModeler CG offers the possibility of generating minimized 3D models of functionalized metal NPs with extensive user control. The resulting models are output in traditional file formats (.gro and .pdb). Overall, the server supports four different crystal lattices that can be sculpted into eight different shapes and functionalized with homogeneous monolayers or seven different mixed morphologies. Additional features include the tuning of the core size, the ligand grafting density, and the core bead radius, making this new release of NanoModeler a versatile way to computationally model monolayer-protected metal NPs.

## 2. *Building user-tailored topologies for nanoparticles*

In addition to a reliable 3D model of the functionalized metal NP, running MD simulations demands a set of bonded and nonbonded parameters. NanoModeler CG implements the same notation for its parameters as the default Martini force field (i.e. the same functional form of the force field). For the bonded energy terms, the stretching and bending potentials are modeled by harmonic functions described by a spring constant and an equilibrium (zero) value, whereas



torsion potentials are modeled as a sum of periodic functions, each described by an amplitude, an equilibrium value, and a multiplicity. Furthermore, nonbonded interactions include two terms, namely electrostatics and van der Waals forces. Electrostatics act according to Coulomb's potential determined by the beads' partial charge. Van der Waals forces are modeled with a 6-12 Lennard-Jones potential computed according to a transferable and predefined interaction matrix proper of the force field.

As with the generation of the 3D model, NanoModeler CG separates the assignment of parameters for the core and for the ligands. The webserver models the core as a set of neutral beads that interact with the environment (and each other) through van der Waals forces exclusively. In this way, the hydrophobicity of the core is determined by the bead type selected by the user. Notably, the Lennard-Jones parameters are not explicitly written in the output topology, but rather are referred from a secondary file containing the interaction matrix. Although NanoModeler CG offers a copy of Martini's interaction matrix by default, a single manual modification to the final topology can make the output files easily transferable to a custom force field. This feature embraces multiple parametrization schemes that other researchers have used to simulate functionalized metal NPs at a CG resolution.<sup>303,410,411</sup>

Current synthetic methods allow the preparation of non-spherical cores; however, the growth of these bodies is material-specific and fundamentally depends on the surface energies of the crystal motif.<sup>272,412</sup> Nonetheless, the material's surface energies are not always available, and adding this as a requirement would require time-consuming experiments or high-level quantum mechanical calculations prior to the modeling. To circumvent this, NanoModeler CG uses a purely geometric sculpting approach that is compatible with CG approaches. To ensure the core's rigidity, the server can also impose an elastic network over the core. This elastic network is implemented as a series of bonds between each bead and all its first neighbors in the crystal lattice. The user can customize the strength of the restrictions.

The mass of the beads is an additional free parameter that is not explicitly involved in computing the system's energy, but that is needed to calculate the forces exerted on each bead. In CG MD simulations, the mass of the beads must be adjusted according to the chemical moiety that they represent. This is particularly relevant for the core beads because, in general, the default masses in the Martini force field will not add up to the total mass of the actual core. For this reason, NanoModeler CG explicitly assigns the appropriate mass to each bead by equally distributing the real mass of the core in the total number of beads. The total mass of

the core is estimated from the bulk density parsed by the user as an input and from the core's shape and size.

The coating ligands are the final component in the parametrization of the NP models. Similarly to the core beads, the nonbonded parameters of the ligands are dictated by the bead types assigned, and the referral to the interaction matrix from the final topology file. The server offers full control over the type of each bead that comprises the target ligand. For the bonded parameters, the Martini force field does not count with predetermined values because these may vary according to the molecule being mapped. Consequently, the bonded parameters of the ligands are assigned in compliance with bond, angle, and dihedral definitions provided by the user through a file in .itp format, the file format for collections of parameters preferred by the Gromacs MD engine. Finally, the mass associated with each bead type can also be set freely, which guarantees the accurate representation of the atomistic image.

In brief, NanoModeler CG sequentially parametrizes monolayer-protected metal NPs, assigning the parameters of the core and then of the ligand. The new release is a versatile platform that offers full control over the bonded and nonbonded parameters in the system. The parameters in the resulting systems are derived from the bead type definitions provided by the user, making the output models transferable to purpose-specific interaction matrices and mapping schemes.

### *3. Molecular dynamics simulations and case study*

The topologies generated with NanoModeler CG were validated by reproducing previously published data from experiments and atomistic MD simulations of monolayer-protected AuNPs. Taken together, these test cases illustrate the server's capabilities and the insights that CG MD simulations can deliver. First, we used 100-ns-long CG MD simulations to compute the monolayer thickness of spherical 10 nm AuNPs coated with different polyoxyethylene alkylethers (PAE). Second, we calculated the average tilt angle of alkyl chains of different lengths grafted onto spherical 3, 5, and 7 nm AuNPs at various temperatures. Lastly, we simulated spherical 4.5 nm AuNPs coated with randomly mixed monolayers of polyethylene glycol (PEG) and 11-mercaptoundecanoic acid (MUA).

For our first test case, PAE-coated AuNPs, we calculated the normalized cumulative radial distribution function (RDF) of the monolayer beads with respect to the core's center of mass (COM). Then, the monolayer thickness was derived from the limiting radii, within which the

monolayer beads were found with a 90% probability (**Figure 36a**). The computed values are in excellent agreement with the widths measured with differential centrifugal sedimentation (DCS) experiments.<sup>413</sup> The qualitative trend is perfectly reproduced, with the monolayer becoming wider as the length of the thiols increased. Moreover, the data corresponded quantitatively with the experimental values. Specifically, our computed widths displayed mean absolute error of  $0.11 \pm 0.07$  nm, which coincided with the expected error from the DCS measurements. These results revealed that the modeling scheme implemented in NanoModeler CG allows the ligands to be properly packed in homogeneous monolayers.

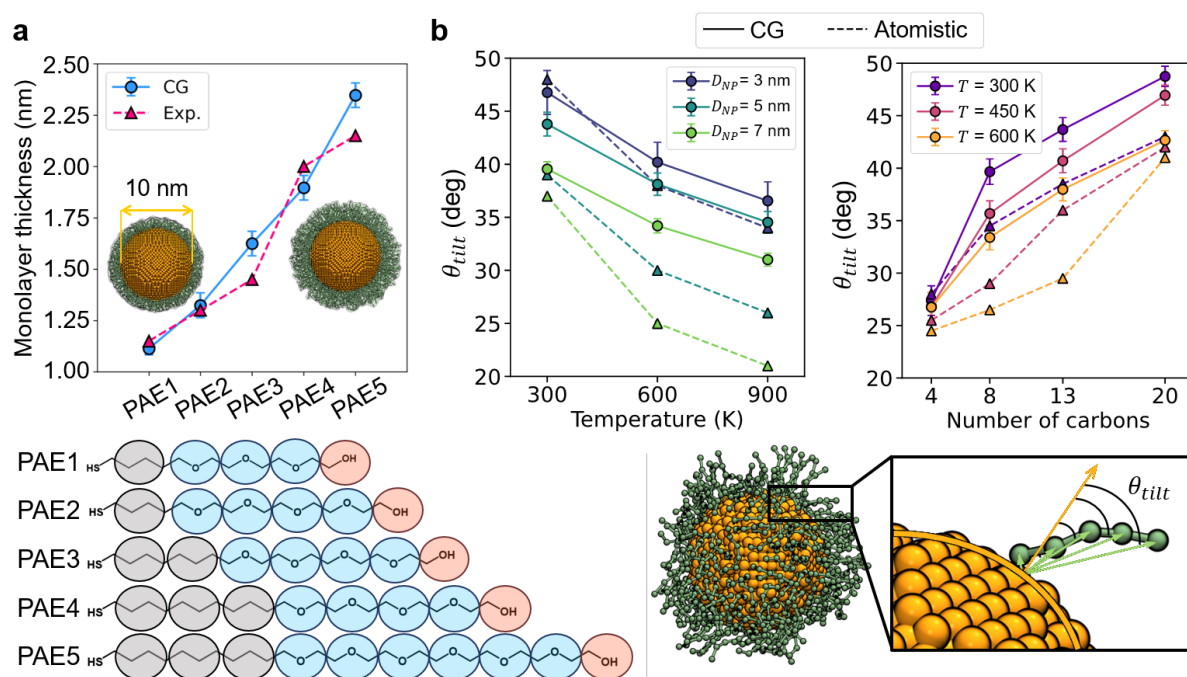


**Figure 36.** Validation results for models generated with NanoModeler CG. **a.** Computed and experimental monolayer widths for 10 nm AuNPs coated with PAE variations of different lengths. The CG mapping scheme is shown in the bottom panel. In our models, the sulfur atoms were considered part of the cores' anchor beads. The colored circles represent three different bead types and the CG mapping scheme adopted. **b.** Tilt angles for alkylthiolated AuNPs derived from CG and atomistic MD simulations. The left plot includes the angles of 3, 5, and 7 nm AuNPs coated with 3-bead (13-carbon) chains. The right plot includes data for 5 nm AuNPs coated with chains of varying length and at 300, 450, and 600 K. The bottom panel and its inset illustrate the definition and calculation procedure for the tilt angle  $\theta_{tilt}$  of a 5-bead-long ligand. The angles reported were averaged over all the beads in the ligand, all the ligands in the AuNP, and all the frames in the simulation trajectory. Core beads are in orange and ligand beads are in green.

In our second test case, we studied the effect of chain length, core diameter ( $D_{NP}$ ), and temperature on the chain-tilting of alkylthiolated AuNPs. We prepared CG models of 3, 5, and 7 nm AuNPs coated with different alkyl chains, and we compared the chains' average tilt angle

(with respect to a radially outgoing vector) with those estimated from atomistic MD simulations reported elsewhere (**Figure 36b** inset).<sup>414</sup> In their original publication, Ghorai and Glotzer studied AuNPs coated with chains of 4, 8, 13, and 20 carbon atoms. In this work, we modeled the same aliphatic thiols as 1, 2, 3, and 5-bead chains in compliance with Martini's four-to-one mapping scheme. Importantly, in all cases, our CG simulations reproduced the published atomistic trends. For AuNPs coated with 13-carbon chains, the average tilt angle was diminished as the core size increased, which suggests that the models perceive the effect of the core's curvature on the motion of the ligands (**Figure 36b** left panel). In fact, as the AuNPs' size increases, the core's curvature decreases. This effect reduced the available volume-per-chain in our simulations, ushering the ligands into an extended and more organized configuration.

Our simulations on alkylthiolated AuNPs also reproduced a reduction in the average tilt angle as the temperature increased. Here, our data deviated more strongly from the atomistic simulations at elevated temperatures (600 and 900 K, **Figure 36b** left panel).<sup>414</sup> This effect was likely due to the fewer degrees of freedom in CG models compared to atomistic representations, which led to fewer microstates and thus an underestimation in the conformational entropy of the AuNPs. The dysregulation between enthalpic and entropic contributions in CG force fields has led to the appearance of similar phenomena in systems containing proteins and membranes.<sup>415-417</sup> Finally, the computed tilt angles also reproduced semi-quantitatively the predictions made by the atomistic simulations of 5 nm AuNPs coated with chains of varying length (**Figure 36b** right panel). As before, an increase in the temperature (450 and 600 K) resulted in a decrease of the tilt angle. Moreover, if we fix the temperature and focus on the effect of the chain length, it appears that longer alkyl chains more effectively sampled their bent configurations (high tilt angles), suggesting an increased flexibility of the terminal beads.

As a final test case, we considered AuNPs protected by PEG:MUA monolayers randomly mixed at different fractions ( $f_m$ ). Dynamic light scattering (DLS) experiments have shown that increasing the abundance of 50-unit-long PEG chains (i.e. higher  $f_m$ ) leads to a 2-fold increase in the hydrodynamic radius of AuNPs with a 9 nm core.<sup>418</sup> We thus studied these systems with smaller models that retained the same core-ligand size scale. In detail, we simulated 4.5 nm AuNPs coated by randomly mixed monolayers of 25-unit-long PEG chains and MUA. From our simulations at different values of  $f_m$ , we calculated the radius of gyration of the AuNP, a

measure that scales linearly with the hydrodynamic radius in globular bodies (**Figure 37a**).<sup>419</sup> As demonstrated in DLS experiments, our simulations indicated that higher concentrations of PEG led to a larger AuNP radius.

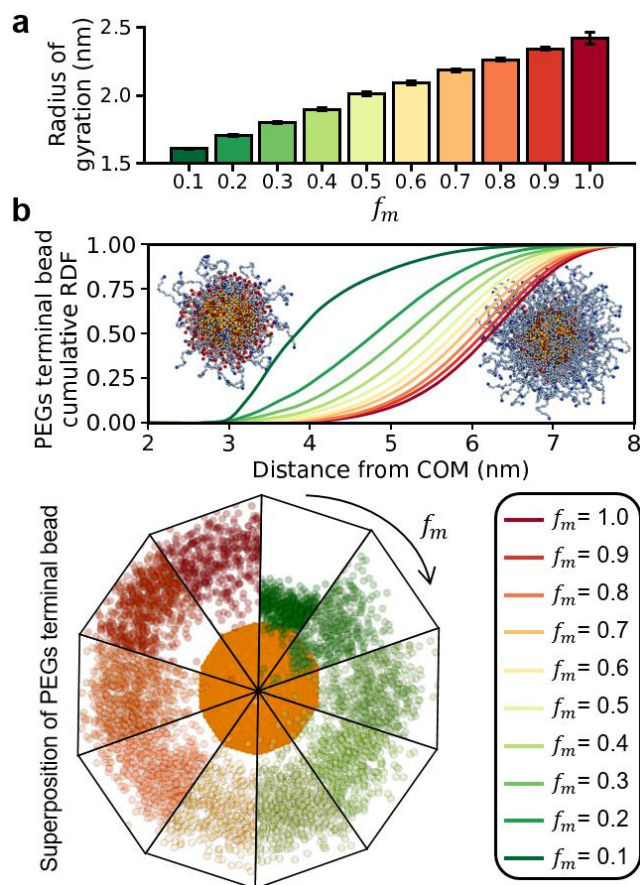


**Figure 37.** CG MD simulations of 4.5 nm AuNPs coated with a mixed monolayer of PEG and MUA. **a.** Radius of gyration of the AuNPs as the fraction of PEG ligands ( $f_m$ ) increases. **b.** Cumulative RDF (normalized to 1.0 at long distances) of the terminal bead in the PEG chains. The top panel includes the structure of an AuNP with  $f_m = 0.1$  (left) and  $f_m = 1.0$  (right). Core beads are in orange, PEG molecules are in light blue, and MUA molecules are in pink. In the bottom panel, the PEG terminal beads are superimposed for various frames to illustrate the bending of the PEG chains as their relative abundance increased. The relative abundance of PEG increases from green to red.

We further studied the structural features of PEG:MUA-coated AuNPs by computing the normalized cumulative RDF of the PEG chains' terminal bead with respect to the COM (**Figure 37b**). As more PEG chains were grafted onto the AuNP, the RDF curves were shifted toward greater distances, indicating a conformational rearrangement of the PEG polymers. As  $f_m$  increased, the PEG chains, which were 21 beads longer than the MUA ligands, formed a bulkier monolayer that forced the grafted polymers into an elongated conformation. In contrast, as  $f_m$  decreased, the PEG chains bent inwards into coiled conformation. These contrasting

structural features of PEG at different mixing fraction coincided with the brush-to-mushroom transition demonstrated for other PEGylated biological systems.<sup>208,209</sup>

Taken together, the test cases demonstrate the potential uses of the NanoModeler CG server. The generated models semi-quantitatively reproduce the structural features of monolayer-protected metal NPs observed in atomistic simulations and experiments. Moreover, the type of simulations discussed here can also be used to inspect and monitor the conformational rearrangements that lead to variations in experimentally measurable quantities such as the hydrodynamic radius.

## C. Webserver building

The NanoModeler webserver comprises two main branches: the frontend and the backend. The frontend is a single-page application developed with Angular 10, an open-source platform engineered by Google for building desktop and web applications. The GUI embraces Material Design principles through the Angular Material component library, allowing good responsiveness and usage from various devices and platforms. The backend is an aggregation of Microservices running in Docker containers. Some, like the orchestrator and data persistence layer, are built on top of NodeJS, whereas the code to assemble nanosystems and their topology is written in Python.

### 1. Construction and parametrization of packed cores

The assembly of ligand-coated metal NPs is divided into two processes: the building of the core and the building of the coating molecules. Both processes are customizable by the user. In total, the cores made by NanoModeler CG support four crystal lattices (primitive, BCC, FCC, and HCP), eight shapes (shell, sphere, octahedron, cylinder, rod, pyramid, ellipsoid, and rectangular prism), and eight ligand morphologies (homogeneous, random, Janus-X, Janus-Y, Janus-Z, stripe-X, stripe-Y, and stripe-Z).

The construction of the core follows four steps: i) The replication of a crystal lattice into a cubic block, ii) the sculpting of the lattice into the target shape, iii) the identification of the anchoring sites for the posterior placing of the ligands, and iv) the labeling of the anchors. In the first step, a unitary cell is generated in accordance with the crystal motif specified by the user (**Figure 38a**). NanoModeler CG supports the most common lattices found in bulk metallic systems. The unit cell is replicated in all three dimensions to produce a cubic block that fits the

target metal NP. In the special case of a hollow shell, no lattice needs to be specified. In the second step, the block is sculpted into the selected shape (**Figure 38b**). Note that, depending on the intended shape, the user must provide different geometrical parameters. In detail, a radius must be parsed to build a sphere or a shell, an edge-length for an octahedron, a radius and a length for a cylinder or a rod, a base-length and height for a pyramid, three semi-axes for an ellipsoid, and three edge-lengths for a rectangular prism. In the third step, the pivoting beads for the attachment of the coating ligands are identified (i.e. the anchors, **Figure 38c**). The total number of anchors,  $N_{lig}$ , is calculated from the grafting density (i.e. nm<sup>2</sup> per ligand) parsed by the user and the core's surface area. In order to select the anchors,  $N_{lig}$  virtual sites are randomly placed on a unitary sphere. The distance between points is then maximized following a Metropolis-Hastings algorithm under the constraint that they remain on the sphere. That is, we maximize the sum of distances  $D_u$  (Equation 82) subject to the unitary constraints  $g_{c,i}$  (Equation 83).

$$D_u(\mathbf{r}) = \sum_i \sum_{j>i} [(x_i - x_j)^2 + (y_i - y_j)^2 + (z_i - z_j)^2]^{1/2} \quad (82)$$

$$g_{c,i}(\mathbf{r}_i) = x_i^2 + y_i^2 + z_i^2 - 1 = 0 \quad (83)$$

The angular distance between these points and the core's surface beads is then computed. The  $N_{lig}$  core beads closest to the optimized virtual sites are stored as the anchors. If a bead is selected twice, one of the selections is exchanged for the nearest available surface bead. Here, the vector normal to the core's surface at each anchor is also stored. In the fourth and final step, the anchors are assigned a flag indicating which ligand to place in each position (**Figure 38d**). This, in turn, fixes the NP's ligand morphology. For example, if the morphology is set to 'homogeneous,' all anchors will be assigned the same label. In contrast, if a 'random' morphology of occurrence rate 0.5 is being built, half of the anchors will be assigned the 'Ligand 1' flag, and the other half will be recognized as 'Ligand 2.' Note that, in the case of a random morphology, the user can ensure reproducible results by setting a random seed. Moreover, the Janus and striped monolayers allow the user to control the ligands' relative abundance and the number of stripes, respectively.

As with the core, the building of the coating monolayer is a three-step sequence: i) The construction of an individual ligand, ii) the roto-translation of the ligand around the core, and iii) the optimization of each ligand's principal component axis. The algorithm for the first step

requires a parameters file. If the user does not provide one, the ligands' beads are placed collinearly. In contrast, when the parameters are available, the ligands are still built in an elongated conformation but in accordance with the equilibrium bond lengths and bending angles in the file (**Figure 38e**). For this, each bead is appended sequentially, while simultaneously maximizing the length of the molecule along its main axis (*PCI*), i.e. minimizing the angle between *PCI* and the reference X-axis. In the second step, the ligand is roto-translated with a quaternion matrix toward each of the anchoring sites (**Figure 38f**). This transformation aligns *PCI* with the vector normal to the anchor. Note that this transformation is not unique, and it may result in structural overlaps within the structure. To avoid such internal clashes, in the third step, the ligand is rotated for 20 iterations around *PCI*, storing the configuration that maximizes the shortest distance between the ligand and the rest of the system.

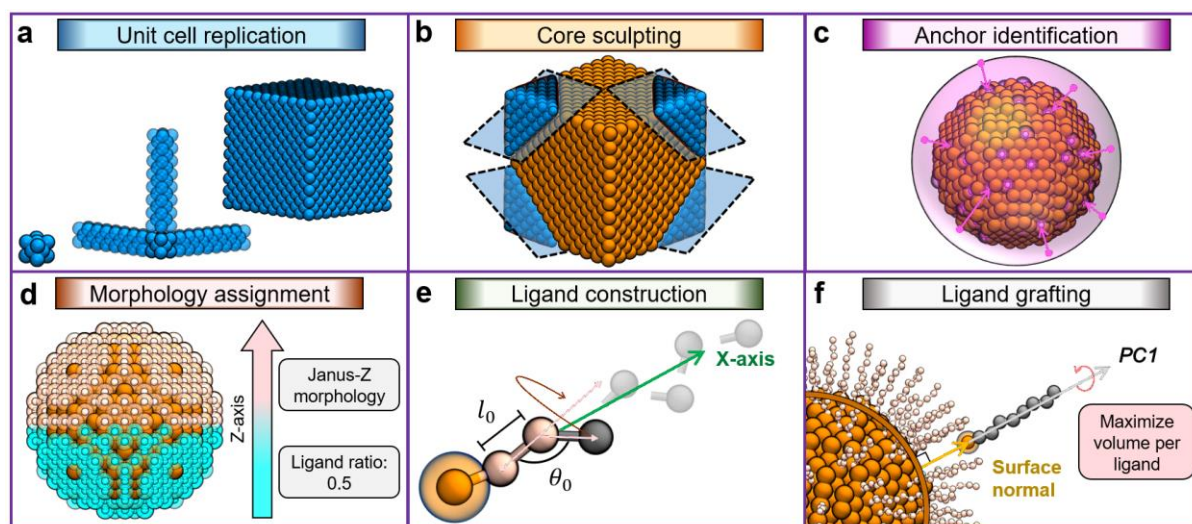


**Figure 38.** Steps followed by NanoModeler CG when generating the output models. **a.** Replication of a unit cell along the XYZ coordinates. **b.** The sculpting of the block into the user-selected shape. **c.** Placement of the anchors according to the angular distance between spherically distributed virtual sites and the core's surface beads. **d.** Labeling of the anchors to assign a monolayer morphology. The figure illustrates a Janus-Z morphology with a ligand ratio of 0.5. **e.** Construction of the ligand along a reference axis following the equilibrium bond lengths ( $l_0$ ) and bending angles ( $\theta_0$ ) provided as inputs. **f.** Roto-translation of a ligand aligning its principal component *PCI* with the vector normal to the core at an anchor's location. Every ligand is rotated along its molecular axis to minimize the likelihood of clashes. Lattice beads are in blue, core beads in orange, virtual sites in purple, the anchors of two example ligands are in white and cyan, and the coating ligands in pink.



## 2. 3D modeling of nanoparticles

The webserver may be used to generate 3D models of monolayer-protected metal NPs (.pdb and .gro files), using the algorithm described above. In addition, the server can also generate topology files for running MD simulations with the Gromacs engine.<sup>320,322</sup> In this regard, the NPs' bonded and nonbonded parameters are fully customizable by the user by providing a file with force constants, equilibrium values, and bead type definitions. The parameters should be uploaded in an 'include topology' (.itp) file following Gromacs' formatting directives. The server is then able to assign the bonded parameters and bead types to the NP in compliance with the parsed file. This feature makes the final topology compatible with the user's CG force field of preference. Note that the nonbonded parameters in CG force fields are typically derived from combination rules or fitting schemes unknown a priori. For this reason, the final topology file refers to an external database (included in the output) containing the interaction matrix associated with the Martini-v2.2P force field.<sup>152,181,213</sup> If the users wish to overwrite the parameters of this force field or use a different one, they simply change the line referring to the force field in the final topology (.top) file. In this way, the user has maximum control over the system parameters, and the approach remains compatible with the Martini scheme, one of the most commonly used force fields for simulating NPs and biomacromolecules.

To prepare the 3D model, the assignment of parameters is processed sequentially for the internal core first and then the outer monolayer. The CG core must weigh the same as an equivalent atomically detailed representation. For this reason, NanoModeler CG requires the bulk density of the core material as an input. With this information and the volume of the core, the server calculates the real mass of the bulk NP, which is then distributed over the available beads. NanoModeler CG also allows its users to impose an elastic network over the internal beads to ensure the shape of the core is maintained throughout a simulation. In doing so, bonds are formed between each of the beads and their nearest neighbors. The number of nearest neighbors varies according to the crystal lattice selected to build the metal NP (i.e. 6 for primitive, 8 for BCC, 12 for FCC, and 12 for HCP). The nearest neighbors are characterized by being located two-bead-radius-away from the reference site (**Figure 34b**). Notably, the core beads' radius and the spring constant of the elastic network are also free parameters for the user to specify. When the core is a hollow shell, the elastic network unites each bead with its 6 nearest neighbors and the diametrically opposite bead (antipodal bead).

The mass and charge of the ligand beads are dictated by the user's input. NanoModeler CG explicitly writes the mass and charge of all the ligand beads in the resulting NP. The mass and charges of these beads vary according to the mapping scheme chosen by the user and the represented molecular moiety. In contrast, the bonded parameters of the ligands are assigned in a 'center out' fashion, starting from the anchoring bead of the core to the tip of the ligands. First, the server identifies the bead types of the bonded pairs, triplets, and quadruplets to assign the bond, angle, and dihedral parameters, respectively. Then, the equilibrium values and spring constants (and multiplicity of dihedrals) are searched in the input parameters file and assigned correspondingly to every copy of the ligand. If the user does not provide parameters for a specific bonded interaction, this is skipped and noted in the job's output documentation. Importantly, some CG force fields require multiple energy functions for the same angle or dihedral. This is easily achievable with NanoModeler CG by appending multiple entries for the same bead combination in the proper sections of the input .itp file. For example, if two sets of parameters are parsed for a specific quadruplet of bead types, then two dihedrals (with their respective parameters) will be assigned to these quadruplets.

### 3. *Molecular dynamics simulations*

To validate the topologies generated with NanoModeler CG, we aimed to reproduce monolayer widths measured experimentally<sup>413</sup> and carbon tilt angles computed from atomistic MD simulations.<sup>414</sup> In addition, we performed simulations for a third set of NPs that shed light on the conformational rearrangements of mixed monolayer AuNPs. First, to reproduce experimental data, we built five AuNPs with a 10 nm spherical core coated by one of the five PAE molecules shown in **Figure 36a**.<sup>413</sup> Second, to match data from atomistic MD simulations, we prepared AuNPs with core diameters 3, 5, and 7 nm coated by 3-bead alkyl chains (**Figure 36b** left panel). We also prepared 5 nm cores and coated them with alkyl chains formed by 1, 2, 3, and 5 beads (**Figure 36b** right panel).<sup>414</sup> Finally, the mixed monolayer AuNPs consisted of a 4.5 nm core coated by 25-unit-long PEG chains and MUA (**Figure 37**). These AuNPs were built with PEG:MUA ligand ratios ( $f_m$ ) ranging from 0.1 to 1.0.<sup>418</sup> All the AuNPs were constructed from FCC lattices with a core bead radius of 0.17 nm. The core beads were modeled as purely hydrophobic moieties using the C1 Martini bead and applying an elastic network of force constant  $k_b = 32,500 \text{ kJ mol}^{-1} \text{ nm}^{-2}$ .<sup>323,420</sup> Moreover, the gold bulk mass density ( $19.3 \text{ g nm}^{-3}$ ) was passed to the server to calculate the mass of the cores' beads. The coating ligands were grafted at a density of  $0.3 \text{ nm}^2$  per thiol, a typical value for alkylthiolated

AuNPs.<sup>405</sup> The bonded parameters and bead type definitions of all the ligands were taken from Rossi et al.<sup>208,209</sup>

For the MD runs of our first study case (10 nm PAE-coated AuNPs), a simulation box was built to ensure a minimum distance of 2.0 nm between the AuNPs and the box edges. The boxes were then filled with standard Martini water beads.<sup>181</sup> In order to relax the solvent around the particles, a minimization was carried out using the steepest descent method. The systems were thermalized and pressurized for 5 ns to 300 K and 1 bar in the NPT ensemble using the velocity-rescale (*v*-rescale) thermostat ( $\tau_B = 2.0$  ps) and the isotropic Berendsen barostat ( $\tau_P = 5.0$  ps,  $\kappa = 4.5 \times 10^{-5}$  bar<sup>-1</sup>). Once the systems had reached the intended temperature and pressure, they were simulated for 100 ns coupled to the isotropic Parrinello-Rahman barostat ( $\tau_P = 12.0$  ps,  $\kappa = 4.5 \times 10^{-5}$  bar<sup>-1</sup>).<sup>227</sup> For the second study case, we simulated 3, 5, and 7 nm alkylthiolated AuNPs in vacuum to match the conditions used by Ghorai and Glotzer in their atomistic simulations.<sup>414</sup> These systems were initially heated at a constant rate for 0.5 ns using the *v*-rescale thermostat ( $\tau_B = 2.0$  ps) in the NVT ensemble at the target temperature (300, 450, 600, or 900 K). The systems were then simulated for 100 ns under the same conditions.

For our final test case, 4.5 nm AuNPs coated with randomly mixed PEG:MUA monolayers, we followed the same workflow as for the PAE-coated AuNPs. Here, however, we used the refPol water model<sup>213,215</sup> to properly propagate the electrostatic forces of the charged (MUA) ligands. In all our simulations, bonds were constrained using the linear constraints solver algorithm,<sup>319</sup> an integration timestep of 20 fs was used, and frames were saved every 80 ps for posterior analysis. Short-range nonbonded interactions were calculated within a radius of 1.2 nm of each bead. Long-range electrostatic interactions were considered using the fourth-order particle-mesh Ewald method.<sup>231</sup> All simulations were conducted with Gromacs-v5.1.4.<sup>320–322</sup>

Our various simulations allowed us to compare monolayer widths and tilt angles with experimental and atomistic MD simulations, respectively. To calculate the experimental monolayer thickness, we first computed the cumulative normalized RDF of the monolayer beads from the COM of the AuNP (Equation 84).

$$G_{mono}(r) = \frac{4\pi}{N_{mono}^2} \int_0^r \sum_{i=1}^{N_{mono}} \langle \delta_D(r_i - r') \rangle dr' \quad (84)$$

Where  $N_{mono}$  is the number of beads in the monolayer,  $r_i$  the distance from the  $i$ -th bead to the AuNP's COM, and  $\delta_D$  Dirac delta function. Then, we calculated the values  $r_{min}$  and  $r_{max}$  such that  $G_{mono}(r_{min}) = 0.05$  and  $G_{mono}(r_{max}) = 0.95$ , that is, the region where there is a 90% chance of finding the monolayer. The monolayer thickness was computed as  $r_{max} - r_{min}$ . The tilt angle of alkylated AuNPs was calculated as the angle between i) the vector from a ligand's anchor to a ligand bead and ii) the vector normal to the core at the ligand's anchor bead (**Figure 36b** bottom panel). The reported values correspond to an average over all the ligand beads, all the ligands, and all the frames. All the error bars were estimated from bootstrap analysis with 1,000 iterations and a sample size of 1% of the original distributions. The trajectory analysis was carried out with a mixture of Gromacs tools and in-house scripts that used the MDAnalysis-v1.0 library from Python.<sup>370</sup>

## D. Conclusions

Here, we introduce NanoModeler CG, a webserver for assembling and parametrizing functionalized metal NPs at a CG resolution. NanoModeler CG automates and standardizes the modeling of metal NPs larger than 2 nm. NanoModeler CG extends the original (atomistic) methodology to metal NPs with non-spherical cores of up to 50 nm coated by a broader range of monolayer morphologies, consistent with growing synthetic control. Similarly to the first release for atomistic NPs models, NanoModeler CG stratifies the building of the 3D models and the parameter assignment by treating the inner metallic core followed by the coating monolayer. The construction of the inner metallic core supports four different crystal unit cells that can be combined with eight different core shapes. The coating ligands are built on-site, and a model that lies at a local minimum of bonded potential energy is built with bonded parameters parsed by the user.

To illustrate some of the insights that NanoModeler CG and the CG methodology can provide, we modeled 3 representative NP test systems, sampled in several different flavors. MD simulations of 10 nm PAE-coated AuNPs reproduced the experimental monolayer thickness with a precision of 0.1 nm. Similarly, simulations of alkylthiolated AuNPs reproduced semi-quantitatively the tilt angles of the coating thiols at different core sizes, thiol chain lengths, and temperatures. Finally, our simulations of 4.5 nm mixed monolayer AuNPs rationalized the decrease in hydrodynamic radius of PEG:MUA-coated AuNPs in terms of a brush-to-mushroom transition of the passivating PEG chains. Taken together, these results demonstrate that NanoModeler CG is an effective tool for studying structural and dynamical features of

functionalized metal NPs larger than 2 nm. Ultimately, NanoModeler CG facilitates access to the computational modeling of (large) monolayer-protected metal NPs, thus aiding their knowledge-based design.



## **CHAPTER VII.      DISPERSION STATE PHASE DIAGRAM OF CITRATE-COATED METAL NANOPARTICLES IN SALINE SOLUTIONS**

### **Abstract**

The fundamental interactions underlying citrate-mediated chemical stability of metal nanoparticles (NPs), and their surface characteristics dictating particle dispersion/aggregation in aqueous solutions, are largely unclear. Here, we developed a theoretical model to estimate the stoichiometry of small, charged ligands (like citrate) chemisorbed onto spherical metal NPs and coupled it with atomistic molecular dynamics (MD) simulations to define the uncovered solvent-accessible surface area of the NPs. Then, we integrated coarse-grained MD simulations and two-body free energy calculations to define dispersion state phase diagrams for charged metal NPs in a range of medium's ionic strength, a known trigger for aggregation. Ultraviolet-visible spectroscopy experiments of citrate-capped nanocolloids validated our predictions and extended our results to NPs up to 35 nm long. Altogether, our results disclose a complex interplay between the particle size, its surface charge density, and the ionic strength of the medium, which ultimately clarifies how these variables impact colloidal stability.

## A. Introduction

Metal nanoparticles (NPs) with different composition, morphology, and surface chemistry can be used for applications like NP-mediated catalysis,<sup>99,138,421,422</sup> cancer therapy,<sup>46,423,424</sup> and chemosensing.<sup>57,95,425,426</sup> To ensure the solubility of pristine metal NPs in polar solvents, stabilizing agents like citrate and tetraoctylammonium bromide must be introduced into the mixture. This is exemplified by the Turkevich wet synthetic method, in which metal NPs are obtained via the reduction of metal-containing chlorine acids in the presence of sodium citrate.<sup>427</sup> Here, an excess of citrate anions acts as a stabilizing agent that jackets newly formed metallic nucleation sites and keeps them from crystal growth, agglomeration, and precipitation.<sup>428,429</sup> However, the chemisorption of citrate onto the assembled metallic surfaces critically depends on variables such as the particle size, the surface charge density, and the ionic strength of the medium in which the NPs are dispersed. These variables are crucial in modulating the physicochemical properties of the resulting NPs (e.g. chemical reactivity and surface plasmon resonance frequency).<sup>430</sup> Nonetheless, the interplay and relationships of these variables are poorly understood at the molecular level, especially in relation to the dispersion state, which is central when developing new NP-based technologies.<sup>431,432</sup>

So far, binding of citrate onto metals has been scrutinized for gold nanoparticles (AuNPs). Specifically, recent studies have shed light on the binding mode and energetics of citrate molecules onto different gold facets.<sup>433</sup> These studies used a wide range of complementary techniques, including density functional theory calculations,<sup>434</sup> scanning tunneling microscopy,<sup>435</sup> and X-ray photoelectron spectroscopy (XPS).<sup>436</sup> Furthermore, experimental investigations have examined the composition of citrate adlayers sitting over diverse gold surfaces.<sup>423,435–438</sup> For example, Lin et al.<sup>423,437,438</sup> reported a lower threshold of 0.8 bound citrate molecules per nm<sup>2</sup> on gold (111) surfaces, as determined by scanning probe microscopy. Similarly, Park et al.<sup>436</sup> estimated an average coverage of 1.7 citrate molecules per nm<sup>2</sup> on the same gold facets using infrared spectroscopy and XPS. Other studies have reported larger citrate surface coverages. For example, Rostek and co-workers<sup>127</sup> found a value of 3.1 molecules per nm<sup>2</sup> using elemental analysis of 17-nm-sized AuNPs, and Dominguez, G. A. and co-workers<sup>439</sup> found a value of 4.7 molecules per nm<sup>2</sup> using XPS on 5-nm-sized AuNPs. While highly informative, these studies did not resolve the relation between the surface citrate density and the charge of the coated surfaces. In particular, these results differ in regard to the equilibrium surface density of citrate on gold. This also leaves unresolved the fundamental



question of the effective charge of citrate-capped metal colloids and how this reflects into the NP dispersion state in solution.

Importantly, the dispersion state of metal NPs in saline solutions determines the interfacial area of the metallic surfaces, which in turns allows essential chemical processes for material science and pharmaceutical applications.<sup>440</sup> The dispersion of NPs has been extensively investigated with experimental and theoretical approaches. From an experimental standpoint, the colloidal stability is often associated with the experimentally measurable  $\zeta$ -potential, that is, the electrostatic potential at the shear plane of a charged body.<sup>441</sup> Nonetheless, the  $\zeta$ -potential is a descriptor that accounts only for the electrostatic interactions that NPs exert over one another, yet it disregards the equally important van der Waals forces.<sup>442</sup> From a theoretical standpoint, colloidal stability (i.e. the inter-particle interaction) is typically modeled by a Yukawa potential, in accordance with the Derjaguin-Landau-Verwey-Overbeek (DLVO) theory. This theory has proven useful in studying processes such as microbial adhesion,<sup>443</sup> polymer association,<sup>444</sup> and clay aggregation.<sup>445</sup> However, the DLVO theory lacks an atomistic description of the electrical double layer at the surface of NPs, which precludes the examination of the molecular properties of the mobile electrolytes dissolved in the solvent, and eventually aggregating onto the NP.<sup>446,447</sup>

Here, we investigate the interplay between NP charge and size, and the ionic strength of the electrolytic medium, in relation to the stability of citrate-capped metal colloids. For this purpose, we first develop a new theoretical framework that determines the surface coverage of charged ligands onto spherical NPs. This model is used to determine the number of citrate molecules bound to AuNPs. In parallel, we generate models for enhanced sampling molecular dynamics (MD) simulations. Free energy calculations, together with ultraviolet-visible (UV-Vis) spectroscopy experiments, allowed us to rationalize charged-NP dispersion and aggregation in terms of simpler two-body interactions and dissect the driving forces leading to these distinct states. In the end, we combine the results from our theoretical model with our general phase diagrams to describe, at the molecular level, the dispersion state of citrate-capped gold nanocolloids, a system of paramount importance in nanotechnology.

## B. Results

### 1. Stoichiometry of citrate chemisorbed onto metal nanoparticles

The surface coverage of citrate onto AuNPs fluctuates across the current literature, with experimental values ranging from 0.8<sup>437</sup> to 4.7<sup>439</sup> molecules per nm<sup>2</sup> and computational estimates ranging from 0.4<sup>448</sup> to 2.0<sup>449</sup> molecules per nm<sup>2</sup>. Thus, as a first step, we developed a theoretical model to estimate the exact stoichiometry ratio and distribution of the charged ligands forming the protecting adlayer in metal NPs. Moreover, this approach provided a framework consistent with the models for charged NPs that we would use in the rest of the study.

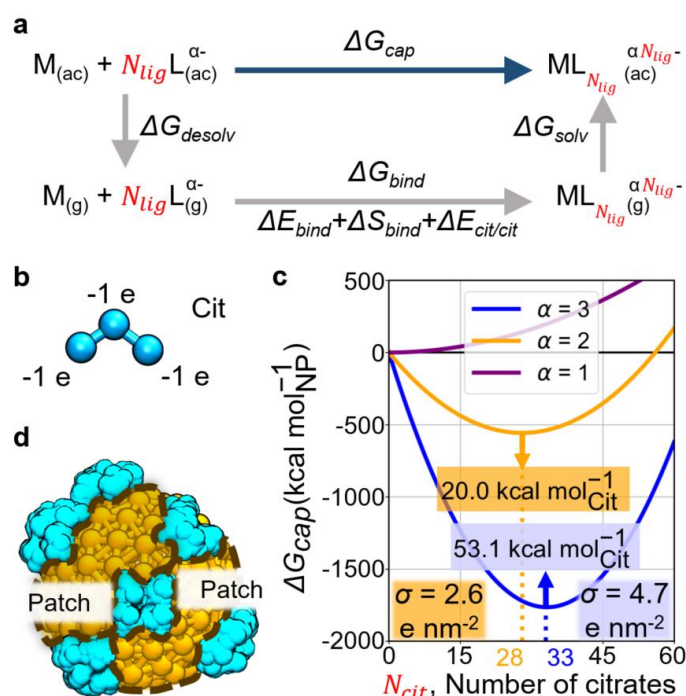


**Figure 39.** Theoretical model for calculating the number of charged ligands bound to a spherical NP. **a.** Thermodynamic cycle on which the proposed theoretical model is based.  $\Delta G_{cap}$  is obtained in this thermodynamic cycle as  $\Delta G_{desolv} + \Delta G_{bind} + \Delta G_{solv}$ , where  $\Delta G_{desolv}$  is the desolvation energy of the NP core ( $M$ ) and  $N_{lig}$  ligand molecules ( $L$ );  $\Delta G_{bind}$  is the energy for binding those ligands onto the NP in vacuum;  $\Delta G_{solv}$  is the solvation free energy of the resulting capped complex, in which the ligands are modeled as an enveloping uniformly charged sphere. **b.** Explicit CG model for citrate molecules (Cit), which was parametrized against atomistic MD simulations (Appendix D.1.6). **c.** Binding energy as a function of the number of bound citrate molecules  $N_{cit}$ . The model is solved for the three deprotonation states of citrate, i.e.  $\alpha = 1, 2, 3$ . The energy minima predict the most likely values for  $N_{cit}$  that, in turn, set the surface charge density ( $\sigma$ ) of the NP. **d.** Conceptual illustration of a citrate-capped (cyan) NP showing the presence of catalytically available hydrophobic patches (orange) as suggested by the estimated surface area coverage.

The theoretical model is based on the thermodynamic cycle shown **Figure 39a** (**Figure D-1** and Chapter VII-C), which computes the free energy of  $N_{lig}$  molecules binding to NPs in solution ( $\Delta G_{cap}$ ). Our model decomposes the binding in solution of  $N_{lig}$  ligands,  $\Delta G_{cap}$ , into three complementary processes that enclose the thermodynamic cycle, namely, (i) the desolvation of the spherical core and  $N_{lig}$  ligands  $\Delta G_{desolv}$ , (ii) the binding in vacuum of the ligands onto the core  $\Delta G_{bind}$ , and (iii) the solvation of the protected nanoparticle  $\Delta G_{solv}$ . Importantly, this framework models the protected NP as a spherical hydrophobic core with a homogeneous charge distribution that describes the electrostatic mean-field effect of the coating ligands. This approach further simplifies the calculation when separating the solvation energy,  $\Delta G_{solv}$ , into an apolar  $\Delta G_{solv}^{apolar}$  and a polar  $\Delta G_{solv}^{polar}$  component. In detail, the polar contribution is calculated with a mean-field formula derived from Newtonian mechanics, whereas the apolar component cancels out with the desolvation energy of the reacting core as contained in  $\Delta G_{desolv}$ . In this way, our theoretical model requires only two parameters, that is, the desolvation energy of the ligand (used to compute the rest of  $\Delta G_{desolv}$ ) and the binding energy of one ligand onto the metallic surface  $\Delta E_{bind}$  (**Figure 39a**). This formulation offers a general and transferable framework to calculate the surface density of small, charged ligands bound to spherical rigid cores.

We then used the developed model to determine the ligand density of citrate onto AuNPs. For this, we computed  $\Delta G_{cap}$  for spherical NPs of diameter 3.0 nm. The first input, the desolvation energy of one citrate molecule, was derived from computer simulations at a coarse-grained (CG) resolution (**Figure 39b**). Specifically, we developed an explicit CG model for citrate at its fully deprotonated form, that is, the most populated state at neutral pH. The explicit CG model for citrate was parametrized against atomistic simulations of citrate in water (Appendix D.1). Notably, the protonation state of ligands may change when these bind to the NPs surface.<sup>435</sup> The second input, the binding energy between citrate and gold surfaces, was taken from quantum mechanical calculations reported elsewhere.<sup>434</sup>

For polyprotic ligands like citrate, the total charge of the capped NP depends on the mean deprotonation state of the bound molecules ( $\alpha$ ). Thus, this model can account for single ( $\alpha = 1$ ), double ( $\alpha = 2$ ), or triple deprotonation ( $\alpha = 3$ ) of bound citrate molecules, with the latter two being the most populated states at a pH greater than 4,<sup>450</sup> a range favorable for metal NPs synthesis, extended colloid half-life, and biological assays.<sup>451–454</sup> In this way, the states  $\alpha = 2$  and  $\alpha = 3$  demarcate a range for the stoichiometric ratio of citrate, which thereby confines the

NP surface charge density ( $\sigma$ ). This is in line with experimental evidence on the varying charges of chemisorbed citrate molecules, which enable the formation of H-bond networks at the surface of gold facets.<sup>436</sup> Our model also grasps the pH dependence on the stability of NPs. Particularly, when  $\alpha = 1$ , the global minimum of  $\Delta G_{cap}$  disappears, indicating that the number of ligands that can bind to the NP is not enough to make it soluble in water (**Figure 39c**). This is in agreement with the experimentally observed agglomeration of AuNPs at pH  $\sim 4$ , conditions at which dihydrogen citrate becomes the dominating species.<sup>455</sup>

Using this approach, we found that the computed number of chemisorbed citrate molecules onto the NPs falls into an interval between  $N_{cit} = 28$  (1.31 molecules per nm<sup>2</sup>,  $\sigma = 2.6$  e nm<sup>-2</sup>) and  $N_{cit} = 33$  (1.55 molecules per nm<sup>2</sup>,  $\sigma = 4.7$  e nm<sup>-2</sup>), for the double and full deprotonation of citrate, respectively (**Figure 39c**). Given our estimate of citrate molecules chemisorbed onto the NP surface, the net charge of our NPs is expected to range from -56 ( $\sigma \sim 2.6$  e nm<sup>-2</sup>) to -99 e ( $\sigma \sim 4.7$  e nm<sup>-2</sup>, Chapter VII-C). Moreover, for each deprotonation state, we also obtained a different value for the binding affinity of citrate onto gold surfaces, which we find in the range of 20.0 ( $\alpha = 2$ ) and 53.1 ( $\alpha = 3$ ) kcal mol<sup>-1</sup>. This range comprises the estimate derived from density functional theory (DFT) simulations in vacuum, i.e. 40.9 kcal mol<sup>-1</sup>,<sup>434</sup> supporting the validity of our theoretical framework. In fact, an interpolation of our data at  $\alpha = 2$  and  $\alpha = 3$  suggests that, to reach a binding affinity of 40.9 kcal mol<sup>-1</sup>, the mean deprotonation state is  $\alpha \sim 2.6$ , in qualitative agreement with XPS experiments.<sup>435</sup>

Importantly, our computed range lies within the boundary values of the experimental measurements of  $N_{cit} \sim 17$  (0.8 molecules per nm<sup>2</sup>) from Lin et al.<sup>423,437,438</sup> and  $N_{cit} \sim 100$  (4.7 molecules per nm<sup>2</sup>) from Dominguez et al.,<sup>439</sup> which were based on scanning tunneling microscopy and XPS, respectively.<sup>456</sup> In particular, our computed values also match very well the estimate of  $N_{cit} \sim 33$  (1.55 molecules per nm<sup>2</sup>) from Park and co-workers<sup>436</sup>, calculated by means of infrared and XPS. In addition, Chong and co-workers<sup>449</sup> performed atomistic MD simulations on citrate molecules explicitly interacting with gold surfaces, predicting  $N_{cit} \sim 42$  (1.98 molecules per nm<sup>2</sup>), which is also in good agreement with our calculations. Notably, these results agree in spite of additional factors that may affect the binding affinity of citrate for the NPs, including i) the curvature of the metallic surfaces; ii) the ratio between metal (gold) atoms embedded in the bulk, surfaces, and edges; iii) the steric hindrance between citrate molecules, and iv) the different proportions of lattice planes.

Our approach also captures the interactions between neighboring citrate molecules and their effect on the polarity of the resulting coated NP. As the citrate molecules become more strongly charged ( $\alpha$  increases), the electrostatic repulsion exerted between vicinal ligands encumbers binding onto the NP. In fact, the repulsive energy between ligands  $\Delta E_{lig/lig}$  scales as  $\sim N_{lig}^2$ , according to our model (**Figure D-1**, **Figure D-2**, and Appendix D.1). In contrast, strongly charged citrate molecules increase the (negative) net charge of the coated NP, thus favoring its dispersion in highly polar solvents like water. This follows from the quadratic relation between the energy from transferring a coated NP between media  $\Delta G_{solv}^{polar}$  and the number of bound citrate molecules  $N_{cit}$  (**Figure D-1**, **Figure D-2**, and Appendix D.1).

Another important aspect is the extent to which the binding of citrate onto NPs hinders specific regions of the metallic surface from contacting the solvent. Thus, based on the shape and radius of our NP ( $R_{NP}$ ), we first estimated the total surface area of the NP as  $4\pi R_{NP}^2$ . Then, the expected area occupied by a single superficial ligand was computed via atomistic MD simulations of citrate in water (Appendix D.2). We computed the projected area of the van der Waals surface for an individual citrate molecule onto an arbitrary plane. Notably, this calculation is made invariant with respect to the chosen plane, as various orientations are sampled for each MD-generated conformer. We considered 100 orientations for each of the 1,000 MD-generated conformers and traced the area's probability density (**Figure D-3**) and the area per citrate of maximum probability ( $0.16 \text{ nm}^2$ ). In this way, the computed area per citrate, together with the calculated interval of  $28 < N_{cit} < 33$ , returns an estimated surface coverage by citrate molecules in the range between 22.5 and 26.5% for 3.0 nm NPs (**Figure 39d**). This range is in good agreement with the lower limit of 35% citrate surface coverage, experimentally estimated for 40 nm AuNPs.<sup>436,455</sup> This means that ca. 70-80% of the surface area of such soluble citrate-coated NPs remains in direct contact with the solvent, fully available, for example, for surface catalysis.<sup>22,51,53,457</sup>

## 2. *Effect of ionic strength and nanoparticle charge on the $\zeta$ -potential*

To study the aggregation state of citrate-capped NPs, we initially examined the effect of the surface charge density ( $\sigma$ ) of the NPs and the ionic strength of the medium ( $I$ ) on the  $\zeta$ -potential of nanospheres of 3.0 nm in size. For this task, we employed implicit-ligand models of coated NPs (**Figure 40a**). In the implemented model, selected surface beads were assigned a charge of  $-2 e$  to mimic the presence of monohydrogencitrate. The charge per bead chosen thus

describes citrate molecules at their most abundant ionization state on capped AuNPs,<sup>435</sup> but it extends to hard anionic species like cyclic oxocarbons and dicarboxylic acids. Implicit-citrate models have gained increasing attention in recent years as they reduce the phase space's dimensionality, while offering a reliable representation of systems otherwise too intricate to simulate. These models rely on the covalent character of the gold-citrate interaction. DFT calculations have quantified a binding affinity of 40.9 kcal mol<sup>-1</sup>.<sup>434</sup> In contrast to chelation and multipolar interactions, the complexation of citrate onto gold surfaces implies the formation of stiff chemical bonds that damps ion competition and ion pairing. Recent XPS experiments have also ratified a weak-coupling between bound citrate molecules and sodium counterions present in electrolytic solutions.<sup>435</sup> Implicit-citrate models have already accomplished semi-quantitative agreement when studying processes like membrane rupture,<sup>131</sup> protein adsorption,<sup>458,459</sup> NP-induced protein denaturation,<sup>438</sup> and synchronized NP internalization.<sup>66</sup>

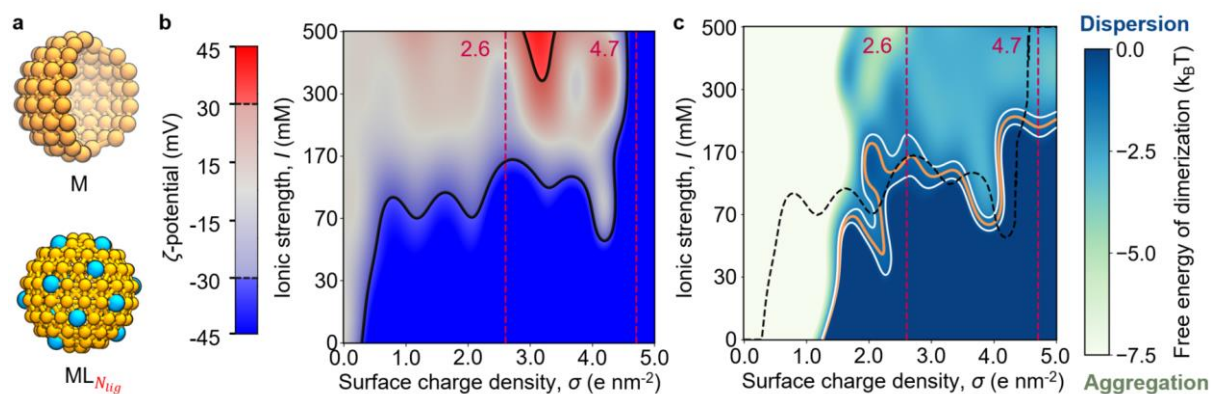


**Figure 40.** Dispersion state phase diagrams of ion-capped metal NPs. **a.** CG models of naked (*M*, top panel, orange) and capped ( $ML_{Nlig}$ , bottom panel) NPs for the construction of the phase diagrams. The cyan beads implicitly account for grafted ligands with a charge of  $-2 e$ . **b.** The relation between the NP surface charge density  $\sigma$ , the environment ionic strength (*I*), and the computed  $\zeta$ -potential. The black contour demarcates the region where the  $\zeta$ -potential lies between  $-30$  mV and  $+30$  mV. The opaque blue and red regions indicate the conditions where the  $\zeta$ -potential computations suggest colloidal stability. **c.** Map of the NPs free energy of dimerization for the various studied systems. The orange and white curves outline the region where the free energy is  $-1.0 \pm 0.5 k_B T$ . The black contour drawn for the  $\zeta$ -potential is superimposed onto this plot. The dark blue and light green indicate the conditions at which the free energy calculations suggest colloidal stability and aggregation, respectively. The dashed red lines indicate the limiting values of  $\sigma$  for citrate-capped NPs as determined by the developed theoretical model.

By means of CG MD simulations, we estimated the  $\zeta$ -potential of the NPs for all possible combinations of  $\sigma$  and *I*, following a protocol introduced elsewhere and described in detail in the Chapter VII-C.<sup>323,460</sup> The  $\zeta$ -potential of all the systems is mapped into a bidimensional plot

displayed in **Figure 40b**. The computed value for the  $\zeta$ -potential ranges between ca. -150 and +40 mV. The shaded region in **Figure 40b** encloses the values for  $\sigma$  and  $I$  at which the  $\zeta$ -potential of the NPs lies between -30 and +30 mV, a minimum requirement for colloidal stability.<sup>461</sup> Thus, the black contour delimits values of the surface charge  $\sigma$  and salt concentration  $I$  that separate colloidal stability vs. instability, with the latter reflecting aggregation in experiments. Notably, the  $\zeta$ -potential is computed as the radial electrostatic potential in the position of the shear plane (Chapter VII-C). The fast decay of the electrostatic potential (described by a Yukawa potential in Debye-Hückel's theory) produces a sensible response between the position of the shear plane and the  $\zeta$ -potential, which results in a wider range of admissible values of  $\zeta$ -potential than those that are experimentally relevant.<sup>441,442</sup>

In detail, when the net charge of the NP is less than -13 e in magnitude ( $\sigma < 0.6 \text{ e nm}^{-2}$ ), the dispersion state of the NPs shows a linear correlation between the critical ionic strength  $I$  and  $\sigma$  (**Figure 40b**). Then, the critical value of  $I$  stays in a plateau at ca. 70 mM for intermediate charges limited by -13 and -87 e (i.e.  $0.6 < \sigma < 4.1 \text{ e nm}^{-2}$ ). In this interval, as expected, we observed an increased attraction of sodium counterions toward the NP, as  $\sigma$  increases. However, we also found that the magnitude of the attraction is such that the increased charge of the NP is quickly screened out by the first adlayer of sodium counterions, which are located within the hydrodynamic radius (i.e. the Stern layer). This means that the measured  $\zeta$ -potential of these NPs is similar to that of a less charged NP at  $I = 0$  ( $\sigma < 0.6 \text{ e nm}^{-2}$ ), a situation in which NPs tend to aggregate more easily. This explains the plateau in the dispersion state phase diagram in **Figure 40b**. Finally, for NPs with charges greater than -87 e ( $\sigma > 4.1 \text{ e nm}^{-2}$ ), the system also acquires very high (absolute) values of  $\zeta$ -potentials (ca. -100 mV). In these conditions, the sodium ions are no longer able to fully neutralize the NP charge. This drastic increase in  $\zeta$ -potential leads to high NP stability, which is also favored by the reduced capacity of the sodium ions in solution to counterbalance the very high charge of the metallic surface. This may be explained by the entropic cost of bringing additional (sufficient) sodium ions onto the highly charged metallic surface (sterically hindered at this point because of sodium saturation).

Based on our results, the electrostatic interactions between a charged NP and an electrolytic solvent fall within one of the regimes described above, according to the net charge of the sphere. These regimes can be classified as i) depolarized ( $\sigma < 0.6 \text{ e nm}^{-2}$ ), where the thermal motion of the sodium counterions overcomes the electrostatic attraction toward the NP,

ii) mildly polarized ( $0.6 < \sigma < 4.1 \text{ e nm}^{-2}$ ), in which the Coulomb forces attract enough ions into the Stern layer to screen out the charge load of the NP, and iii) hyperpolarized ( $\sigma > 4.1 \text{ e nm}^{-2}$ ), the situation at which the counterions' steric and electrostatic hindrance, as well as their loss of translational degrees of freedom, limit their binding onto the NP.

### 3. Role of inter-particle interactions for nanoparticle dimerization

The  $\zeta$ -potential of NPs is a measure of the charge density at the electrophoretic radius of charged bodies, and it is often associated with the stability of colloids. However, this measure does not account for van der Waals forces.<sup>442</sup> Thus, to fully account for inter-particle interactions in colloidal coalescence/aggregation processes, we calculated the free energy of dimerization for our 3.0 nm NPs. We considered all the surface charge densities  $\sigma$  and salt concentrations  $I$  discussed above and listed in the Chapter VII-C. Moreover, to describe the dimerization process, we defined a collective variable,  $CVI$ , as the minimum distance between the van der Waals surfaces of two interacting NPs. By computing the free energy along  $CVI$  for the dimerization process for all the explored  $\sigma$  and  $I$ , we obtained a dispersion state phase diagram.

Based on the assumption that NP dimerization initiates aggregation, we thus used the region where the free energy is  $-1.0 \pm 0.5 \text{ k}_B\text{T}$  (i.e. the minimal free energy for dimerization) to limit the conditions of colloidal (in)stability for metal suspensions (**Figure 40c**). In this way, this region demarcates the conditions at which the systems have a 37% ( $e^{-1}$ ) chance of being dispersed, namely when the thermal motion along  $CVI$  is enough for the NPs to escape the energy well associated with dimerization. Interestingly, this region matches well with the region characterized by a  $\zeta$ -potential of  $\pm 30 \text{ mV}$ , as outlined in **Figure 40b**, confirming that electrostatics is a key player for colloidal stability.

**Figure 40c** suggests that low surface charge densities ( $\sigma < 1.2 \text{ e nm}^{-2}$ ) always lead to an aggregated state. A regime with a similar behavior was derived from our  $\zeta$ -potential calculations ( $\sigma < 0.6 \text{ e nm}^{-2}$ ). It is interesting to note that the threshold is shifted toward higher values of  $\sigma$  when the interactions between NPs are considered explicitly. Arguably, this may be due to the large hydrophobic matching between the metallic cores that leans the system toward aggregation. Then, for surface charge densities in the interval of  $1.2 < \sigma < 4.2 \text{ e nm}^{-2}$ , our free energy calculations suggest that the system remains stably dispersed under salt concentrations of ca. 70 mM. Again, this agrees with the  $\zeta$ -potential calculations. Similarly, in



line with the  $\zeta$ -potential plot, the free energies of dimerization indicate a change in behavior when  $\sigma > 4.2 \text{ e nm}^{-2}$ . At these  $\sigma$  values, the  $\zeta$ -potential plot suggests that NPs become more resistant to aggregation. Nonetheless, our free energy calculations allow highly charged NPs to aggregate at  $I \sim 170 \text{ mM}$ . Remarkably, over the entire range of  $\sigma$ , the  $I$  for inducing aggregation increases irregularly with  $\sigma$ , denoting a non-trivial relationship between the critical ion concentration of the solution and the dispersion state of the NPs.

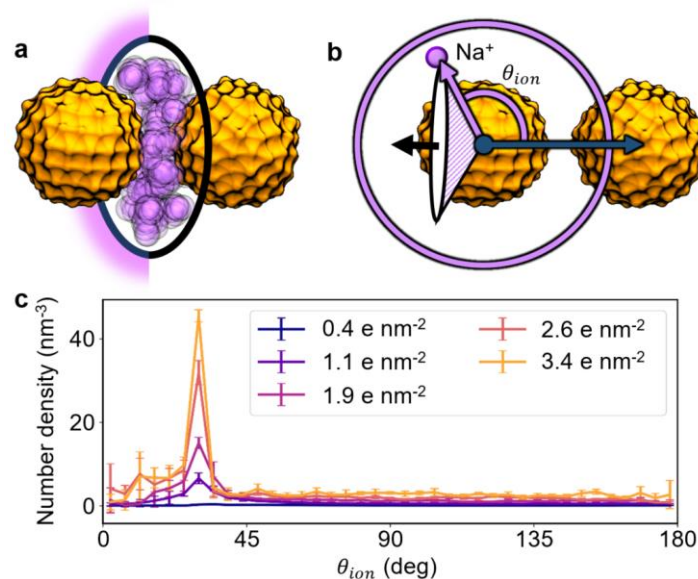


**Figure 41.** Counterion distribution upon NP dimerization. **a.** Halo-like cloud of counterions (purple) accumulated at the edge of the two NPs contacting region. Superposition of various frames of the simulations. NPs are colored orange. **b.** The angle  $\theta_{ion}$  is formed between the direction connecting the two NPs ( $CVI$ ) and the position vector from one NPs COM to a sodium ion. Each value of  $\theta_{ion}$  defines a conic volume around the reference NP. **c.** The number density of ions as a function of the polar angle  $\theta_{ion}$ . The height of the peak found at  $32^\circ$  increases with the surface charge density of the NPs. Error bars indicate the standard deviation calculated over trajectory frames.

NP aggregation can be induced by increasing the salt concentration of the medium,  $I$ , in otherwise dispersed systems, as largely reported in experiments<sup>462–464</sup> and also confirmed in our simulations. In this regard, we found that alterations in the aggregation state of the NPs arise mostly from the screening of the NP charge by the sodium counterions in solution. These ions can rest at the interface of the metallic bodies and form salt bridges that stabilize the NP-NP dimer. Our simulations indicate that, as  $\sigma$  increases, a halo-like cloud of accumulated counterions is more clearly formed near the contact site of the two approaching NPs (**Figure 41a**). To further corroborate this observation, we computed the number density of sodium ions, up to  $2.0 \text{ nm}$  away from the NPs, with respect to the angle defined by  $CVI$  (**Figure 41b**). Notably, this way of analyzing the motion of the counterions in solution provides an explicit

and atomically detailed description of the ion anisotropic placement around the NP dimer. For example, when two NPs of net charge  $-40 e$  ( $\sigma = 1.9 e \text{ nm}^{-2}$ ) reach each other in a solution of ionic strength  $I = 30 \text{ mM}$ , the angular number density of sodium ions near their contact region increases to up to  $15.0 \text{ nm}^{-3}$ , as compared to the  $1.1 \text{ nm}^{-3}$  measured in the opposite end of the contacting axis (**Figure 41c**). Similar trends are observed for different salt concentrations. Also, this analysis overcomes limitations of the mean field-founded DLVO theory at short inter-NP distances.<sup>364</sup>

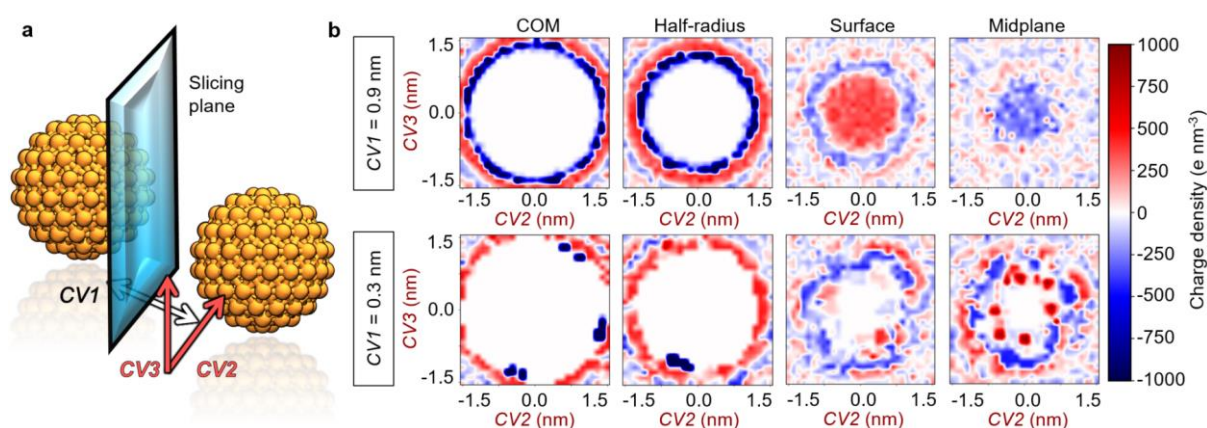


**Figure 42.** Transversal charge density as a function of the distance between the NPs. **a.** Graphical definition of the collective variables of interest.  $CV1$  is the minimum distance between the two NP surfaces (orange).  $CV2$  and  $CV3$  are two bases perpendicular to  $CV1$  chosen arbitrarily. The position of the slicing plane indicates the cuts on which the systems' charge density was estimated. **b.** The charge density of the overall systems averaged over time for various slicing planes at  $CV1 = 0.9 \text{ nm}$  (top panels) and  $CV1 = 0.3 \text{ nm}$  (bottom panels). The four studied planes lie at i) an NP's COM, ii) half-way along the radius of an NP, iii) at the van der Waals surface of an NP, and iv) at the midplane between the two NPs. All plots are derived from systems with NPs loaded with a net charge of  $-40 e$  ( $\sigma = 1.9 e \text{ nm}^{-2}$ ) in an environment of ionic strength  $70 \text{ mM}$ .

It is important to note that in the Martini CG force field, the sodium and chloride ions' beads comprise the first solvation shell of the species. As such, these models offer a qualitative description of the ions' mobility around the charged NPs, rather than structural insights on their binding mode. Nonetheless, we performed supplementary atomistic MD simulations of  $3.0 \text{ nm}$  citrate-capped AuNPs to corroborate the results from our CG simulations. In these simulations, we computed the time for which sodium counterions remained in the vicinity of the capped NPs. Indeed, in both our CG and atomistic simulations, longer residence times for sodium counterions were found as the surface charge of the NP increased (**Figure D-5**).

In addition, we investigated the merging of the electrical double layers formed around the NPs upon dimerization. This chemical event was described by simulations at different values of *CVI* (**Figure 42a**). Each of our simulations restrained the system with an additional harmonic potential centered at a specific value of *CVI*, ranging between 0.0 and 3.0 nm. During these simulations, we monitored the charge density of the overall system and analyzed it for fixed planes perpendicular to *CVI*.

In total, we focused on four different planes located at: i) the center of mass (COM) of one of the NPs, ii) half-radius away from an NP's COM, iii) an NP's van der Waals surface, and iv) the midplane between the two NPs. Specifically, **Figure 42b** shows the sliced planes from simulations of NPs with a charge of  $-40 e$  ( $\sigma = 1.9 e \text{ nm}^{-2}$ ) in an environment of ionic strength  $I = 70 \text{ mM}$ . Initially, these simulations describe the states in which  $CVI = 0.9 \text{ nm}$  (intermediate distance, **Figure 42b** top panels), revealing halos of alternating charge density sign around the NPs. These halos indicate the presence of a nearly unperturbed electrical double layer. This means that, at  $CVI = 0.9 \text{ nm}$ , the ion clouds are mildly affected by the presence of the NPs, yet the layers can be outlined (**Figure 42b** top panels), with the lamellar nature of the electrical double layers preserved. As expected, at this value of *CVI*, the charge of the ligand-representing beads is distributed in a nearly circular shape (**Figure 42b** top left corner) due to the free rotation of the NPs around their COM during the simulations.

In contrast, at  $CVI = 0.3 \text{ nm}$ , the sodium counterions bind to specific sites at the surface of the NPs, generating a few regions of high positive charge density at the dimer's interface (**Figure 42b** bottom right corner). This result reflects the decreased diffusivity of the sodium ions close to the NPs in solution. Also, the negatively charged beads in the metallic bodies (i.e. the ligand beads) appear in discrete locations, which suggests a restricted exploration of the rotation of the two NPs around their respective COM (**Figure 42b** bottom panels, **Figure D-4**, and Appendix D.3). That is, the free rotation of the two NPs is sensibly diminished compared to that of the two NPs at longer *CVI* values. Thus, these results illustrate how the electrical double layers change during dimerization, assisting the strategic accommodation of sodium counterions and the formation of salt bridges for optimal dimer stabilization.

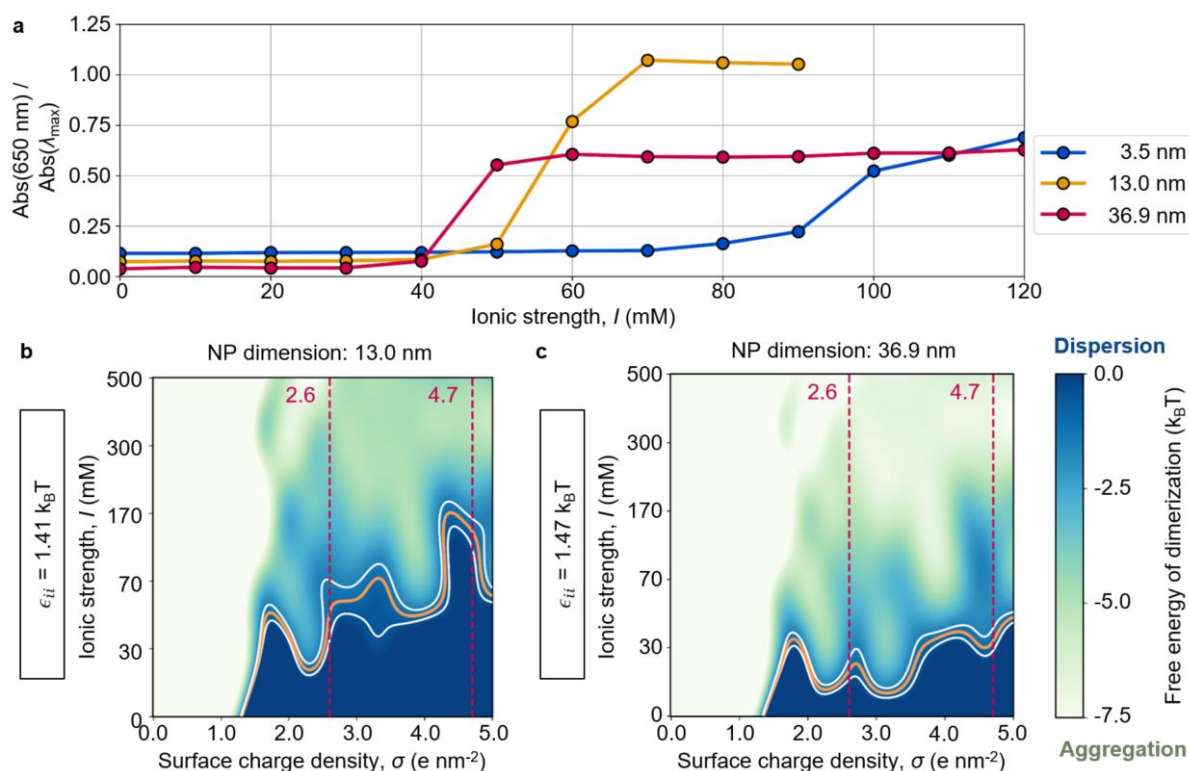


**Figure 43.** UV-Vis experiments and colloidal stability at different NP sizes. **a.** Experimentally measured absorbance of 3.5, 13.0, and 36.9 nm citrate-capped AuNPs at 650 nm relative to the maximum absorbance. The lower plots show the dispersion state phase diagram for citrate-capped NPs with varying hydrophobicity. The free energy of dimerization was calculated for our model NPs, modifying the well depth of the van der Waals interaction between metal beads. The profiles obtained using  $\epsilon_{ii} = 1.41$  (**b**) and  $1.47$  k<sub>B</sub>T (**c**) are in good agreement with experimental data for 13.0 and 36.9 nm, respectively. The orange and white curves outline the regions where the free energy is  $-1.0 \pm 0.5$  k<sub>B</sub>T. The dark blue and light green indicate the conditions at which the free energy calculations suggest colloidal stability and aggregation, respectively. The dashed red lines indicate the limiting values of  $\sigma$  for citrate-capped NPs, as determined by the developed theoretical model.

#### 4. Linking nanoparticle dimerization with colloidal stability

To demonstrate that the multi-body process of NP agglomeration can be rationalized in terms of NP dimerization, we synthesized 3.5, 13.0, and 36.9 nm citrate-capped AuNPs, and we experimentally determined their dispersion state at various salt concentrations. In detail, we tracked the plasmon absorption bands of the synthesized NPs as a function of increasing concentrations of sodium chloride,  $I$  (in the 0-120 mM range), and assessed particle aggregation through the aggregates to monomer bands ratio (i.e. absorbance at 650 nm divided by the maximum absorbance). In all cases, increasing the salt concentration beyond a critical threshold led to aggregation, as indicated by a step-like shift in absorbance (**Figure 43a** and **Figure D-6**). Importantly, the 3.5 nm AuNPs aggregated at a salt concentration of ca. 90 mM,

which is in close agreement with our computed phase diagrams. The 13.0 and 36.9 nm colloids aggregated at lower ionic strengths, ca. 60 and 50 mM, respectively. Hence, as the AuNPs become larger, the critical ionic strength for aggregation decreases. This may be explained by the increase in the hydrophobicity of NPs at larger sizes. Due to the stronger attractive van der Waals term, the NPs would thus require fewer salt bridges (lower values of  $I$ ) to stabilize the agglomerate.

To test this hypothesis about the effect of increased hydrophobicity of NPs with larger sizes, and to evaluate the energetics associated with aggregation upon NP size enlargement, we performed additional simulations, modulating the forces mutually exerted by the nanosized spheres. Due to the apolar nature of the gold-gold bonds and the homogeneity of the electron cloud of the metallic bulk, the interaction between a NP and its surroundings are accounted for with a Lennard-Jones potential that models dispersive van der Waals forces. Hence, the van der Waals radius and well depth ( $\epsilon_{ii}$ ) dictate the affinity between the NPs and their surroundings, i.e. through their hydrophobic interaction. Specifically, the metal-to-metal Lennard-Jones term was modified from its original value of  $\epsilon_{ii} = 1.35$  k<sub>B</sub>T to more attractive potentials, which are contemplated in the standard Martini force field ( $\epsilon_{ii} = 1.75$  k<sub>B</sub>T and  $\epsilon_{ii} = 2.10$  k<sub>B</sub>T). Computing the free energy along *CVI* for NPs with these hydrophobicities, we verified the known linear correlation between the free energy of dimerization and  $\epsilon_{ii}$  (coefficient of determination 0.99, **Figure D-7**). From this regression, we concluded that, for  $\epsilon_{ii} = 1.41$  and  $1.47$  k<sub>B</sub>T, the free energy of dimerization decreased by ca. 1.0 and 2.0 k<sub>B</sub>T, respectively.

Using these new models of larger (more hydrophobic) NPs, we computed the corresponding dispersion state phase diagrams (**Figure 43b** and **Figure 43c**) consistently with those in the previous cases, reported above. Notably, the increased size also influences the curvature of the NP surface, a parameter whose effect on NP aggregation cannot be excluded. Decreasing  $\sigma$ , or increasing  $I$ , leads to values at which the thermal energy cannot prevent aggregation. Moreover, as the hydrophobicity of the NPs becomes stronger (higher values of  $\epsilon_{ii}$ ), fewer sodium counterions are needed to bridge the charged surfaces. Consequently, the critical ionic strength  $I$  to induce dimerization is shifted toward lower values. In detail, when  $\epsilon_{ii} = 1.41$  k<sub>B</sub>T, the critical  $I$  lies at ca. 60 mM, whereas for  $\epsilon_{ii} = 1.47$  k<sub>B</sub>T the threshold is further reduced to ca. 30 mM. This agrees with our experimental measurements, as the computed data indicate that, as citrate-capped NPs grow in size, the NP charge needs to be screened out to a lesser

extent in order to induce ion-mediated aggregation. These results show that the ion-assisted interactions that govern the dimerization of our modeled 3.0 nm NPs are also valid for larger systems. Hence, these results provide a framework for dispersion state phase diagrams for citrate-capped NPs of varying sizes.

In summary, we examined the aqueous stability of citrate-capped metal NPs using both computation and experiments. First, a new theoretical model was implemented to determine the citrate coverage and surface charge density of metal NPs. The computed citrate density was found to be in excellent alignment with experimental data, and it allowed us to characterize the surface properties of citrate-capped AuNPs, specifically the charge density and surface coverage. The calculation of the particles' charge density later enabled us to make predictions on their dispersion state based on their  $\zeta$ -potential and free energy of dimerization. In parallel, by studying NPs with different surface charge values in saline solutions of various ionic strengths, we unraveled the driving forces that lead to nanocolloid aggregation. Our  $\zeta$ -potential calculations indicated that the critical ionic strength for inducing NP aggregation varies non-linearly with the surface charge density of the spherical NPs. Consequently, depending on the surface charge density, the interaction pattern between the capped NPs and an electrolytic medium may be categorized as depolarized, mildly polarized, or hyperpolarized.

To fully account for dispersion forces between multiple NPs during coalescence, we also estimated the free energy of NP dimerization using CG MD simulations. The dispersion state phase diagram derived from these calculations is in good agreement with our  $\zeta$ -potential map, further supporting the critical role of electrostatics in NP aggregation. Moreover, our analyses of the sodium counterions motion in solution unveiled the formation of halo-like structures of sodium, which promotes ion-assisted NP dimerization through salt bridges. Finally, UV-Vis absorbance experiments validated our free-energy-based dispersion state phase diagram and allowed us to extend our observations to NPs of up to 35 nm in size. In this regard, our results indicate that, as the NP hydrophobicity increases, the concentration of ions required to induce aggregation is reduced.

Altogether, our results are a step toward rationalizing the complex relationship between the particle size, the surface charge density, and the ionic strength of the medium, offering new fundamental insights into the mechanism by which these variables modulate colloidal stability.

## C. Methods

### 1. Development of the theoretical model

The free energy required to cap with ligands a metal NP,  $\Delta G_{cap}(N_{lig})$ , was partitioned into three different components according to the thermodynamic cycle exhibited in **Figure 39a**. In this figure, the horizontal processes point to the complexation of the ligand onto an NP, whereas the vertical ones point to the (de)solvation of the various parties. Thus, by minimizing the change of free energy  $\Delta G_{cap}$  we recover the value of  $N_{lig}$  of the highest likelihood. The first contribution,  $\Delta G_{desolv}$ , can be expressed in terms of the desolvation energy of the metal NP ( $\Delta G_{desolv}^M$ ) and that of the ligand ( $\Delta G_{desolv}^{lig}$ ), as shown in Equation 85 (**Figure D-1a**). The first of these terms cancels out with the apolar contribution of  $\Delta G_{solv}$ , and the second was calculated by means of CG MD through the thermodynamic integration approach (Appendix D.1.1).

$$\Delta G_{desolv}(N_{lig}) = \Delta G_{desolv}^M + N_{lig}\Delta G_{desolv}^{lig} \quad (85)$$

The second contribution,  $\Delta G_{bind}$ , corresponds to the binding of  $N_{lig}$  molecules onto the metal NP (**Figure D-1b**). This contribution comprises three terms: i) the electronic binding energy of the ligand onto the metal (gold) surface ( $\Delta E_{bind}$ ) obtained from DFT discussed elsewhere<sup>434</sup>, ii) the entropy of binding ( $\Delta S_{bind}$ ) estimated from the classical theory of ideal gases (found to be negligible), and iii) a correction to account for the repulsion between multiple chemisorbed ligands ( $\Delta E_{lig/lig}$ ) derived from the classical definition of electrostatic potential energy. The generic form of  $\Delta G_{bind}$  is shown in Equation 86 and discussed in detail in Appendix D.1.2 and Appendix D.1.3.

$$\Delta G_{bind}(N_{lig}) = N_{lig}(\Delta E_{bind} - T\Delta S_{bind}) + \Delta E_{lig/lig}(N_{lig}) \quad (86)$$

The last term in the thermodynamic cycle,  $\Delta G_{solv}$  (Equation 87), accounts for the solvation of the capped complex, and it was divided into an apolar and a polar term (**Figure D-1c**). The apolar term cancels out with  $\Delta G_{desolv}^M$ , whereas the polar component arises from the classical interpretation of electrostatic potential energy (Appendix D.1.4).

$$\Delta G_{solv}(N_{lig}) = \Delta G_{solv}^{apolar} + \Delta G_{solv}^{polar} \quad (87)$$

By solving this model for the double ( $\alpha = 2$ ) and full deprotonation ( $\alpha = 3$ ) of citrate, we showed that the limiting values for the number of citrate molecules chemisorbed onto our 3.0 nm NPs were  $N_{cit} = 28$  and  $N_{cit} = 33$ . These values, in turn, fix a charge range for these NPs between -56 and -99 e. The lower value -56 e is equal to -2 e per citrate molecule, multiplied by  $N_{cit} = 28$  citrates, i.e.  $\sigma = 2.6 \text{ e nm}^{-2}$ . The upper value -99 e is equal to -3 e per citrate molecule multiplied by  $N_{cit} = 33$  citrates, i.e.  $\sigma = 4.7 \text{ e nm}^{-2}$ .

## 2. Nanoparticle modeling and $\zeta$ -potential calculations

For our CG MD simulations, we modeled metal NPs as hollow spheres made from 126 beads arranged as stacked rings.<sup>359,465,466</sup> The size of the NPs was measured at the van der Waals surface of the resulting structure (3.0 nm). The beads were assigned the type C1, as implemented in the Martini-v2.2P force field, and a mass of 556 u.m.a. to account for the bulk internal beads. The spherical shape of the NPs was retained by imposing an elastic network with a force constant of  $15,000 \text{ kJ mol}^{-1} \text{ nm}^{-2}$ . The elastic network united each bead with its six nearest neighbors as well as its farthest neighbor. In the case of ion-capped NPs, beads were randomly chosen and assigned a partial charge of -2 e until the target net charge was reached. Here, we explored 14 values for the surface charge density  $\sigma$ , equidistantly sampled in a range between 0.0 and  $5.0 \text{ e nm}^{-2}$ .

To determine the  $\zeta$ -potential of our modeled NPs, we performed CG MD simulations of our NPs in saline solutions. One capped NP was initially placed in a simulation box, leaving a minimum distance to the faces of 3.5 nm. The box was then immersed in water using the refPol force field.<sup>213,215</sup> Additional polarizable sodium and chloride ions<sup>215</sup> were included to reach ionic strengths of 0, 30, 70, 170, 300, and 500 mM. A minimization was carried out using the steepest descent method to relax the solvent around the particles. The systems were then thermalized to 310 K and pressurized to 1 bar in the span of 1 ns in the NPT ensemble. For this, the velocity-rescale (v-rescale) thermostat ( $\tau_B = 2.0 \text{ ps}$ ) and the isotropic Berendsen barostat ( $\tau_P = 5.0 \text{ ps}$ ,  $\kappa = 4.5 \times 10^{-4} \text{ bar}^{-1}$ ) were activated, and an integration timestep of 2 fs was used. For the 100-ns-long production runs, we increased the integration timestep to 20 fs and implemented the Parrinello-Rahman barostat ( $\tau_P = 14.0 \text{ ps}$ ,  $\kappa = 4.5 \times 10^{-4} \text{ bar}^{-1}$ ).<sup>227</sup> All bonds were constrained with the linear constraints solver algorithm.<sup>319</sup> Short-range nonbonded interactions were calculated within a radius of 1.2 nm from each bead, whereas long-range electrostatic interactions were considered using the fourth-ordered particle-mesh Ewald method.<sup>231</sup> All simulations were conducted with Gromacs-v2019.2.<sup>321</sup>



To calculate the shear plane, we adopted a methodology similar to the one used by Heikkilä et al.<sup>460</sup> The shear plane, the radial position at which the distribution of the sodium counterions starts deviating from Debye-Hückel's description, was derived from the simulations at  $I = 0$ . We calculated the RDF of the sodium ions with respect to the NPs COM. Then, the function  $\gamma_0 e^{-\gamma_1 r}/r + \gamma_2$  was fitted to the RDF curves. The fitting was performed for the points at distances greater than  $r_i$ , where  $r_i$  assumed 20 equidistant values in the range between 1.9 and 3.0 nm. Thus, for each NP (i.e. different  $\sigma$  values), 20 fittings were performed. From each of the fittings, the shear plane was defined as the position in which the RDF deviated by at least 0.1 from its fitted curve. Consequently, for each value of  $\sigma$ , we obtained a distribution of positions (**Figure D-8**). The final shear plane was the median of these distributions. Finally, the reported  $\zeta$ -potentials correspond to the electrostatic potential (calculated by means of Gauss' law) at the NPs corresponding shear plane.

### 3. Free energy calculations

To calculate the free energy of NP dimerization, we performed potential of mean force (PMF) calculations. Two capped NPs were initially placed with their COM 6.0 nm away from each other ( $CVI = 3.0$  nm, **Figure D-9**). Then, the systems were solvated, ionized, and minimized as in the  $\zeta$ -potential calculations. The systems were then thermalized to 310 K and pressurized to 1 bar in the span of 1 ns in the NPT ensemble. For this, the v-rescale thermostat ( $\tau_B = 2.0$  ps) and the isotropic Berendsen barostat ( $\tau_P = 5.0$  ps,  $\kappa = 4.5 \times 10^{-4}$  bar<sup>-1</sup>) were activated, and an integration timestep of 2 fs was used. This was followed by a second equilibration under the same conditions, increasing the timestep to 10 fs for 5 ns. Once the systems had reached the intended temperature and pressure, the Berendsen barostat was replaced for its Parrinello-Rahman counterpart ( $\tau_P = 14.0$  ps,  $\kappa = 4.5 \times 10^{-4}$  bar<sup>-1</sup>).<sup>227</sup> The rest of the parameters were set as in the single-NP simulations discussed above.

To sample the dimerizing reaction coordinate, we performed steered MD simulations in which the two rigid bodies were dragged toward each other along  $CVI$  (the minimum distance between the NPs van der Waals surfaces). The equilibrium distance between the COM of the NPs was thus reduced at a rate of 0.125 nm ns<sup>-1</sup> with a force constant of 5,000 kJ mol<sup>-1</sup> nm<sup>-2</sup>. To estimate the free energy of aggregation, we used the umbrella sampling method. When the particles were far away from each other ( $CVI > 1.2$  nm), windows were extracted every 0.1 nm. The value of  $CVI$  was restrained with a harmonic force constant of 5,000 kJ mol<sup>-1</sup> nm<sup>-2</sup>.<sup>240</sup> Each of these windows was simulated for 25 ns, and the first 5 ns were discarded as

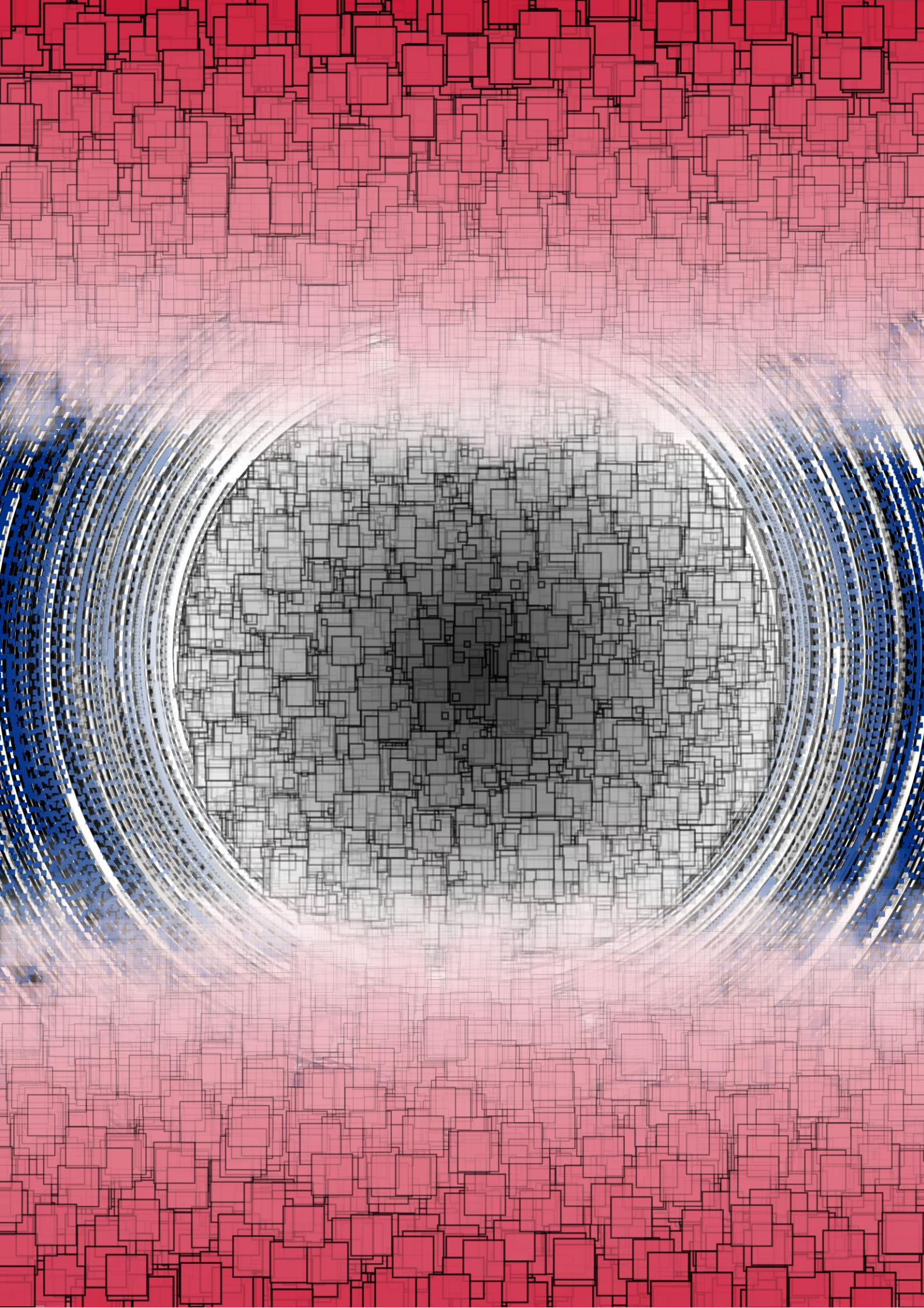
equilibration for the weighted histogram analysis method.<sup>243</sup> When the particles were closer together ( $CVI \leq 1.2$  nm), windows were extracted every 0.05 nm, and the same force constant ( $5,000 \text{ kJ mol}^{-1} \text{ nm}^{-2}$ ) was used to restrain the systems. These windows were subject to a simulated annealing in which the systems were heated to 450 K within the first 5 ns and cooled until 310 K in the span of 20 ns. Then, production runs of 225 ns were launched. These parameters were found to be optimal for exploring the NPs' rotational degrees of freedom (Appendix D.3).

#### 4. Nanoparticle synthesis, absorbance experiments, and imaging

The 3.5 nm citrate-capped AuNPs were synthesized as reported in the literature.<sup>467</sup> In a round-bottomed flask, 0.6 mL of freshly prepared 0.1 M  $\text{NaBH}_4$  (Sigma-Aldrich-Merck) was added to 100 mL ice-cold aqueous solution containing 0.25 mM  $\text{HAuCl}_4$  (Alfa Aesar) and 0.25 mM trisodium citrate (Sigma-Aldrich-Merck), while stirring. The suspension turned red-brown immediately, due to NP formation. For the 13.0 nm citrate-capped AuNPs, we used the classical Turkevich-Frens method.<sup>468</sup> 150 mL of 0.25 mM aqueous solution of  $\text{HAuCl}_4$  was transferred into a two-neck round-bottomed flask, connected to a bulb condenser, and placed in a heating mantle. After reaching boiling point, 25 mL of 38.8 mM aqueous solution of trisodium citrate were added. The solution was kept gently boiling for 30 minutes, until a red wine color appeared, indicating NP formation. Lastly, the 36.9 nm citrate-capped AuNPs were prepared by seeded growth of 15 nm AuNPs.<sup>467</sup> In a round-bottomed flask, under vigorous stirring and at room temperature, 1 mL of 15 nm AuNPs were diluted into 120 mL of Milli-Q water, followed by the addition of 0.4 mL of 0.1 M hydroxylamine sulfate (Sigma-Aldrich-Merck) solution. Then, 10 mL of 2 mM aqueous solution of  $\text{HAuCl}_4$  were added dropwise. After that, 2.65 mL of 0.1 M trisodium citrate solution were added to stabilize the NPs.

In a low-volume cuvette, 100  $\mu\text{L}$  of 400 pM AuNPs were added to 300  $\mu\text{L}$  of increasing concentrations of NaCl solution (0-120 mM) in 2 mM trisodium citrate. UV-Vis spectra (190-840 nm) were acquired by a NanoDrop 2000c UV-Vis Spectrophotometer (Thermo Fisher Scientific).

Transmission electron microscopy (TEM) images of AuNPs deposited on 300 mesh carbon coated grids were acquired by TEM JEOL-JEM 1011 (**Figure D-10**).



## **CHAPTER VIII. MEMBRANOTROPIC NANOPARTICLES HARVEST CHOLESTEROL TO PROMOTE THEIR PASSIVE CELLULAR UPTAKE**

### **Abstract**

Functionalized metal nanoparticles (NPs) hold promises as innovative nanomedicines. However, one of the main challenges is how to achieve their passive cellular uptake, which is critical for their effective delivery. Recent findings point to a passive internalization of NPs coated with the polycationic cell-penetrating peptide gH625-644 (gH), although the underlying internalization mechanism is poorly understood. Here, we use extended coarse-grained molecular dynamics simulations and cellular assays to investigate, at the molecular level, the internalization mechanism of 2.5 nm platinum NPs coated with gH (gHNPs). By comparing multiple membrane and (membranotropic) NP models, we show that gHNP internalization occurs through the formation of a unique stable intermediate state, characterized by specific stabilizing interactions. These are formed by gH with the extracellular solvent and polar membrane surface, while the NP core interacts with the transmembrane (cholesterol-rich) fatty phase, as confirmed here by scanning transmission electron microscopy images. Notably, we found that the NP core avidly harvests cholesterol at the membrane, triggering an enhanced membrane stiffness around the coated NPs. In addition, we noted a membrane slimming upon gHNP insertion, which would further favor the passive cellular uptake of gHNPs. Together, these results and the proposed cholesterol-harvesting mechanism are compatible with the passive uptake of gHNPs, as observed in our experiments.

## A. Introduction

Functionalized metal nanoparticles (NPs) are gaining attention because they display a tunable surface chemistry that is dictated by a coating monolayer of organic molecules (i.e. ligands).<sup>11,55,57,95,257</sup> These NPs hold promise in numerous biomedical applications from imaging<sup>39</sup> to cancer therapy,<sup>252</sup> most of which require the accumulation of NPs in the cytosolic space of cells.<sup>3</sup> But cellular internalization of these NPs typically occurs through endocytic pathways that entrap the NPs in a liposomal compartment, isolating them from the cytosol and promoting NP clearance.<sup>331</sup> Passive diffusion is therefore preferred for effectively delivering these NPs into cells, although it is challenging to modulate this mechanism.<sup>60,90</sup> The cellular internalization pathway of these NPs is therefore crucial for their practical application in medicine.

Cellular internalization is extremely sensitive to the NPs' physicochemical properties, including their size,<sup>469,470</sup> shape,<sup>69,256</sup> hydrophobicity,<sup>73</sup> and ligand density.<sup>471</sup> For example, zwitterionic,<sup>36</sup> polyethylene-glycol-capped,<sup>88</sup> lipid-based,<sup>85</sup> and jettisoning guest-host ligands<sup>93</sup> have been shown to promote the passive uptake of functionalized metal NPs. Other key factors for modulating cellular internalization include environmental variables such as culture media,<sup>338,423,472</sup> membrane curvature,<sup>89</sup> and, of relevance to this study, cholesterol (CHOL) abundance in the membrane.<sup>473</sup>

Of these coating strategies and factors, peptide-based monolayers are effective alternatives that can enhance the internalization rate of NPs while fostering a safe toxicological profile.<sup>52</sup> In particular, cell-penetrating peptides (CPPs, a family of oligopeptides less than 30 amino acids long) efficiently translocate across plasma membranes and can deliver cargo into cells, as is often found with viruses.<sup>360,474</sup> One prototypical example is the glycoprotein H of the Herpes simplex virus type 1 (HSV-1), where a specific CPP membranotropic subsequence (625-644) can translocate into cells without membrane disruption.<sup>475,476</sup> This finding has motivated the synthesis of macromolecules functionalized with gH625-644 (gH) peptides, which is an efficient strategy for increasing the internalization rates of NPs. Indeed, by conjugating gH peptides onto nanomaterials like liposomes,<sup>393</sup> dendrimers,<sup>477</sup> brush copolymers,<sup>478,479</sup> and quantum dots,<sup>480,481</sup> one can increase the carriers' cellular uptake relative to their naked counterparts. This was recently demonstrated by Guarnieri et al. with platinum NPs coated with gH peptides that enter cells through passive internalization.<sup>482</sup>

Despite this wealth of experimental evidence, there is still poor understanding of the NP features and molecular mechanisms for passive cellular internalization. In addition, despite the consistently positive results of NPs coated with peptide-based monolayers, the overall molecular mechanism under which gH extends its membranotropic properties to macromolecular assemblies is largely unclear. To address these fundamental questions, we here use extended coarse-grained (CG) molecular dynamics (MD) simulations coupled with cellular assays and scanning transmission electron microscopy (STEM) imaging. In this way, we characterized a cholesterol-harvesting effect that enhances the membrane stiffness around coated NPs, and so favors the passive uptake of NPs observed in our experiments.

## **B. Methods**

### *1. Our methodological approach*

Here, we study the cellular uptake of 2.5 nm platinum NPs functionalized with the gH oligopeptide. For the computations, we modeled four representative nanocarriers: i) a platinum NP coated by six gH peptides (gHNP, **Figure 44a**), ii) an individual gH peptide (gH, **Figure 44b**), iii) a spherical purely hydrophobic NP (NP0, **Figure 44c**), and iv) a spherical citrate-capped NP (CitNP, **Figure 44d**). All the carriers were allowed to interact with a pure 1-palmitoyl-2-oleoyl-sn-glycero-3-phosphocholine (POPC) bilayer (**Figure 44e**) or with a POPC bilayer loaded with CHOL (POPC:CHOL, **Figure 44f**). The second membrane used a POPC:CHOL molar ratio of 55:45 to reproduce the conditions of previous gH fusion experiments.<sup>483</sup> We examined the association mechanism for each carrier-membrane pair using three replicas of 1- $\mu$ s-long CG MD simulations and five replicas of potential of mean force (PMF) calculations. For the experiments, the same platinum gHNPs were synthesized<sup>482</sup> and used for incubation experiments with human cervix epithelioid carcinoma (HeLa) cells. We used STEM to image the bound complex formed between gHNPs and cell membranes.

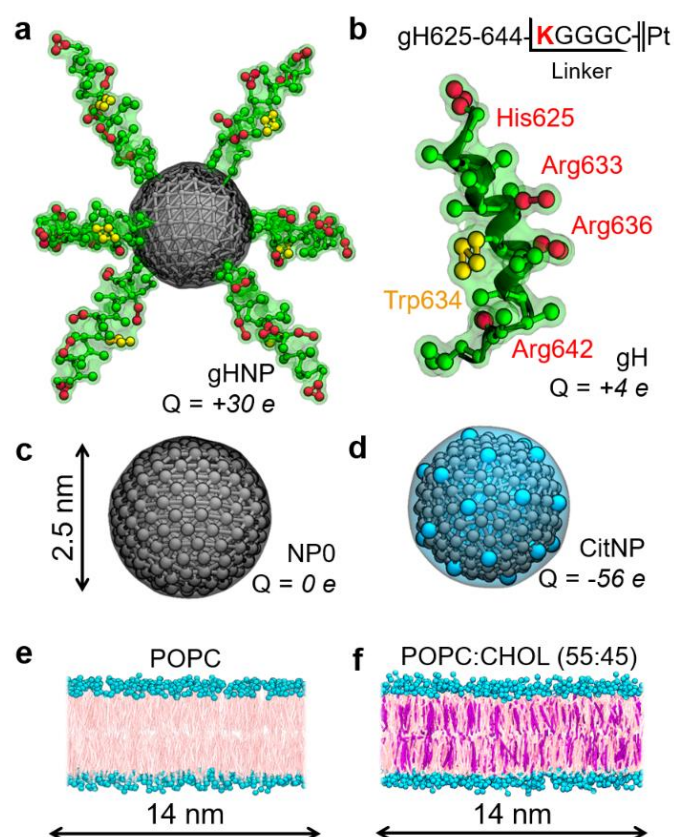


**Figure 44.** CG representation of the studied nanocarriers and lipid bilayers. **a.** Spherical platinum NP functionalized with six gH peptides (gHNP). **b.** The gH peptide and the amino acid linker sequence used for its conjugation to the platinum core. **c.** A naked hydrophobic NP with a diameter of 2.5 nm (NP0). **d.** A citrate-capped NP with citrate is represented implicitly by  $-2 e$  partial charges placed in beads uniformly distributed on the NP's surface (CitNP).<sup>160</sup> **e.** Pure POPC bilayer. **f.** CHOL-loaded POPC bilayer (POPC:CHOL). Neutral amino acids are displayed in green, cationic residues in red, Trp634 in orange, metal beads in gray, citrate beads in cyan, PC headgroups in aquamarine, lipid tails in pink, and CHOL in purple.

## 2. System preparation

The initial structure of the glycoprotein H from HSV-1 was taken from the Protein Data Bank entry 2LQY.<sup>484</sup> The peptide was mapped into the Martini-v2.2P force field using the *martinize.py* script. An elastic network consisting of a series of harmonic potentials was used to retain the secondary structure of the protein.<sup>179</sup> The elastic network used a force constant of  $k_b = 500 \text{ kJ mol}^{-1} \text{ nm}^{-2}$ , and it was applied to all the protein bead pairs at a distance between 0.5 and 0.9 nm. The peptide was immersed in a box of polarizable (refPOL)<sup>213</sup> water molecules with an NaCl concentration of 150 mM.<sup>215</sup> The system was then minimized with the steepest descent method, and simulated for 10 ns with a velocity-rescale (v-rescale) thermostat (310 K,  $\tau_B = 2.0 \text{ ps}$ ) and a Berendsen barostat (1 bar,  $\tau_P = 5.0 \text{ ps}$ ,  $\kappa = 4.5 \times 10^{-4} \text{ bar}^{-1}$ ).<sup>225</sup> Then, the

system was equilibrated for 1  $\mu$ s, exchanging the Berendsen barostat for a Parrinello-Rahman barostat ( $\tau_P = 12.0$  ps).<sup>227</sup>

The metallic core of the NPs was assembled by uniformly placing 187 beads on a sphere of diameter 2.5 nm, a size chosen to match the corresponding experimental conditions.<sup>482</sup> The NP beads were assigned the hydrophobic bead type C1 as in previous CG studies of metal NPs.<sup>160</sup> In order to retain the eccentricity of the sphere, each bead was bonded through a harmonic potential ( $k_b = 2,250$  kJ mol<sup>-1</sup> nm<sup>-2</sup>) to its six nearest neighbors and its radially opposing neighbor (antipodal bead). The NPs were then minimized with the steepest descent method. The citrate-capped metal NPs were modeled following a previously reported protocol in which 28 surface beads are added a partial charge of -2 e (for a total charge of -56 e).<sup>160</sup> The gH-coated NPs consisted of a hydrophobic core coated by six gH peptides, as resolved experimentally, placed at the cardinal points of the sphere.<sup>359</sup> Notably, gHNPs were functionalized with a modified version of gH, in which a glycine linker is added to the C-terminal to facilitate the NP's synthesis.<sup>482</sup> The peptide-bearing NPs were equilibrated following the same procedure as for gH in water.

In this study, we prepared two model membranes with the *insane.py* Martini script.<sup>280</sup> The first of these bilayers consisted of pure POPC, whereas the second contained CHOL at a molar ratio of 55:45 (POPC:CHOL). The CG parameters for CHOL were taken from Daily et al.<sup>485</sup> The membrane structures generated were parallel to the XY plane and had initial dimensions of 14 $\times$ 14 nm. The lipid molecules were fully solvated by leaving a minimum distance of 2 nm between the lipids and the box edges in the Z-direction.<sup>486</sup> The membranes were minimized using the steepest descent method and simulated for 10 ns with a v-rescale thermostat (310 K,  $\tau_B = 2.0$  ps) and a semi-isotropic Berendsen barostat (1 bar,  $\tau_P = 5.0$ , ps,  $\kappa = 4.5 \times 10^{-4}$  bar<sup>-1</sup>).<sup>225</sup> Then, the systems were equilibrated for 1  $\mu$ s, exchanging the Berendsen barostat for its Parrinello-Rahman semi-isotropic counterpart ( $\tau_P = 12.0$ ).<sup>227</sup> The convergence of the bilayer thickness, area per lipid, and acyl order parameters during these simulations verified the equilibration of the membranes.

### 3. Molecular dynamics simulations and free energy calculations

All of our production simulations involved one of the model membranes (POPC or POPC:CHOL) in the presence of gH or an NP. For this, we extracted the last frame of the equilibration runs of the two respective components, and they were merged into a single



simulation box, leaving a distance of 5.0 nm between their COM (along the Z-axis). The systems were immersed in a box of polarizable (refPOL)<sup>213</sup> water at a salt concentration of 150 mM<sup>215</sup> before they were subject to a minimization with the steepest descent method. The systems were then thermalized and pressurized in a 10-ns-long simulation applying, a v-rescale thermostat (310 K,  $\tau_B = 2.0$  ps), a semi-isotropic Berendsen barostat (1 bar,  $\tau_P = 5.0$  ps,  $\kappa = 4.5 \times 10^{-4}$  bar<sup>-1</sup>),<sup>225</sup> and with a timestep of 10 fs. Then, the production runs were launched using a Parrinello-Rahman semi-isotropic barostat ( $\tau_P = 12.0$ ),<sup>227</sup> and increasing the timestep to 20 fs. In all our simulations, the Lennard-Jones and electrostatic interactions were truncated at a distance of 1.2 nm. Long-range electrostatics were computed with the fourth-ordered particle-mesh Ewald method.<sup>231</sup> Frames were saved every 40 ps for analysis. The Gromacs-v5.1.4 MD engine was used for the entirety of the work.<sup>320</sup> We performed three 1- $\mu$ s-long replica simulations for each of our systems. Importantly, the binding times reported here are indications of the timescale on which binding occurs rather than quantitative measurements.

We implemented a PMF protocol for calculating the free energy associated with the interaction between carriers (peptide and NPs) and membranes. In this case, the selected collective variable (CV) was the Z-component of the distance between the COM of the carriers and the bilayer. We first performed a steered MD simulation to pull both components toward one another and sampled the reaction coordinate. With this method, we applied a harmonic potential ( $k_{bias} = 2,000$  kJ mol<sup>-1</sup> nm<sup>-2</sup>) with an equilibrium value that started at 5.0 nm and shrank at a rate of 0.15 nm ns<sup>-1</sup>. Then, 51 frames were extracted from the trajectory so as to sample the CV every 0.1 nm.

The free energy calculations relied on the umbrella sampling technique. With this method, the windows extracted from our steered MD simulations were used as initial configurations for simulations sampling a limited range of the CV. In these simulations, the original value of the CV at each window was restrained by a harmonic potential ( $k_{bias} = 2,000$  kJ mol<sup>-1</sup> nm<sup>-2</sup>). Then, the windows were simulated for 100 ns each, saving the CV every 1 ps and using the same parameters described above for the unbiased runs. The simulated time summed was 150  $\mu$ s in total. The free energy profiles were finally reconstructed by merging the CV's histograms of each simulated window with the weighted histogram analysis method.<sup>244</sup> Five PMF replicas were performed for gHNP and gH, and one replica was performed for NP0 and CitNP.

#### 4. Trajectory analysis

In this study, two geometrical parameters were computed for gH-containing simulations, namely the polar angle  $\theta_{inc}$  and rolling angle  $\varphi_{roll}$ . The first of these is defined as the angle between the peptide's  $\alpha$ -helix and the vector normal to the bilayer (Z-axis). The helix's axis was determined as the vector from the backbone bead of Leu627 to the backbone bead of Ala639. An angle of  $\theta_{inc} = 0^\circ$  indicates that the N-terminal of the peptide points toward the membrane, whereas  $\theta_{inc} = 180^\circ$  means that the C-terminal points toward at the membrane. In contrast,  $\varphi_{roll}$  is defined as the torsion angle between two planes defined by three vectors. The first vector is the Z-axis, the second is the vector from Trp634 to Thr630, and the third is the vector from Thr630 to Thr632. According to the bonded parameters of the peptide (as assigned by the Martini-v2.2P force field), at  $\varphi_{roll} \sim 90^\circ$ , the sidechain of Trp634 points toward the bilayer's interior.

The radial distribution functions (RDF) of unit  $U1$  with respect to unit  $U2$  were calculated from Equation 88. In Equation 88,  $\delta_D(r)$  is Dirac's Delta function, and  $N_{U1}$  and  $N_{U2}$  are the number of beads in units  $U1$  and  $U2$ , respectively.

$$G_{U1-U2}(r) = \frac{1}{N_{U1}N_{U2}} \sum_{i=1}^{N_{U1}} \sum_{j=1}^{N_{U2}} \langle \delta_D(r_{ij} - r) \rangle \quad (88)$$

All the bidimensional plots presented here were mapped from 50×50 grids. The membrane thickness was calculated as the mean distance between the three nearest phosphate beads to each grid point. The area per lipid was calculated by performing a Voronoi analysis to the XY coordinates of the phosphate beads for each frame in the trajectory. In this case, each grid point was assigned the average area per lipid of its three nearest lipids. Lastly, the lipid order parameter was calculated from Legendre's second-order polynomial (Equation 89), where the ensemble is averaged over time, molecules, and beads. The angle of bead  $i$ , namely  $\omega_{i,z}$ , is the angle formed between the Z-axis and the vector uniting bead  $i-1$  with bead  $i+1$ . The trajectory analysis was carried out with in-house scripts using the MDAnalysis-v1.0 library from Python.<sup>370</sup>

$$P_2(\cos \omega_z) = \frac{1}{2} \langle 3 \cos^2 \omega_z - 1 \rangle \quad (89)$$

## 5. Cell culture and transmission electron microscopy

HeLa American Type Culture Collection (ATCC) cells were cultured in Dulbecco's modified eagles medium (DMEM, Invitrogen) supplemented with 10% (v/v) fetal bovine serum (Hyclone), 100 U mL<sup>-1</sup> penicillin, and 100 mg mL<sup>-1</sup> streptomycin (Invitrogen). Cells were maintained in an incubator in a humidified controlled atmosphere at 37°C and 5% CO<sub>2</sub>. For STEM observations, HeLa cells were incubated for 24 hours with platinum gHNPs that were 2.5 nm in diameter as previously reported.<sup>482</sup> The cells were then processed as described elsewhere.<sup>138</sup> The images were acquired in STEM mode working in high angular annular dark field geometry, using a FEI Tecnai F20 transmission electron microscope operating at 200 kV and equipped with a Schottky field-emission gun.

## C. Results

### 1. Functionalized peptide-coated nanoparticles adopt a biphasic binding mode at lipid membranes

We first studied the change in free energy for gHNPs binding to one of the two considered lipid bilayers, i.e. with and without CHOL. All systems are shown in **Figure 44**, including the POPC and POPC:CHOL bilayers (Chapter VIII-B). The PMF for gHNP-membrane binding was computed along the direction connecting the COM of the nanocarrier and that of the bilayer. The PMF calculations displayed a free energy basin, labeled M1, at ca. 1.6 nm, regardless of the presence of CHOL (**Figure 45a**). In this global minimum, the platinum core was embedded halfway into the bilayer, forming favorable dispersive interactions with the lipids' tails. In contrast to the metallic core, the coating peptides remained on the surface of the membrane, establishing a salt bridge network with the zwitterionic phosphatidylcholine (PC) lipid headgroups.

This energy well corresponded to a free energy of association of  $-105.7 \pm 8.4$  kcal mol<sup>-1</sup> at  $1.46 \pm 0.04$  nm for POPC, and  $-98.2 \pm 29.5$  kcal mol<sup>-1</sup> at  $1.70 \pm 0.09$  nm for POPC:CHOL. Notably, all our equilibrium CG MD simulations also visited M1. For POPC, the state M1 was reached at 550, 862, and 895 ns. For POPC:CHOL, M1 was reached at 227, 533, and 864 ns (**Figure E-1**). Importantly, once in M1, gHNP always remained stably bound to the membrane until the end of the simulations. For POPC:CHOL, the metallic core interacted preferentially with CHOL molecules (**Figure 45b**). The CG MD trajectories showed a layer of CHOL cocooning

the hydrophobic metallic core. The RDF computed for CHOL and lipid tails (**Figure 45b**) demonstrated an increased occurrence of CHOL molecules around gHNP. However, gHNP also interacted with the outer aqueous phase, leading to a biphasic fatty/aqueous binding mode that mined the membranotropic capacities of gH and the hydrophobic character of bulk metals.

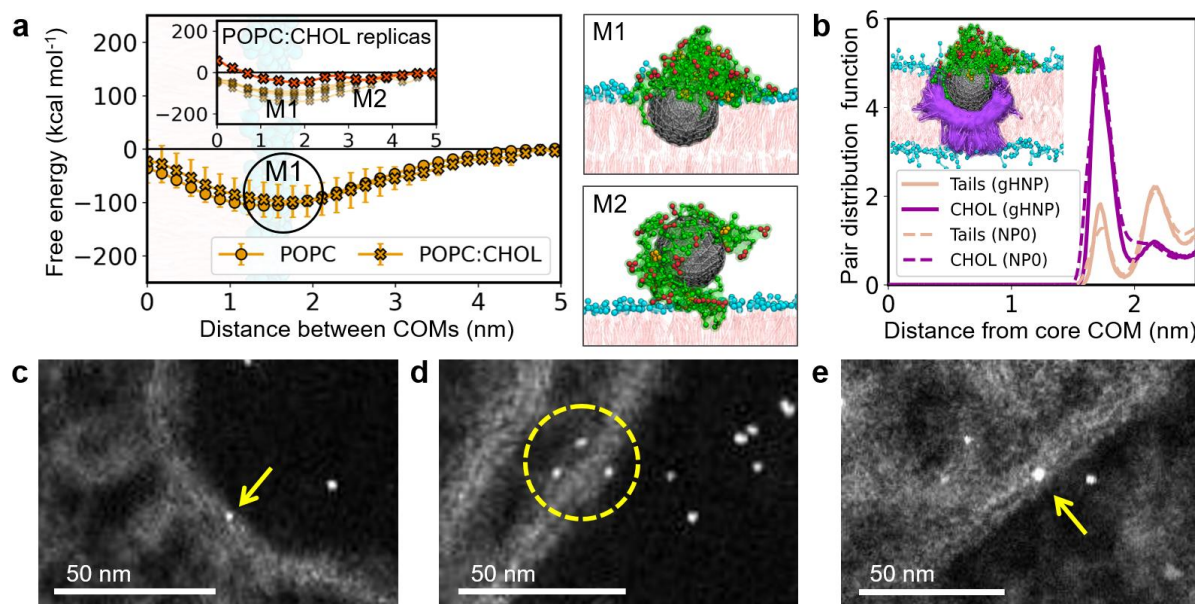


**Figure 45.** Interaction pattern between gHNPs and lipid bilayers. **a.** Free energy profiles for the peptide-functionalized gHNP binding to the POPC and POPC:CHOL membranes. The binding process is defined in terms of the distance between the COM of gHNP and the bilayer. The inset shows the five-replica PMF profile obtained for the POPC:CHOL system. One of the replicas revealed two free energy minima (M1 and M2). **b.** RDF of lipid tails and CHOL with respect to the distance from the core's COM. The inset superposes multiple frames to illustrate the formation of the CHOL cocoon. **c-e.** STEM images of 2.5 nm platinum gHNPs interacting with the membrane of HeLa cells after 24 hours of incubation at 50  $\mu\text{g mL}^{-1}$  particle concentration. The yellow arrows and dashed circle show single gHNPs at different stages of their translocation across cell (**c** and **d**) and endo-lysosomal membranes (**e**). The color scheme is the same as that used in **Figure 44**.

Notably, one of the PMF replicas for POPC:CHOL presented one additional energy well, M2 (**Figure 45a** inset). Although M1 continued to be the global minimum, this second metastable local minimum showed a peptidic cushion between the membrane and the metallic core. Interestingly, this gH-based cushion is characterized by stabilizing electrostatic interactions formed between the coating peptides and the POPC headgroups, which transiently trapped gHNP in this minimum. Indeed, one equilibrium CG MD simulation of gHNP interacting with POPC:CHOL diffused freely from the bulk solvent into the M2 state at 126 ns, yet the system fell into M1 at 864 ns. The metastable state M2 was also visited by gHNP when interacting with the pure POPC bilayer in one of the equilibrium CG MD replica simulations. In this case,

gHNP diffused from the solvent into M2 at 393 ns, and then fell into the global minimum M1 at 550 ns (**Figure E-1**), where it stayed for the remainder of the simulations, endorsing the transitory occupancy of the M2 state.

We then used cellular assays and microscopy techniques to investigate the interfacial binding mode M1, as suggested by our simulations of gHNPs bound to lipid membranes. Platinum gHNPs were synthesized as previously described<sup>482</sup> and incubated with HeLa cells for 24 hours (Chapter VIII-B). The rested cell culture was then imaged at various regions with STEM microscopy (**Figure 45c-e**). The extracted STEM images showed the functionalized gHNPs at different stages of their passive translocation across cell and endo-lysosomal membranes (**Figure 45c-e**). Notably, these experiments showed the platinum gHNPs persistently embedded in the lipid bilayer in a mode that is consistent with the M1 biphasic bound state described above.

## *2. Membrane binding of primitive peptides suggests a unique binding mechanism for peptide-coated nanoparticles*

To understand the membranotropic properties of gHNPs, we compared these NPs with an individual gH peptide interacting with POPC and POPC:CHOL. All PMF replicas of individual gH peptides interacting with the membranes identified the same free energy minimum, in which gH was fused to the bilayer (**Figure 46a**). For POPC, this optimal state was characterized by a distance between COMs of 1.73 nm (standard deviation < 0.01 nm between the 5 PMF profiles) and a free energy of association to the membrane of  $-22.3 \pm 0.7$  kcal mol<sup>-1</sup>. Consistently, our equilibrium CG MD simulations showed the gH peptide, initially placed 3 nm above the bilayer, binding spontaneously to the POPC bilayer 45, 313, and 728 ns after the simulations had started (**Figure E-2**). The peptide always remained stably bound until the end of the simulation. Importantly, these results are consistent with previous circular dichroism and fluorescence quenching experiments where gH was found to stably adsorb on the surface of the PC lipid bilayers.<sup>483</sup>

The gH peptide returned similar results when interacting with POPC:CHOL. The corresponding PMF profiles again indicated a single minimum, this time at a separation of 1.99 nm (standard deviation < 0.01 nm between the 5 PMF profiles). In this case, the free energy of association with POPC:CHOL was  $-23.5 \pm 0.6$  kcal mol<sup>-1</sup>, suggesting a minimal effect of CHOL on gH binding (**Figure 46a**). Notably, fluorometric titrations had previously estimated

a 10-fold increase in the partition coefficient of gH on POPC:CHOL (55:45), as compared to pure POPC.<sup>483</sup> This difference corresponds to a decrease in free energy of roughly 1.4 kcal mol<sup>-1</sup>, which falls within the statistical error of PMF methods. In light of this, our free energy calculations do hint toward the same experimental trend. Notably, our equilibrium CG MD simulations also showed the peptide's irreversible binding to the membrane within the same nanosecond timescale as before (38, 46, and 50 ns).

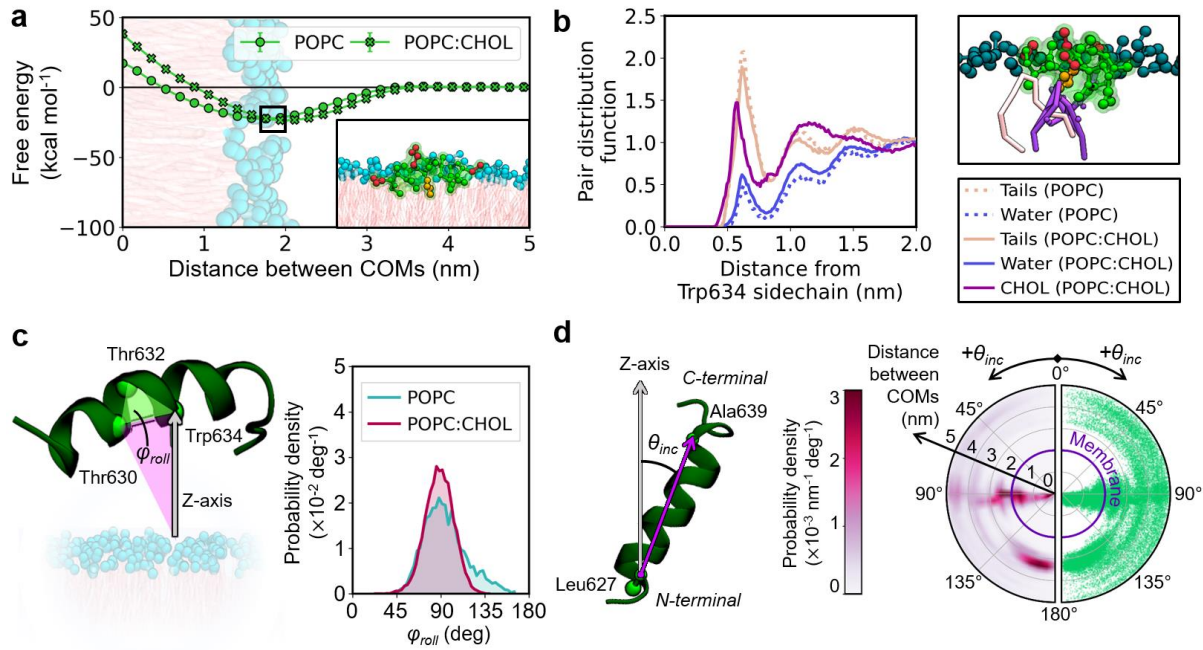


**Figure 46.** Interaction pattern between gH peptides and lipid bilayers. **a.** Free energy profiles for gH binding onto POPC and POPC:CHOL membranes. The binding process is described as the distance between the COM of the peptide and the bilayer. The inset shows the bound complex. **b.** RDF of lipid tails, water, and CHOL with respect to Trp634 when bound to both POPC and POPC:CHOL (left panel). The gH peptide interacting with a POPC lipid and a CHOL molecule when bound to the membrane (right panel). **c.** Definition of the rolling angle  $\varphi_{roll}$  that describes the rotation of the peptide's helix around its axis. The angle  $\varphi_{roll}$  is defined in terms of the backbone bead of Thr630, Thr632, and Trp634, shown as green spheres (left panel). The distributions of  $\varphi_{roll}$  are shown for the bound complex found with POPC and POPC:CHOL (right panel). **d.** Definition of the polar angle  $\theta_{inc}$ , which describes the peptide's preferred orientation at varying distances from the membrane. The angle  $\theta_{inc}$  is defined in terms of the backbone beads of Leu627 and Ala639, shown as green spheres (left panel). The states sampled during the simulations are represented as scattered green points, and the associated probability density is shown as a pink map (right panel). The color scheme is the same as that used in **Figure 44**.

The effect of CHOL on gH binding was further investigated by characterizing the gH-membrane complex for POPC and POPC:CHOL, as found in our equilibrium CG MD simulations. In particular, we resolved the local chemical environment for gH by computing the RDF of the hydrophobic tails, water, and CHOL with respect to Trp634 (**Figure 46b**), a

residue labeled in fluorescence experiments.<sup>476</sup> Interestingly, the local density of water and lipids around Trp634 remained nearly constant for both studied membranes. However, the first peak for CHOL appeared at shorter distances than the water and lipid tails, indicating that Trp634 packed more tightly with CHOL than with the other two components.

The close packing of CHOL around gH also influenced the rotation of gH along its axis when bound to POPC:CHOL. To illustrate this effect, we monitored the evolution of  $\varphi_{roll}$  (**Figure 46c**), an angle that described the rolling of the  $\alpha$ -helix on the surface of the membrane. In particular, when  $\varphi_{roll} \sim 90^\circ$ , the sidechain of Trp634 pointed toward the bilayer core, promoting that residue's insertion. The distribution of the rolling angle  $\varphi_{roll}$  changed from  $94 \pm 22^\circ$  in POPC to  $88 \pm 14^\circ$  in POPC:CHOL. As expected, these distributions overlap. But CHOL led to a narrower distribution of  $\varphi_{roll}$ , suggesting that the gH-CHOL interaction may hamper the rolling of gH peptides on the membrane, stiffening the gH-membrane complex. Notably, for gHNPs bound to POPC and POPC:CHOL, the distribution of  $\varphi_{roll}$  preferred by gH peptides vanished, with each of the peptides adopting a different conformation (**Figure E-3**).

Our PMF calculations also showed two highly populated peptide conformations that were conserved among the POPC and POPC:CHOL systems, as identified by tracking the orientation of the peptide's  $\alpha$ -helix ( $\theta_{inc}$ , **Figure 46d**) during peptide binding. The first conformation, found at the bilayer's surface, matched the free energy minimum discussed above, in which the peptide sat parallel to the membrane ( $\theta_{inc} \sim 90^\circ$ ). Conversely, the second conformation appeared at distances of between 3 and 4 nm from the bilayer midplane. At this stage, the peptide adopted an anti-parallel conformation ( $\theta_{inc} \sim 180^\circ$ ), meaning that the C-terminal of gH preferentially pointed toward the membrane. This suggests that the charged Arg642 likely initiated the peptide's anchoring to the phospholipids' headgroups. Notably, previous mutagenesis experiments have shown that replacing Arg642 (the only arginine residue close to the C-terminal) with a serine inhibits the fusion activity of the peptide,<sup>476,487</sup> which is consistent with the proposed orientation-specific binding mechanism of gH.

Importantly, these results highlight that gH interacts differently with the membrane when alone and attached to a metallic core. Note that the monolayer of gHNPs was grafted onto the core through the C-terminal of the gH peptides. In this way, the key interaction of Arg642 for anchoring gH to the membrane cannot occur in gHNPs. That is, for gHNPs, Arg642 cannot be positioned in such a way as to initiate membrane binding. This key structural difference implies

that gHNPs interact and bind to membranes through a different mechanism than gH peptides. Despite this different binding mechanism for peptide-membrane anchoring, we found that the final bound state of gH and gHNP ends with the peptide(s) adsorbed similarly on the surface of the membrane. This reflects that, despite a unique mechanism for membrane adhesion, gHNPs conserve the membranotropic properties of their CPP component.

### *3. Functionalized peptide-coated nanoparticles harvest cholesterol molecules and lipid tails, aiding passive diffusion*

We proceeded to study the role of the inner metallic core in the overall association of gHNPs with lipid membranes. As for the previous systems, we computed the PMF along the carrier-membrane distance. The free energy profiles displayed a single minimum when the naked NP0 was fully embedded in the bilayer, that is, at a distance of 0 nm (**Figure 47a** and **Figure E-4**). The free energy of insertion was  $-187.1 \pm 0.1$  kcal mol<sup>-1</sup> for POPC and  $-228.1 \pm 0.1$  kcal mol<sup>-1</sup> for POPC:CHOL, in quantitative agreement with computational studies on analogous systems.<sup>488,489</sup> The accentuation of free energy in CHOL-loaded membranes resulted from a stronger interaction between NP0 and CHOL over NP0 and POPC lipids, as already expected based on our simulations on gHNPs (**Figure 45b**).

Our equilibrium CG MD simulations endorsed the results of our PMF calculations on NP0, as we observed the spontaneous insertion of NP0 into both POPC and POPC:CHOL (**Figure E-4**). Moreover, our simulations of NP0 with POPC:CHOL provided deeper insights into the formation of the CHOL cocoon, which we observed forming around gHNP (**Figure 45b**). We computed the RDF of CHOL around NP0 (**Figure 45b**), as well as the lateral number density of CHOL in the membrane (**Figure 47b**). Interestingly, these two metrics showed an oscillatory behavior in the packing of CHOL, which seemingly arranged in layers of intercalating density by aggregating and depleting regionally. The hydrophobic matching between NP0 and CHOL led to an apolar solvation shell reminiscent of the electrical double layer formed around charged solutes in electrolytic media.<sup>490,491</sup>

In addition to the purely hydrophobic NP0, we investigated membrane association in the presence of citrate ligands (CitNP), a coating that enables the colloidal stability of metal NPs in polar environments.<sup>160</sup> In contrast to NP0, the PMF profiles of CitNP showed a free energy barrier for membrane association, obstructing its translocation across lipid bilayers (**Figure 47a** and **Figure E-5**). The height of this barrier was  $106.5 \pm 0.1$  kcal mol<sup>-1</sup> for POPC and



$179.3 \pm 0.1 \text{ kcal mol}^{-1}$  for POPC:CHOL, suggesting a weak affinity and hence reduced cellular uptake rates for CitNPs (compared to gHNPs). Interestingly, inductively coupled plasma atomic emission spectroscopy (ICP/AES) experiments previously reported that the uptake of CitNPs by HeLa cells was 12-fold lower than for gHNPs.<sup>482</sup> The values obtained for the free energy barriers were also consistent with those reported for similar spherical charged systems.<sup>83,411</sup> Notably, both the POPC and POPC:CHOL profiles displayed two different slopes before and after 1.8 nm (**Figure 47a**), which coincided with the distance at which CitNPs were embedded halfway into the bilayer. This change in slope illustrated the two forces governing CitNP-membrane fusion, that is, i) the electrostatic pairing of citrate with the lipid headgroups and the solvent, and ii) the hydrophobic matching of the metallic core with the lipid tails.

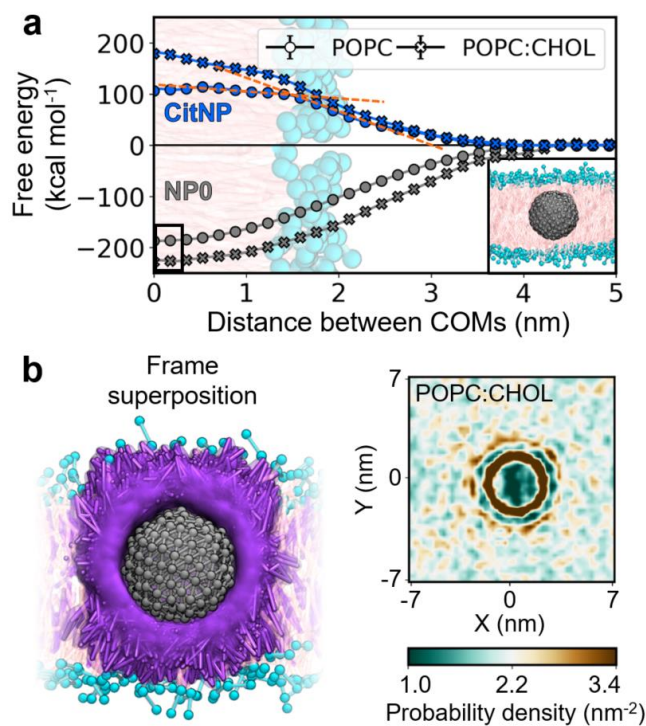


**Figure 47.** Interaction pattern between naked and capped NPs with lipid bilayers. **a.** Free energy profiles for NP0 and CitNP binding to the POPC and POPC:CHOL membranes. The binding process is described as the distance between the COM of the NPs and the bilayer. The intersection of the dashed orange lines marks an inflection point of the free energy curve. **b.** Density of CHOL after NP0 embedding into the membrane (right panel). CHOL molecules aggregate around the metallic core forming a caging cocoon (left panel). The color scheme is the same as that used in **Figure 44**.

In our simulations, as in experiments,<sup>482</sup> gHNP formed a stable complex with the lipid bilayer without affecting the overall structural integrity of the membrane, unlike other cationic metal NPs that have consistently led to heavy membrane disruption.<sup>327,333</sup> However, the binding of gHNP caused a local increase in the area per lipid from  $0.66 \pm 0.01$  to  $1.50 \pm 0.24 \text{ nm}^2$  in POPC

and from  $0.81 \pm 0.06$  to  $1.77 \pm 0.36$  nm<sup>2</sup> in POPC:CHOL. This finding hints a local permeabilization of the membrane,<sup>492</sup> reflecting the increased spatial distancing of lipids observed in our simulations.

The area per lipid of the membrane also changed for individual gH peptides, increasing to  $0.75 \pm 0.01$  nm<sup>2</sup> in POPC and to  $0.97 \pm 0.06$  nm<sup>2</sup> in POPC:CHOL. Similar to gHNP, the distancing of lipids surrounding gH could explain the extracellular release of small molecules, like fluorescent dyes, as observed for pure gH peptides in leakage experiments.<sup>483,487,493</sup> Notably, the increased distancing of lipids could even be linked to the transient formation of channels in the membrane, which may ultimately be responsible for the passive translocation of gH peptides into the cytosol, as already demonstrated for other CPPs.<sup>480,494</sup> Transient channels may also enable the passive translocation of gHNPs into the cytosol, not only through the cell membrane but also across the endo-lysosomal compartment, as experimentally reported in **Figure 45c-e**.<sup>482</sup> While the transient formation of these channels in the membrane remains to be clarified, our simulations suggested that, either free or grafted, gH peptides preferentially bind to lipid bilayers in a horizontal conformation, pushing away neighboring lipids, yet retaining the overall structural integrity of the membrane. These results collectively recover the membranotropic character that gH features during the transfection of HSV-1<sup>483</sup> and that is extended to functional platinum gHNPs.

Beyond an increased area per lipid, the binding of gHNP led to non-additive local distortions in the membrane that differed from what was observed for gH and NP0 separately. With gHNP, the membrane thickness increased underneath the coating peptides, leading to values of  $4.22 \pm 0.18$  nm in POPC (6% increase with respect to  $3.97 \pm 0.18$  nm in an unperturbed membrane) and  $4.88 \pm 0.18$  nm in POPC:CHOL (12% increase with respect to  $4.33 \pm 0.15$  nm in an unperturbed membrane). In contrast, the binding of individual gH peptides did not change the membrane thickness. Furthermore, for gHNPs, the membranes became thinner at the metallic core's location, reaching values of  $3.55 \pm 0.21$  nm (11% decrease) in POPC and  $4.05 \pm 0.16$  nm (7% decrease) in POPC:CHOL (**Figure 48a**). Interestingly, the slimming around gHNP's metallic core is in contrast to the thickening observed for NP0, which caused the thickness to increase to  $4.58 \pm 0.19$  nm in POPC (15% increase with respect to the nominal value) and to  $5.40 \pm 0.19$  nm in POPC:CHOL (25% increase with respect to the nominal value, **Figure 48b**). These opposing trends for the spherical core in gHNP and NP0 suggest that the grafted gH plays a key role in modulating the membrane thickness (Chapter VIII-D).

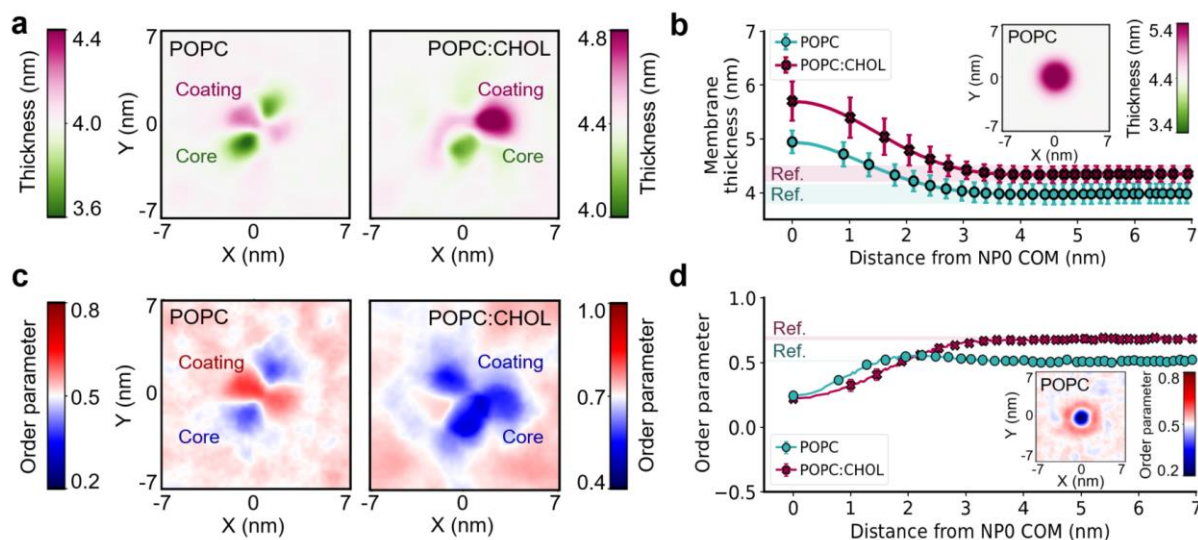


**Figure 48.** Membrane distortion upon binding of gHNPs and NP0 onto lipid membranes. **a.** Top view of the mapped membrane thickness averaged over the frames where gHNP was bound to POPC (left panel) and POPC:CHOL (right panel). The thinner patches match the regions where the core was located, and the thicker areas coincide with the binding spot of the coating peptides. **b.** Membrane thickness as a function of the distance from NP0's COM. The reference values for the POPC and POPC:CHOL membranes were obtained from separate simulations of equilibrated membranes. The inset shows the membrane thickness of POPC when NP0 was embedded. **c.** Top view of the mapped lipid order parameter averaged over time for POPC (left panel) and POPC:CHOL (right panel). **d.** The mean lipid order parameter as a function of the distance from NP0's COM. The inset shows the lipid order parameter of POPC when NP0 was embedded.

Similar non-additive local distortions were also found when assessing the organization of the lipid tails. The binding of gHNP induced a heterogeneous packing of the neighboring lipids. The second-order parameter of the lipid tails increased around the coating peptides in the absence of CHOL (**Figure 48c**). However, in the presence of CHOL, this effect is overshadowed by the metallic core, which consistently reduced the lipids' order. In gHNP and NP0, the metallic body acts as an excluded volume that caused the local liquefaction of the membrane (i.e. less lipid order).<sup>495</sup> The metallic core forces the lipid tails to circumvent the NP, i.e. bending toward larger angles with respect to the membrane's normal (Z-) axis, thus decreasing the lipid order parameter (**Figure 48d**). In the presence of CHOL, the effective volume of the NP increases due to the formation of the CHOL cocoon, extending the area within which the lipids are disordered. Considering all our results, we note that gHNP induces local and heterogeneous membrane alterations that are unique to the coated gHNP and that are affected by the content of CHOL in the membrane.

## D. Discussion

In this work, we investigate the molecular mechanism for passive translocation into cells of 2.5 nm platinum NPs coated with the gH CPP. We combine CG MD simulations, free energy calculations, cellular assays, and STEM to explain the interaction between gHNPs and lipid membranes in terms of the energetic and structural role of the particles' primordial components, i.e. individual gH peptides and naked metal NPs (NP0).

First, our free energy calculations depict a mechanistic landscape for the fusion of individual gH peptides with lipid membranes. We find that the Arg642 residue, which resides at the C-terminal of the gH peptide, is the first residue to interact with the membrane, thus triggering the anchoring of gH to the membrane. This crucial interaction is mostly with the lipid headgroups, leading gH to later rest horizontally on the surface of the membrane (binding free energy  $-22.3 \pm 0.7$  kcal mol<sup>-1</sup> in POPC and  $-23.5 \pm 0.6$  kcal mol<sup>-1</sup> in POPC:CHOL). Notably, this orientation-dependent mechanism is in agreement with previous mutagenesis and circular dichroism experiments.<sup>476,483,487</sup> However, in gHNPs, the peptides are grafted onto the metallic core through their C-terminal, thus locating this crucial anchoring Arg642 near the NP core. This structural arrangement preventing Arg642 from interacting with the membrane during binding thus forcing gHNPs into an alternative binding mechanism. Our equilibrium CG MD simulations show that the binding of gHNPs onto lipid membranes occurs through non-specific electrostatic interactions between the polycationic coating monolayer (comprising six gH peptides) and the zwitterionic headgroup of POPC lipids (**Figure 49** top panels). These results support the idea that gH favors membrane binding in gHNPs, even if this occurs through alternative anchoring interactions.

After membrane docking, gHNPs form a stable complex with lipid bilayers. This complex combines structural features from pure gH peptides and naked NP0 cores (binding free energy  $-105.7 \pm 8.4$  kcal mol<sup>-1</sup> in POPC and  $-98.2 \pm 29.5$  kcal mol<sup>-1</sup> in POPC:CHOL). In the bound complex, the monolayer of gHNPs reorganizes to let the charged amino acids form a salt bridge network with the lipid headgroups at the surface of the membrane. At the same time, the inner metallic core is embedded halfway into the lipid bilayer, stabilized by dispersive interactions with the lipid tails (RDF reaches 2.1 in the core's first solvation shell, **Figure 45b**). Thus, the amphipathicity of gHNPs enables a dual interaction that simultaneously harnesses the high charge density of the cationic coating and the hydrophobicity of the metallic core, leading

gHNPs to form a biphasic binding mode stabilized by both the outer aqueous phase and the transmembrane fatty phase.

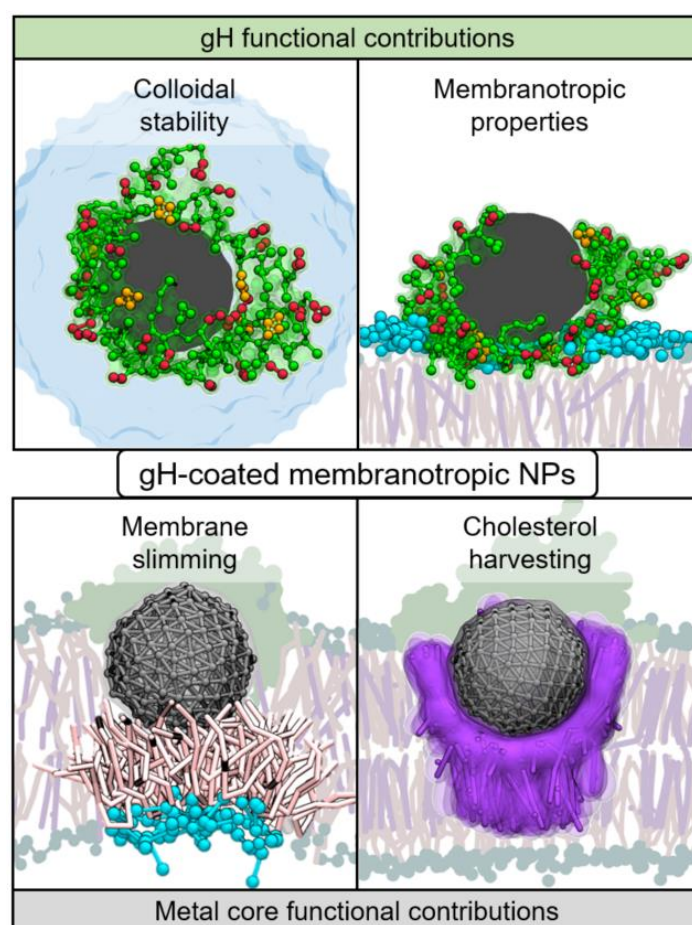


**Figure 49.** Properties of platinum gHNPs. The top panels show the functional contributions of the gH coating, i.e. colloidal stability (left panel) and membranotropic properties (right panel). The gH peptides and lipid headgroups are shown in 3D representations while the solvent, lipid tails, and CHOL molecules are shown as flat drawings. The bottom panels show the functional contributions of the inner metallic core, i.e. CHOL harvesting (right panel) and membrane slimming (left panel). The metallic core and its vicinal lipids and CHOL molecules are shown in 3D representations, while the gH peptides and the rest of the membrane are shown as flat drawings. The color scheme is the same used in **Figure 44**.

Incubation experiments with HeLa cells and STEM imaging provided further evidence of gHNPs' biphasic interaction at the membrane. Our STEM images show platinum gHNPs at different stages of translocation across cell and endo-lysosomal membranes (**Figure 45c-e**). The functionalized gHNPs are persistently found bound to the lipid bilayers, in remarkable consistency with our computational models. In this regard, we account for the complexity of multi-component mammalian membranes with simulations of CHOL-containing bilayers. We find that individual gH peptides and naked metal cores pack more closely with CHOL

molecules than with lipid tails. This mutual preference further stabilizes the bound complex of gHNP with CHOL-containing membranes by forming a dense CHOL cocoon around the functionalized NP. These CHOL cocoons show a 5-fold increase in the sterol's density around the core with respect to an equilibrated membrane (**Figure 45b** and **Figure 47b**). Importantly, higher concentrations of CHOL are known to increase the rigidity of membranes.<sup>496</sup> Thus, the aggregation of CHOL around gHNP should penalize the bending of the surrounding membrane patch, as demonstrated in analogous systems,<sup>497</sup> slowing the wrapping rates and increasing the likelihood of rare events such as passive translocation (**Figure 49** bottom right panel).<sup>482</sup>

Previous MD simulations have studied 3.0 nm anionic NPs embedded (snorkeling) in CHOL-containing membranes without witnessing the CHOL-harvesting effect that we report here.<sup>400,465</sup> Importantly, the coating monolayer of our gHNPs was more flexible and less charged than those discussed in the previous study. Specifically, those simulations used NPs coated by 134 short (3-bead-long) ligands with a charge of -1 e each (i.e. total charge of -134 e), while our gHNPs were coated (as determined experimentally) by six amphipathic peptides with a charge of 5 e each (i.e. total charge of 30 e). This comparison indicated that the formation of the CHOL cocoon is critically affected by the NP charge, ligand grafting density, and ligand flexibility, ultimately endorsing the complex cross-dependence between NP features and their interactions with membranes.

ICP/AES experiments have previously determined that platinum gHNPs can be passively internalized by HeLa cells.<sup>482</sup> In this context, our simulations reveal that the binding of gHNPs causes local distortions on the lipid membrane that may prelude the particles' passive uptake. As a matter of fact, gHNPs increase the area per lipid of the membranes to  $1.50 \pm 0.24 \text{ nm}^2$  in POPC and to  $1.77 \pm 0.36 \text{ nm}^2$  in POPC:CHOL. Intriguingly, this spatial distancing of the lipids hints at the formation of transient channels. However, these may only be fully formed at longer timescales. While the formation of these channels remains to be clarified, we note that these would indeed enable gHNPs to passively translocate into the cytosol or escape lysosomal compartments. Furthermore, when gHNPs are bound to the membrane, the metallic core dangles from the upper (extracellular) leaflet, attracting the lipid tails of the lower (intracellular) leaflet. The hydrophobic pairing between the metal and the lower lipid tails slims the bilayer thickness by 11% in POPC and 7% in POPC:CHOL, likely facilitating the opening of transmembrane channels at selected patches (**Figure 49** bottom left panel). Notably, the observed slimming of the membrane requires that the metallic core is only partially embedded

into the membrane, explaining why the passive translocation of bigger platinum gHNPs is reduced in experiments, i.e. 6-fold reduction with 5 nm gHNPs and complete inhibition with 20 nm gHNPs.<sup>482</sup>

Taken together, our comparative analyses of multiple membrane and (membranotropic) NP models show that the internalization mechanism of gHNP occurs through the formation of a stable intermediate biphasic state. In this state, the NP core harvests CHOL at the membrane, prompting an enhanced membrane stiffness around the coated NPs. Then, membrane slimming upon gHNP insertion further promotes the passive cellular translocation of gHNPs, in agreement with the experimental evidence.<sup>482</sup> We describe distinct yet synergistic effects by the two main components in gHNPs, i.e. the peptide and the metallic core. The former drives membrane association, while the latter enhances core embedding into the membrane. These two factors together contribute to the formation of local distortions at the membrane, which ultimately seems to promote passive translocation.

## **E. Conclusions**

We investigate the cellular uptake of 2.5 nm platinum NPs functionalized with the cell-penetrating peptide gH(625-644) using CG MD simulations, free energy calculations, and cellular assays. Our simulations show that the membranotropic properties of gHNPs are driven by non-specific electrostatic interactions between the polycationic monolayer and the polar lipid headgroups. In this state, gHNPs form a biphasic complex with the membrane in which the coating peptides spread on the polar surface of the membrane and the metallic core embeds halfway into the fatty transmembrane phase. This biphasic binding mode is consistent with cellular assays and STEM experiments. Following membrane-binding, our simulations show that gHNPs increase the local density of CHOL, which hampers membrane bending.<sup>497</sup> We also observed a membrane slimming effect that arises from the partly inserted NP core, which attracts the lipid tails of the intracellular leaflet. It is tempting to speculate that these local membrane distortions promote rare events like the passive translocation observed in ICP/AES experiments.<sup>482</sup> The passive internalization of gHNPs is also preceded by a slimming of the membrane, which is due to the partly inserted core attracting the lipid tails of the intracellular leaflet.

Taken together, our results lay out, at the molecular level, the mechanism for gH-coated platinum NPs to associate with cell membranes. We find that gH-coated membranotropic metal

NPs passively translocate across cell membranes through a multifaceted mechanistic strategy that exploits the coating peptides and the metallic core. With the advent of the rational design of functionalized NPs,<sup>2</sup> our results may help researchers to design membranotropic NPs that harvest CHOL molecules to damp endocytosis in favor of passive diffusion.



## CHAPTER IX. FINAL REMARKS AND PERSPECTIVES

Monolayer-protected metal nanoparticles (NPs) are supramolecular assemblies with a tunable surface chemistry. The plasticity and chemical variability of the coating monolayers are cementing metal NPs as versatile platforms for targeted functions, and we, as a scientific community, are only starting to scratch the surface of the broad applicability that we project for such NPs. In this regard, the engineering of NPs will be honed as we get a better understanding of the interactions between NPs and other molecular entities and the underlying physical principles that govern them. The work presented here contributes to the multidisciplinary field of nanotechnology from three focal points: structural modeling, method development, and biomedical applicability.

In the context of structural modeling, we developed NanoModeler ([www.nanomodeler.eu](http://www.nanomodeler.eu)), the first webserver for building and parametrizing functionalized metal NPs for molecular dynamics (MD) simulations. The NanoModeler webserver offers a standardized methodology for the computational modeling of NPs at atomistic and coarse-grained (CG) resolutions. As demonstrated in Chapter III and Chapter VI, the models generated with NanoModeler can be used effectively to study structural and dynamical features of functionalized NPs. Indeed, all the simulations discussed throughout the entirety of this work are a testament to NanoModeler's reach.

Before NanoModeler, the computational modeling of functionalized NPs was restricted to scientists with sufficient programming skills, time, and resources to single-handedly assemble and parametrize models for such systems. Since its deployment in November 2018, NanoModeler has been facilitating the access to the computational modeling of monolayer-protected NPs. While the second release, NanoModeler CG, is scheduled to go online in early 2021, the webserver has already registered more than 130 users worldwide. Thus, this tool is already encouraging faster scientific advances in functionalized metal NPs by researchers of all academic and cultural backgrounds.

The models generated by NanoModeler also offer the foundations to more elaborate methodologies. In the context of method development, this work presents a computational protocol for screening libraries of gold NPs in the quest of sensible chemosensors (Chapter V).

This protocol identifies nanoreceptors with twice the accuracy of random classifiers. More importantly, the method extracted a set of gold NPs that strongly bind, seemingly, to 3-methoxytyramine, a diagnostic and prognostic biomarker of asymptomatic child neuroblastoma. The framework developed holds great potential for accelerating the design of AuNP-based chemosensors, which have immediate applications in biomedical and environmental sciences.

Embracing metal NPs as therapeutic agents demands the particles' colloidal stability in aqueous matrices. In this regard, this work also addresses the NP features and media conditions that determine the colloidal dispersivity of charged metal NPs (Chapter VII). As a matter of fact, a new theoretical model is formulated to characterize, at the molecular level, the metal-solvent interface of ion-capped NPs. Moreover, phase diagrams included in this work rationalize the dispersion state of NP suspensions in terms of the particles' size and charge, as well as the medium's ionic strength. Ultimately, the present work clarifies the fundamental principles that govern NP-NP adhesion and unravels the driving forces that lead to colloid aggregation. These findings contribute to the design of stable nanomedicines that are safely transported without clogging in biological streams.

Effective therapeutic performance also requires that metal NPs reach their target destination, which, generally, implies crossing a cell membrane. This work offers a molecular understanding of how membranotropic NPs can permeabilize lipid membranes and promote NP internalization. Interestingly, metal NPs can benefit from the 'arginine-magic' effect exploited by naturally occurring glycoproteins during virus transfection processes (Chapter IV). Likewise, metal NPs coated by cell-penetrating peptides display unique membranotropic properties that are only accessible through the collaboration of hydrophobic metal cores and amphipathic coating peptides (Chapter VIII). In sum, this work is a step toward the controlled cellular delivery of nanomedicines.

Functionalized metal NPs with theranostics applications are gaining increasing attention in the biotechnology community. Nonetheless, there is still much to be understood about the nano-biointerface before incorporating NPs into clinical practices, especially in regard to their intracellular trafficking rates. The work presented here comprises online tools, physics-based methods, and molecular insights that expand our understanding of the structure-function relation in metal NPs, while steering nanotechnology toward the greatest benefit for humankind.

# APPENDIX A. NANOMODELER USER MANUAL

## A.1 Overview

NanoModeler is a web server that allows you to build monolayer-protected AuNPs. With NanoModeler you can obtain coordinate files (.pdb and .gro format) and parameters files (.top format). The output structure and topology files are ready for use with the Gromacs MD engine, and the parameters offered here are based on the AMBER family of force fields. The service is already online at [www.nanomodeler.eu](http://www.nanomodeler.eu).

To use NanoModeler, you must provide the structure file (.mol2 format with partial charges) of one or two compounds, which can then be arranged in different ways on the gold cores. NanoModeler currently supports 16 gold cores with diameters ranging from 0.9-2.1 nm. The number of available cores is expected to grow as new structures are elucidated. Notably, the gold-to-sulfur stoichiometric ratio is determined by the selected core, so it cannot be modified.

In this documentation section, you will find a full description of the usable options and a how-to guide for the server with test cases.

## A.2 Options

When running a job in NanoModeler, you can modify several options to customize the output. Here, we explain what each field means. All options must be specified from the GUI. This improves the user experience and reduces the number of files that the user has to provide. Below, you will find the names, data types, and important information on all the current options:

- **Job name** (*string*): The name given to the job in the queueing system. Each job must have a unique name. This field does not determine the name of the output files.
- **Description** (*string*): Description of the running job. With this field, the user can more easily track each job.
- **Core** (*string*): One core must be selected from the drop-down list in the field.
- **Ligand 1 and Ligand 2 boxes:**

- **Mol2 file** (*file*): The structure file (.mol2 format) of the ligands. Each file must follow the directives of the .mol2 file format. The minimum requirements are the sections '@<TRIPOS>MOLECULE,' '@<TRIPOS>ATOM,' and '@<TRIPOS>BOND.' The first nine columns of each row in the '@<TRIPOS>ATOM' section must contain the following information in this order: Atom number, atom name, XYZ coordinates, AMBER atom type, residue number, residue name, and partial charge. Importantly, each file must contain only one residue, meaning that all the atoms must share the same residue name and residue number. Moreover, the residue name of the ligands must consist of three or less characters to ensure their compatibility with the resulting .pdb files. Consider that .pdb files of your ligands can be processed by 'antechamber' (AmberTools) or the R.E.D. Server to assign AMBER atom types. The atom names must be unique. 'ST' is forbidden as an atom name because it is reserved for the sulfur atom linking the ligands to the metallic core. The compounds may or may not contain the linking sulfur atom, but this must be specified in the S/C option. The compounds may be capped on the linking terminal.
- **Capping** (*integers*): If the structure file of the ligand is capped with an additional group on the linking terminal of the compound, it can be removed with this option. The atom numbers conforming this group must be specified one at a time with the '+' button. The total charge of the capping group will be equally distributed to the rest of the molecule, so we recommend that it has a charge of (nearly) zero.
- **S/C** (*boolean, integer*): This option must be specified with two values. First, you must specify if the input structure file of the ligand contains the thiol's sulfur atom or not. If it does, then select **S**; if it does not, then select **C**. Second, you must indicate the number of the atom that will connect the ligand to the gold core. If **S** is selected, then you must specify the atom number of the sulfur atom. If **C** is selected, then you must specify the number of the first carbon atom of the ligand. The atom numbers are read from the input structure file, so they are not affected by the removal of an eventual capping group.
- **Mixed monolayer box:**
  - **Morphology** (*string*): If you wish to build a mixed-monolayer-protected AuNP (i.e. two ligand structure files are supplied), you can use this option to select the thiol arrangement. NanoModeler supports three arrangements: 'Random,' 'Janus' and 'Stripe.' With 'Random,' Ligand 1 and Ligand 2 are randomly distributed on the

gold core. With ‘Janus,’ the AuNP is partitioned in two hemispheres, each coated with a different ligand. With ‘Stripe,’ the sulfur atoms in the gold core are sorted into intercalating domains based on their azimuthal angle.

- **Ligand 1 fraction** (*float*): This field is only enabled if **Morphology** is set to ‘Random’ or ‘Janus.’ Enter a value between 0 and 1 to indicate what fraction of Ligand 1 to use. If the value is set to 1 or 0, a homogeneous monolayer is obtained for Ligand 1 and Ligand 2, respectively.
- **Random seed** (*integer*): This field is only enabled when **Morphology** is set to ‘Random.’ Specify a random seed to generate the distribution of Ligand 1 and Ligand 2. Different seeds result in different output structures. If no value is given, it will be selected randomly. The selected seed is always prompted to the user once the job has finished.
- **Stripes** (*integer*): This field is only enabled when **Morphology** is set to ‘Stripe.’ Specify the number of stripes in which to allocate Ligand 1 and Ligand 2.
- **Additional Options box:**
  - **Force field modification file** (*file*): A parameters file (.frcmod format) for overwriting or completing the default parameters used in AmberTools19. The bonded parameters of the staples cannot be overwritten.
  - **Elongated** (*boolean*): Selecting this option removes the carbon atoms in the core structures. In turn, carbon atoms are placed 0.18 nm away from the sulfur atoms along the centroid-sulfur vectors. This option is useful when trying to place bulky ligands since it reduces the chances of steric clashes in the final structure. However, the final structure will presumably be farther away from an energy minimum.

### A.3 Test cases – Tutorials

To use NanoModeler, you will need to create an account. Once you are logged in, you can access the job submission page by clicking on the ‘Let’s submit your first job!’ button on the homepage, or the ‘Submit your first job!’ button that is always visible in the upper right corner. Below, you will find four tutorials with different input files. You can follow the tutorials and generate your own files side-by-side, or you can download all the input and output files here (<https://github.com/cebasfu93/NanoModeler-Tutorial>). Let’s get started!

### A.3.1 Test case 1: Ligands with an open valence (homogeneous monolayer)

In this first scenario, we will generate an AuNC ( $\text{Au}_{25}$ ) coated by 18 molecules of butanethiol (BUT). It will become apparent, as you follow this tutorial, that there is more than one way to generate the same output structure. The input files may be generated with different approaches depending on your needs and preferences. In the first test case, we will use a ligand with open valence, which is NanoModeler's recommended mode of use. Here, we will build the nanocluster  $\text{Au}_{25}(\text{BUT})_{18}$  from a .mol2 file containing a butane molecule with open valence. NanoModeler always requires a .mol2 file with the partial atomic charges. If you are not sure how to calculate atomic charges with charge constraints in order to obtain a ligand with an open valence, we recommend the R.E.D. Server tutorial (<http://upjv.q4md-forcefieldtools.org/Tutorial/Tutorial-4.php>). To continue with NanoModeler's tutorial without calculating atomic charges, simply download the example file found at [https://github.com/cebasfu93/NanoModeler-Tutorial/blob/master/Au25\(BUT\)18/BUT.mol2](https://github.com/cebasfu93/NanoModeler-Tutorial/blob/master/Au25(BUT)18/BUT.mol2).

- i. **Name and description:** Once you are in the job submission page, begin by giving your job a (mandatory) name and (optional) description.
- ii. **Core selection:** To choose the core, select the desired gold-to-sulfur ratio from the drop-down list. In this tutorial, we will use  $\text{Au}_{25}(\text{SR})_{18}$ . After you select the core, its structure is displayed in the right panel with a coloring scheme based on its staple distribution (light green for STR, light purple for STC, and red for STV, Chapter III).
- iii. **Ligand 1:** This box contains all the information about the first coating thiol of the cluster's monolayer. If you prepared your own .mol2 file, upload your own file here. Otherwise, download the example .mol2 file and use it for this tutorial. Since the ligand has an open valence, there is no need to remove any atom from the structure (capping group). Plus, the ligand structure does not contain the thiol's sulfur atom, which means that the ligand will be attached to the core via the first carbon atom, i.e. the one with the open valence. Thus, we must check the **C** box and indicate the atom number of the carbon with the open valence, as numbered in the .mol2 file. If you are using the example file for this tutorial, check the **C** box and type '1.'
- iv. **Ligand 2:** In this tutorial, we are generating a homogeneous-monolayer-protected AuNCs, so we will not upload a file for Ligand 2.
- v. **Mixed monolayer:** In this tutorial, we only uploaded the file for Ligand 1, so the **Mixed monolayer** box is disabled by default.

- vi. **Additional force field parameters:** In this tutorial, we will use GAFF's default parameters, so we will not upload an .frcmod file to add or overwrite the default parameters.
- vii. **Elongated:** We are interested in keeping the *cis-trans* staple configurations as in the original Au<sub>25</sub>(SR)<sub>18</sub> structure, so we will not check the **Elongated** box.
- viii. **Submission:** To submit your job, click the 'Submit' button at the bottom of the page. If you wish to return all fields to their default values, click the 'Reset' button.
- ix. **After job submission:** Once the job is submitted, you will be redirected to your profile. There, you will find a list with your jobs and their current status. You may wait for the job to finish, but you will also receive an email to your registered address, notifying you when it has finished.
- x. **Results download and availability:** To download the results, log in to your NanoModeler account and access your job list. Alternatively, click on the link in the notification email. Both options will take you to a message with information about the run and, if the job failed, additional information for troubleshooting. This message also contains all the input options used to execute the job. Your results are available for download as a zipped file for up to ten days after job submission. If you would like to take a look at the results from this tutorial, feel free to download an example output from [https://github.com/cebasfu93/NanoModeler-Tutorial/tree/master/Au25\(BUT\)18](https://github.com/cebasfu93/NanoModeler-Tutorial/tree/master/Au25(BUT)18).

That is it. You are all set to run your MD simulations. Good luck!

### A.3.2 Test case 2: Ligands with capping groups (homogeneous monolayer)

Here, we will generate an AuNC (Au<sub>38</sub>) coated with 24 molecules of phenylethanethiol (PET). In contrast to the first tutorial, we will use a capped ligand. We will build the nanocluster Au<sub>38</sub>(PET)<sub>24</sub> from a .mol2 file containing a phenylethyl molecule capped with a methyl group (i.e. phenylpropane). NanoModeler always requires a .mol2 file with the partial atomic charges. In the first tutorial, you had to calculate the atomic partial charges with a charge constraint on the atom with an open valence. In this tutorial, you just need a ligand with charges assigned to all the atoms present. You can download the exemplified input file from [https://github.com/cebasfu93/NanoModeler-Tutorial/blob/master/Au38\(PET\)24/PET.mol2](https://github.com/cebasfu93/NanoModeler-Tutorial/blob/master/Au38(PET)24/PET.mol2).

- i. **Name and description:** Once you are in the job submission page, begin by giving your job a (mandatory) name and (optional) description.

- ii. **Core selection:** To choose the core, select the desired gold-to-sulfur ratio from the drop-down list. In this tutorial, we will use  $\text{Au}_{38}(\text{SR})_{24}$ . After you select the core, its structure is displayed in the right panel with a coloring scheme based on its staple distribution (light green for STR, light purple for STC, and red for STV, Chapter III).
- iii. **Ligand 1:** This box contains all the information about the first coating thiol of the cluster's monolayer. If you prepared your own .mol2 file, upload your own file here. Otherwise, download the example file and use it for this tutorial. First, we must remove the capping group to obtain the phenylethane ligand that we actually want to use. Note that the charge of the capping atoms is equally distributed on the rest of the atoms of the ligand. To remove the capping group, enter the atom numbers of the methyl substituent (four in total) in the 'Atom to be removed' field. The atom numbers must match those from the input .mol2 file. If you are using the example files, add the atom numbers 18, 19, 20, and 21, one at a time. The phenylethane's file does not contain the thiol's sulfur atom. Rather, the ligand will be attached to the core via the first carbon atom after the capping methyl group. To ensure this, check the **C** box and indicate the atom number of this carbon atom. This selection is independent of the removal of the capping group, i.e. the numbering must still match that of the input .mol2 file. If you are using the example files, check the **C** box and type '15.'
- iv. **Ligand 2:** In this tutorial, we are generating a homogeneous-monolayer-protected AuNC, so we will not upload a file for Ligand 2.
- v. **Mixed monolayer:** In this tutorial, we only uploaded the file for Ligand 1, so the **Mixed monolayer** box is disabled by default.
- vi. **Additional force field parameters:** In this tutorial, we will use GAFF's default parameters, so we will not upload an .frcmod file to add or overwrite the default parameters.
- vii. **Elongated:** We are interested in keeping the *cis-trans* staple configurations as in the original  $\text{Au}_{38}(\text{SR})_{24}$  structure, so we will not check the **Elongated**.
- viii. **Submission:** To submit your job, click the 'Submit' button at the bottom of the page. If you wish to return all fields to their default values, click the 'Reset' button.
- ix. **After job submission:** Once the job is submitted, you will be redirected to your profile. There, you will find a list with your jobs and their current status. You may wait for the job to finish, but you will also receive an email to your registered address, notifying you when it has finished.



- x. **Results download and availability:** To download the results, log in to your NanoModeler account and access your job list. Alternatively, click on the link in the notification email. Both options will take you to a message with information about the run and, if the job failed, additional information for troubleshooting. If you would like to take a look at the results from this tutorial, feel free to download the example output found at [https://github.com/cebasfu93/NanoModeler-Tutorial/tree/master/Au38\(PET\)24](https://github.com/cebasfu93/NanoModeler-Tutorial/tree/master/Au38(PET)24). This message also contains all the input options used to execute the job. Your results are available for download as a zipped file for up to ten days after job submission.

And that is it. You are all set to run your MD simulations. Good luck!

### *A.3.3 Test case 3: Thiols with an open valence (homogeneous monolayer)*

In this third tutorial, we will generate an AuNP ( $\text{Au}_{68}$ ) coated by 34 molecules of benzenethiol (BEN). As in the first tutorial, we will use a capped ligand. We will build the nanocluster  $\text{Au}_{68}(\text{BEN})_{34}$  from a .mol2 file containing a benzenethiol molecule with an open valence at the sulfur atom (i.e. the hydrogen atom of the thiol group is absent, but the net charge of the molecule is zero). NanoModeler always requires a .mol2 file with the partial atomic charges. As in the first tutorial, you must calculate the atomic partial charges with a charge constraint on the atom with open valence. If you are not sure how to calculate atomic charges, we recommend the R.E.D. Server tutorial (<http://upjv.q4md-forcefieldtools.org/Tutorial/Tutorial-4.php>). To continue with NanoModeler's tutorial without calculating atomic charges, simply download the example file found at <https://raw.githubusercontent.com/cebasfu93/NanoModeler-Tutorial/master/BEN.mol2>.

- i. **Name and description:** Once you are in the job submission page, begin by giving your job a (mandatory) name and (optional) description.
- ii. **Core selection:** To choose the core, select the desired gold-to-sulfur ratio from the drop-down list. In this tutorial, we will use  $\text{Au}_{68}(\text{SR})_{32}\text{-I2}$ . After you select the core, its structure is displayed in the right panel with a coloring scheme based on its staple distribution (light green for STR, light purple for STC, and red for STV, Chapter III). In this particular case, we are using the isoform I2 of the  $\text{Au}_{68}(\text{SR})_{32}$  core, which should be the configuration of lowest energy as originally reported.<sup>287</sup> However, the list offers other three isoforms with different staple distributions.

- iii. **Ligand 1:** This box contains all the information regarding the first coating thiol of the cluster's monolayer. If you prepared your own .mol2 file, upload it now. Otherwise, download the example file and use it for this tutorial. The ligand has an open valence, so there is no need to remove atoms from the structure (capping group). In contrast to the first tutorial, the ligand here does have the thiol's sulfur atom. Therefore, we must check the **S** box and indicate the atom number of the atom with the open valence, as numbered in the input .mol2 file. If you are using the example files, check the **S** box and type '12.'
- iv. **Ligand 2:** In this tutorial, we are generating a homogeneous-monolayer-protected AuNP, so we will not upload a file for Ligand 2.
- v. **Mixed monolayer:** In this tutorial, we only uploaded the file for Ligand 1, so the **Mixed monolayer** box is disabled by default.
- vi. **Additional force field parameters:** In this tutorial, we will use GAFF's default parameters, so we will not upload an .frcmod file to add or overwrite the default parameters.
- vii. **Elongated:** The BEN molecule is a short coating thiol as compared to more common alkyl chains. To reduce the likelihood of producing a structure with steric clashes, check the **Elongated** box.
- viii. **Submission:** To submit your job, click the 'Submit' button at the bottom of the page. If you wish to return all fields to their default values, click the 'Reset' button.
- ix. **After job submission:** Once the job is submitted, you will be redirected to your profile. There, you will find a list with your jobs and their current status. You may wait for the job to finish, but you will also receive an email to your registered address notifying you when it has finished.
- x. **Results download and availability:** To download the results, log in to your NanoModeler account and access your job list. Alternatively, click on the link in the notification email. Both options will take you to a message with information about the run and, if the job failed, additional information for troubleshooting. If you would like to take a look at the results from this tutorial, feel free to download an example output from [https://github.com/cebasfu93/NanoModeler-Tutorial/tree/master/Au68\(BEN\)32](https://github.com/cebasfu93/NanoModeler-Tutorial/tree/master/Au68(BEN)32). This message also contains all the input options used to execute the job. Your results are available for download as a zipped file for up to ten days after job submission.

And that is it. You are all set to run your MD simulations. Good luck!

#### A.3.4 Thiols with capping groups (mixed monolayer)

In the fourth tutorial, we will generate an AuNP ( $\text{Au}_{314}$ ) coated by a randomly mixed monolayer. In total, we will place 96 coating thiols. Of these, 25% (24 sites) will be 11-mercaptopoundecasilfonate (MUS) and 75% (72 sites) octanethiol (OCT). To prepare the  $\text{Au}_{314}(\text{MUS})_{24}(\text{OCT})_{72}$ , we need two .mol2 files. Unlike in the first three tutorials, here we will build the system from .mol2 files of capped thiols. In this tutorial, the capping groups will be methyl groups. Consequently, one .mol2 file should contain the structure of MUS with a methyl group attached to the thiol's sulfur atom. The second .mol2 file should contain the structure of OCT with an additional methyl group (i.e. methyl octyl sulfide). NanoModeler always requires a .mol2 file with the partial atomic charges. To continue with NanoModeler's tutorial without calculating atomic charges, simply download the example files found at [https://github.com/cebasfu93/NanoModeler-Tutorial/tree/master/Au314\(MUS\)24\(OCT\)72](https://github.com/cebasfu93/NanoModeler-Tutorial/tree/master/Au314(MUS)24(OCT)72).

- i. **Name and description:** Once you are in the job submission page, begin by giving your job a (mandatory) name and (optional) description.
- ii. **Core selection:** To choose the core, select the desired gold-to-sulfur ratio from the drop-down list. In this tutorial, we will use  $\text{Au}_{314}(\text{SR})_{96}$ . After you select the core, its structure is displayed in the right panel with a coloring scheme based on its staple distribution (light green for STR, light purple for STC, and red for STV, Chapter III).
- iii. **Ligand 1:** This box contains all the information regarding the first coating thiol of the AuNP's monolayer. Here, we will work with MUS as the first ligand. If you prepared your own .mol2 file, upload your own file here. Otherwise, download the example file and use it for this tutorial. First, we must remove the capping group to obtain the ligand that we actually want to coat the core with. Note that the charge of the capping atoms is equally distributed on the rest of the atoms of the ligand. To remove the capping group, add the atom numbers of the methyl substituent (four in total) to the 'Atom to be removed' field. The atom numbers must match those from the input .mol2 file. So, if you are using the example files, add the atom numbers 5, 6, 7, and 8, one at a time. The resulting structure of the ligand still contains the thiol's sulfur atom, so check the **S** box. Then, in the text box, enter the atom number corresponding to the thiol's sulfur atom ('4' for the example files). This selection is independent of the removal of the capping group, i.e. the numbering must still match that of the input .mol2 file.

- iv. **Ligand 2:** In this tutorial, we are generating a mixed-monolayer-protected AuNP, so we will use this box. As in the previous step, upload the ligand's .mol2 file, indicate the atom number of the capping group, one at a time (27, 28, 29, and 30), check the **S** box, and indicate the atom number corresponding to the thiol's sulfur atom ('26').
- v. **Mixed monolayer:** In this tutorial, we uploaded a structure file for Ligand 2, so the **Mixed monolayer** box is enabled. To assemble a randomly mixed monolayer, select 'Random' from the Morphology drop-down list. Then, to place 25% of the total number of ligands as MUS, enter 0.25 in the 'Ligand 1 fraction' field. Ligand 2 (OCT) will be automatically assigned to the remaining 75% of sites. Also, we will put a value of 1 in the 'Random seed' field. This will allow us to reproduce the same mixed monolayer given the same input files.
- vi. **Additional force field parameters:** In this tutorial, we will use GAFF's default parameters, so we will not upload an .frcmod file to add or overwrite the default parameters.
- vii. **Elongated:** We are interested in keeping the *cis-trans* staple configurations the same as in the original Au<sub>314</sub>(SR)<sub>96</sub>, so we will not check the **Elongated** box.
- viii. **Submission:** To submit your job, click the 'Submit' button at the bottom of the page. If you wish to return all fields to their default values, click the 'Reset' button.
- ix. **After job submission:** Once the job is submitted, you will be redirected to your profile. There, you will find a list with your jobs and their current status. You may wait for the job to finish, but you will also receive an email to your registered address, notifying you when it has finished.
- x. **Results download and availability:** To download the results, log in to your NanoModeler account and access your job list. Alternatively, click on the link in the notification email. Both options will take you to a message with information about the run and, if the job failed, additional information for troubleshooting. If you would like to take a look at the results from this tutorial, feel free to download an example output from [https://github.com/cebasfu93/NanoModeler-Tutorial/tree/master/Au314\(MUS\)24\(OCT\)72](https://github.com/cebasfu93/NanoModeler-Tutorial/tree/master/Au314(MUS)24(OCT)72). This message also contains all the input options used to execute the job. Your results are available for download as a zipped file for up to ten days after job submission.

And that is it. You are all set to run your MD simulations. Good luck!

## APPENDIX B. SYNTHESIS, CHARACTERIZATION, AND SUPPLEMENTARY SIMULATIONS OF CATIONIC NANOPARTICLES

### B.1 Polydispersity and $\zeta$ -potential

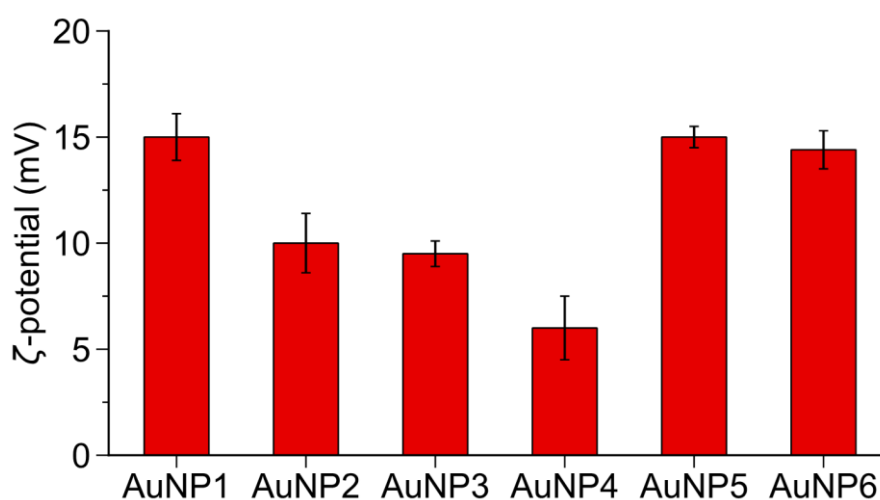


**Figure B-1.**  $\zeta$ -Potential of the six AuNPs in PBS 10 mM, pH 7.0, 25°C.

**Table B-1.** Summary table of hydrodynamic diameters (HEPES 10 mM, NaCl 100 mM, pH 7.0, 25°C) and  $\zeta$ -potentials (PBS 10 mM, pH 7.0, 25°C) values for the prepared liposomes.

Entry	Liposome	Dye	Size (nm)	PDI	$\zeta$ -Potential (mV)
1	PC	Calcein	79.3	0.15	-1.74
2	PC:PG	Calcein	98.47	0.06	-7.69
3	PC:CHOL	Calcein	96.62	0.15	-0.69
4	PC	Nile red	96.98	0.15	-1.62
5	PC:PG	Nile red	95.63	0.07	-5.76

## B.2 Dyes and synthesis of Lig1-6

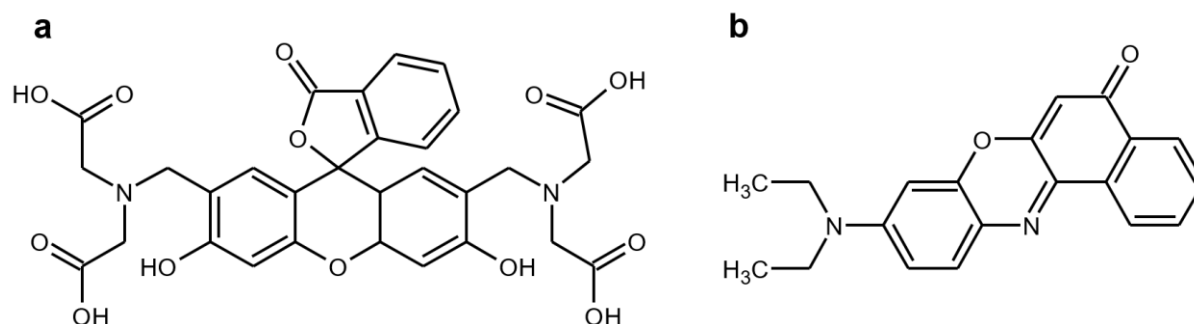


**Figure B-2.** Chemical structure of the dyes employed throughout the work. **a.** Calcein. **b.** Nile red.

### B.2.1 Synthesis of Lig1

- i. Synthesis of 7-azidohept-1-ene. 7-Bromohept-1-ene (516 mg, 3.14 mmol) and sodium azide (220 mg, 9.157 mmol) were dissolved in aqueous Dimethylformamide (DMF, 10 ml). After 10 hours stirring, the mixture was washed with water and extracted with dichloromethane (DCM). The combined organic layer was concentrated in vacuum and used in the next step without any purification.
- ii. Synthesis of hept-6-en-1-amine hydrochloride. 7-Azido-hept-1-ene (1.179 g, 8.47 mmol) was dissolved in water (5 mL) and tetrahydrofuran (THF, 13 mL). Triphenylphosphine (4.400 g, 33.88 mmol) was then added to the mixture. The solution was stirred for 12 hours at room temperature. After the completion of the reaction, the mixture was washed with DCM and extracted with an HCl solution (1 M). The combined aqueous solution was evaporated to dryness in vacuum. 785 mg (82%) were obtained as a white solid.  $^1\text{H-NMR}$  (500 MHz,  $\text{D}_2\text{O}$ )  $\delta$  5.89-5.73 (m, 1H), 5.02-4.86 (dd, 2H), 2.94-2.87 (t, 2H), 2.05-1.94 (q, 2H), 1.63-1.50 (q, 2H), 1.40-1.24 (m, 4H).  $^{13}\text{C-NMR}$  (126 MHz,  $\text{D}_2\text{O}$ )  $\delta$  139.67, 114.32, 39.42, 32.69, 27.41, 26.47, 25.00. ESI-MS ( $m/z$ ): 114.1 [ $\text{M}+\text{H}^+$ ].
- iii. Synthesis of 1,3-bis(tert-butoxycarbonyl)-1-(hept-6-enyl)-guanidine. Hept-6-en-1-amine hydrochloride (200 mg, 1.36 mmol) and  $\text{N,N}'$ -bis(tert-butoxycarbonyl)- $\text{N}''$ -triflylguanidine (443.6 mg, 1.12 mmol) were dissolved in DCM. Then  $\text{N,N}$ -diisopropylethylamine (0.592 ml, 3.4 mmol) was added to the solution. The mixture was stirred for 25 hours at room temperature. After the solvent evaporation, the crude product was purified by flash chromatography (silica gel, eluent petroleum ether (PE):ethyl acetate (EtOAc) 9.5:0.5). 264 mg (55%) were obtained.  $^1\text{H-NMR}$  (500 MHz,

- CDCl<sub>3</sub>)  $\delta$  5.86-5.75 (m, 1H), 5.06-4.91 (m, 2H), 3.46-3.39 (q, 2H), 2.11-2.04 (q, 2H), 1.63-1.56 (m, 2H), 1.55-1.49 (d, 18H), 1.48-1.35 (m, 4H). <sup>13</sup>C-NMR (126 MHz, CDCl<sub>3</sub>)  $\delta$  156.09, 153.33, 138.71, 114.39, 83.04, 79.23, 40.93, 33.54, 28.83, 28.47, 28.32, 28.08, 26.30. ESI-MS (*m/z*): 356.2561 [M+H<sup>+</sup>].
- iv. Synthesis of S-(7-((2,2,10,10-tetramethyl-4,8-dioxo-3,9-dioxa-5,7-diazaundecan-6-ylidene)amino)heptyl) ethanethiolate. Carbamate derivative (110 mg, 0.309 mmol) was dissolved in MeOH (3 mL). Nitrogen was injected into the solution for 30 minutes to remove oxygen. Afterwards, 2, 2-dimethoxy-2-phenylacetophenone (4.0 mg, 0.015 mmol) and thioacetic acid (94.08 mg, 1.236 mmol) were added. The mixture was left under irradiation (UV, 365 nm) for 3 hours. After solvent evaporation, the crude product was purified by flash chromatography (silica gel, eluent PE:EtOAc 9.5:0.5). 110 mg (82%) were obtained. <sup>1</sup>H-NMR (500 MHz, deuterated methanol (MeOD))  $\delta$  3.39-3.34 (t, 2H), 2.91-2.86 (t, 2H), 2.32-2.30 (s, 3H), 1.63-1.56 (m, 4H), 1.55 (s, 9H), 1.49 (s, 9H), 1.44-1.35 (m, 6H). <sup>13</sup>C-NMR (126 MHz, MeOD)  $\delta$  196.15, 163.17, 156.17, 152.85, 83.04, 78.93, 40.31, 29.24, 29.09, 28.55, 28.39, 28.31, 28.22, 27.17, 26.82, 26.23.
- v. Synthesis of 2-(7-mercaptoheptyl)guanidine. Thioacetate derivative (110 mg, 0.255 mmol) was dissolved in ethanol (EtOH, 5.2 mL). A 6 M HCl solution in water (5.2 mL) was added and the mixture was stirred at 78°C for 3 hours. The reaction mixture was allowed to cool, and the solvent was evaporated to obtain 70 mg (quantitative). <sup>1</sup>H-NMR (500 MHz, MeOD)  $\delta$  3.23-3.17 (t, 2H), 2.54-2.48 (t, 2H), 1.65-1.56 (m, 4H), 1.48-1.33 (m, 6H). <sup>13</sup>C-NMR (126 MHz, MeOD)  $\delta$  157.23, 41.12, 33.68, 30.05, 28.42, 28.36, 27.84, 26.2. ESI-MS (*m/z*): 190.1398 [M+H<sup>+</sup>].

### B.2.2 Synthesis of Lig2

- i. Synthesis of 11-((5-bromopentyl)oxy)undec-1-ene. 11-Undecen-1-ol (1.18 mL, 5.87 mmol) was dissolved in dimethyl sulfoxide (12 mL), and KOH (1.32 g, 23.5 mmol) was then added under stirring at room temperature. After 10 minutes 1,5-dibromopentane (3.18 mL, 23.5 mmol) was introduced. After 3 hours of stirring, the mixture was extracted with diethyl ether (3×30 mL), the combined ether phases were then washed with water (3×30mL). After evaporation, the product was purified by flash column chromatography (silica gel, eluent gradient from PE to PE:EtOAc 9:1). 1.59 g (84%) of product were obtained. <sup>1</sup>H-NMR (500 MHz, CDCl<sub>3</sub>)  $\delta$  5.82 (ddt, 1H), 4.99

(m, 2H), 3.42 (m, 6H), 2.05 (dd, 2H), 1.90 (qn, 2H), 1.58 (m, 6H), 1.35 (m, 12H). <sup>13</sup>C-NMR (126 MHz, CDCl<sub>3</sub>) δ 139.22, 114.12, 71.05, 70.48, 33.83, 33.76, 32.65, 29.76, 29.55, 29.49, 29.45, 29.14, 28.93, 26.19, 24.96.

ii. Synthesis of 1,3-bis(tert-butoxycarbonyl)-1-(5-(undec-10-en-1-iloxy)pentyl)guanidine. Guanidine hydrochloride (0.99 g, 10.4 mmol, 1 eq) and NaOH (1.66 g, 41.6 mmol) were added to a mixture of dioxane (20 mL) and water (10 mL). The solution was cooled to 0°C and (di-tert-butyl dicarbonate)<sub>2</sub>O (5.00 g, 22.9 mmol) was added. The mixture was stirred at room temperature for 36 hours. After evaporation, the product was purified by flash column chromatography (silica gel, eluent DCM:MeOH 97:3) obtaining 1.471 g (57%) of product and using it for the next step. 11-((5-Bromopentyl)oxy)undec-1-ene (476 mg, 1.49 mmol), 1,3-bis(tert-butoxycarbonyl)guanidine (773 mg, 2.97 mmol), and KOH (334 mg, 5.96 mmol) were dissolved in DMF (4 mL). The mixture was stirred for 24 hours at 75°C. After evaporation of the solvent the product was purified by flash column chromatography (silica gel, eluent gradient from PE:EtOAc 95:5 to 23:2). 591 mg (80%) of product were obtained. <sup>1</sup>H-NMR (500 MHz, CDCl<sub>3</sub>) δ 9.40 (br, 1H), 5.82 (ddt, 1H), 4.96 (ddd, 2H), 3.90 (t, 2H), 3.40 (2t, 4H), 2.04 (dt, 2H), 1.59 (m, 6H), 1.53 (s, 9H), 1.50 (s, 9H), 1.42-1.23 (m, 14H). <sup>13</sup>C-NMR (126 MHz, CDCl<sub>3</sub>) δ 163.95, 160.70, 155.16, 139.20, 114.10, 83.46, 78.62, 71.03, 70.66, 44.60, 33.79, 29.77, 29.52, 29.48, 29.42, 29.11, 28.91, 28.57, 28.32, 27.80, 26.18, 23.38. ESI-MS (*m/z*): 498 [M+H<sup>+</sup>].

iii. Synthesis of 1,3-bis(tert-butoxycarbonyl)-1-(5-((11-(acetylthio)undecyl)oxy)pentyl)guanidine. 1,3-Bis(tert-butoxycarbonyl)-1-(5-(undec-10-en-1-iloxy)pentyl)guanidine (150 mg, 0.3 mmol), thioacetic acid (0.23 mL, 2.8 mmol), and 2,2-dimethoxy-2-phenylacetophenone (7.8 mg, 0.03 mmol) were added to degassed MeOH (3 mL) in a quartz cuvette. The mixture was irradiated with a filtered (long-pass filter, 350 nm cutoff) high pressure mercury lamp (100 W) under stirring for 8 hours. After evaporation, the product was purified by flash column chromatography (silica gel, eluent PE:EtOAc 8:2). 70 mg (41%) of product were obtained. <sup>1</sup>H-NMR (500 MHz, CDCl<sub>3</sub>) δ 9.39 (br, 1H), 9.20 (br, 1H), 3.89 (t, 2H), 3.39 (t, 4H), 2.86 (t, 2H), 2.32 (s, 3H), 1.59 (m, 8H), 1.52 (s, 9H), 1.49 (s, 9H), 1.33 (m, 16H). <sup>13</sup>C-NMR (126 MHz, CDCl<sub>3</sub>) δ 196.08, 163.95, 160.70, 155.15, 83.46, 78.63, 71.04, 70.66, 44.58, 30.65, 29.78, 29.55, 29.50, 29.45, 29.42, 29.13, 29.10, 28.81, 28.56, 28.31, 28.03, 26.19, 23.38.



- iv. Synthesis of 1-(5-((11-mercaptoundecyl)oxy)pentyl)guanidinium chloride. 1,3-Bis(tert-butoxycarbonyl)-1-(5-((11-(acetylthio)undecyl)oxy)pentyl)guanidine (70 mg) was dissolved in MeOH (2 mL), and HCl (37%, 0.2 mL) was added while stirring under nitrogen atmosphere. The solution was stirred at 77°C for 4 hours. After evaporation, the product was used as it was for the ligand exchange reaction.

### B.2.3 Synthesis of Lig3 and 4

The synthesis of Lig3 and 4 were performed as previously reported elsewhere.<sup>97,369</sup>

### B.2.4 Synthesis of Lig5

- i. Synthesis of 5-(undec-10-en-1-iloxy)-N,N,N-trimethylpentan-1-aminium bromide. 11-((5-Bromopentyl)oxy)undec-1-ene (250 mg, 0.78 mmol) and trimethylamine (4.2 M in EtOH, 4.75 mL, 15.7 mmol) were mixed in a pressure tube and stirred at 78°C for 4 days. After evaporation, the product was purified by flash chromatography column (basic alumina, eluent gradient from DCM:MeOH 24:1 to MeOH). 247 mg (83%) of product were obtained. <sup>1</sup>H-NMR (500 MHz, MeOD)  $\delta$  5.82 (ddt, 1H), 5.00 (ddd, 1H), 4.96-4.90 (m, 1H), 3.49 (t, 2H), 3.45 (t, 2H), 3.43-3.37 (m, 2H), 3.18 (s, 9H), 2.05 (m, 2H), 1.85 (m, 2H), 1.68 (m, 2H), 1.57 (m, 2H), 1.47 (m, 2H), 1.43-1.26 (m, 12H). <sup>13</sup>C-NMR (126 MHz, MeOD)  $\delta$  138.78, 113.50, 70.68, 70.08, 66.43, 52.40, 33.50, 29.34, 29.28, 29.18, 29.15, 28.80, 28.73, 28.70, 25.86, 22.74, 22.41. ESI-MS (*m/z*): 298 [M-Br]<sup>+</sup>.
- ii. Synthesis of 5-((11-(acetylthio)undecyl)oxy)-N,N,N-trimethylpentan-1-aminium bromide. 5-(Undec-10-en-1-iloxy)-N,N,N-trimethylpentan-1-aminium bromide (225 mg, 0.59 mmol), thioacetic acid (400  $\mu$ L, 5.47 mmol), and 2,2-dimethoxy-2-phenylacetophenone (15.4 mg, 0.059 mmol) were dissolved in degassed MeOH (1.8 mL) in a quartz cuvette. The mixture was irradiated with a filtered (long-pass filter, 350 nm cut-off) high pressure mercury lamp (100 W) under stirring for 5 hours. After evaporation, the product was purified by flash column chromatography (basic alumina, eluent gradient from DCM:MeOH 24:1 to 8:2) 130 mg (48%) of product were obtained. <sup>1</sup>H-NMR (500 MHz, MeOD)  $\delta$  3.48 (t, 2H), 3.45 (t, 2H), 3.41 (m, 2H), 3.19 (s, 9H), 2.88 (t, 2H), 2.33 (s, 3H), 1.85 (m, 2H) 1.68 (m, 2H), 1.57 (m, 4H), 1.48 (dt, 2H), 1.43-1.25 (m, 14H). <sup>13</sup>C-NMR (126 MHz, MeOD)  $\delta$  196.33, 70.65, 70.02, 66.39, 52.29,

29.41, 29.36, 29.31, 29.25, 29.20, 28.82, 28.80, 28.51, 28.41, 25.91, 22.80, 22.40. ESI-MS ( $m/z$ ): 374 [M-Br]<sup>+</sup>

- iii. Synthesis of 5-((11-mercaptoundecyl)oxy)-N,N,N-trimethylpentan-1-aminium bromide. 5-((11-(Acetylthio)undecyl)oxy)-N,N,N-trimethylpentan-1-aminium bromide (55.9 mg, 0.123 mmol) was dissolved in degassed MeOH (2 mL) and HCl (37%, 200  $\mu$ L) was added under nitrogen atmosphere. The solution was refluxed for 6 hours. The product, after evaporation, was used without further purification for the ligand exchange reaction.

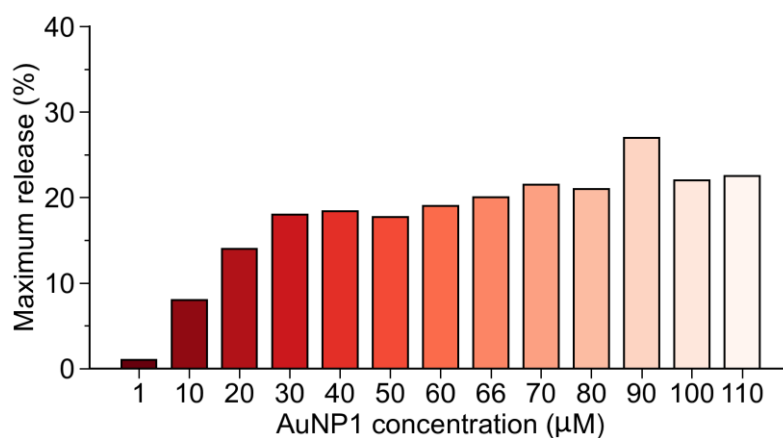
### B.2.5 Synthesis of Lig6

- i. Synthesis of 17-bromoheptadec-1-ene. Magnesium turnings (100 mg, 4.11 mmol), and dry THF (1 mL) were added to a previously dried flask. 1,2-Dibromoethane (15  $\mu$ L) was added to activate the magnesium. Previously vacuum-distilled 11-bromoundecene (500  $\mu$ L, 3.14 mmol) was dissolved in dry THF (2 mL), and the solution was added dropwise under stirring at 50°C. After 4 hours, the mixture was cooled in an ice bath. A solution of LiCuCl<sub>4</sub> was prepared dissolving LiCl (5.3 mg, 0.12 mmol) and anhydrous CuCl<sub>2</sub> (8.3 mg, 0.062 mmol) in dry THF (0.6 mL), to this solution was then added 1,6-dibromohexane (967  $\mu$ L, 6.29 mmol) dissolved in dry THF (2 mL). The Grignard solution was then added dropwise to the other organic solution while stirring under nitrogen atmosphere in an ice bath. After 2.5 hours, the reaction was quenched with a saturated solution of NH<sub>4</sub>Cl in water. The aqueous phase was extracted with DCM (3×5 mL), and the organic phases were collected and combined with the initial THF one. After evaporation, the product was purified by flash column chromatography (silica gel, eluent n-hexane). 405 mg (41%) of product were collected. <sup>1</sup>H-NMR (500 MHz, CDCl<sub>3</sub>)  $\delta$  5.84 (ddt, 1H), 5.01 (ddd, 1H), 4.95 (ddt, 1H), 3.43 (m, 2H), 2.06 (m, 2H), 1.87 (m, 2H), 1.51 - 1.21 (m, 24H). <sup>13</sup>C-NMR (126 MHz, CDCl<sub>3</sub>)  $\delta$  139.27, 114.09, 34.04, 33.84, 32.86, 29.67, 29.63, 29.56, 29.53, 29.46, 29.17, 28.96, 28.79, 28.20.
- ii. Synthesis of N,N,N-trimethylheptadec-16-en-1-aminium bromide. 17-Bromoheptadec-1-ene (260 mg, 0.82 mmol) was mixed with a trimethylamine solution (4.2 M in EtOH, 4.0 mL) in a pressure tube. The mixture was stirred at 78°C for 3 days. The solvent was then evaporated, and the product was purified by flash column chromatography (silica gel, eluent gradient from DCM:MeOH 9:1 to 8:2 + 10 mL/L Et<sub>3</sub>N). 292 mg (95%) of

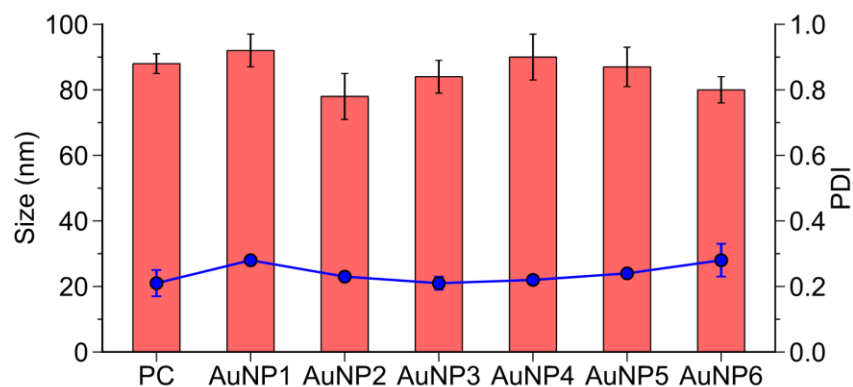
product were collected.  $^1\text{H-NMR}$  (500 MHz, MeOD)  $\delta$  5.82 (ddt, 1H), 5.00 (ddd, 1H), 4.93 (ddd, 1H), 3.40 (m, 2H), 3.18 (s, 9H), 2.06 (m, 2H), 1.82 (m, 2H), 1.51-1.23 (m, 24H).  $^{13}\text{C-NMR}$  (126 MHz, MeOD)  $\delta$  138.75, 113.44, 66.50, 52.30, 33.53, 29.40, 29.37, 29.28, 29.23, 29.21, 28.88, 28.85, 28.74, 25.99, 22.61.

- iii. Synthesis of 17-(acetylthio)-N,N,N-trimethylheptadecan-1-aminium bromide. N,N,N-Trimethylheptadec-16-en-1-aminium bromide (94 mg, 0.25 mmol) and thioacetic acid (168  $\mu\text{L}$ , 2.30 mmol) were dissolved in degassed MeOH (1.5 mL) in a quartz cuvette. The mixture was irradiated with a filtered (long-pass filter, 350 nm) high pressure mercury lamp (100 W) under stirring. After 5.5 hours, the mixture was evaporated, and the product was purified by flash column chromatography (silica gel, eluent gradient from DCM:MeOH 95:5 to MeOH). 66 mg (58%) of product were obtained.  $^1\text{H-NMR}$  (500 MHz, MeOD)  $\delta$  3.38 (m, 2H), 3.17 (s, 9H), 2.88 (t, 2H), 2.32 (s, 3H), 1.82 (m, 2H), 1.57 (m, 2H), 1.48-1.25 (m, 26H).  $^{13}\text{C-NMR}$  (126 MHz, MeOD)  $\delta$  196.17, 66.48, 52.17, 29.38, 29.36, 29.29, 29.27, 29.21, 29.18, 28.86, 28.83, 28.48, 28.42, 25.98, 22.57. ESI-MS ( $m/z$ ): 372.4 [M-Br] $^+$ .
- iv. Synthesis of N-17-(mercapto)-N,N,N-trimethylheptadecan-1-aminium bromide. Under nitrogen atmosphere, 17-(acetylthio)-N,N,N-trimethylheptadecan-1-aminium bromide (55.7 mg, 0.123 mmol) was dissolved in MeOH (2 mL), and HCl (37%, 200  $\mu\text{L}$ ) was added. The solution was refluxed under nitrogen atmosphere for 6 hours. After evaporation, EtOH (2 mL) was added and evaporated again. The product was used as it was for the AuNP synthesis without further purification.

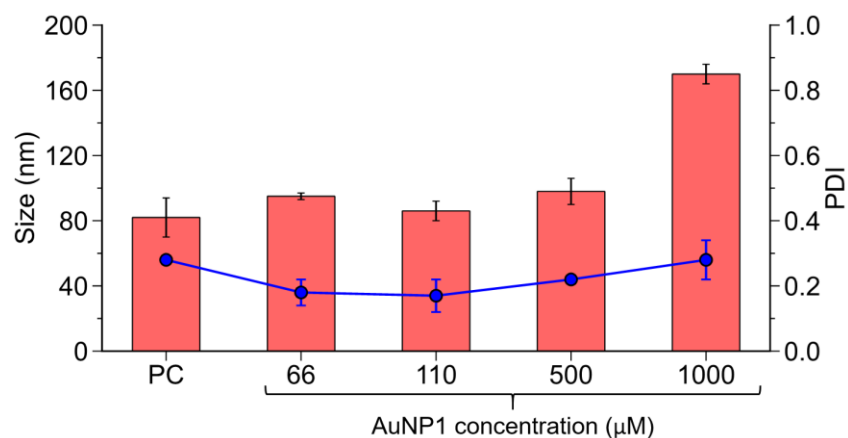
### B.3 Additional experiments on calcein-loaded liposomes



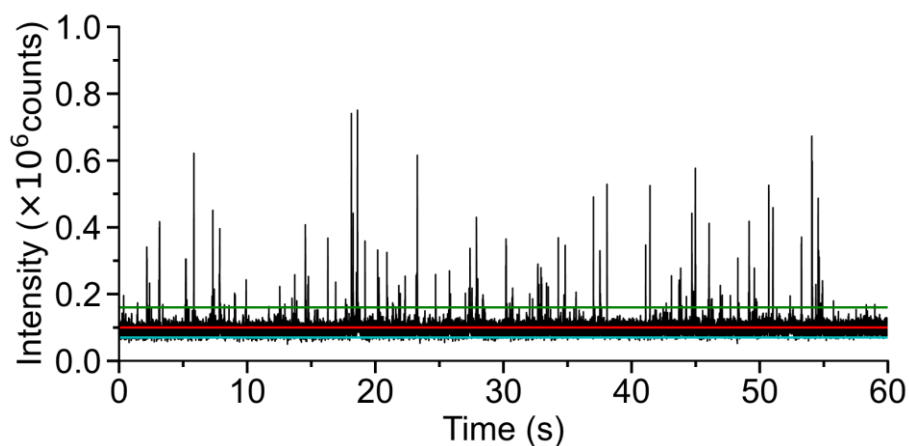
**Figure B-3.** Maximum release of calcein after incubation with increasing concentrations of AuNP1 (HEPES 10 mM, NaCl 100 mM, pH 7.0, [PC] = 22  $\mu\text{M}$ , 25 $^\circ\text{C}$ ).



**Figure B-4.** Hydrodynamic size (red bars) and PDI (blue dots) of PC liposomes before and after the addition of each of the six AuNPs. Experimental conditions: [HEPES] = 10 mM, [NaCl] = 100 mM, pH 7.0, [PC] = 22  $\mu$ M, 25°C.

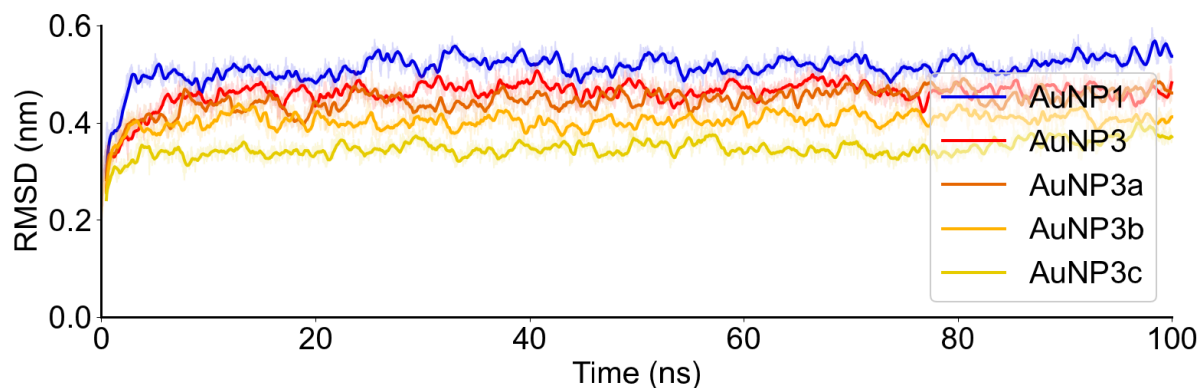


**Figure B-5.** Hydrodynamic size (red bars) and PDI (blue dots) of PC liposomes before and after the addition of AuNP1. Experimental conditions: [HEPES] = 10 mM, [NaCl] = 100 mM, pH 7.0, [PC] = 22  $\mu$ M, 25°C.

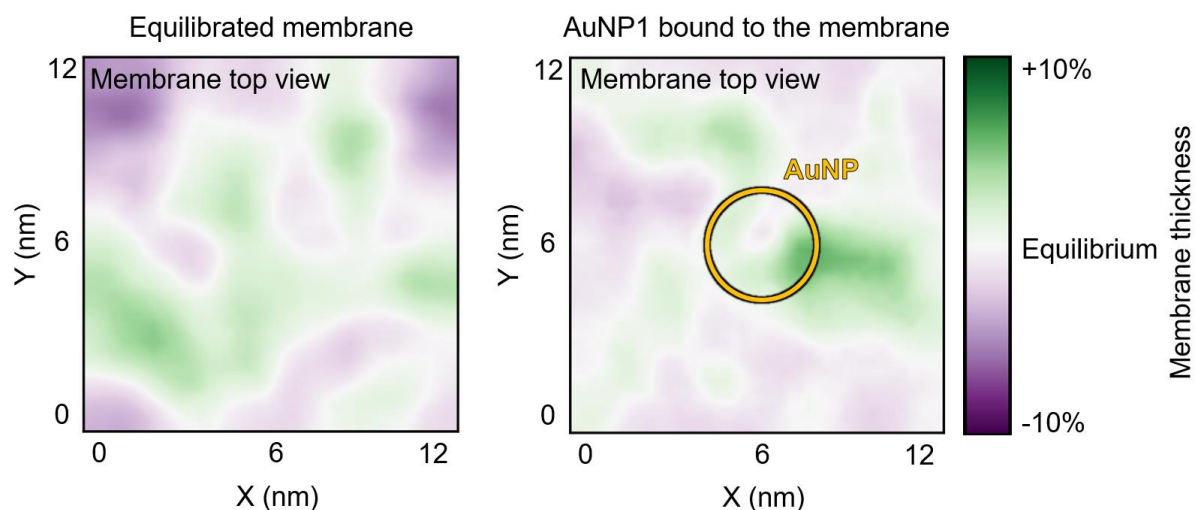


**Figure B-6.** Time dependent emission intensity of PC charged liposomes (black) and intensity of the set threshold: 0.07 (cyan), 0.10 (red), and 0.16 (green).

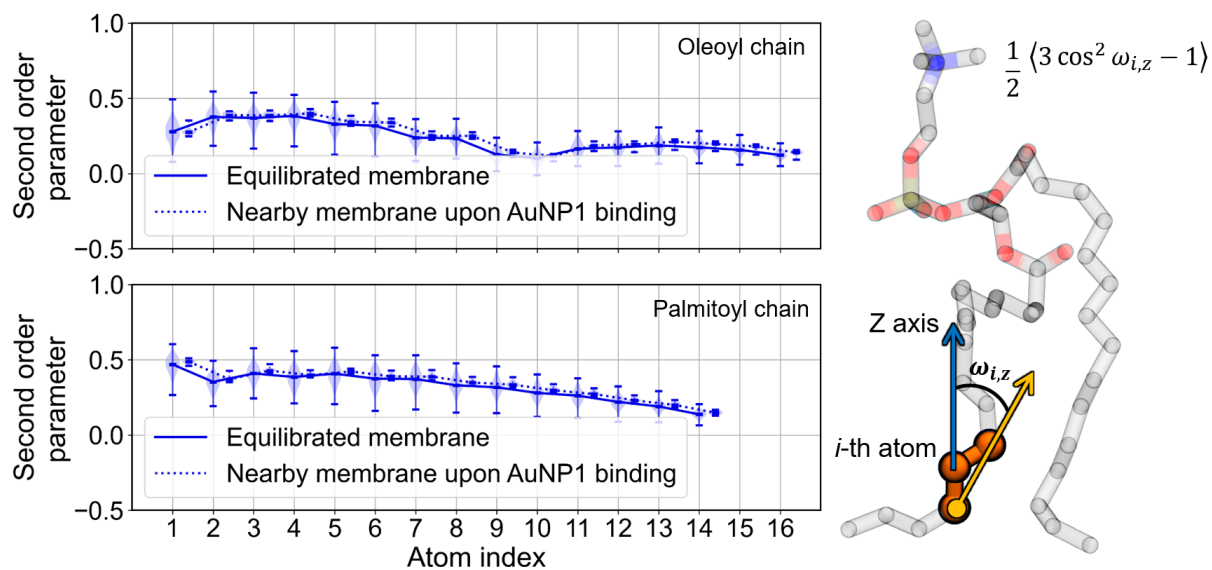
## B.4 Additional computational analysis



**Figure B-7.** RMSD of the AuNPs. All the structures converged within the first 5 ns of simulation as evidenced by the flattening of the curves.



**Figure B-8.** Map of the membrane thickness from a top view. The unperturbed equilibrated membrane displayed an equilibrium value of  $3.79 \pm 0.27$  nm. Upon the binding of AuNP1, the lipids with XY coordinates closer than 3.5 nm from the XY coordinates of the AuNPs COM showed an unchanged thickness of  $3.83 \pm 0.25$  nm.

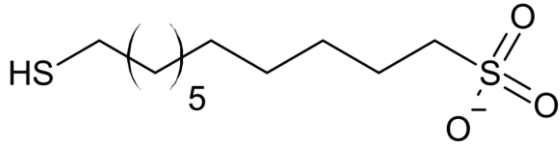
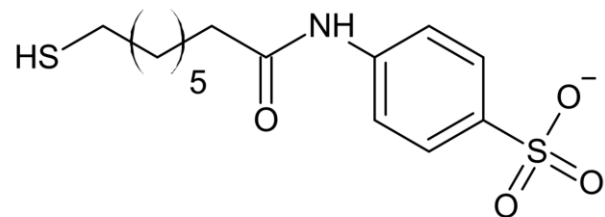
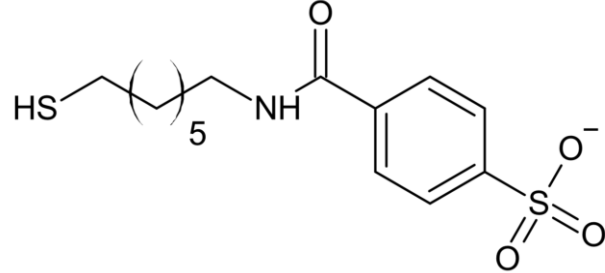
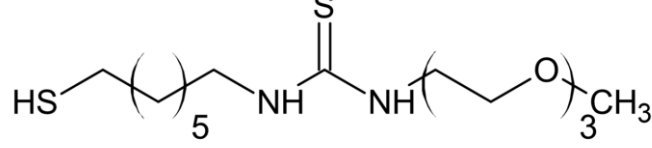
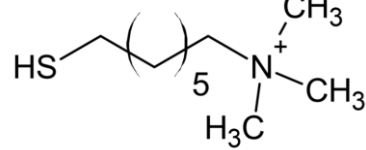


**Figure B-9.** Lipid order parameter for the oleoyl (top panel) and palmitoyl (bottom panel) tails of the POPC lipids. The order parameters of the membrane-AuNP complex are calculated for lipids at the contacting region, as defined in the caption of **Figure B-8**. One lipid molecule is shown in gray transparency.

# APPENDIX C. CHEMOSENSOR-ANALYTE DATASET, CATECHOLAMINES IN THE HUMAN BRAIN, AND VIRTUAL SCREENING RESULTS

## C.1 Training dataset

**Table C-1.** Chemical structure of the 11 unique coating thiols present in our training dataset.

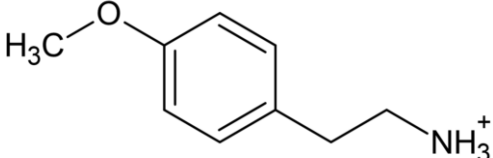
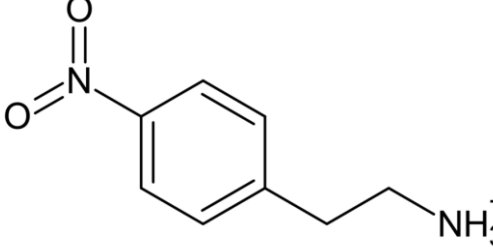
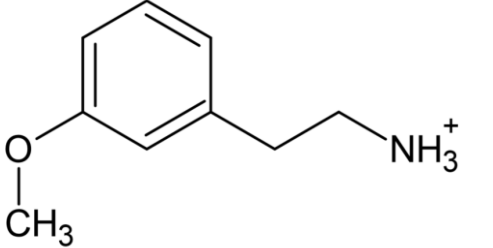
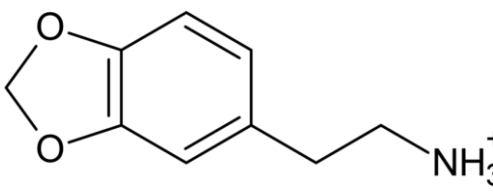
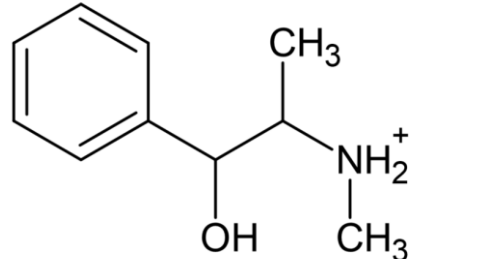
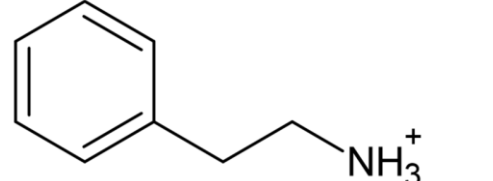
Ligand ID	Ligand structure
1	
2	
3	
4	
5	

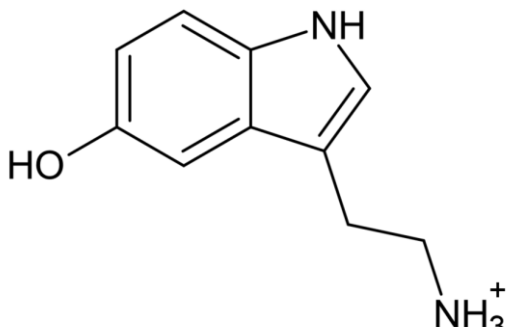
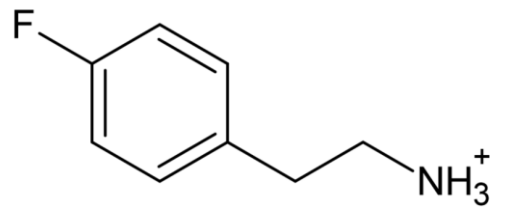
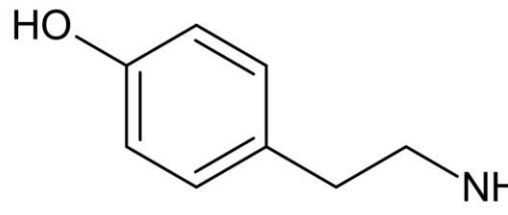
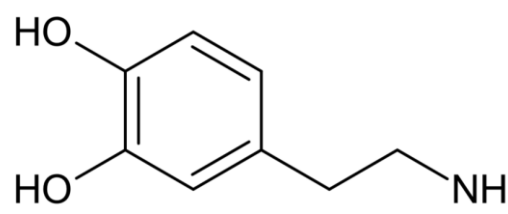
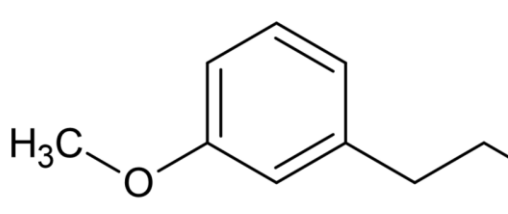
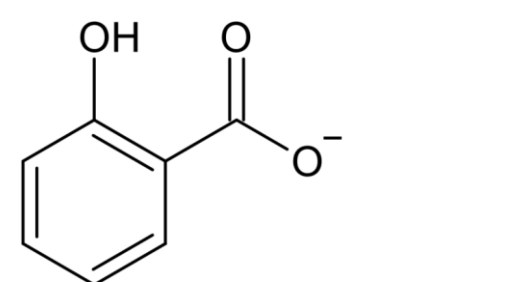
6	
7	
8	
9	
10	
11	

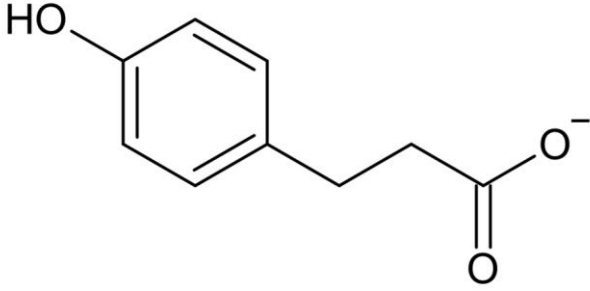
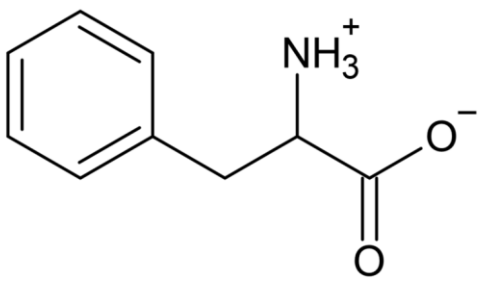
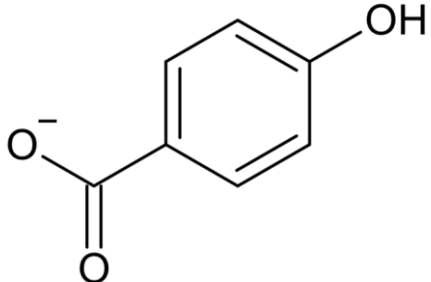
**Table C-2.** Chemical structure of the 17 unique analytes present in our training dataset.

Analyte ID	Analyte structure
1	
2	



3	 <p>Chemical structure of 4-(3-(methoxyphenyl)propyl)ammonium ion. It consists of a benzene ring with a methoxy group (<math>\text{H}_3\text{C}-\text{O}</math>) at the 3-position and a propyl chain at the 4-position, terminating in a protonated primary amine group (<math>\text{NH}_3^+</math>).</p>
4	 <p>Chemical structure of 4-(3-(nitrophenyl)propyl)ammonium ion. It consists of a benzene ring with a nitro group (<math>\text{O}=\text{N}</math>) at the 3-position and a propyl chain at the 4-position, terminating in a protonated primary amine group (<math>\text{NH}_3^+</math>).</p>
5	 <p>Chemical structure of 4-(3-(methoxyphenyl)propyl)ammonium ion. It consists of a benzene ring with a methoxy group (<math>\text{O}-\text{CH}_3</math>) at the 3-position and a propyl chain at the 4-position, terminating in a protonated primary amine group (<math>\text{NH}_3^+</math>).</p>
6	 <p>Chemical structure of 4-(3-(1,3-dioxol-5-yl)phenyl)propylammonium ion. It consists of a benzene ring with a 1,3-dioxol-5-yl group at the 3-position and a propyl chain at the 4-position, terminating in a protonated primary amine group (<math>\text{NH}_3^+</math>).</p>
7	 <p>Chemical structure of 1-(1-hydroxy-2-methylphenylethyl)propan-2-aminium ion. It consists of a benzene ring with a 1-hydroxy-2-methylphenylethyl group at the 1-position and a methylammonium group (<math>\text{NH}_2^+</math>) with a methyl group (<math>\text{CH}_3</math>) attached to the nitrogen at the 2-position.</p>
8	 <p>Chemical structure of 4-phenylpropylammonium ion. It consists of a benzene ring with a propyl chain at the 4-position, terminating in a protonated primary amine group (<math>\text{NH}_3^+</math>).</p>

9	 <p>Chemical structure of 5-(2-aminoethyl)-7-hydroxytryptamine (5-HT). It consists of an indole ring system with a hydroxyl group at the 7-position and a 2-aminoethyl chain at the 3-position.</p>
10	 <p>Chemical structure of 4-(2-aminoethyl)aniline. It consists of a benzene ring with a fluorine atom at the 1-position and a 2-aminoethyl chain at the 4-position.</p>
11	 <p>Chemical structure of 4-(2-aminoethyl)phenol. It consists of a benzene ring with a hydroxyl group at the 1-position and a 2-aminoethyl chain at the 4-position.</p>
12	 <p>Chemical structure of 3,4-dihydroxyphenylethylamine (DOPA). It consists of a benzene ring with hydroxyl groups at the 3 and 4 positions and a 2-aminoethyl chain at the 1-position.</p>
13	 <p>Chemical structure of 3-(2-aminoethyl)anisole. It consists of a benzene ring with a methoxy group at the 1-position and a 2-aminoethyl chain at the 3-position.</p>
14	 <p>Chemical structure of 3-hydroxybenzoate. It consists of a benzene ring with a hydroxyl group at the 3-position and a carboxylate group at the 1-position.</p>

15	 <p>Chemical structure of 4-(4-hydroxyphenyl)butanoate ion. It consists of a benzene ring with a hydroxyl group (HO-) at the para position relative to a propyl chain. The propyl chain is attached to the benzene ring at the 4-position and ends in a carboxylate group (-COO<sup>-</sup>).</p>
16	 <p>Chemical structure of 2-amino-3-phenylpropanoate ion. It consists of a benzene ring attached to a propyl chain. The propyl chain has an amino group (-NH<sub>3</sub><sup>+</sup>) at the 2-position and a carboxylate group (-COO<sup>-</sup>) at the 1-position.</p>
17	 <p>Chemical structure of 4-hydroxybenzoate ion. It consists of a benzene ring with a hydroxyl group (-OH) at the para position relative to a carboxylate group (-COO<sup>-</sup>).</p>

**Table C-3.** AuNP-analyte dyads included in the dataset used for training our MD-based protocol. The chemical structure of the coating thiols and the analytes are shown in **Table C-1** and **Table C-2**, respectively.

Dyad ID	Ligand ID	Analyte ID	Original ligand ID <sup>a</sup>	Original analyte ID <sup>b</sup>	Reference	$K_{bind}^{exp}$	$\sigma_K^c$	$\Delta G_{bind}^{exp}$ (kcal mol <sup>-1</sup> )	$\sigma_G^d$ (kcal mol <sup>-1</sup> )
1	1	1	S1	19	<sup>96</sup>	$2.2 \times 10^6$	$0.1 \times 10^6$	8.7	< 0.1 > -0.1
2	2	1	S2	19	<sup>96</sup>	$1.3 \times 10^6$	$0.1 \times 10^6$	8.4	< 0.1 > -0.1
3	1	2	S1	18	<sup>96</sup>	$6.1 \times 10^5$	$1.4 \times 10^5$	7.9	+0.1 -0.2
4	2	2	S2	18	<sup>96</sup>	$5.1 \times 10^5$	$0.3 \times 10^5$	7.8	< 0.1 > -0.1
5	1	3	S1	11	<sup>96</sup>	$4.8 \times 10^5$	$0.5 \times 10^5$	7.8	+0.1 -0.1
6	1	4	S1	14	<sup>96</sup>	$4.6 \times 10^5$	-	7.8	- -
7	1	5	S1	10	<sup>96</sup>	$4.1 \times 10^5$	$0.4 \times 10^5$	7.7	+0.1 -0.1
8	1	6	S1	12	<sup>96</sup>	$3.9 \times 10^5$	$0.3 \times 10^5$	7.7	< 0.1 > -0.1
9	1	7	S1	15	<sup>96</sup>	$3.7 \times 10^5$	-	7.6	- -
10	3	1	S3	19	<sup>96</sup>	$3.6 \times 10^5$	$0.1 \times 10^5$	7.6	< 0.1 > -0.1
11	1	8	S1	1	<sup>96</sup>	$3.6 \times 10^5$	-	7.6	- -
12	1	9	S1	13	<sup>96</sup>	$2.7 \times 10^5$	$0.3 \times 10^5$	7.5	+0.1 -0.1

13	1	10	S1	7	<sup>96</sup>	2.6×10 <sup>5</sup>	0.6×10 <sup>5</sup>	7.4	+0.1 -0.2
14	1	11	S1	8	<sup>96</sup>	1.3×10 <sup>5</sup>	0.2×10 <sup>5</sup>	7.0	+0.1 -0.1
15	1	12	S1	9	<sup>96</sup>	1.2×10 <sup>5</sup>	0.2×10 <sup>5</sup>	7.0	+0.1 -0.1
16	2	13	S2	10	<sup>96</sup>	9.3×10 <sup>4</sup>	1.2×10 <sup>4</sup>	6.8	+0.1 -0.1
17	2	3	S2	11	<sup>96</sup>	8.5×10 <sup>4</sup>	1.5×10 <sup>4</sup>	6.8	+0.1 -0.1
18	4	14	-	-	Per. Comm. <sup>e</sup>	5.0×10 <sup>4</sup>	-	6.4	- -
19	5	14	1	Salicylate	<sup>97</sup>	4.5×10 <sup>4</sup>	-	6.4	- -
20	6	14	3	Salicylate	<sup>95</sup>	1.1×10 <sup>3</sup>	-	4.2	- -
21	7	14	-	-	Per. Comm. <sup>e</sup>	3.0×10 <sup>2</sup>	-	3.4	- -
22	8	14	1	4	<sup>376</sup>	1.2×10 <sup>2</sup>	0.1×10 <sup>2</sup>	2.8	< 0.1 > -0.1
23	3	2	S3	18	<sup>96</sup>	-	-	-	- -
24	3	3	S3	11	<sup>96</sup>	-	-	-	- -
25	3	13	S3	10	<sup>96</sup>	-	-	-	- -
26	1	15	S1	17	<sup>96</sup>	-	-	-	- -
27	1	16	S1	16	<sup>96</sup>	-	-	-	- -

28	8	17	1	4-hydroxy benzoate	95	-	-	-	-
29	9	14	4	Salicylate	95	-	-	-	-
30	10	14	-	-	Per. Comm. <sup>e</sup>	-	-	-	-
31	11	14	2	Salicylate	95	-	-	-	-

<sup>a</sup>Original ligand ID as reported in the source reference. <sup>b</sup>Original analyte ID as reported in the source reference. <sup>c</sup> $\sigma_K$ : Experimental standard deviation of the measurements for  $K_{bind}^{exp}$ . <sup>d</sup> $\sigma_G$ : Standard deviation of the binding free energy  $\Delta G_{bind}^{exp}$  propagated from  $\sigma_K$ . <sup>e</sup>Per. Comm.: Personal communication from Prof. Fabrizio Mancin (University of Padova) on November 26, 2019.

## C.2 Biosynthetic pathways for catecholamines

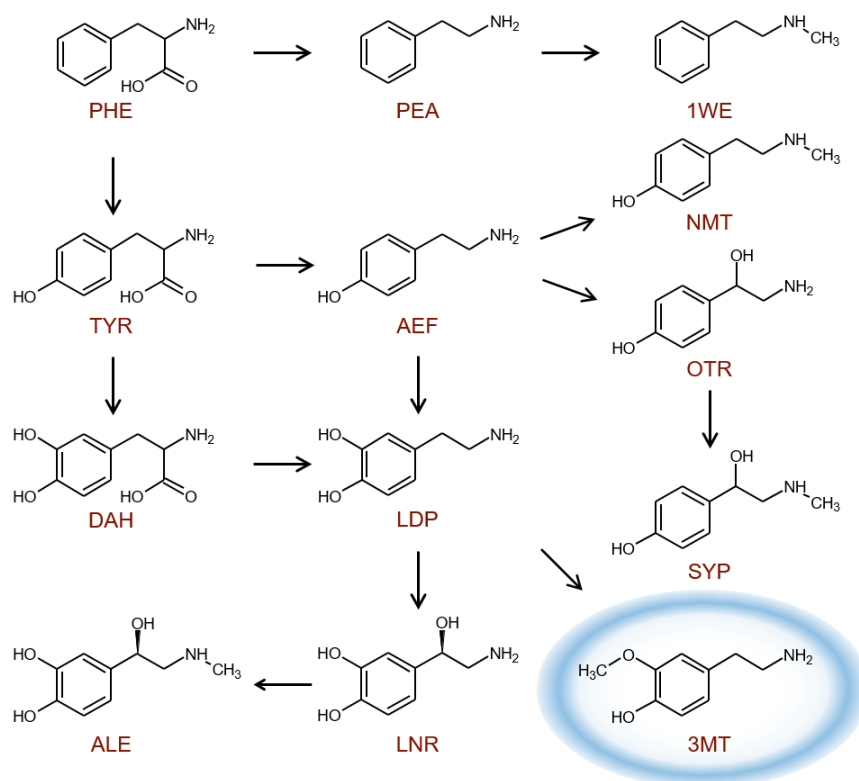


**Figure C-1.** Biosynthetic pathways for catecholamines and trace amines in the human brain. Each of the 13 molecules is joined by its identifier from the PDB database. The name of each molecule can be found in **Table C-4**.

**Table C-4.** Number of crystal structures from the PDB database that are bound to any of the 13 molecules present in the biosynthetic pathways for catecholamines and trace amines.

PDB code	Name	Crystal structures
PHE	L-Phenylalanine	67
PEA	Phenethylamine	8
1WE	N-Methylphenethylamine	2
TYR	L-Tyrosine	57
AEF	p-Tyramine	3
NMT	N-Methyltyramine	0
OTR	p-Octopamine	6
DAH	L-3,4-Dihydroxyphenylalanine	5
LDP	L-Dopamine	13
SYP	Synephrine	0
ALE	Epinephrine	3
LNR	Norepinephrine	7
3MT	3-Methoxytyramine	0
<b>Total</b>		171

### C.3 Chemosensor screening results

**Table C-5.** Results obtained from applying our MD-based protocol to our library of 100 thiols. The calculated binding free energies are for 3MT. The pocket similarity index is also reported.

<i>AA1</i>	<i>AA2</i>	$\Delta G_{bind}$ (kcal mol <sup>-1</sup> )	$SE_G^a$ (kcal mol <sup>-1</sup> )	$\eta_P$
Pro	Leu	17.3	0.6	0.75
Phe	Gln	16.1	0.4	0.82
Phe	Ser	14.5	0.4	0.85
Ile	Gln	14.3	0.5	0.60
Ile	Trp	13.0	0.3	0.43
Gln	Gly	12.8	0.5	0.78
Gly	Ile	12.8	0.5	0.75
Trp	Phe	12.8	0.6	0.64
Ala	Tyr	12.6	0.4	0.93
Pro	Pro	12.2	0.3	0.51
Leu	Trp	11.7	0.3	0.63
Ser	Leu	11.6	0.4	0.85
Tyr	Leu	11.6	0.4	0.99
Trp	Leu	11.3	0.2	0.63
Phe	Leu	11.2	0.4	0.99
Gly	Ser	11.1	0.4	0.82
Phe	Pro	11.0	0.3	0.75
Pro	Gln	10.9	0.3	0.57
Trp	Trp	10.9	0.5	0.28
Ala	Ile	10.7	0.4	0.72
Pro	Tyr	10.6	0.4	0.75
Gly	Ala	10.4	0.5	0.90

Gln	Pro	10.2	0.4	0.57
Trp	Ala	10.2	0.4	0.57
Leu	Ile	10.2	0.6	0.78
Leu	Gly	10.1	0.6	0.96
Ile	Gly	10.1	0.5	0.75
Tyr	Phe	10.1	0.3	1.00
Leu	Leu	10.1	0.5	0.98
Tyr	Ile	10.0	0.4	0.79
Ala	Leu	10.0	0.6	0.92
Trp	Gln	9.9	0.3	0.46
Ile	Pro	9.9	0.5	0.54
Ser	Ser	9.8	0.5	0.71
Pro	Ile	9.7	0.3	0.54
Gln	Tyr	9.5	0.5	0.82
Ile	Ser	9.4	0.5	0.64
Pro	Gly	9.4	0.7	0.72
Ser	Ile	9.4	0.5	0.64
Pro	Ala	9.3	0.4	0.68
Ile	Leu	9.2	0.5	0.78
Gln	Trp	9.1	0.5	0.46
Ala	Trp	9.0	0.4	0.57
Ala	Gln	8.9	0.5	0.75
Leu	Phe	8.9	0.4	0.99
Tyr	Pro	8.9	0.1	0.75
Ala	Gly	8.6	0.6	0.90
Ala	Ser	8.5	0.5	0.79
Ala	Phe	8.5	0.7	0.93
Pro	Ser	8.4	0.6	0.61
Leu	Pro	8.4	0.4	0.75
Tyr	Ser	8.4	0.5	0.86



Gly	Tyr	8.3	0.5	0.97
Phe	Trp	8.3	0.5	0.64
Tyr	Ala	8.0	0.6	0.93
Phe	Ala	7.9	0.5	0.93
Tyr	Tyr	7.8	0.3	1.00
Ser	Pro	7.8	0.3	0.61
Trp	Ile	7.6	0.2	0.43
Gly	Phe	7.4	0.2	0.96
Gln	Ile	7.4	0.5	0.60
Ser	Ala	7.3	0.5	0.79
Ala	Ala	7.3	0.5	0.86
Trp	Gly	7.2	0.4	0.60
Trp	Tyr	7.2	0.4	0.64
Ile	Phe	7.1	0.4	0.78
Phe	Ile	7.1	0.3	0.78
Phe	Gly	7.1	0.4	0.96
Trp	Pro	7.0	0.1	0.39
Ser	Trp	7.0	0.2	0.49
Ser	Gln	6.8	0.3	0.67
Leu	Ser	6.8	0.5	0.85
Tyr	Gly	6.8	0.4	0.97
Gln	Gln	6.8	0.1	0.64
Ser	Gly	6.8	0.5	0.82
Gly	Gly	6.7	0.3	0.93
Leu	Ala	6.7	0.4	0.92

Ile	Tyr	6.7	0.5	0.79
Gln	Phe	6.6	0.5	0.82
Gln	Leu	6.6	0.4	0.81
Pro	Trp	6.5	0.4	0.39
Ala	Pro	6.4	0.2	0.68
Ile	Ala	6.4	0.4	0.72
Gly	Gln	6.2	0.5	0.78
Gly	Trp	6.2	0.3	0.60
Gly	Leu	6.1	0.2	0.96
Ser	Phe	6.0	0.4	0.85
Pro	Phe	6.0	0.4	0.75
Gln	Ala	5.9	0.4	0.75
Gln	Ser	5.9	0.3	0.67
Ile	Ile	5.9	0.5	0.57
Ser	Tyr	5.9	0.5	0.86
Phe	Tyr	5.5	0.2	1.00
Leu	Tyr	5.3	0.1	0.99
Tyr	Gln	5.3	0.2	0.82
Tyr	Trp	5.1	0.2	0.64
Phe	Phe	4.8	0.1	0.99
Gly	Pro	4.4	0.1	0.72
Trp	Ser	3.4	0.3	0.49
Leu	Gln	3.1	0.1	0.81

<sup>a</sup> $SE_G$ : Standard error of the computed binding free energies.

# APPENDIX D. THEORETICAL AND COARSE-GRAINED MODELING OF ION-CAPPED METAL NANOPARTICLES

## D.1 Model development

As described in the main text, by minimizing the change of free energy  $\Delta G_{cap}$  we recover the value of  $N_{lig}$  of the highest likelihood. The first contribution,  $\Delta G_{desolv}$ , can be expressed in terms of the desolvation energy of a single ligand ( $\Delta G_{desolv}^{lig}$ ) multiplied by  $N_{lig}$  and that of the metal NP ( $\Delta G_{desolv}^M$ ). The linear trend followed by  $\Delta G_{desolv}^{lig}$  is plotted as a function of  $N_{lig}$  in **Figure D-1**. Note that  $\Delta G_{desolv}^M$  cancels out with the apolar contribution from the solvation energy of the capped NP  $\Delta G_{solv}^{apolar}$ .

### D.1.1 Solvation free energy calculations – thermodynamic integration protocol

In order to calculate the solvation free energy  $\Delta G_{desolv}^{lig}$ , we adopted the thermodynamic integration methodology. In our case, we first immersed an explicit CG citrate molecule in a box of polarizable water molecules parametrized with the refPol force field.<sup>213–215</sup> The free energy calculation was stratified into 31 runs with increasing values of the coupling parameter,  $\xi$ . The spacing between windows was of 0.05 for  $\xi < 0.6$  and 0.02 elsewhere. A value of 0.5 was used as the alpha parameter in the soft core potential.<sup>249,250</sup> For each window in the calculation, two minimizations were performed for a maximum of 5,000 steps each. The first of them used the steepest descent method, and the second one followed the Broyden-Fletcher-Goldfarb-Shanno algorithm. Once the systems were minimized, we proceeded to thermalize and pressurize to 310 K and 1 bar with a 10-ns-long simulation in the NPT statistical ensemble. This employed the Berendsen thermostat ( $\tau_B = 2.0$  ps) and the isotropic Berendsen barostat ( $\tau_P = 5.0$  ps,  $\kappa = 4.5 \times 10^{-4}$  bar<sup>-1</sup>). After the equilibration, a production run was performed for each window for 25 ns using a timestep of 20 fs and switching the Berendsen barostat for a Parrinello-Rahman barostat ( $\tau_P = 14.0$  ps,  $\kappa = 4.5 \times 10^{-4}$  bar<sup>-1</sup>).<sup>227</sup> The variations in the Hamiltonian and its derivative with respect to  $\xi$  were saved every 10 steps (0.2 ps). Finally, the solvation free energy was estimated with Bennett’s acceptance ratio method.<sup>248</sup> The aforementioned procedure was performed twice to sequentially switch off the electrostatic and van der Waals interactions, respectively.

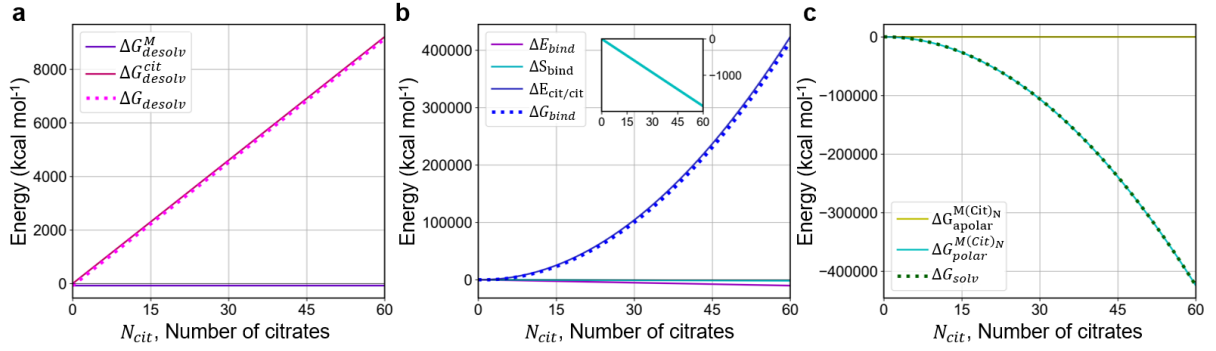


**Figure D-1.** The different contributions accounted by the main terms included in the theoretical model as a function of the number of bound citrate molecules. The plots shown are built for  $\alpha = 3$ . **a.** Breakdown of  $\Delta G_{desolv}$ . **b.** Breakdown of  $\Delta G_{bind}$ . **c.** Breakdown of  $\Delta G_{solv}$ .

### D.1.2 Citrate binding electronic energy

In order to determine the number of equivalent binding modes of citrate onto gold surfaces, we first generated a realistic, atomistic representation of an AuNP. For this, we used the NanoCrystal webserver.<sup>272</sup> The circumradius parsed to the server was 1.5 nm, and the surface energies for the gold facets were those derived by Skriver and co-workers.<sup>412</sup> The result was an AuNP formed by six (100) planes and eight (111) planes as those depicted in **Figure D-2**. As described by Al-Johani et al.,<sup>434</sup> the binding of citrate may take place via one (mono-) or two (bidentate) carboxylate groups. The multiplicities ( $\delta_m$ ) of each type of monodentate and bidentate binding modes are shown in **Figure D-2**. The displayed multiplicities consider the interchangeability of the three available carboxylate groups and that of their two oxygen atoms. Importantly, these values are expressed for individual planes, not for the entire AuNP. Notably, for the bidentate modes, each pose has a different associated binding energy depending on the pair of carboxylates involved. That is, if the two terminal groups are bound, the energetics resemble those of glutarate, whereas if the binding takes place with one terminal and the center carboxylate, the energetics resemble those of succinate. Thus, with this information, we used Equation D-1 to calculate the ensemble average of the binding electronic energy for citrate onto gold in vacuum.

$$\Delta E_{bind} = \frac{\sum_i^{modes} E_i \delta_{m,i} e^{-\frac{E_i}{k_B T}}}{\sum_i^{modes} \delta_{m,i} e^{-\frac{E_i}{k_B T}}} \quad (\text{D-1})$$

Here,  $E_i$  is the electronic binding energy associated with the  $i$ -th binding mode,  $\delta_{m,i}$  its multiplicity, and  $e^{-\frac{E_i}{k_B T}}$  the corresponding Boltzmann weighting factor. Following this scheme,

we estimated the average electronic binding energy between citrate and gold to be  $-40.9 \text{ kcal mol}^{-1}$ .

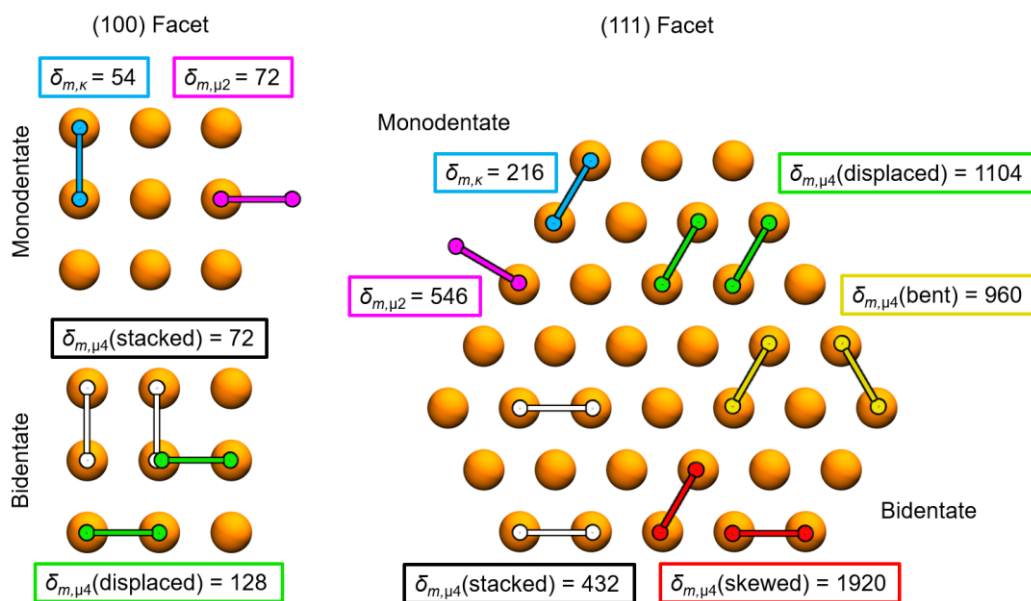


**Figure D-2.** Graphical representation of all the possible binding modes for acetate, succinate, and glutarate as described by Al-Johani et al.<sup>434</sup> using their same nomenclature. Each binding mode is accompanied by its multiplicity, that is, equivalent binding orientations in the grid considering the interchangeability of the carboxylate groups and their respective oxygen atoms. Gold atoms are shown in orange.

### D.1.3 Entropic contribution to binding

In order to account for the entropic contribution of binding a ligand (e.g. citrate) onto a metallic surface, three terms were considered. These terms account for the decrease in translational and rotational degrees of freedom, as well as the insurgence of vibrational modes upon binding. The total change in entropy can thus be written as in Equation D-2.

$$\Delta S_{bind} = \Delta S_{trans}^{\downarrow} + \Delta S_{rot}^{\downarrow} + \Delta S_{vib}^{\uparrow} \quad (\text{D-2})$$

The translational loss of entropy is calculated from the entropy of an ideal gas employing the Sackur-Tetrode equation (Equation D-3).

$$\Delta S_{trans}^{\downarrow} = R \left[ \log \left( \frac{10^{-3}}{c_{lig} N_A \Lambda^3} \right) + \frac{5}{2} \right] \quad (\text{D-3})$$

Where  $c_{lig}$  is the molar concentration of the ligand,  $R$  is the ideal gas constant,  $N_A$  is Avogadro's number, and  $\Lambda$  is the thermal de Broglie wavelength given by Equation D-4:

$$\Lambda = \left( \frac{h^2}{2\pi m_{lig} k_B T} \right)^{\frac{1}{2}} \quad (\text{D-4})$$

Where  $m_{lig}$  is the mass of one ligand molecule,  $k_B$  is the Boltzmann constant, and  $T$  the absolute temperature in this case set to 310 K. Similarly, the loss of molecular rotational entropy was calculated from Equation D-5.

$$\Delta S_{rot}^{\downarrow} = 3R \left[ \frac{1}{2} + \log \left( \frac{8\pi^2 I_g k_B T}{h^2} \right) \right] \quad (\text{D-5})$$

Where  $I_g$  is the geometric mean of the molecule's moments of inertia, as stated by Equation D-6.

$$I_g = \sqrt[3]{I_1 I_2 I_3} \quad (\text{D-6})$$

Where  $I_1$ ,  $I_2$ , and  $I_3$  are the three principal moments of inertia calculated from the diagonalization of the tensor of inertia. In our case, we derived the moments of inertia from an atomistic MD simulation of a single citrate molecule immersed in water. The setup of this simulation is described in Appendix D.1.6. Finally, the decrease in vibrational entropy arises from the formation of metal-ligand bonds. Their contribution was estimated from Equation D-7.

$$\Delta S_{vib}^{\uparrow} = R \left[ \frac{1}{2} - \ln \frac{2\pi k_B T}{h\omega_b} \right] \quad (\text{D-7})$$

Where  $\omega_b$  is the stretching frequency of the formed bond. For the specific case of citrate, the frequency for the Au-O bonds was taken as  $1,638 \text{ cm}^{-1}$ , as measured by Wulandari et al.<sup>498</sup> It is noteworthy that, as evidenced in **Figure D-1**, the entropic correction for citrate binding onto gold is negligible compared to the process's enthalpy.

#### D.1.4 Derivation of $\Delta E_{lig/lig}$

The electric potential energy of a charge density distribution  $\rho_e(\mathbf{r})$  is given by Equation D-8.

$$U_{elec}(\mathbf{r}) = \frac{1}{2} \int \psi(\mathbf{r}) \rho_e(\mathbf{r}) dV \quad (\text{D-8})$$

In which  $\psi(\mathbf{r})$  is the electric potential generated by the charge distribution,  $\rho_e(\mathbf{r})$ , and the integral covers the entire space. For the case of a hollow sphere with uniform surface charge density, the charge distribution function can be written as in Equation D-9.

$$\rho_e(N_{lig}, \mathbf{r}) = \frac{q(N_{lig})}{4\pi r^2} \delta_D(r - R_{NP}) \quad (\text{D-9})$$

Where  $R_{NP}$  is the radius of the NP,  $q(N)$  is the total charge. In order to generalize our model, we consider a generic polyprotic ligand that adopts a mean deprotonation state  $\alpha$  when bound to the NP. For a ligand with three acid protons like citrate, the mean deprotonation state lies between 0 and 3, that is  $\alpha \subseteq [0, 3]$ . Then, the total charge may be written as in Equation D-10.

$$q(N_{lig}) = -\alpha N_{lig} \quad (\text{D-10})$$

On the other hand, combining Equation D-9 with Gauss's law, it is possible to obtain the electric potential generated by the charge distribution in a medium of dielectric constant  $\epsilon_r$ . This is given by Equation D-11.

$$\psi(N_{lig}, \mathbf{r}) = \begin{cases} 0, & r < R_{NP} \\ -\frac{\alpha N_{lig}}{4\pi\epsilon_0\epsilon_r}, & r \geq R_{NP} \end{cases} \quad (\text{D-11})$$

Substituting Equation D-9 and Equation D-11 into Equation D-8, and solving the integral, we obtain an expression for the electric potential energy as a function of the number of bound ligands (Equation D-12).

$$U_{elec}(N_{lig}, \epsilon_r) = \frac{\alpha^2 N_{lig}^2}{8\pi\epsilon_0\epsilon_r R_{NP}} \quad (\text{D-12})$$

Note that this expression assumes each incoming charge as independent from the rest; however, each ligand constrains the incorporation of  $\alpha$  fundamental charges to the system. Thus, we can write  $\Delta E_{lig/lig}$  as in Equation D-13 and Equation D-14.

$$\Delta E_{lig/lig}(N_{lig}) = U_{elec}(N_{lig}, \epsilon_r = 1) - N_{lig} * U_{elec}(N_{lig} = 1, \epsilon_r = 1) \quad (\text{D-13})$$

$$\Delta E_{lig/lig}(N_{lig}) = \frac{\alpha^2 N_{lig}}{8\pi\epsilon_0 R_{NP}} (N_{lig} - 1) \quad (\text{D-14})$$

### D.1.5 Derivation of the polar solvation term

The polar component for the solvation of a sphere with a charge distribution given by  $\rho_e(N_{lig}, \mathbf{r})$  can be written as in Equation D-15.

$$\Delta G_{solv}^{polar}(N_{lig}) = U_{elec}(N_{lig}, \epsilon_r = \epsilon_{H_2O}) - U_{elec}(N_{lig}, \epsilon_r = 1) \quad (D-15)$$

By substituting Equation D-12 into Equation D-15, we obtain Equation D-16.

$$\Delta G_{solv}(N_{lig}) = \frac{\alpha^2 N_{lig}^2}{8\pi\epsilon_0 R_{NP}} \left( \frac{1}{\epsilon_{H_2O}} - 1 \right) \quad (D-16)$$

Equation D-14 and Equation D-16 imply that the citrate-citrate and citrate-solvent interactions is mainly electrostatic. Thus, the theoretical framework presented here remains valid for small, charged ligands that do not affect greatly the NP's hydrophobicity.

### D.1.6 Explicit citrate coarse-grained model for solvation free energy calculations

For the calculation of the solvation free energy of one citrate molecule (i.e.  $\Delta G_{desolv}^{lig}$ , Appendix D.1.1), we adopted an explicit CG representation. The model for citrate corresponded to three consecutive beads of type Qda as implemented in the standard Martini force field. Each bead had a charge of -1 e to reproduce the most populated protonation state of fully solvated citrate molecules. The parameters used for the chemical bonds were  $k_b = 5,000 \text{ kJ mol}^{-1} \text{ nm}^{-2}$  and  $l_0 = 0.52 \text{ nm}$ , the typical inter-bead distance in the Martini force field. The parameters used for the angle between the beads were  $k_\theta = 5,000 \text{ kJ mol}^{-1} \text{ rad}^{-2}$  and  $\theta_0 = 111.11^\circ$ .

The explicit-citrate CG model was parametrized against atomistic MD simulations. In detail, the equilibrium angle  $\theta_0$  was obtained from a 100-ns-long, atomistic MD simulation of citrate parametrized with the Generalized Amber Force Field (GAFF)<sup>197</sup> in TIP3P water.<sup>191</sup> This simulation was also used to calculate the three main moments of inertia for a citrate molecule ( $I_i$ , Appendix D.1.3). In addition, the same atomistic simulation was used to obtain the projected area per citrate molecule onto our AuNPs (Appendix D.2).

## D.2 Estimation of citrate surface coverage

The fraction of the surface area covered by citrate molecules,  $\chi_{cit}$ , was calculated by means of Equation D-17.

$$\chi_{cit}(N_{cit}) = \frac{N_{cit}a_{cit}}{a_{NP}} \quad (\text{D-17})$$

In which  $a_{NP}$  is the total surface area of the NP and  $a_{cit}$  is the area covered by one citrate molecule. The total area,  $a_{NP}$ , was estimated as  $4\pi rR_{NP}^2$  yielding a value of 21.2 nm<sup>2</sup>. The number  $N_{cit}$  was estimated to be between 28 and 33 from the model described in Chapter VII and deepened in Appendix D.1. The area per citrate molecule  $a_{cit}$  was calculated from the atomistic MD simulations of citrate in water described in Appendix D.1.6. This calculation was performed by projecting the van der Waals surface of one citrate molecule onto the XY plane for a series of MD-accessed conformers and calculating the projected area. Specifically, the structure of citrate was withdrawn every 10 ps from the trajectory file. For each of these states, 100 random rotations were generated. Then, the molecular surface of each of these configurations was projected onto the XY plane, and the area was estimated. The distribution of all the calculated areas is shown in **Figure D-3**.

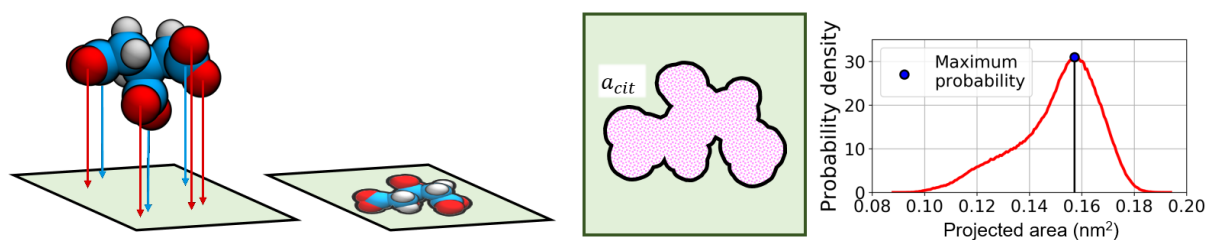


**Figure D-3.** Illustration of the method employed for the calculation of the projected surface area of citrate. For every frame in the trajectory, a series of orientations were sampled. The van der Waals surface was then projected onto the XY plane, and its area was calculated. The figure also shows the probability distribution function of the projected area, which has a maximal probability at 0.16 nm<sup>2</sup>. Carbon atoms are shown in cyan, oxygen atoms in red, and hydrogen atoms in white. The XY plane is colored green.

### D.3 Counterion residence time analysis and sampling of slow degrees of freedom

For this study, we had to ensure that the rotational degrees of freedom of the implicit-citrate CG NPs were exhaustively sampled at short values of  $CVI$ . To understand the effectiveness of our PMF calculations, we evaluated four distinct sampling protocols. The first protocol (referred to as P1) consisted of short 25-ns-long window simulations. In the second protocol, P2, the setup was similar. The frames where  $CVI > 1.2$  nm were simulated as in P1, but the windows with  $CVI \leq 1.2$  nm were simulated for 250 ns. P3, the third protocol, implied more



brusque modifications onto the coordinates files of frames with  $CVI \leq 1.2$  nm. From these frames on P2, the counterions residing 0.7 nm from any metal bead for at least 50 ns were exchanged with water molecules in the bulk. Once the ions were displaced, the same frames were simulated for 250 ns. The last protocol, P4, included the simulated annealing described in Chapter VII. The described protocols were tested on two systems. Both systems involved NPs with a total charge of -40 e (charge density  $1.9 \text{ e nm}^{-2}$ ), and they had respective ionic strengths of 30 and 70 mM.

As can be seen from **Figure D-4**, the estimated free energy of dimerization varies significantly depending on the assumed sampling protocol. Even though the charged beads follow a uniform distribution on the NPs, their placement is not perfectly symmetrical. This leads to the distinguishability of states depending on the relative orientation of both NPs. When P1 and P2 are compared, it becomes evident that the energy profiles are smoothed as longer times were sampled in each window. This indicates that the NP explored more widely their rotational degrees of freedom. The local energy minima visited by the NPs is a consequence of the formation of a suboptimal network of salt bridges between metal charged beads and sodium counterions at different NP orientations.

To understand better the dynamics of the surrounding ions, we computed the residence time of each binding event onto the metallic surfaces. **Figure D-4b** shows the residence time for P2 (i.e. sampling for 250 ns when  $CVI \leq 1.2$  nm) in the two test cases, that is, an NP with total charge -40 e (charge density  $1.9 \text{ e nm}^{-2}$ ) at an ionic strength of 30 and 70 mM. Even though most of the binding events persisted for less than 50 ns, there was a non-negligible number of ions permanently bound to the particles. In order to ensure that these ions were not kept in their position by steric traps, we calculated the same residence times as a function of the inter-particle distance ( $CVI$ , **Figure D-4c**). Interestingly, as the NPs came closer together, the number of high-residence binding events increased. This trend suggests that the binding of the ions was mediated by electrostatic interactions, which were enhanced as the two rigid bodies approached each other.

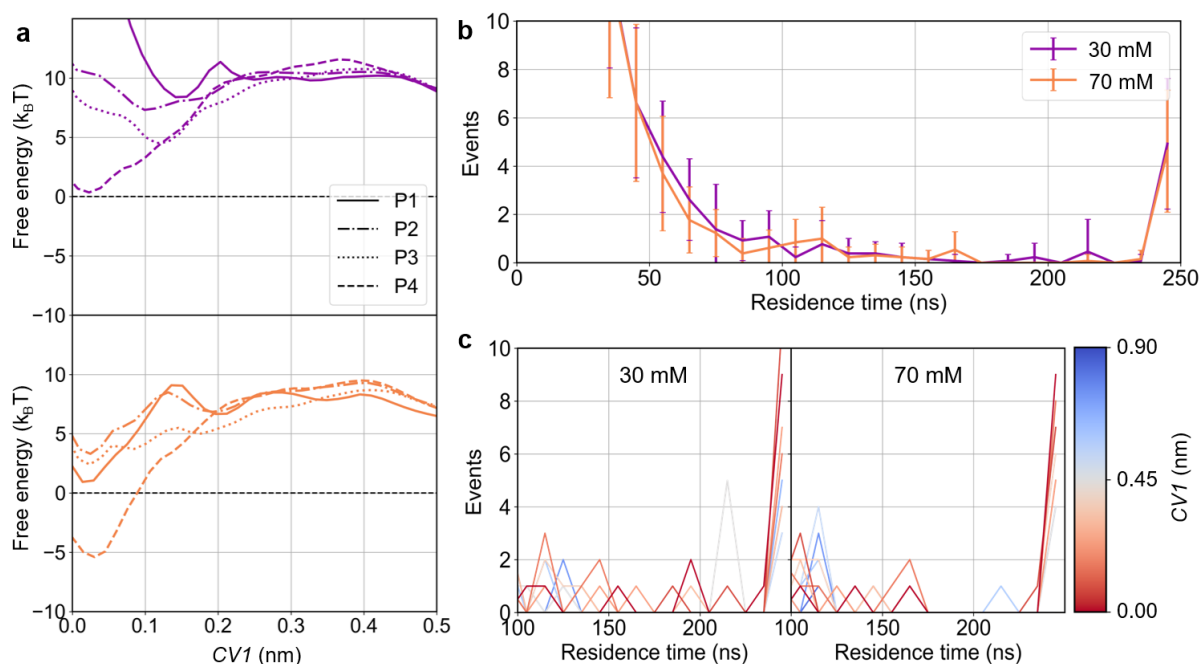


**Figure D-4.** Assessment of the best sampling protocol. **a.** PMF profiles obtained for NPs with a net charge of  $-40 e$  (charge density  $1.9 e \text{ nm}^{-2}$ ) in a solution of ionic strength 30 mM (top panel) and 70 mM (bottom panel). **b.** Residence time of sodium ions binding onto the surface of the NPs for the protocol P2. The solid lines show the average and standard deviation calculated from the windows with  $CVI \leq 1.2 \text{ nm}$ . **c.** The residence time of sodium ions as a function of the inter-particle distance  $CVI$  for protocol P2.

Based on these results, we adopted two approaches that could enhance the sampling of the diffusion of the sodium counterions. The first of these approaches, P3, consisted of the manual replacement of the persistent ions with bulk water molecules. Upon this replacement, a new set of ions appeared in the same halo-like structure (**Figure 41**). Since the relative position of the hydrophobic NPs and the respective salt bridges differ from P1 and P2, the free energy profiles varied slightly (**Figure D-4a**). Nonetheless, P3 introduced an abrupt alteration to the free energy landscape leading to an instantaneous push of the system away from its thermodynamic equilibrium. In light of these observations, a final strategy, P4, was considered. In the protocol P4, the conformational space of the counterions was extensively sampled by performing a simulated annealing prior to the data collection run. As can be seen from the two test cases exhibited in **Figure D-4a**, the proper phase space sampling leads to a significant decrease in the free energy of aggregation. P4 was the chosen sampling protocol for the simulations discussed in Chapter VII.

It is important to note that the sodium ions' residence times computed from our CG models offer a qualitative description of the lability of the counterions present, rather than structural

insights on their exact binding mode onto metal NPs. Thus, in order to verify the results of our CG models, we performed MD simulations with atomistic representations of equivalent citrate-capped AuNPs in electrolytic solutions. These simulations enabled us to calculate, at a finer resolution, the residence time of the sodium counterions. Indeed, our atomistic simulations of citrate-capped AuNPs displayed the same trend. As the charge density of the NP increased, the sodium ions became more affine for the NP's surface, thus binding for longer times (**Figure D-5**).

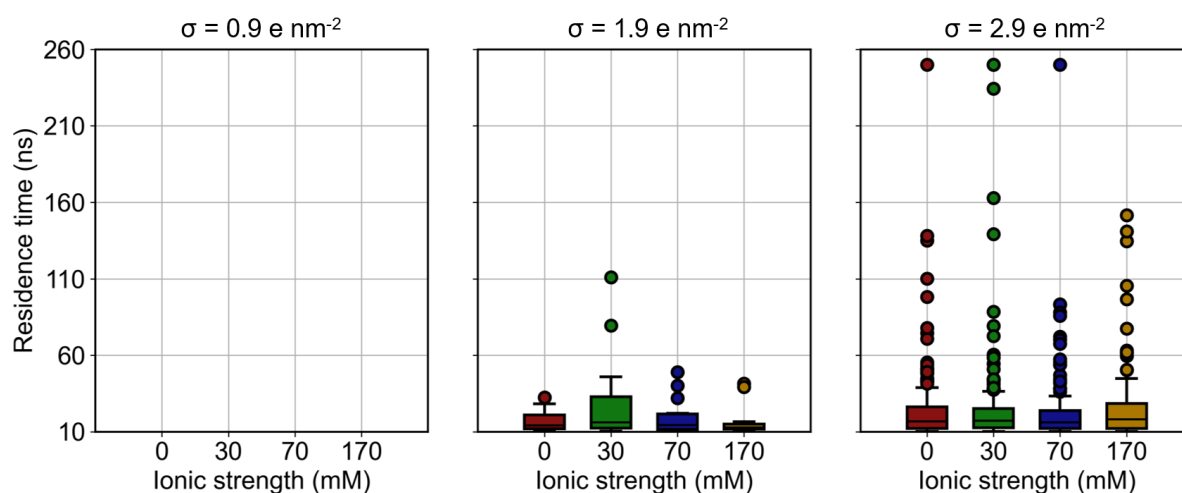


**Figure D-5.** Distribution of the residence times of sodium ions onto citrate-capped AuNPs. Only the persistent binding events are considered (i.e. residence times longer than 10 ns). The boxplots show the median of the distributions, and the error bars indicate the first and third quartiles. Simulations at ionic concentrations of 0, 30, 70, and 170 mM are shown in red, green, blue, and yellow, respectively.

The setup of these atomistic simulations consisted of individual 3 nm AuNPs coated with 10, 20, and 30 monohydrogen citrate molecules, i.e. surface charge density of 0.9, 1.9, and 2.9 e nm<sup>-2</sup>, respectively. The atomistic metallic core was constructed with the Wolff method implemented in the NanoCrystal webserver,<sup>272</sup> as described in Appendix D.1, and its nonbonded parameters were taken from Heinz and co-workers.<sup>304</sup> The monohydrogen citrate molecules were parametrized with the GAFF force field<sup>197</sup> (charges derived with the restrained electrostatic potential method<sup>203,317</sup>). The coating ligands, which were frozen throughout the simulation, were placed with their two terminal carboxylate groups pointing toward the gold core, as elucidated with DFT calculations.<sup>434</sup> The system was solvated in electrolytic solutions ( $I = 0, 30, 70,$  and  $170$  mM) using the TIP3P water model<sup>191</sup> and AMBER14SB ions.<sup>499</sup> Each combination of surface charge and ionic strength was simulated for 250 ns.

## D.4 Absorbance profiles

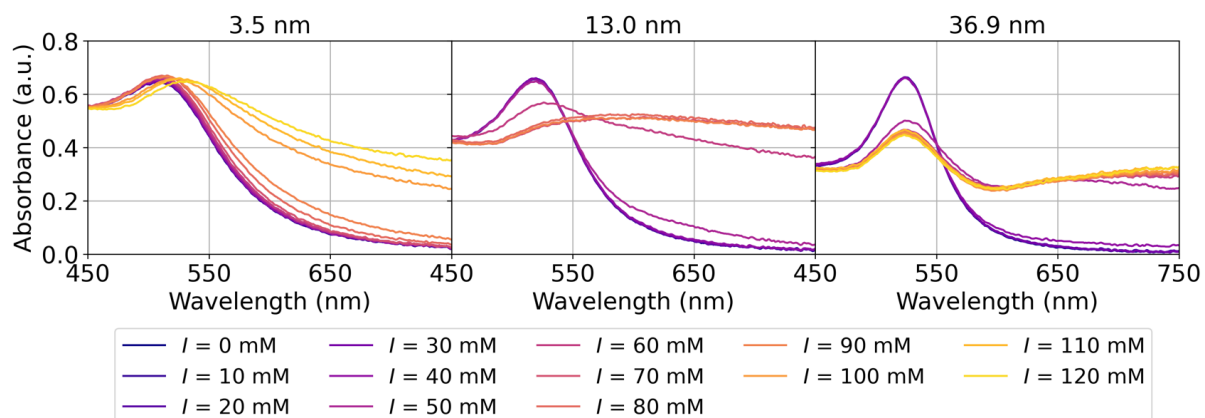


**Figure D-6.** UV-Vis absorbance profiles for 3.5 (a), 13.0 (b), and 36.9 nm (c) citrate-capped AuNPs at different sodium chloride concentrations.

## D.5 Correlation between well depth $\epsilon_{ii}$ and free energy of dimerization

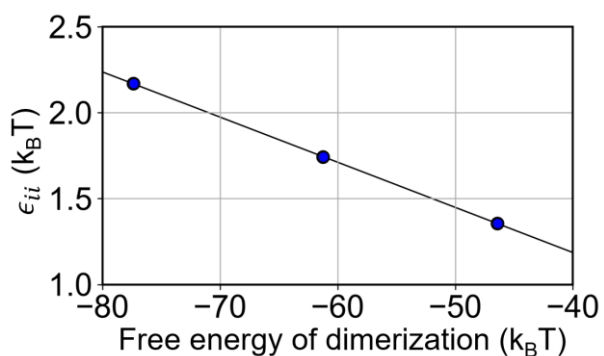


**Figure D-7.** Correlation between the hydrophobicity of the metal NPs (as described by the well depth  $\epsilon_{ii}$ ) and the free energy of NP dimerization.

## D.6 Shear planes distributions

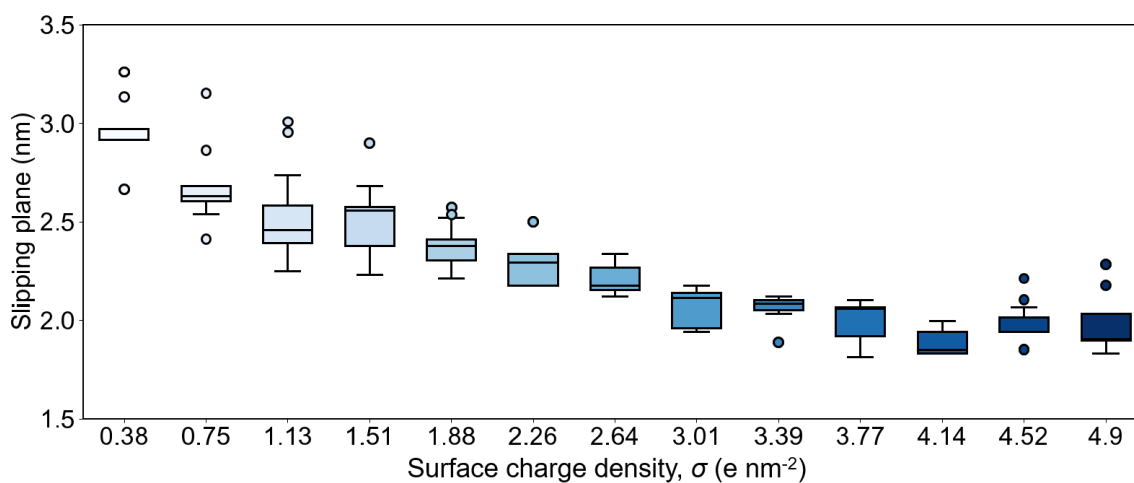


**Figure D-8.** Distribution of the position of the shear planes of each surface charge density  $\sigma$ . The points of each distribution result from a fit for a different number of points of the sodium ions' RDF. The boxplots show the median of the distributions, the upper whiskers extend to the last datum smaller than the third quartile plus the first-third inter-quartile distance, and the lower whiskers extend to the first datum greater than the first quartile minus the first-third inter-quartile distance.

## D.7 Coarse-grain models for metal nanoparticles

### D.7.1 The building of coarse-grained hydrophobic nanoparticles

The metal NP employed in this study consisted of 126 beads arranged in rings stacked on top of each other as described elsewhere (**Figure D-9a**).<sup>294,303,400,465</sup> The beads were assigned the C1 type as incorporated in the Martini-v2.2P force field,<sup>181,212</sup> and which corresponds to a purely hydrophobic moiety. Moreover, the mass of an NP represented at the atomic level was distributed on all the available beads of the CG model. This mass corresponded to a value of 556 u.m.a. per bead. The spherical shape of the NPs was retained by imposing an elastic network with a force constant of  $15,000 \text{ kJ mol}^{-1} \text{ nm}^{-2}$ . The elastic network united each bead with its six nearest neighbors as well as its farthest neighbor (**Figure D-9a**).

### D.7.2 The building of charged nanoparticles for the building of dispersion state phase diagrams

In this study, we used implicit-ligand models for our charged metal NPs. In detail, our capped NPs were represented as hydrophobic cores with a partial charge in certain surface beads. For the construction of these bodies, we employed the same algorithm as for naked NPs (Appendix D.7.1) modifying the charge of selected hydrophobic beads according to the target charge of

the NP (**Figure D-9b**). The sites were selected by uniformly shuffling all the beads according to their spherical coordinates. The charge of each bead was chosen as  $-2 e$  to mimic the most populated deprotonation state of citrate molecules onto spherical AuNPs.<sup>435</sup> For example, an NP with a total charge of  $-40 e$  (charge density  $1.9 e \text{ nm}^{-2}$ ), had 20 surface beads with a charge of  $-2 e$ , each. Importantly, our charged-sphere-models are valid for AuNPs coated with small dianionic capping agents. Consequently, the phase diagrams derived from these model NPs describe the dispersion state of AuNPs in the presence of ligands like citrate, cyclic oxocarbons, and dicarboxylic acids.

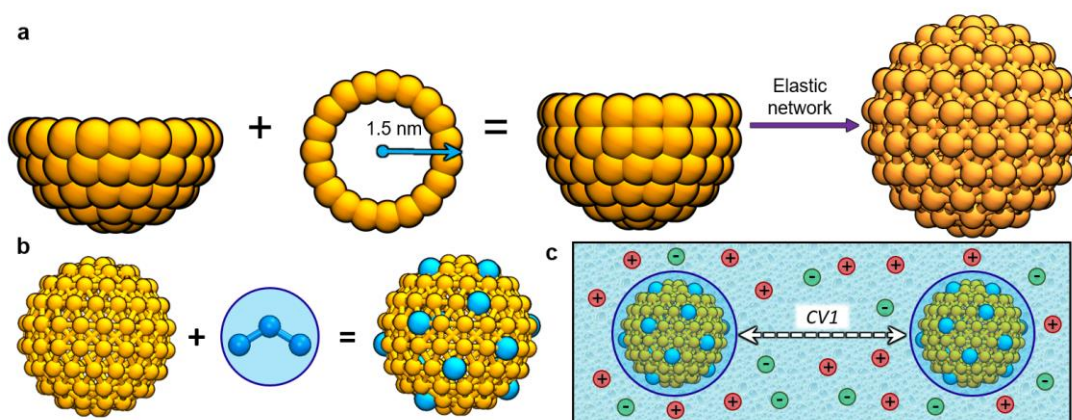


**Figure D-9.** Graphical representation of the models employed for the various studied components. **a.** The naked metal NPs (orange) were constructed from a series of concentric rings stacked over one another and held together by an elastic network. **b.** An explicit CG model for citrate (cyan) was built as three charged beads, and it was used only to calculate  $\Delta G_{desolv}^{lig}$ . The citrate-capped NPs used to derive the dispersion state phase diagrams were modeled as hollow spheres conformed by hydrophobic beads, some of which carried a formal charge. The number of charged sites was proportional to the net charge of the NP. **c.** Initial placement of two NPs immersed in a saline solution for the PMF calculations.

## D.8 Gold nanoparticles transmission electron microscopy images

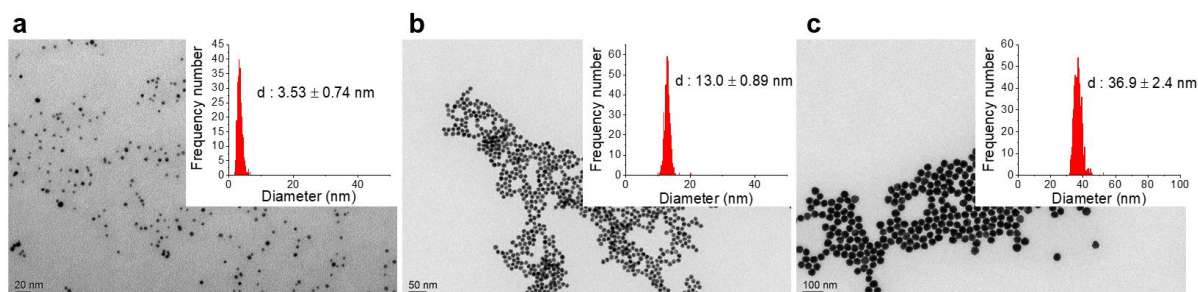


**Figure D-10.** TEM images and size distribution of the synthesized AuNPs. **a.** 3.5 nm AuNPs ( $3.53 \pm 0.74 \text{ nm}$ ). **b.** 13.0 nm AuNPs ( $13.0 \pm 0.89 \text{ nm}$ ). **c.** 36.9 nm AuNPs ( $36.9 \pm 2.4 \text{ nm}$ ).

## APPENDIX E. SUPPLEMENTARY SIMULATIONS OF PEPTIDE-COATED METAL NANOPARTICLES

### E.1 Nanocarrier binding in equilibrium simulations

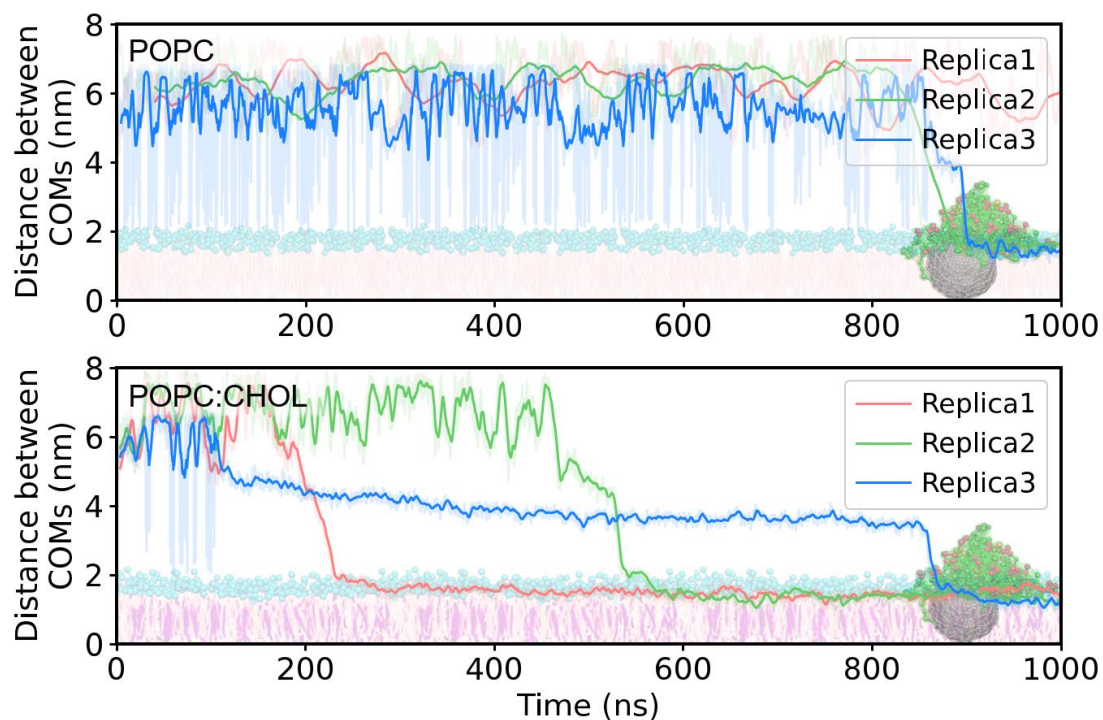


**Figure E-1.** Distance between the COM of the functionalized gHNP and the COM of the membrane for each of the three CG MD replica simulations. The two membranes used throughout the study were pure POPC (top panel) and POPC:CHOL (55:45, bottom panel).

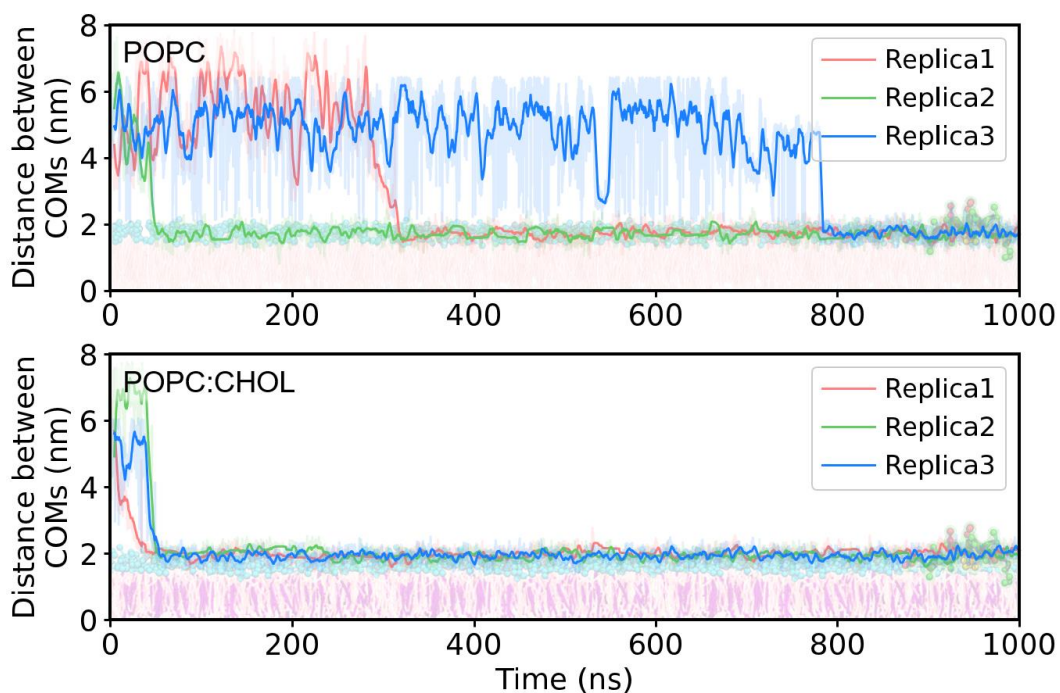


**Figure E-2.** Distance between the COM of the gH peptide and the COM of the membrane for each of the three CG MD replica simulations. The two membranes used throughout the study were pure POPC (top panel) and POPC:CHOL (55:45, bottom panel).

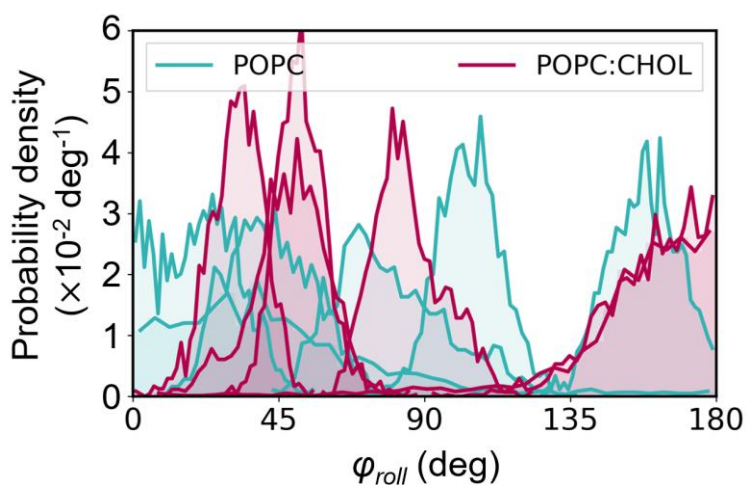


**Figure E-3.** Distribution of the rolling angle  $\varphi_{roll}$  for each of the six gH peptides grafted to the functionalized gHNP. The distributions are shown for both POPC (green) and POPC:CHOL (red) membranes.



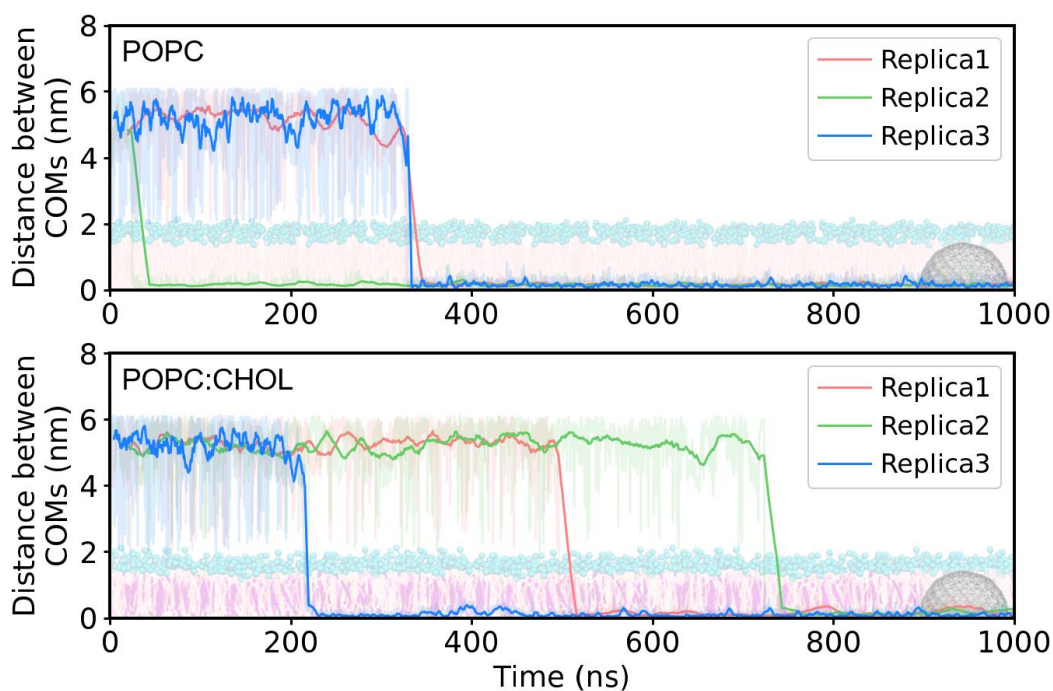


**Figure E-4.** Distance between the COM of the naked NP0 and the COM of the membrane for each of the three CG MD replica simulations. The two membranes used throughout the study were pure POPC (top panel) and POPC:CHOL (55:45, bottom panel).

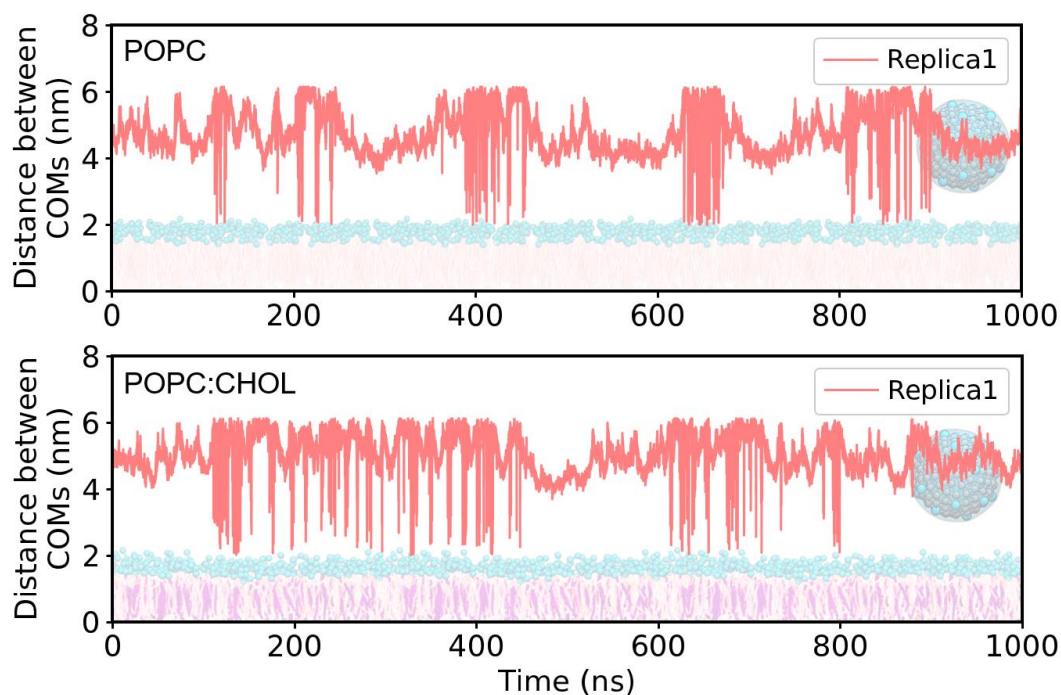


**Figure E-5.** Distance between the COM of CitNP and the COM of the membrane. The two membranes used throughout the study were pure POPC (top panel) and POPC:CHOL (55:45, bottom panel).

## ABBREVIATIONS

<b>Abbreviation</b>	<b>Meaning</b>
3MT	3-Methoxytyramine
AEF	p-Tyramine
AES	Atomic emission spectroscopy
Ala	Alanine
Arg	Arginine
Asn	Asparagine
Asp	Aspartate
ATCC	American Type Culture Collection
AuNC	Gold nanocluster
AuNP	Gold nanoparticle
BCC	Body-centered cubic
BEN	Benzanethiol
BUT	Butanethiol
CG	Coarse-grain
CHOL	Cholesterol
COM	Center of mass
CPP	Cell-penetrating peptide
CSS	Cascade Style Sheets
CV	Collective variable
Cys	Cysteine
DCM	Dichloromethane
DCS	Differential centrifugal sedimentation
DLS	Dynamic light scattering
DLVO	Derjaguin-Landau-Verwey-Overbeek
DMEM	Dulbecco's modified eagles medium
DMF	Dimethylformamide
DMSO	Dimethyl sulfoxide
DOI	Digital object identifier
DOSY	Diffusion ordered spectroscopy
ESI-MS	Electrospray ionization-mass spectrometry
EtOAc	Ethyl acetate
EtOH	Ethanol
FCC	Face-centered cubic
FDA	Food and Drug Administration
FF	Force field
FN	False negatives
FP	False positives

GAFF	Generalized Amber force field
Gln	Glutamine
Glu	Glutamate
Gly	Glycine
GUI	Graphical user interface
HCP	Hexagonal closely packed
HeLa	Human cervix epithelioid carcinoma
HEPES	4-(2-Hydroxyethyl)-1-piperazineethanesulfonic acid
His	Histidine
HSV-1	Herpes simplex virus type 1
HTML	Hypertext Markup Language
ICP	Inductively coupled plasma
Ile	Isoleucine
IR	Infrared
LDP	L-Dopamine
Leu	Leucine
Lys	Lysine
MC	Monte Carlo
MD	Molecular dynamics
MeOD	Deuterated methanol
MeOH	Methanol
Met	Methionine
MM	Molecular mechanics
MST	Microscale thermophoresis
MUA	11-Mercaptoundecanoic acid
MUS	Mercaptoundecasilfonate
NC	Nanocluster
NIR	Near-infrared
NMR	Nuclear magnetic resonance
NP	Nanoparticle
NPT	Isobaric-isothermal ensemble
NVE	Isochoric-isoenergetic (microcanonical) ensemble
NVT	Isochoric-isothermal (canonical) ensemble
OT	Octanethiol
PAE	Polyoxyethylene alkyl ethers
PAGE	Polyacrylamide gel electrophoresis
PBC	Periodic boundary conditions
PBS	Phosphate buffer saline
PC	Phosphatidylcholine
PDB	Protein Data Bank
PDI	Polydispersity index
PE	Petroleum ether
PEG	Polyethylene glycol

PET	Phenylethanethiol
PG	Phosphatidylglycerol
Phe	Phenylalanine
PLA	Pulsed laser ablation
PMF	Potential of mean force
POPC	1-palmitoyl-2-oleoyl-sn-glycero-3-phosphocholine
Pro	Proline
QM	Quantum mechanics
RDF	Radial distribution function
RESP	Restrained electrostatic potential
RMSD	Root mean squared displacement
SAXS	Small angle X-ray scattering
SDS	Sodium dodecyl sulfate
SEM	Scanning electron microscopy
Ser	Serine
SPAD	Single-photon avalanche photodiode
SPR	Surface plasmon resonance
STEM	Scanning transmission electron microscopy
TEM	Transmission electron microscopy
THF	Tetrahydrofuran
Thr	Threonine
TI	Thermodynamic integration
TN	True negatives
TOAB	Tetraoctylammonium bromide
TP	True positives
Trp	Tryptophan
Tyr	Tyrosine
UA	United atom
US	Umbrella sampling
UV	Ultraviolet
Val	Valine
VCD	Vibrational circular dichroism
Vis	Visible
v-rescale	Velocity rescale
WHAM	Weighted histogram analysis method

## BIBLIOGRAPHY

1. Zeng, C. Precision at the nanoscale: On the structure and property evolution of gold nanoclusters. in *Pure and Applied Chemistry* vol. 90 1409–1427 (De Gruyter, 2018).
2. Behzadi, S. *et al.* Cellular uptake of nanoparticles: Journey inside the cell. *Chemical Society Reviews* vol. 46 4218–4244 (2017).
3. Blanco, E., Shen, H. & Ferrari, M. Principles of nanoparticle design for overcoming biological barriers to drug delivery. *Nature Biotechnology* vol. 33 941–951 (2015).
4. Cui, C. *et al.* Cellular uptake, intracellular trafficking, and antitumor efficacy of doxorubicin-loaded reduction-sensitive micelles. *Biomaterials* **34**, 3858–3869 (2013).
5. Wilhelm, S. *et al.* Analysis of nanoparticle delivery to tumours. *Nature Reviews Materials* vol. 1 16014 (2016).
6. Pelaz, B. *et al.* Diverse Applications of Nanomedicine. *ACS Nano* **11**, 2313–2381 (2017).
7. Bobo, D., Robinson, K. J., Islam, J., Thurecht, K. J. & Corrie, S. R. Nanoparticle-Based Medicines: A Review of FDA-Approved Materials and Clinical Trials to Date. *Pharmaceutical Research* vol. 33 2373–2387 (2016).
8. Anselmo, A. C., Mitragotri, | Samir, Mitragotri, S. & Paulson, J. A. Nanoparticles in the clinic: An update. *Bioeng Transl Med* **4**, (2019).
9. F F A-Andrew D Jones III, D. I., Mi, G. & Webster, T. J. *A Status Report on FDA Approval of Medical Devices Containing Nanostructured Materials. Trends in Biotechnology* vol. 37 (2019).
10. Colvin, V. L. The potential environmental impact of engineered nanomaterials. *Nature Biotechnology* vol. 21 1166–1170 (2003).
11. Nel, A. E. *et al.* Understanding biophysicochemical interactions at the nano-bio interface. *Nature Materials* vol. 8 543–557 (2009).

12. Kang, X. & Zhu, M. Tailoring the photoluminescence of atomically precise nanoclusters. *Chem. Soc. Rev.* **48**, 2422–2457 (2019).
13. Stauber, J. M. *et al.* An Organometallic Strategy for Assembling Atomically Precise Hybrid Nanomaterials. *J. Am. Chem. Soc.* **142**, 327–334 (2020).
14. Tiwari, P., Vig, K., Dennis, V. & Singh, S. Functionalized Gold Nanoparticles and Their Biomedical Applications. *Nanomaterials* **1**, 31–63 (2011).
15. Zheng, Y., Lai, L., Liu, W., Jiang, H. & Wang, X. Recent advances in biomedical applications of fluorescent gold nanoclusters. *Adv. Colloid Interface Sci.* **242**, 1–16 (2017).
16. Egorova, E. A. *et al.* One Peptide for Them All: Gold Nanoparticles of Different Sizes Are Stabilized by a Common Peptide Amphiphile. *ACS Nano* **14**, 5874–5886 (2020).
17. Moros, M. *et al.* DNA-Coated Gold Nanoparticles for the Detection of mRNA in Live Hydra Vulgaris Animals. *ACS Appl. Mater. Interfaces* **11**, 13905–13911 (2019).
18. Marega, R. *et al.* Antibody-functionalized polymer-coated gold nanoparticles targeting cancer cells: An in vitro and in vivo study. *J. Mater. Chem.* **22**, 21305–21312 (2012).
19. Kumar, S. *et al.* Carbohydrate-Coated Gold-Silver Nanoparticles for Efficient Elimination of Multidrug Resistant Bacteria and in Vivo Wound Healing. *ACS Appl. Mater. Interfaces* **11**, 42998–43017 (2019).
20. Burrows, N. D. *et al.* Anisotropic Nanoparticles and Anisotropic Surface Chemistry. *J. Phys. Chem. Lett.* **7**, 632–641 (2016).
21. Riccardi, L. *et al.* Dynamic origin of chirality transfer between chiral surface and achiral ligand in Au<sub>38</sub> clusters. *ACS Nano* **13**, 7127–7134 (2019).
22. Li, H. *et al.* Magic-number gold nanoclusters with diameters from 1 to 3.5 nm: Relative stability and catalytic activity for CO oxidation. *Nano Lett.* **15**, 682–688 (2015).
23. Cleveland, C. L. *et al.* Structural evolution of smaller gold nanocrystals: The truncated decahedral motif. *Phys. Rev. Lett.* **79**, 1873–1876 (1997).
24. Jensen, K. M. Ø. *et al.* Polymorphism in magic-sized Au<sub>144</sub> (SR)<sub>60</sub> clusters. *Nat.*

- Commun.* **7**, 11859 (2016).
25. Häkkinen, H. The gold-sulfur interface at the nanoscale. *Nature Chemistry* vol. 4 443–455 (2012).
  26. Badia, A., Cuccia, L., Demers, L., Morin, F. & Lennox, R. B. Structure and dynamics in alkanethiolate monolayers self-assembled on gold nanoparticles: A DSC, FT-IR, and deuterium NMR study. *J. Am. Chem. Soc.* **119**, 2682–2692 (1997).
  27. Tero, T. R. *et al.* Dynamic Stabilization of the Ligand-Metal Interface in Atomically Precise Gold Nanoclusters Au<sub>68</sub> and Au<sub>144</sub> Protected by meta-Mercaptobenzoic Acid. *ACS Nano* **11**, 11872–11879 (2017).
  28. Vilanova, O. *et al.* Understanding the Kinetics of Protein-Nanoparticle Corona Formation. *ACS Nano* **10**, 10842–10850 (2016).
  29. Pederzoli, F. *et al.* Protein corona and nanoparticles: how can we investigate on? *Wiley Interdisciplinary Reviews: Nanomedicine and Nanobiotechnology* vol. 9 1–23 (2017).
  30. Pelaz, B. *et al.* Surface Functionalization of Nanoparticles with Polyethylene Glycol: Effects on Protein Adsorption and Cellular Uptake. *ACS Nano* **9**, 6996–7008 (2015).
  31. Li, Y. & Hu, Y. Computational investigation of the influence of chain length on the shielding effect of PEGylated nanoparticles. *RSC Adv.* **4**, 51022–51031 (2014).
  32. Ensing, B. *et al.* On the origin of the extremely different solubilities of polyethers in water. *Nat. Commun.* **10**, 1–8 (2019).
  33. Kanaras, A. G., Kamounah, F. S., Schaumburg, K., Kiely, C. J. & Brust, M. Thioalkylated tetraethylene glycol: A new ligand for water soluble monolayer protected gold clusters. *Chem. Commun.* **20**, 2294–2295 (2002).
  34. Magarkar, A., Karakas, E., Stepniewski, M., Róg, T. & Bunker, A. Molecular dynamics simulation of PEGylated bilayer interacting with salt ions: A model of the liposome surface in the bloodstream. *J. Phys. Chem. B* **116**, 4212–4219 (2012).
  35. Simonelli, F., Rossi, G. & Monticelli, L. Role of Ligand Conformation on Nanoparticle–Protein Interactions. *J. Phys. Chem. B* **123**, 1764–1769 (2019).

36. Huo, S. *et al.* Fully Zwitterionic Nanoparticle Antimicrobial Agents through Tuning of Core Size and Ligand Structure. *ACS Nano* **10**, 8732–8737 (2016).
37. Malola, S., Lehtovaara, L., Enkovaara, J. & Häkkinen, H. Birth of the localized surface plasmon resonance in monolayer-protected gold nanoclusters. *ACS Nano* **7**, 10263–10270 (2013).
38. Cole, L. E., Ross, R. D., Tilley, J. M., Vargo-Gogola, T. & Roeder, R. K. Gold nanoparticles as contrast agents in X-ray imaging and computed tomography. *Nanomedicine* vol. 10 321–341 (2015).
39. Popovtzer, R. *et al.* Targeted gold nanoparticles enable molecular CT imaging of cancer. *Nano Lett.* **8**, 4593–4596 (2008).
40. Huang, X., Liu, Y., Yung, B., Xiong, Y. & Chen, X. Nanotechnology-Enhanced No-Wash Biosensors for in Vitro Diagnostics of Cancer. *ACS Nano* **11**, 5238–5292 (2017).
41. Crawford, S. E., Hartmann, M. J. & Millstone, J. E. Surface Chemistry-Mediated Near-Infrared Emission of Small Coinage Metal Nanoparticles. *Acc. Chem. Res.* **52**, 695–703 (2019).
42. Chen, L. Y., Wang, C. W., Yuan, Z. & Chang, H. T. Fluorescent gold nanoclusters: Recent advances in sensing and imaging. *Anal. Chem.* **87**, 216–229 (2015).
43. Shang, L. *et al.* Effect of protein adsorption on the fluorescence of ultrasmall gold nanoclusters. *Small* **8**, 661–665 (2012).
44. Deng, H. H. *et al.* Fabrication of Water-Soluble, Green-Emitting Gold Nanoclusters with a 65% Photoluminescence Quantum Yield via Host-Guest Recognition. *Chem. Mater.* **29**, 1362–1369 (2017).
45. Kennedy, L. C. *et al.* A new era for cancer treatment: Gold-nanoparticle-mediated thermal therapies. *Small* vol. 7 169–183 (2011).
46. Manikandan, M., Hasan, N. & Wu, H. F. Platinum nanoparticles for the photothermal treatment of Neuro 2A cancer cells. *Biomaterials* **34**, 5833–5842 (2013).
47. Rastinehad, A. R. *et al.* Gold nanoshell-localized photothermal ablation of prostate



- tumors in a clinical pilot device study. *Proc. Natl. Acad. Sci. U. S. A.* **116**, 18590–18596 (2019).
48. Stern, J. M. *et al.* Initial Evaluation of the Safety of Nanoshell-Directed Photothermal Therapy in the Treatment of Prostate Disease. *Int. J. Toxicol.* **35**, 38–46 (2016).
  49. Panapitiya, G. *et al.* Machine-Learning Prediction of CO Adsorption in Thiolated, Ag-Alloyed Au Nanoclusters. *J. Am. Chem. Soc.* **140**, 17508–17514 (2018).
  50. Phala, N. S. & van Steen, E. Intrinsic reactivity of gold nanoparticles: Classical, semi-empirical and DFT studies. *Gold Bull.* **40**, 150–153 (2007).
  51. Hashmi, A. S. K. & Hutchings, G. J. Gold Catalysis. *Angew. Chemie Int. Ed.* **45**, 7896–7936 (2006).
  52. Sabella, S. *et al.* A general mechanism for intracellular toxicity of metal-containing nanoparticles. *Nanoscale* **6**, 7052 (2014).
  53. Zhang, L. *et al.* Reducing Stress on Cells with Apoferritin-Encapsulated Platinum Nanoparticles. *Nano Lett.* **10**, 219–223 (2010).
  54. Guarnieri, D. *et al.* Transport across the cell-membrane dictates nanoparticle fate and toxicity: A new paradigm in nanotoxicology. *Nanoscale* **6**, 10264–10273 (2014).
  55. Bürgi, T. Properties of the gold-sulphur interface: from self-assembled monolayers to clusters. *Nanoscale* **7**, 15553–15567 (2015).
  56. Scrimin, P. M. *et al.* A Gold Nanoparticle Nanonuclease Relying on a Zn(II) Mononuclear Complex. *Angew. Chemie* ang.202012513 (2020) doi:10.1002/ange.202012513.
  57. Riccardi, L. *et al.* Nanoparticle-Based Receptors Mimic Protein-Ligand Recognition. *Chem* **3**, 92–109 (2017).
  58. Beddoes, C. M., Case, C. P. & Briscoe, W. H. Understanding nanoparticle cellular entry: A physicochemical perspective. *Advances in Colloid and Interface Science* vol. 218 48–68 (2015).
  59. Gurtovenko, A. A., Anwar, J. & Vattulainen, I. Defect-mediated trafficking across cell

- membranes: Insights from in silico modeling. *Chem. Rev.* **110**, 6077–6103 (2010).
60. Zhang, S., Gao, H. & Bao, G. Physical Principles of Nanoparticle Cellular Endocytosis. *ACS Nano* **9**, 8655–8671 (2015).
  61. Ge, Z. & Wang, Y. Computer Simulation and Modeling Techniques in the Study of Nanoparticle-Membrane Interactions. *Annu. Rep. Comput. Chem.* **12**, 159–200 (2016).
  62. Pfeiffer, T. *et al.* Nanoparticles at Biomimetic Interfaces: Combined Experimental and Simulation Study on Charged Gold Nanoparticles/Lipid Bilayer Interfaces. *J. Phys. Chem. Lett.* **10**, 129–137 (2019).
  63. Nakamura, H. & Watano, S. Direct permeation of nanoparticles across cell membrane: A review. *KONA Powder and Particle Journal* vol. 2018 49–65 (2018).
  64. Tian, F., Yue, T., Li, Y. & Zhang, X. Computer simulation studies on the interactions between nanoparticles and cell membrane. *Sci. China Chem.* **57**, 1662–1671 (2014).
  65. Feng, Z. V. *et al.* Impacts of gold nanoparticle charge and ligand type on surface binding and toxicity to Gram-negative and Gram-positive bacteria. *Chem. Sci.* **6**, 5186–5196 (2015).
  66. Li, Y. *et al.* Counterintuitive cooperative endocytosis of like-charged nanoparticles in cellular internalization: Computer simulation and experiment. *Nanotechnology* **28**, 085102 (2017).
  67. Heikkilä, E., Martinez-Seara, H., Gurtovenko, A. A., Vattulainen, I. & Akola, J. Atomistic simulations of anionic Au<sub>144</sub>(SR)<sub>60</sub> nanoparticles interacting with asymmetric model lipid membranes. *Biochim. Biophys. Acta - Biomembr.* **1838**, 2852–2860 (2014).
  68. Wang, B., Zhang, L., Sung, C. B. & Granick, S. Nanoparticle-induced surface reconstruction of phospholipid membranes. *Proc. Natl. Acad. Sci. U. S. A.* **105**, 18171–18175 (2008).
  69. Yang, K. & Ma, Y.-Q. Q. Computer simulation of the translocation of nanoparticles with different shapes across a lipid bilayer. *Nat. Nanotechnol.* **5**, 579–583 (2010).

70. Lin, X., Li, Y. & Gu, N. Nanoparticle's size effect on its translocation across a lipid bilayer: A molecular dynamics simulation. *J. Comput. Theor. Nanosci.* **7**, 269–276 (2010).
71. Vácha, R., Martinez-Veracoechea, F. J. & Frenkel, D. Receptor-mediated endocytosis of nanoparticles of various shapes. *Nano Lett.* **11**, 5391–5395 (2011).
72. Huang, C., Zhang, Y., Yuan, H., Gao, H. & Zhang, S. Role of nanoparticle geometry in endocytosis: Laying down to stand up. *Nano Lett.* **13**, 4546–4550 (2013).
73. Su, C. F., Merlitz, H., Rabbel, H. & Sommer, J. U. Nanoparticles of Various Degrees of Hydrophobicity Interacting with Lipid Membranes. *J. Phys. Chem. Lett.* **8**, 4069–4076 (2017).
74. D'Rozario, R. S. G., Wee, C. L., Jayne Wallace, E. & Sansom, M. S. P. The interaction of C60 and its derivatives with a lipid bilayer via molecular dynamics simulations. *Nanotechnology* **20**, 115102 (2009).
75. Li, Y., Chen, X. & Gu, N. Computational Investigation of Interaction between Nanoparticles and Membranes : Hydrophobic / Hydrophilic Effect Computational Investigation of Interaction between Nanoparticles and Membranes : Hydrophobic / Hydrophilic Effect. *J. Phys. Chem. B* **112**, 16647–16653 (2008).
76. Yan, Z. *et al.* Curvature-mediated cooperative wrapping of multiple nanoparticles at the same and opposite membrane sides. *Nanoscale* **11**, 19751–19762 (2019).
77. Bahrami, A. H., Lipowsky, R. & Weikl, T. R. The role of membrane curvature for the wrapping of nanoparticles. *Soft Matter* **12**, 581–587 (2016).
78. Arai, N., Yasuoka, K. & Zeng, X. C. A vesicle cell under collision with a Janus or homogeneous nanoparticle: Translocation dynamics and late-stage morphology. *Nanoscale* **5**, 9089–9100 (2013).
79. Yi, X., Shi, X. & Gao, H. Cellular uptake of elastic nanoparticles. *Phys. Rev. Lett.* **107**, 098101 (2011).
80. Shen, Z., Ye, H. & Li, Y. Understanding receptor-mediated endocytosis of elastic nanoparticles through coarse grained molecular dynamic simulation. *Phys. Chem.*

- Chem. Phys.* **20**, 16372–16385 (2018).
81. Yuan, H., Li, J., Bao, G. & Zhang, S. Variable nanoparticle-cell adhesion strength regulates cellular uptake. *Phys. Rev. Lett.* **105**, 138101 (2010).
  82. Ding, H. ming & Ma, Y. qiang. Role of physicochemical properties of coating ligands in receptor-mediated endocytosis of nanoparticles. *Biomaterials* **33**, 5798–5802 (2012).
  83. Chen, X., Tieleman, D. P. & Liang, Q. Modulating interactions between ligand-coated nanoparticles and phase-separated lipid bilayers by varying the ligand density and the surface charge. *Nanoscale* **10**, 2481–2491 (2018).
  84. Ding, H. M., Tian, W. De & Ma, Y. Q. Designing nanoparticle translocation through membranes by computer simulations. *ACS Nano* **6**, 1230–1238 (2012).
  85. Guo, Y., Terazzi, E., Seemann, R., Fleury, J. B. & Baulin, V. A. Direct proof of spontaneous translocation of lipid-covered Hydrophobic nanoparticles through a phospholipid bilayer. *Sci. Adv.* **2**, e1600261–e1600261 (2016).
  86. Jiang, Y. *et al.* The Interplay of Size and Surface Functionality on the Cellular Uptake of Sub-10 nm Gold Nanoparticles. *ACS Nano* **9**, 9986–9993 (2015).
  87. De La Fuente, J. M. & Berry, C. C. Tat peptide as an efficient molecule to translocate gold nanoparticles into the cell nucleus. *Bioconjug. Chem.* **16**, 1176–1180 (2005).
  88. Oh, E. *et al.* Cellular uptake and fate of PEGylated gold nanoparticles is dependent on both cell-penetration peptides and particle size. *ACS Nano* **5**, 6434–6448 (2011).
  89. Van Lehn, R. C. *et al.* Lipid tail protrusions mediate the insertion of nanoparticles into model cell membranes. *Nat. Commun.* **5**, 4482 (2014).
  90. Verma, A. *et al.* Surface-structure-regulated cell-membrane penetration by monolayer-protected nanoparticles. *Nat. Mater.* **7**, 588–595 (2008).
  91. Atukorale, P. U. *et al.* Structure-Property Relationships of Amphiphilic Nanoparticles That Penetrate or Fuse Lipid Membranes. *Bioconjug. Chem.* **29**, 1131–1140 (2018).
  92. Xia, Q. S., Ding, H. M. & Ma, Y. Q. Can dual-ligand targeting enhance cellular uptake of nanoparticles? *Nanoscale* **9**, 8982–8989 (2017).

93. Mosquera, J. *et al.* Cellular Uptake of Gold Nanoparticles Triggered by Host-Guest Interactions. *J. Am. Chem. Soc.* **140**, 4469–4472 (2018).
94. Salvia, M. V., Salassa, G., Rastrelli, F. & Mancin, F. Turning Supramolecular Receptors into Chemosensors by Nanoparticle-Assisted ‘nMR Chemosensing’. *J. Am. Chem. Soc.* **137**, 11399–11406 (2015).
95. Sun, X. *et al.* Molecular-Dynamics-Simulation-Directed Rational Design of Nanoreceptors with Targeted Affinity. *Angew. Chemie - Int. Ed.* **58**, 7702–7707 (2019).
96. Gabrielli, L. *et al.* Detection and identification of designer drugs by nanoparticle-based NMR chemosensing. *Chem. Sci.* **9**, 4777–4784 (2018).
97. Sun, X., Liu, P. & Mancin, F. Sensor arrays made by self-organized nanoreceptors for detection and discrimination of carboxylate drugs. *Analyst* **143**, 5754–5763 (2018).
98. Manea, F., Houillon, F. B., Pasquato, L. & Scrimin, P. Nanozymes: Gold-Nanoparticle-Based Transphosphorylation Catalysts. *Angew. Chemie* **43**, 6165–6169 (2004).
99. Pasquato, L., Pengo, P. & Scrimin, P. Nanozymes: Functional Nanoparticle-based Catalysts. *Supramol. Chem.* **17**, 163–171 (2005).
100. Pasquato, L., Pengo, P. & Scrimin, P. Functional gold nanoparticles for recognition and catalysis. *J. Mater. Chem.* **14**, 3481–3487 (2004).
101. Diez-Castellnou, M., Mancin, F. & Scrimin, P. Efficient phosphodiester cleaving nanozymes resulting from multivalency and local medium polarity control. *J. Am. Chem. Soc.* **136**, 1158–1161 (2014).
102. Mikolajczak, D. J., Berger, A. A. & Kokschi, B. Catalytically Active Peptide–Gold Nanoparticle Conjugates: Prospecting for Artificial Enzymes. *Angew. Chemie - Int. Ed.* 2–12 (2020) doi:10.1002/anie.201908625.
103. Sylvestre, J.-P. *et al.* Surface Chemistry of Gold Nanoparticles Produced by Laser Ablation in Aqueous Media. *J. Phys. Chem. B* **108**, 16864–16869 (2004).
104. Rousset, J. L. *et al.* Comparative X-ray photoemission spectroscopy study of Au, Ni, and AuNi clusters produced by laser vaporization of bulk metals. *J. Phys. Chem. B* **104**,

- 5430–5435 (2000).
105. Compagnini, G., Scalisi, A. A. & Puglisi, O. Ablation of noble metals in liquids: A method to obtain nanoparticles in a thin polymeric film. *Phys. Chem. Chem. Phys.* **4**, 2787–2791 (2002).
  106. Mafuné, F., Kohno, J. Y., Takeda, Y., Kondow, T. & Sawabe, H. Formation of gold nanoparticles by laser ablation in aqueous solution of surfactant. *J. Phys. Chem. B* **105**, 5114–5120 (2001).
  107. Kanitz, A. *et al.* Review on experimental and theoretical investigations of the early stage, femtoseconds to microseconds processes during laser ablation in liquid-phase for the synthesis of colloidal nanoparticles. *Plasma Sources Sci. Technol.* **28**, 103001 (2019).
  108. Husseiny, M. I., El-Aziz, M. A., Badr, Y. & Mahmoud, M. A. Biosynthesis of gold nanoparticles using *Pseudomonas aeruginosa*. *Spectrochim. Acta - Part A Mol. Biomol. Spectrosc.* **67**, 1003–1006 (2007).
  109. Kim, H. Y. & Song, H. G. Purification and characterization of NAD(P)H-dependent nitroreductase I from *Klebsiella* sp. C1 and enzymatic transformation of 2,4,6-trinitrotoluene. *Appl. Microbiol. Biotechnol.* **68**, 766–773 (2005).
  110. Zakaria, H. M. *et al.* Small molecule- and amino acid-induced aggregation of gold nanoparticles. *Langmuir* **29**, 7661–7673 (2013).
  111. Ahmed, S., Annu, Ikram, S. & Yudha, S. Biosynthesis of gold nanoparticles: A green approach. *Journal of Photochemistry and Photobiology B: Biology* vol. 161 141–153 (2016).
  112. Sengani, M., Grumezescu, A. M. & Rajeswari, V. D. Recent trends and methodologies in gold nanoparticle synthesis – A prospective review on drug delivery aspect. *OpenNano* vol. 2 37–46 (2017).
  113. Enüstün, B. V. & Turkevich, J. Coagulation of Colloidal Gold. *J. Am. Chem. Soc.* **85**, 3317–3328 (1963).
  114. Wuithschick, M. *et al.* Turkevich in New Robes: Key Questions Answered for the Most

- Common Gold Nanoparticle Synthesis. *ACS Nano* **9**, 7052–7071 (2015).
115. Turkevich, J. Colloidal gold. Part I - Historical and preparative aspects, morphology and structure. *Gold Bull.* **18**, 86–91 (1985).
  116. Colangelo, E. *et al.* Characterizing self-assembled monolayers on gold nanoparticles. *Bioconjug. Chem.* **28**, 11–22 (2017).
  117. Brust, M., Walker, M., Bethell, D., Schiffrin, D. J. & Whyman, R. Synthesis of thiol-derivatised gold nanoparticles in a two-phase liquid-liquid system. *J. Chem. Soc. Chem. Commun.* 801–802 (1994) doi:10.1039/C39940000801.
  118. Zhao, P., Li, N. & Astruc, D. State of the art in gold nanoparticle synthesis. *Coordination Chemistry Reviews* vol. 257 638–665 (2013).
  119. Perala, S. R. K. & Kumar, S. On the mechanism of metal nanoparticle synthesis in the Brust-Schiffrin method. *Langmuir* **29**, 9863–9873 (2013).
  120. Zaluzhna, O., Li, Y., Zangmeister, C., Allison, T. C. & Tong, Y. Y. J. Mechanistic insights on one-phase vs. Two-phase Brust-Schiffrin method synthesis of Au nanoparticles with dioctyl-diselenides. *Chem. Commun.* **48**, 362–364 (2012).
  121. Das, A. *et al.* Cyclopentanethiolato-protected Au<sub>36</sub>(SC<sub>5</sub>H<sub>9</sub>)<sub>24</sub> nanocluster: Crystal structure and implications for the steric and electronic effects of ligand. *J. Phys. Chem. A* **118**, 8264–8269 (2014).
  122. Malay, A. D. *et al.* An ultra-stable gold-coordinated protein cage displaying reversible assembly. *Nature* vol. 569 438–442 (2019).
  123. Yu, M., Yankovich, A. B., Kaczmarowski, A., Morgan, D. & Voyles, P. M. Integrated Computational and Experimental Structure Refinement for Nanoparticles. *ACS Nano* **10**, 4031–4038 (2016).
  124. Knoppe, S. & Bürgi, T. Chirality in thiolate-protected gold clusters. *Acc. Chem. Res.* **47**, 1318–1326 (2014).
  125. Dolamic, I., Varnholt, B. & Bürgi, T. Chirality transfer from gold nanocluster to adsorbate evidenced by vibrational circular dichroism. *Nat. Commun.* **6**, 7117 (2015).

126. Templeton, A. C., Hostetler, M. J., Kraft, C. T. & Murray, R. W. Reactivity of Monolayer-Protected Gold Cluster Molecules: Steric Effects. *J. Am. Chem. Soc.* **120**, 1906–1911 (1998).
127. Rostek, A., Mahl, D. & Epple, M. Chemical composition of surface-functionalized gold nanoparticles. *J. Nanoparticle Res.* **13**, 4809–4814 (2011).
128. Terrill, R. H. *et al.* Monolayers in Three Dimensions: NMR, SAXS, Thermal, and Electron Hopping Studies of Alkanethiol Stabilized Gold Clusters. *J. Am. Chem. Soc.* **117**, 12537–12548 (1995).
129. Liu, X., Yu, M., Kim, H., Marnett, M. & Stellacci, F. Determination of monolayer-protected gold nanoparticle ligand-shell morphology using NMR. *Nat. Commun.* **3**, 1182–1189 (2012).
130. Ong, Q. K. *et al.* High-Resolution Scanning Tunneling Microscopy Characterization of Mixed Monolayer Protected Gold Nanoparticles. *ACS Nano* **7**, 8529–8539 (2013).
131. Lee, K., Zhang, L., Yi, Y., Wang, X. & Yu, Y. Rupture of Lipid Membranes Induced by Amphiphilic Janus Nanoparticles. *ACS Nano* **12**, 3646–3657 (2018).
132. Guarnieri, D. *et al.* Shuttle-Mediated Nanoparticle Delivery to the Blood-Brain Barrier. *Small* **9**, 853–862 (2013).
133. Falanga, A. *et al.* Elucidation of the interaction mechanism with liposomes of gH625-peptide functionalized dendrimers. *PLoS One* **9**, e112128 (2014).
134. Badia, A. *et al.* Self-Assembled Monolayers on Gold Nanoparticles. *Chem. - A Eur. J.* **2**, 359–363 (1996).
135. Salorinne, K. *et al.* Nondestructive size determination of thiol-stabilized gold nanoclusters in solution by diffusion ordered NMR spectroscopy. *Anal. Chem.* **85**, 3489–3492 (2013).
136. Grisham, D. R. & Nanda, V. Hydrodynamic radius coincides with the slip plane position in the electrokinetic behavior of lysozyme. *Proteins Struct. Funct. Bioinforma.* **86**, 515–523 (2018).



137. Corvaglia, S., Guarnieri, D. & Pompa, P. P. Boosting the therapeutic efficiency of nanovectors: Exocytosis engineering. *Nanoscale* **9**, 3757–3765 (2017).
138. Moglianetti, M. *et al.* Platinum nanozymes recover cellular ROS homeostasis in an oxidative stress-mediated disease model. *Nanoscale* **8**, 3739–3752 (2016).
139. Carney, R. P., Carney, T. M., Mueller, M. & Stellacci, F. Dynamic Cellular Uptake of Mixed-Monolayer Protected Nanoparticles. *Biointerphases* **7**, 17 (2012).
140. Contini, C., Schneemilch, M., Gaisford, S. & Quirke, N. Nanoparticle–membrane interactions. *Journal of Experimental Nanoscience* vol. 13 62–81 (2018).
141. Cifuentes-Rius, A. *et al.* Gold Nanocluster-Mediated Cellular Death under Electromagnetic Radiation. *ACS Appl. Mater. Interfaces* **9**, 41159–41167 (2017).
142. Cassano, D. *et al.* Photothermal effect by NIR-responsive excretable ultrasmall-in-nano architectures. *Mater. Horizons* **6**, 531–537 (2019).
143. Lodola, A. & De Vivo, M. The increasing role of QM/MM in drug discovery. in *Advances in Protein Chemistry and Structural Biology* vol. 87 337–362 (2012).
144. De Vivo, M. Bridging quantum mechanics and structure-based drug design. *Front. Biosci.* **16**, 1619–1633 (2011).
145. Halawa, M. I., Lai, J. & Xu, G. Gold nanoclusters: synthetic strategies and recent advances in fluorescent sensing. *Mater. Today Nano* **3**, 9–27 (2018).
146. Abbas, M. A., Kamat, P. V. & Bang, J. H. Thiolated Gold Nanoclusters for Light Energy Conversion. *ACS Energy Lett.* **3**, 840–854 (2018).
147. Szabo, A. & Ostlund, N. S. *Modern Quantum Chemistry: Introduction to Advanced Electronic Structure Theory. Revised.* McGraw-Hili, New York (Dover Publications, 1989).
148. Leach, A. R. *Molecular modelling principles and applications.* (Prentice Hall, 2001).
149. Solomon, K. A. *Molecular modelling and drug design.* (MJP Publishers, 2006). doi:10.1107/97809553602060000770.

150. Rossi, G. & Monticelli, L. Gold nanoparticles in model biological membranes: A computational perspective. *Biochim. Biophys. Acta - Biomembr.* **1858**, 2380–2389 (2016).
151. An, D. *et al.* A Peptide-Coated Gold Nanocluster Exhibits Unique Behavior in Protein Activity Inhibition. *J. Am. Chem. Soc.* **137**, 8412–8418 (2015).
152. Periole, X. & Marrink, S.-J. The Martini Coarse-Grained Force Field. in *Biomolecular Simulations. Methods in Molecular Biology (Methods and Protocols)* 533–565 (2013). doi:10.1007/978-1-62703-017-5\_20.
153. Hoogerbrugge, P. J. & Koelman, J. M. V. A. Simulating microscopic hydrodynamic phenomena with dissipative particle dynamics. *EPL* vol. 19 155–160 (1992).
154. Espanol, P. & Warren, P. Statistical mechanics of dissipative particle dynamics. *EPL* **30**, 191–196 (1995).
155. Yue, T. & Zhang, X. Molecular understanding of receptor-mediated membrane responses to ligand-coated nanoparticles. *Soft Matter* **7**, 9104–9112 (2011).
156. Li, Y., Yue, T., Yang, K. & Zhang, X. Molecular modeling of the relationship between nanoparticle shape anisotropy and endocytosis kinetics. *Biomaterials* **33**, 4965–4973 (2012).
157. Yue, T. & Zhang, X. Cooperative effect in receptor-mediated endocytosis of multiple nanoparticles. *ACS Nano* **6**, 3196–3205 (2012).
158. Liu, Y. *et al.* Design of Small Nanoparticles Decorated with Amphiphilic Ligands: Self-Preservation Effect and Translocation into a Plasma Membrane. *ACS Appl. Mater. Interfaces* **11**, 23822–23831 (2019).
159. Ding, H. M. & Ma, Y. Q. Design strategy of surface decoration for efficient delivery of nanoparticles by computer simulation. *Sci. Rep.* **6**, 1–10 (2016).
160. Franco-Ulloa, S. *et al.* Dispersion State Phase Diagram of Citrate-Coated Metallic Nanoparticles in Saline Solutions. *Nat. Commun.* **11**, (2020).
161. Van Lehn, R. C. & Alexander-Katz, A. Fusion of ligand-coated nanoparticles with lipid

- bilayers: Effect of ligand flexibility. *J. Phys. Chem. A* **118**, 5848–5856 (2014).
162. Van Lehn, R. C. *et al.* Effect of particle diameter and surface composition on the spontaneous fusion of monolayer-protected gold nanoparticles with lipid bilayers. *Nano Lett.* **13**, 4060–4067 (2013).
163. Fetisov, E. O. & Siepmann, J. I. Structure and Phase Behavior of Mixed Self-Assembled Alkanethiolate Monolayers on Gold Nanoparticles: A Monte Carlo Study. *J. Phys. Chem. B* **120**, 1972–1978 (2016).
164. Munaò, G. *et al.* Molecular structure and multi-body potential of mean force in silica-polystyrene nanocomposites. *Nanoscale* **10**, 21656–21670 (2018).
165. Bore, S. L., Milano, G. & Cascella, M. Hybrid Particle-Field Model for Conformational Dynamics of Peptide Chains. *J. Chem. Theory Comput.* **14**, 1120–1130 (2018).
166. Deserno, M. & Bickel, T. Wrapping of a spherical colloid by a fluid membrane. *Europhys. Lett.* **62**, 767–774 (2003).
167. Gao, H., Shi, W. & Freund, L. B. Mechanics of receptor-mediated endocytosis. *Proc. Natl. Acad. Sci. U. S. A.* **102**, 9469–9474 (2005).
168. Sanz-Herrera, J. A. & Reina-Romo, E. Cell-biomaterial mechanical interaction in the framework of tissue engineering: Insights, computational modeling and perspectives. *International Journal of Molecular Sciences* vol. 12 8217–8244 (2011).
169. Zheng, L., Alhossary, A. A., Kwok, C. K. & Mu, Y. Molecular dynamics and simulation. in *Encyclopedia of Bioinformatics and Computational Biology: ABC of Bioinformatics* vols 1–3 550–566 (Elsevier, 2018).
170. Jorgensen, W. L. & Tirado-Rives, J. The OPLS Potential Functions for Proteins. Energy Minimizations for Crystals of Cyclic Peptides and Crambin. *J. Am. Chem. Soc.* **110**, 1657–1666 (1988).
171. Vanommeslaeghe, K., Raman, E. P. & MacKerell, A. D. J. Automation of the CHARMM General Force Field (CGenFF) II: assignment of bonded parameters and partial atomic charges. *J. Chem. Inf. Model.* **52**, 3155–68 (2012).

172. De Vivo, M., Masetti, M., Bottegoni, G. & Cavalli, A. Role of molecular dynamics and related methods in drug discovery. *J. Med. Chem.* **59**, 4035–4061 (2016).
173. Nikitin, A., Milchevskiy, Y. & Lyubartsev, A. AMBER-II: New Combining Rules and Force Field for Perfluoroalkanes. *J. Phys. Chem. B* **119**, 14563–14573 (2015).
174. Klauda, J. B. Perspective: Computational modeling of accurate cellular membranes with molecular resolution. *J. Chem. Phys.* **149**, 220901 (2018).
175. Todd, B. D. & Daivis, P. J. *Nonequilibrium Molecular Dynamics*. (Cambridge University Press, 2017). doi:10.1017/9781139017848.
176. Fitzgerald, G., DeJoannis, J. & Meunier, M. Multiscale modeling of nanomaterials. in *Modeling, Characterization, and Production of Nanomaterials* 3–53 (Elsevier, 2015). doi:10.1016/B978-1-78242-228-0.00001-6.
177. Ramezanzpour, M. *et al.* Computational and experimental approaches for investigating nanoparticle-based drug delivery systems. *Biochim. Biophys. Acta - Biomembr.* **1858**, 1688–1709 (2016).
178. Ding, H. M. & Ma, Y. Q. Theoretical and computational investigations of nanoparticle-biomembrane interactions in cellular delivery. *Small* vol. 11 1055–1071 (2015).
179. Periolo, X., Cavalli, M., Marrink, S.-J. & Ceruso, M. A. Combining an Elastic Network With a Coarse-Grained Molecular Force Field: Structure, Dynamics, and Intermolecular Recognition. *J. Chem. Theory Comput.* **5**, 2531–2543 (2009).
180. Poma, A. B., Cieplak, M. & Theodorakis, P. E. Combining the MARTINI and Structure-Based Coarse-Grained Approaches for the Molecular Dynamics Studies of Conformational Transitions in Proteins. *J. Chem. Theory Comput.* **13**, 1366–1374 (2017).
181. Marrink, S. J., Risselada, H. J., Yefimov, S., Tieleman, D. P. & De Vries, A. H. The MARTINI force field: Coarse grained model for biomolecular simulations. *J. Phys. Chem. B* **111**, 7812–7824 (2007).
182. Marrink, S. J., De Vries, A. H. & Mark, A. E. Coarse Grained Model for Semiquantitative Lipid Simulations. *J. Phys. Chem. B* **108**, 750–760 (2004).

183. Orozco, M. *et al.* Coarse-grained representation of protein flexibility. Foundations, Successes, and Shortcomings. in *Advances in Protein Chemistry and Structural Biology* vol. 85 183–215 (Academic Press Inc., 2011).
184. Kar, P. & Feig, M. Recent advances in transferable coarse-grained modeling of proteins. in *Advances in Protein Chemistry and Structural Biology* vol. 96 143–180 (Academic Press Inc., 2014).
185. L. Jorgensen, W., S. Maxwell, D. & Tirado-Rives, J. Development and Testing of the OPLS All-Atom Force Field on Conformational Energetics and Properties of Organic Liquids. *J. Am. Chem. Soc.* **118**, 11225–11236 (1996).
186. Schmid, N. *et al.* Definition and testing of the GROMOS force-field versions 54A7 and 54B7. *Eur. Biophys. J.* **40**, 843–856 (2011).
187. Vlachakis, D., Bencurova, E., Papangelopoulos, N. & Kossida, S. Current state-of-the-art molecular dynamics methods and applications. in *Advances in Protein Chemistry and Structural Biology* vol. 94 269–313 (Academic Press Inc., 2014).
188. Wu, Y., Tepper, H. L. & Voth, G. A. Flexible simple point-charge water model with improved liquid-state properties. *J. Chem. Phys.* **124**, 024503 (2006).
189. Horn, H. W. *et al.* Development of an improved four-site water model for biomolecular simulations: TIP4P-Ew. *J. Chem. Phys.* **120**, 9665–9678 (2004).
190. Zhao, C. L. *et al.* Seven-Site Effective Pair Potential for Simulating Liquid Water. *J. Phys. Chem. B* **123**, 4594–4603 (2019).
191. Jorgensen, W. L., Chandrasekhar, J., Madura, J. D., Impey, R. W. & Klein, M. L. Comparison of simple potential functions for simulating liquid water. *J. Chem. Phys.* **79**, 926–935 (1983).
192. Mahoney, M. W. & Jorgensen, W. L. A five-site model for liquid water and the reproduction of the density anomaly by rigid, nonpolarizable potential functions. *J. Chem. Phys.* **112**, 8910–8922 (2000).
193. Martín-Santamaría, S. *Computational Tools for Chemical Biology*. (2017). doi:10.1039/9781788010139.

194. Maier, J. A. *et al.* ff14SB: Improving the Accuracy of Protein Side Chain and Backbone Parameters from ff99SB. *J. Chem. Theory Comput.* **11**, 3696–3713 (2015).
195. Pérez, A. *et al.* Refinement of the AMBER force field for nucleic acids: Improving the description of  $\alpha/\gamma$  conformers. *Biophys. J.* **92**, 3817–3829 (2007).
196. Ivani, I. *et al.* Parmbsc1: A refined force field for DNA simulations. *Nat. Methods* **13**, 55–58 (2015).
197. Wang, J., Wolf, R. M., Caldwell, J. W., Kollman, P. A. & Case, D. A. Development and testing of a general Amber force field. *J. Comput. Chem.* **25**, 1157–1174 (2004).
198. Skjevik, Å. A., Madej, B. D., Walker, R. C. & Teigen, K. LIPID11: A modular framework for lipid simulations using amber. *J. Phys. Chem. B* **116**, 11124–11136 (2012).
199. Dickson, C. J. *et al.* Lipid14: The amber lipid force field. *J. Chem. Theory Comput.* **10**, 865–879 (2014).
200. Pohjolainen, E., Chen, X., Malola, S., Groenhof, G. & Häkkinen, H. A Unified AMBER-Compatible Molecular Mechanics Force Field for Thiolate-Protected Gold Nanoclusters. *J. Chem. Theory Comput.* **12**, 1342–1350 (2016).
201. Kusalik, P. G. & Svishchev, I. M. The spatial structure in liquid water. *Science* **265**, 1219–1221 (1994).
202. Wang, J., Wang, W., Kollman, P. A. & Case, D. A. Automatic atom type and bond type perception in molecular mechanical calculations. *J. Mol. Graph. Model.* **25**, 247–260 (2006).
203. Wang, J., Cieplak, P. & Kollman, P. A. How Well Does a Restrained Electrostatic Potential (RESP) Model Perform in Calculating Conformational Energies of Organic and Biological Molecules? *J. Comput. Chem.* **21**, 1049–1074 (2000).
204. Bayly, C. I., Cieplak, P., Cornell, W. D. & Kollman, P. A. A well-behaved electrostatic potential based method using charge restraints for deriving atomic charges: The RESP model. *J. Phys. Chem.* **97**, 10269–10280 (1993).

205. Carvalho, A. T. P., Teixeira, A. F. S. & Ramos, M. J. Parameters for molecular dynamics simulations of iron-sulfur proteins. *J. Comput. Chem.* **34**, 1540–1548 (2013).
206. Seminario, J. M. Calculation of intramolecular force fields from second-derivative tensors. *Int. J. Quantum Chem.* **60**, 1271–1277 (1996).
207. Alessandri, R. *et al.* Pitfalls of the Martini Model. *J. Chem. Theory Comput.* **15**, 5448–5460 (2019).
208. Rossi, G., Fuchs, P. F. J., Barnoud, J. & Monticelli, L. A Coarse-Grained MARTINI Model of Polyethylene Glycol and of Polyoxyethylene Alkyl Ether Surfactants. *J. Phys. Chem. B* **116**, 14353–14362 (2012).
209. Grunewald, F., Rossi, G., de Vries, A. H., Marrink, S. J. & Monticelli, L. Transferable MARTINI Model of Poly(ethylene Oxide). *J. Phys. Chem. B* **122**, 7436–7449 (2018).
210. Vögele, M., Holm, C. & Smiatek, J. Coarse-grained simulations of polyelectrolyte complexes: MARTINI models for poly(styrene sulfonate) and poly(diallyldimethylammonium). *J. Chem. Phys.* **143**, 243151 (2015).
211. De Jong, D. H., Baoukina, S., Ingólfsson, H. I. & Marrink, S. J. Martini straight: Boosting performance using a shorter cutoff and GPUs. *Comput. Phys. Commun.* **199**, 1–7 (2016).
212. De Jong, D. H. *et al.* Improved parameters for the martini coarse-grained protein force field. *J. Chem. Theory Comput.* **9**, 687–697 (2013).
213. Michalowsky, J., Schäfer, L. V., Holm, C. & Smiatek, J. A refined polarizable water model for the coarse-grained MARTINI force field with long-range electrostatic interactions. *J. Chem. Phys.* **146**, 054501 (2017).
214. Yesylevskyy, S. O., Schäfer, L. V., Sengupta, D. & Marrink, S. J. Polarizable water model for the coarse-grained MARTINI force field. *PLoS Comput. Biol.* **6**, 1–17 (2010).
215. Michalowsky, J., Zeman, J., Holm, C. & Smiatek, J. A polarizable MARTINI model for monovalent ions in aqueous solution. *J. Chem. Phys.* **149**, 163319 (2018).
216. Wu, Z., Cui, Q. & Yethiraj, A. A new coarse-grained model for water: The importance

- of electrostatic interactions. *J. Phys. Chem. B* **114**, 10524–10529 (2010).
217. Rapaport, D. C. *The Art of Molecular Dynamics Simulation*. vol. 3 (Cambridge University Press, 2004).
218. Goldstein, H., Poole, C., Safko, J. & Addison, S. R. Classical Mechanics, 3rd ed. *Am. J. Phys.* **70**, 782–783 (2002).
219. Donnelly, D. & Rogers, E. Symplectic integrators: An introduction. *Am. J. Phys.* **73**, 938–945 (2005).
220. Hünenberger, P. H. Thermostat algorithms for molecular dynamics simulations. *Adv. Polym. Sci.* **173**, 105–147 (2005).
221. Torchi, A., Simonelli, F., Ferrando, R. & Rossi, G. Local Enhancement of Lipid Membrane Permeability Induced by Irradiated Gold Nanoparticles. *ACS Nano* **11**, 12553–12561 (2017).
222. Gould, H. *et al.* *Thermal and Statistical Physics Simulations. Computers in Physics* vol. 10 (1996).
223. Bussi, G., Donadio, D. & Parrinello, M. Canonical sampling through velocity rescaling. *J. Chem. Phys.* **126**, 014101 (2007).
224. Yatsyshin, P. & Goddard, B. D. Mesoscopic virial equation for nonequilibrium statistical mechanics Related content Nonequilibrium temperature response for stochastic overdamped systems G Falasco and M Baiesi-General framework for fluctuating dynamic density functional theory Miguel A D. (2016) doi:10.1088/1367-2630/18/9/093043.
225. Berendsen, H. J. C., Postma, J. P. M., Van Gunsteren, W. F., Dinola, A. & Haak, J. R. Molecular dynamics with coupling to an external bath. *J. Chem. Phys.* **81**, 3684–3690 (1984).
226. Miller, R. E., Tadmor, E. B., Gibson, J. S., Bernstein, N. & Pavia, F. Molecular dynamics at constant Cauchy stress. *J. Chem. Phys.* **144**, 184107 (2016).
227. Parrinello, M. & Rahman, A. Polymorphic transitions in single crystals: A new



- molecular dynamics method. *J. Appl. Phys.* **52**, 7182–7190 (1981).
228. Ewald, P. P. Die Berechnung optischer und elektrostatischer Gitterpotentiale. *Ann. Phys.* **369**, 253–287 (1921).
229. Frigo, M. & Johnson, S. G. *The Fastest Fourier Transform in the West*. <http://theory.lcs.mit.edu/> (1997).
230. Frigo, M. & Johnson, S. G. *FFTW: AN ADAPTIVE SOFTWARE ARCHITECTURE FOR THE FFT*.
231. Darden, T., York, D. & Pedersen, L. Particle mesh Ewald: An N·log(N) method for Ewald sums in large systems. *J. Chem. Phys.* **98**, 10089–10092 (1993).
232. Ingólfsson, H. I. *et al.* The power of coarse graining in biomolecular simulations. *Wiley Interdisciplinary Reviews: Computational Molecular Science* vol. 4 225–248 (2014).
233. Voth, G. A. *Coarse-Graining of Condensed Phase and Biomolecular Systems*. *Coarse-Graining of Condensed Phase and Biomolecular Systems* (CRC Press, 2008). doi:10.1201/9781420059564.
234. Marrink, S. J. & Tieleman, D. P. Perspective on the martini model. *Chem. Soc. Rev.* **42**, 6801–6822 (2013).
235. Christ, C. D., Mark, A. E. & Van Gunsteren, W. F. Basic ingredients of free energy calculations: A review. *Journal of Computational Chemistry* vol. 31 1569–1582 (2010).
236. Bussi, G. & Laio, A. Using metadynamics to explore complex free-energy landscapes. *Nat. Rev. Phys.* (2020) doi:10.1038/s42254-020-0153-0.
237. Pohorille, A., Jarzynski, C. & Chipot, C. Good practices in free-energy calculations. *J. Phys. Chem. B* **114**, 10235–10253 (2010).
238. Camilloni, C. & Pietrucci, F. Advanced simulation techniques for the thermodynamic and kinetic characterization of biological systems. *Advances in Physics: X* vol. 3 885–916 (2018).
239. Roux, B. The calculation of the potential of mean force using computer simulations. *Comput. Phys. Commun.* **91**, 275–282 (1995).

240. Kästner, J. Umbrella sampling. *Wiley Interdiscip. Rev. Comput. Mol. Sci.* **1**, 932–942 (2011).
241. Kästner, J. Umbrella integration in two or more reaction coordinates. *J. Chem. Phys.* **131**, 034109 (2009).
242. Kästner, J. & Thiel, W. Analysis of the statistical error in umbrella sampling simulations by umbrella integration. *J. Chem. Phys.* **124**, (2006).
243. Kumar, S., Rosenberg, J. M., Bouzida, D., Swendsen, R. H. & Kollman, P. A. THE weighted histogram analysis method for free-energy calculations on biomolecules. I. The method. *J. Comput. Chem.* **13**, 1011–1021 (1992).
244. Kumar, S., Rosenberg, J. M., Bouzida, D., Swendsen, R. H. & Kollman, P. A. The weighted histogram analysis method for free-energy calculations on biomolecules. I. The method. *J. Comput. Chem.* **13**, 1011–1021 (1992).
245. Kästner, J. & Thiel, W. Bridging the gap between thermodynamic integration and umbrella sampling provides a novel analysis method: ‘umbrella integration’. *J. Chem. Phys.* **123**, (2005).
246. Shivakumar, D. *et al.* Prediction of absolute solvation free energies using molecular dynamics free energy perturbation and the oplis force field. *J. Chem. Theory Comput.* **6**, 1509–1519 (2010).
247. Villa, A. & Mark, A. E. Calculation of the free energy of solvation for neutral analogs of amino acid side chains. *J. Comput. Chem.* **23**, 548–553 (2002).
248. Bennett, C. H. Efficient estimation of free energy differences from Monte Carlo data. *J. Comput. Phys.* **22**, 245–268 (1976).
249. Steinbrecher, T., Mobley, D. L. & Case, D. A. Nonlinear scaling schemes for Lennard-Jones interactions in free energy calculations. *J. Chem. Phys.* **127**, 214108 (2007).
250. Pitera, J. W. & van Gunsteren, W. F. A Comparison of Non-Bonded Scaling Approaches for Free Energy Calculations. *Mol. Simul.* **28**, 45–65 (2002).
251. Makarucha, A. J., Todorova, N. & Yarovsky, I. Nanomaterials in biological

- environment: A review of computer modelling studies. *European Biophysics Journal* vol. 40 103–115 (2011).
252. Riley, R. S. & Day, E. S. Gold nanoparticle-mediated photothermal therapy: applications and opportunities for multimodal cancer treatment. *Wiley Interdisciplinary Reviews: Nanomedicine and Nanobiotechnology* vol. 9 e1449 (2017).
253. Lee, B. K., Yun, Y. H. & Park, K. Smart nanoparticles for drug delivery: Boundaries and opportunities. *Chem. Eng. Sci.* **125**, 158–164 (2015).
254. Yang, Y., Ren, L. & Wang, H. Strategies in the design of gold nanoparticles for intracellular targeting: Opportunities and challenges. *Therapeutic Delivery* vol. 8 879–897 (2017).
255. Guarise, C., Pasquato, L., De Filippis, V. & Scrimin, P. Gold nanoparticles-based protease assay. *Proc. Natl. Acad. Sci.* **103**, 3978–3982 (2006).
256. Kinnear, C., Moore, T. L., Rodriguez-Lorenzo, L., Rothen-Rutishauser, B. & Petri-Fink, A. Form Follows Function: Nanoparticle Shape and Its Implications for Nanomedicine. *Chemical Reviews* vol. 117 11476–11521 (2017).
257. Pedone, D., Moglianetti, M., De Luca, E., Bardi, G. & Pompa, P. P. Platinum nanoparticles in nanobiomedicine. *Chemical Society Reviews* vol. 46 4951–4975 (2017).
258. Jha, S. *et al.* Binding and uptake into human hepatocellular carcinoma cells of peptide-functionalized gold nanoparticles. *Bioconjug. Chem.* **28**, 222–229 (2017).
259. Liu, X., Yu, M., Kim, H., Marnett, M. & Stellacci, F. Determination of monolayer-protected gold nanoparticle ligand–shell morphology using NMR. *Nat. Commun.* **3**, 1182 (2012).
260. De Vivo, M. & Cavalli, A. Recent advances in dynamic docking for drug discovery. *Wiley Interdiscip. Rev. Comput. Mol. Sci.* **7**, e1320 (2017).
261. Salorinne, K. *et al.* Conformation and dynamics of the ligand shell of a water-soluble Au 102 nanoparticle. *Nat. Commun.* **7**, 10401 (2016).
262. Van Lehn, R. C. & Alexander-Katz, A. Pathway for insertion of amphiphilic

- nanoparticles into defect-free lipid bilayers from atomistic molecular dynamics simulations. *Soft Matter* **11**, 3165–3175 (2015).
263. Van Lehn, R. C. & Alexander-Katz, A. Membrane-embedded nanoparticles induce lipid rearrangements similar to those exhibited by biological membrane proteins. *J. Phys. Chem. B* **118**, 12586–12598 (2014).
264. Patitsa, M. *et al.* Magnetic nanoparticles coated with polyarabic acid demonstrate enhanced drug delivery and imaging properties for cancer theranostic applications. *Sci. Rep.* **7**, 775 (2017).
265. Heikkilä, E. *et al.* Cationic Au nanoparticle binding with plasma membrane-like lipid bilayers: Potential mechanism for spontaneous permeation to cells revealed by atomistic simulations. *J. Phys. Chem. C* **118**, 11131–11141 (2014).
266. Salassi, S., Simonelli, F., Bochicchio, D., Ferrando, R. & Rossi, G. Au Nanoparticles in Lipid Bilayers: A Comparison between Atomistic and Coarse-Grained Models. *J. Phys. Chem. C* **121**, 10927–10935 (2017).
267. Van Lehn, R. C. & Alexander-Katz, A. Energy landscape for the insertion of amphiphilic nanoparticles into lipid membranes: A computational study. *PLoS One* **14**, e0209492 (2019).
268. Ding, F. *et al.* Direct observation of a single nanoparticle-ubiquitin corona formation. *Nanoscale* **5**, 9162–9169 (2013).
269. Olenick, L. L. *et al.* Lipid Corona Formation from Nanoparticle Interactions with Bilayers. *Chem* **4**, 2709–2723 (2018).
270. Villarreal, O. D., Rodriguez, R. A., Yu, L. & Wambo, T. O. Molecular dynamics simulations on the effect of size and shape on the interactions between negative Au<sub>18</sub>(SR)<sub>14</sub>, Au<sub>102</sub>(SR)<sub>44</sub> and Au<sub>144</sub>(SR)<sub>60</sub> nanoparticles in physiological saline. *Colloids Surfaces A Physicochem. Eng. Asp.* **503**, 70–78 (2016).
271. Villarreal, O. D., Chen, L. Y., Whetten, R. L. & Yacaman, M. J. Ligand-modulated interactions between charged monolayer-protected Au<sub>144</sub>(SR)<sub>60</sub> gold nanoparticles in physiological saline. *Phys. Chem. Chem. Phys.* **17**, 3680–3688 (2015).

272. Chatzigoulas, A., Karathanou, K., Dellis, D. & Cournia, Z. NanoCrystal: A Web-Based Crystallographic Tool for the Construction of Nanoparticles Based on Their Crystal Habit. *J. Chem. Inf. Model.* **58**, 2380–2386 (2018).
273. Case, D. A. *et al.* Amber 2016. *Univ. California, San Fr.* (2016).
274. Anandkrishnan, R., Aguilar, B. & Onufriev, A. V. H++ 3.0: Automating pK prediction and the preparation of biomolecular structures for atomistic molecular modeling and simulations. *Nucleic Acids Res.* **40**, W537–W541 (2012).
275. van Dijk, M. & Bonvin, A. M. J. J. 3D-DART: a DNA structure modelling server. *Nucleic Acids Res.* **37**, W235–W239 (2009).
276. Colasanti, A. V, Lu, X. J. & Olson, W. K. Analyzing and building nucleic acid structures with 3DNA. *J. Vis. Exp.* e4401 (2013) doi:10.3791/4401.
277. Dodda, L. S., De Vaca, I. C., Tirado-Rives, J. & Jorgensen, W. L. LigParGen web server: An automatic OPLS-AA parameter generator for organic ligands. *Nucleic Acids Res.* **45**, W331–W336 (2017).
278. Jo, S., Kim, T., Iyer, V. G. & Im, W. CHARMM-GUI: A web-based graphical user interface for CHARMM. *J. Comput. Chem.* **29**, 1859–1865 (2008).
279. Ghahremanpour, M. M., Arab, S. S., Aghazadeh, S. B., Zhang, J. & Van Der Spoel, D. MemBuilder: A web-based graphical interface to build heterogeneously mixed membrane bilayers for the GROMACS biomolecular simulation program. *Bioinformatics* **30**, 439–441 (2014).
280. Wassenaar, T. A., Ingólfsson, H. I., Böckmann, R. A., Tieleman, D. P. & Marrink, S. J. Computational lipidomics with insane: A versatile tool for generating custom membranes for molecular simulations. *J. Chem. Theory Comput.* **11**, 2144–2155 (2015).
281. Sakthivel, N. A., Theivendran, S., Ganeshraj, V., Oliver, A. G. & Dass, A. Crystal Structure of Faradaurate-279: Au<sub>279</sub>(SPh-tBu)<sub>84</sub> Plasmonic Nanocrystal Molecules. *J. Am. Chem. Soc.* **139**, 15450–15459 (2017).
282. Bahena, D. *et al.* STEM electron diffraction and high-resolution images used in the determination of the crystal structure of the Au<sub>144</sub>(SR)<sub>60</sub> cluster. *J. Phys. Chem. Lett.*

- 4, 975–981 (2013).
283. Lucarini, M. & Pasquato, L. ESR spectroscopy as a tool to investigate the properties of self-assembled monolayers protecting gold nanoparticles. *Nanoscale* **2**, 668–676 (2010).
284. Zhu, M., Aikens, C. M., Hollander, F. J., Schatz, G. C. & Jin, R. Correlating the crystal structure of a thiol-protected Au<sub>25</sub> cluster and optical properties. *J. Am. Chem. Soc.* **130**, 5883–5885 (2008).
285. Qian, H., Eckenhoff, W. T., Zhu, Y., Pintauer, T. & Jin, R. Total structure determination of thiolate-protected Au<sub>38</sub> nanoparticles. *J. Am. Chem. Soc.* **132**, 8280–8281 (2010).
286. Pei, Y., Lin, S., Su, J. & Liu, C. Structure prediction of Au<sub>44</sub>(SR)<sub>28</sub>: A chiral superatom cluster. *J. Am. Chem. Soc.* **135**, 19060–19063 (2013).
287. Xu, W. W., Gao, Y. & Zeng, X. C. Unraveling structures of protection ligands on gold nanoparticle Au<sub>68</sub>(SH)<sub>32</sub>. *Sci. Adv.* **1**, e1400211 (2015).
288. Xu, W. W. & Gao, Y. Unraveling the atomic structures of the Au<sub>68</sub>(SR)<sub>34</sub> nanoparticles. *J. Phys. Chem. C* **119**, 14224–14229 (2015).
289. Jadzinsky, P. D., Calero, G., Ackerson, C. J., Bushnell, D. A. & Kornberg, R. D. Structure of a thiol monolayer-protected gold nanoparticle at 1.1 Å resolution. *Science* **318**, 430–433 (2007).
290. Zeng, C. *et al.* Structural patterns at all scales in a nonmetallic chiral Au<sub>133</sub>(SR)<sub>52</sub> nanoparticle. *Sci. Adv.* **1**, e1500045 (2015).
291. Lopez-Acevedo, O., Akola, J., Whetten, R. L., Grönbeck, H. & Häkkinen, H. Structure and bonding in the ubiquitous icosahedral metallic gold cluster Au<sub>144</sub>(SR)<sub>60</sub>. *J. Phys. Chem. C* **113**, 5035–5038 (2009).
292. Dolamic, I., Varnholt, B. & Bürgi, T. Far-infrared spectra of well-defined thiolate-protected gold clusters. *Phys. Chem. Chem. Phys.* **15**, 19561–19565 (2013).
293. Luo, Z. *et al.* Mass spectrometry and Monte Carlo method mapping of nanoparticle ligand shell morphology. *Nat. Commun.* **9**, 4478 (2018).
294. Gkeka, P., Sarkisov, L. & Angelikopoulos, P. Homogeneous hydrophobic-hydrophilic

- surface patterns enhance permeation of nanoparticles through lipid membranes. *J. Phys. Chem. Lett.* **4**, 1907–1912 (2013).
295. Pengo, P. *et al.* Gold nanoparticles with patterned surface monolayers for nanomedicine: current perspectives. *European Biophysics Journal* vol. 46 749–771 (2017).
296. Lee, M. W. *et al.* Interactions between Membranes and ‘metaphilic’ Polypeptide Architectures with Diverse Side-Chain Populations. *ACS Nano* **11**, 2858–2871 (2017).
297. Walther, A. & Müller, A. H. E. Janus particles: Synthesis, self-assembly, physical properties, and applications. *Chemical Reviews* vol. 113 5194–5261 (2013).
298. Huang, J., Kim, F., Tao, A. R., Connor, S. & Yang, P. Spontaneous formation of nanoparticle stripe patterns through dewetting. *Nature Materials* vol. 4 896–900 (2005).
299. Stirling, J. *et al.* Critical assessment of the evidence for striped nanoparticles. *PLoS One* **9**, e108482 (2014).
300. Ong, Q. K. & Stellacci, F. Response to “Critical Assessment of the Evidence for Striped Nanoparticles”. *PLoS One* **10**, e0135594 (2015).
301. Velachi, V., Bhandary, D., Singh, J. K. & Cordeiro, M. N. D. S. Structure of mixed self-assembled monolayers on gold nanoparticles at three different arrangements. *J. Phys. Chem. C* **119**, 3199–3209 (2015).
302. Verma, A. & Stellacci, F. Effect of surface properties on nanoparticle-cell interactions. *Small* vol. 6 12–21 (2010).
303. Gkeka, P. & Angelikopoulos, P. The Role of Patterned Hydrophilic Domains in Nanoparticle-Membrane Interactions. *Curr. Nanosci.* **7**, 690–698 (2011).
304. Heinz, H., Vaia, R. A., Farmer, B. L. & Naik, R. R. Accurate simulation of surfaces and interfaces of face-centered cubic metals using 12-6 and 9-6 lennard-jones potentials. *J. Phys. Chem. C* **112**, 17281–17290 (2008).
305. Heikkilä, E. *et al.* Atomistic simulations of functional Au 144(SR) 60 gold nanoparticles in aqueous environment. *J. Phys. Chem. C* **116**, 9805–9811 (2012).
306. Sousa Da Silva, A. W. & Vranken, W. F. ACPYPE - AnteChamber PYthon Parser

- interfacE. *BMC Res. Notes* **5**, 367 (2012).
307. Lindorff-Larsen, K. *et al.* Improved side-chain torsion potentials for the Amber ff99SB protein force field. *Proteins Struct. Funct. Bioinforma.* **78**, 1950–1958 (2010).
308. Genna, V., Vidossich, P., Ippoliti, E., Carloni, P. & Vivo, M. De. A Self-Activated Mechanism for Nucleic Acid Polymerization Catalyzed by DNA/RNA Polymerases. *J. Am. Chem. Soc.* **138**, 14592–14598 (2016).
309. Genna, V., Carloni, P. & De Vivo, M. A Strategically Located Arg/Lys Residue Promotes Correct Base Paring during Nucleic Acid Biosynthesis in Polymerases. *J. Am. Chem. Soc.* **140**, 3312–3321 (2018).
310. Genna, V., Gaspari, R., Dal Peraro, M. & De Vivo, M. Cooperative motion of a key positively charged residue and metal ions for DNA replication catalyzed by human DNA Polymerase- $\eta$ . *Nucleic Acids Res.* **44**, 2827–2836 (2016).
311. Riccardi, L. *et al.* Lid domain plasticity and lipid flexibility modulate enzyme specificity in human monoacylglycerol lipase. *Biochim. Biophys. Acta - Mol. Cell Biol. Lipids* **1862**, 441–451 (2017).
312. Kirschner, K. N. *et al.* GLYCAM06: A generalizable biomolecular force field. carbohydrates. *J. Comput. Chem.* **29**, 622–655 (2008).
313. Lin, J., Zhang, H., Chen, Z. & Zheng, Y. Penetration of Lipid Membranes by Gold Nanoparticles: Insights into Cellular Uptake, Cytotoxicity, and Their Relationship. *ACS Nano* **4**, 5421–5429 (2010).
314. Piserchia, A. *et al.* Conformational Mobility in Monolayer-Protected Nanoparticles: From Torsional Free Energy Profiles to NMR Relaxation. *J. Phys. Chem. C* **119**, 20100–20110 (2015).
315. Trinajstić, N. Calculation of carbon-sulphur bond lengths. *Tetrahedron Lett.* **9**, 1529–1532 (1968).
316. Cornell, W. D., Cieplak, P., Bayly, C. I. & Kollman, P. A. Application of RESP Charges To Calculate Conformational Energies, Hydrogen Bond Energies, and Free Energies of Solvation. *J. Am. Chem. Soc.* **115**, 9620–9631 (1993).



317. Vanquelef, E. *et al.* R.E.D. Server: A web service for deriving RESP and ESP charges and building force field libraries for new molecules and molecular fragments. *Nucleic Acids Res.* **39**, W511–W517 (2011).
318. Caleman, C. *et al.* Force field benchmark of organic liquids: Density, enthalpy of vaporization, heat capacities, surface tension, isothermal compressibility, volumetric expansion coefficient, and dielectric constant. *J. Chem. Theory Comput.* **8**, 61–74 (2012).
319. Hess, B., Bekker, H., Berendsen, H. J. C. & Fraaije, J. G. E. M. LINCS: A Linear Constraint Solver for molecular simulations. *J. Comput. Chem.* **18**, 1463–1472 (1997).
320. Hess, B., Kutzner, C., van der Spoel, D. & Lindahl, E. GROMACS 4: Algorithms for Highly Efficient, Load-Balanced, and Scalable Molecular Simulation. *J. Chem. Theory Comput.* **4**, 435–447 (2008).
321. Van Der Spoel, D. *et al.* GROMACS: Fast, flexible, and free. *J. Comput. Chem.* **26**, 1701–1718 (2005).
322. Abraham, M. J. *et al.* Gromacs: High performance molecular simulations through multi-level parallelism from laptops to supercomputers. *SoftwareX* **1–2**, 19–25 (2015).
323. Simonelli, F., Bochicchio, D., Ferrando, R. & Rossi, G. Monolayer-protected anionic Au nanoparticles walk into lipid membranes step by step. *J. Phys. Chem. Lett.* **6**, 3175–3179 (2015).
324. Riccardi, L., Genna, V. & De Vivo, M. Metal–ligand interactions in drug design. *Nat. Rev. Chem.* **2**, 100–112 (2018).
325. Zhang, Y. *et al.* Influence of the Spatial Distribution of Cationic Functional Groups at Nanoparticle Surfaces on Bacterial Viability and Membrane Interactions. *J. Am. Chem. Soc.* **142**, 10814–10823 (2020).
326. Torrano, A. A., Pereira, Â. S., Oliveira, O. N. & Barros-Timmons, A. Probing the interaction of oppositely charged gold nanoparticles with DPPG and DPPC Langmuir monolayers as cell membrane models. *Colloids Surfaces B Biointerfaces* **108**, 120–126 (2013).

327. Leroueil, P. R. *et al.* Wide varieties of cationic nanoparticles induce defects in supported lipid bilayers. *Nano Lett.* **8**, 420–424 (2008).
328. Leroueil, P. R. *et al.* Nanoparticle interaction with biological membranes: Does nanotechnology present a janus face? *Acc. Chem. Res.* **40**, 335–342 (2007).
329. Lin, J. *et al.* Understanding the synergistic effect of physicochemical properties of nanoparticles and their cellular entry pathways. *Commun. Biol.* **3**, 1–10 (2020).
330. Tahir, M. A. *et al.* Calcium-triggered fusion of lipid membranes is enabled by amphiphilic nanoparticles. *Proc. Natl. Acad. Sci.* **117**, 18470–18476 (2020).
331. Dreaden, E. C., Alkilany, A. M., Huang, X., Murphy, C. J. & El-Sayed, M. A. The golden age: Gold nanoparticles for biomedicine. *Chemical Society Reviews* vol. 41 2740–2779 (2012).
332. Arvizo, R. R. *et al.* Effect of nanoparticle surface charge at the plasma membrane and beyond. *Nano Lett.* **10**, 2543–2548 (2010).
333. Goodman, C. M., McCusker, C. D., Yilmaz, T. & Rotello, V. M. Toxicity of gold nanoparticles functionalized with cationic and anionic side chains. *Bioconjug. Chem.* **15**, 897–900 (2004).
334. Wang, X. *et al.* Nanoparticle Ligand Exchange and Its Effects at the Nanoparticle– Cell Membrane Interface. *Nano Lett* **19**, 20 (2019).
335. Li, S. & Malmstadt, N. Deformation and poration of lipid bilayer membranes by cationic nanoparticles. *Soft Matter* **9**, 4969–4976 (2013).
336. Chen, J. *et al.* Cationic Nanoparticles Induce Nanoscale Disruption in Living Cell Plasma Membranes. *J. Phys. Chem. B* **113**, 11179–11185 (2009).
337. Mecke, A. *et al.* Lipid Bilayer Disruption by Polycationic Polymers: The Roles of Size and Chemical Functional Group. *Langmuir* **21**, 10348–10354 (2005).
338. Lin, J. & Alexander-Katz, A. Cell membranes open ‘doors’ for cationic nanoparticles/ biomolecules: Insights into uptake kinetics. *ACS Nano* **7**, 10799–10808 (2013).
339. Sakai, N. & Matile, S. Anion-Mediated Transfer of Polyarginine across Liquid and

- Bilayer Membranes. *J. Am. Chem. Soc.* **125**, 14348–14356 (2003).
340. Contini, C. *et al.* Size dependency of gold nanoparticles interacting with model membranes. *Commun. Chem.* **3**, 130 (2020).
341. Pantos, A., Tsogas, I. & Paleos, C. M. Guanidinium group: A versatile moiety inducing transport and multicompartmentalization in complementary membranes. *Biochimica et Biophysica Acta - Biomembranes* vol. 1778 811–823 (2008).
342. Lombardo, D. *et al.* Effect of anionic and cationic polyamidoamine (PAMAM) dendrimers on a model lipid membrane. *Biochim. Biophys. Acta - Biomembr.* **1858**, 2769–2777 (2016).
343. Shai, Y. Mechanism of the binding, insertion and destabilization of phospholipid bilayer membranes by  $\alpha$ -helical antimicrobial and cell non-selective membrane-lytic peptides. *Biochim. Biophys. Acta - Biomembr.* **1462**, 55–70 (1999).
344. Yesylevskyy, S., Marrink, S. J. & Mark, A. E. Alternative mechanisms for the interaction of the cell-penetrating peptides penetratin and the TAT peptide with lipid bilayers. *Biophys. J.* **97**, 40–49 (2009).
345. Gasparini, G. *et al.* Cellular Uptake of Substrate-Initiated Cell-Penetrating Poly(disulfide)s. *J. Am. Chem. Soc.* **136**, 6069–6074 (2014).
346. Salvio, R. & Cincotti, A. Guanidine based self-assembled monolayers on Au nanoparticles as artificial phosphodiesterases. *RSC Adv.* **4**, 28678–28682 (2014).
347. Paltrinieri, L. *et al.* Fe<sub>3</sub>O<sub>4</sub> nanoparticles coated with a guanidinium-functionalized polyelectrolyte extend the pH range for phosphate binding. *J. Mater. Chem. A* **5**, 18476–18485 (2017).
348. Savelli, C. & Salvio, R. Guanidine-Based Polymer Brushes Grafted onto Silica Nanoparticles as Efficient Artificial Phosphodiesterases. *Chem. - A Eur. J.* **21**, 5856–5863 (2015).
349. Chuard, N. *et al.* Activation of Cell-Penetrating Peptides with Ionpair- $\pi$  Interactions and Fluorophiles. *J. Am. Chem. Soc.* **138**, 11264–11271 (2016).

350. Fujisawa, K. *et al.* Ion Pair– $\pi$  Interactions. *J. Am. Chem. Soc* **137**, 44 (2015).
351. Soleimanpour, S. *et al.* Headgroup engineering in mechanosensitive membrane probes †. *14450 | Chem. Commun* **52**, 14450 (2016).
352. Dal Molin, M. *et al.* Fluorescent Flippers for Mechanosensitive Membrane Probes. *J. Am. Chem. Soc* **137**, 571 (2015).
353. Chuard, N. *et al.* Strain-Promoted Thiol-Mediated Cellular Uptake of Giant Substrates: Liposomes and Polymersomes. *Angew. Chemie Int. Ed.* **56**, 2947–2950 (2017).
354. Gasparini, G., Bang, E.-K. K., Montenegro, J. & Matile, S. Cellular uptake: lessons from supramolecular organic chemistry. *Chem. Commun.* **51**, 10389–10402 (2015).
355. Abegg, D. *et al.* Strained Cyclic Disulfides Enable Cellular Uptake by Reacting with the Transferrin Receptor. *J. Am. Chem. Soc.* **139**, 231–238 (2017).
356. Chuard, N., Gasparini, G., Roux, A., Sakai, N. & Matile, S. Cell-penetrating poly(disulfide)s: the dependence of activity, depolymerization kinetics and intracellular localization on their length. *Org. Biomol. Chem.* **13**, 64–67 (2015).
357. Gorman, A., Hossain, K. R., Cornelius, F. & Clarke, R. J. Penetration of phospholipid membranes by poly-l-lysine depends on cholesterol and phospholipid composition. *Biochim. Biophys. Acta - Biomembr.* **1862**, 183128 (2020).
358. Ohvo-Rekilä, H., Ramstedt, B., Leppimäki, P. & Peter Slotte, J. Cholesterol interactions with phospholipids in membranes. *Progress in Lipid Research* vol. 41 66–97 (2002).
359. Franco-Ulloa, S., Riccardi, L., Rimembrana, F., Pini, M. & De Vivo, M. NanoModeler: A Webserver for Molecular Simulations and Engineering of Nanoparticles. *J. Chem. Theory Comput.* **15**, 2022–2032 (2019).
360. Vazdar, M. *et al.* Arginine ‘magic’: Guanidinium Like-Charge Ion Pairing from Aqueous Salts to Cell Penetrating Peptides. *Acc. Chem. Res.* **51**, 1455–1464 (2018).
361. Heikkilä, E. *et al.* Atomistic simulations of functional Au<sub>144</sub>(SR)<sub>60</sub> gold nanoparticles in aqueous environment. *J. Phys. Chem. C* **116**, 9805–9815 (2012).
362. Shimizu, K., Nakamura, H. & Watano, S. MD simulation study of direct permeation of

- a nanoparticle across the cell membrane under an external electric field. *Nanoscale* **8**, 11897–11906 (2016).
363. Ma, Y., Poole, K., Goyette, J. & Gaus, K. Introducing Membrane Charge and Membrane Potential to T Cell Signaling. *Front. Immunol.* **8**, 1 (2017).
364. Silvera Batista, C. A. *et al.* Nonadditivity of nanoparticle interactions. *Science* **350**, 1242477–1242477 (2015).
365. Hong, R. *et al.* Control of Protein Structure and Function through Surface Recognition by Tailored Nanoparticle Scaffolds. *J. Am. Chem. Soc.* **126**, 739–743 (2004).
366. Moyano, D. F. & Rotello, V. M. Nano Meets Biology: Structure and Function at the Nanoparticle Interface. *Langmuir* **27**, 10376–10385 (2011).
367. Cagno, V. *et al.* Broad-spectrum non-toxic antiviral nanoparticles with a virucidal inhibition mechanism. *Nat. Mater.* **17**, 195–203 (2018).
368. Zacheo, A. *et al.* Multi-sulfonated ligands on gold nanoparticles as virucidal antiviral for Dengue virus. *Sci. Rep.* **10**, 9052 (2020).
369. Bonomi, R., Cazzolaro, A. & Prins, L. J. Assessment of the morphology of mixed SAMs on Au nanoparticles using a fluorescent probe. *Chem. Commun.* **47**, 445–447 (2011).
370. Michaud-Agrawal, N., Denning, E. J., Woolf, T. B. & Beckstein, O. MDAAnalysis: A toolkit for the analysis of molecular dynamics simulations. *J. Comput. Chem.* **32**, 2319–2327 (2011).
371. Czarnik, A. W. Supramolecular Chemistry, Fluorescence, and Sensing. in vol. 17 1–9 (UTC, 1993).
372. Bell, T. W. & Hext, N. M. Supramolecular optical chemosensors for organic analytes. *Chem. Soc. Rev.* **33**, 589–598 (2004).
373. Shellaiah, M. & Sun, K. Luminescent Metal Nanoclusters for Potential Chemosensor Applications. *Chemosensors* **5**, 36 (2017).
374. Jazayeri, M. H., Aghaie, T., Avan, A., Vatankhah, A. & Ghaffari, M. R. S. Colorimetric detection based on gold nano particles (GNPs): An easy, fast, inexpensive, low-cost and

- short time method in detection of analytes (protein, DNA, and ion). *Sensing and Bio-Sensing Research* vol. 20 1–8 (2018).
375. Thakur, A., Sardar, S. & Ghosh, S. A highly selective redox, chromogenic, and fluorescent chemosensor for Hg<sup>2+</sup> in aqueous solution based on ferrocene-glycine bioconjugates. *Inorg. Chem.* **50**, 7066–7073 (2011).
376. Perrone, B., Springhetti, S., Ramadori, F., Rastrelli, F. & Mancin, F. ‘NMR chemosensing’ using monolayer-protected nanoparticles as receptors. *J. Am. Chem. Soc.* **135**, 11768–11771 (2013).
377. Sabela, M., Balme, S., Bechelany, M., Janot, J. M. & Bisetty, K. A Review of Gold and Silver Nanoparticle-Based Colorimetric Sensing Assays. *Advanced Engineering Materials* vol. 19 1700270 (2017).
378. Priyadarshini, E. & Pradhan, N. Gold nanoparticles as efficient sensors in colorimetric detection of toxic metal ions: A review. *Sensors and Actuators, B: Chemical* vol. 238 888–902 (2017).
379. Aldewachi, H. *et al.* Gold nanoparticle-based colorimetric biosensors. *Nanoscale* vol. 10 18–33 (2018).
380. Daniel, M.-C. & Astruc, D. Gold nanoparticles: assembly, supramolecular chemistry, quantum-size-related properties, and applications toward biology, catalysis, and nanotechnology. *Chem. Rev.* **104**, 293–346 (2004).
381. Oliveira, E. *et al.* Revisiting the use of gold and silver functionalised nanoparticles as colorimetric and fluorometric chemosensors for metal ions. *Sensors and Actuators, B: Chemical* vol. 212 297–328 (2015).
382. Chang, C. C. *et al.* Gold nanoparticle-based colorimetric strategies for chemical and biological sensing applications. *Nanomaterials* vol. 9 (2019).
383. De Biasi, F., Rosa-Gastaldo, D., Sun, X., Mancin, F. & Rastrelli, F. Nanoparticle-Assisted NMR Spectroscopy: Enhanced Detection of Analytes by Water-Mediated Saturation Transfer. *J. Am. Chem. Soc.* **141**, 4870–4877 (2019).
384. Verly, I. R. N. *et al.* Catecholamines profiles at diagnosis: Increased diagnostic

- sensitivity and correlation with biological and clinical features in neuroblastoma patients. *Eur. J. Cancer* **72**, 235–243 (2017).
385. Verly, I. R. N. *et al.* 3-Methoxytyramine: An independent prognostic biomarker that associates with high-risk disease and poor clinical outcome in neuroblastoma patients. *Eur. J. Cancer* **90**, 102–110 (2018).
386. Peitzsch, M. *et al.* Biochemical testing for neuroblastoma using plasma free 3-O-methyldopa, 3-methoxytyramine, and normetanephrine. *Pediatr. Blood Cancer* **67**, (2020).
387. Olsson, M. H. M., SØndergaard, C. R., Rostkowski, M. & Jensen, J. H. PROPKA3: Consistent treatment of internal and surface residues in empirical p K a predictions. *J. Chem. Theory Comput.* **7**, 525–537 (2011).
388. Ross, G. A., Rustenburg, A. S., Grinaway, P. B., Fass, J. & Chodera, J. D. Biomolecular Simulations under Realistic Macroscopic Salt Conditions. *J. Phys. Chem. B* **122**, 5466–5486 (2018).
389. Dodge, Y. Kolmogorov–Smirnov Test. in *The Concise Encyclopedia of Statistics* 283–287 (Springer New York, 2008). doi:10.1007/978-0-387-32833-1\_214.
390. Parmentier, Y., Bossant, M.-J., Bertrand, M. & Walther, B. In Vitro Studies of Drug Metabolism. in *Comprehensive Medicinal Chemistry II* 231–257 (Elsevier, 2007). doi:10.1016/B0-08-045044-X/00125-5.
391. Chakraborty, I. & Pradeep, T. Atomically Precise Clusters of Noble Metals: Emerging Link between Atoms and Nanoparticles. *Chemical Reviews* vol. 117 8208–8271 (2017).
392. Zhang, J., Mou, L. & Jiang, X. Surface chemistry of gold nanoparticles for health-related applications. *Chem. Sci.* **11**, 923–936 (2020).
393. Tarallo, R. *et al.* Clickable functionalization of liposomes with the gH625 peptide from herpes simplex virus type i for intracellular drug delivery. *Chem. - A Eur. J.* **17**, 12659–12668 (2011).
394. Li, Y., Zhang, X. & Cao, D. Nanoparticle hardness controls the internalization pathway for drug delivery. *Nanoscale* **7**, 2758–2769 (2015).

395. Han, X., Xu, K., Taratula, O. & Farsad, K. Applications of nanoparticles in biomedical imaging. *Nanoscale* **11**, 799–819 (2019).
396. Uzun, O. *et al.* Water-soluble amphiphilic gold nanoparticles with structured ligand shells. *Chem. Commun.* 196–198 (2008) doi:10.1039/b713143g.
397. Septiadi, D., Crippa, F., Moore, T. L., Rothen-Rutishauser, B. & Petri-Fink, A. Nanoparticle–Cell Interaction: A Cell Mechanics Perspective. *Adv. Mater.* **30**, 1–30 (2018).
398. Heuer-Jungemann, A. *et al.* The Role of Ligands in the Chemical Synthesis and Applications of Inorganic Nanoparticles. (2019) doi:10.1021/acs.chemrev.8b00733.
399. Ginzburg, V. V. & Balijepalli, S. Modeling the thermodynamics of the interaction of nanoparticles with cell membranes. *Nano Lett.* **7**, 3716–3722 (2007).
400. Angelikopoulos, P., Sarkisov, L., Cournia, Z. & Gkeka, P. Self-assembly of anionic, ligand-coated nanoparticles in lipid membranes. *Nanoscale* **9**, 1040–1048 (2017).
401. Villarreal, O. D., Chen, L. Y., Whetten, R. L. & Yacaman, M. J. Ligand-modulated interactions between charged monolayer-protected Au<sub>144</sub>(SR)<sub>60</sub> gold nanoparticles in physiological saline. *Phys. Chem. Chem. Phys.* **17**, 3680–3688 (2015).
402. Czaplewski, C., Karczyńska, A., Sieradzan, A. K. & Liwo, A. UNRES server for physics-based coarse-grained simulations and prediction of protein structure, dynamics and thermodynamics. *Nucleic Acids Res.* **46**, W304–W309 (2018).
403. Damre, M., Marchetto, A. & Giorgetti, A. MERMAID: dedicated web server to prepare and run coarse-grained membrane protein dynamics. *Nucleic Acids Res.* **47**, W456–W461 (2019).
404. De Bruin, L. & Maddocks, J. H. cgDNAweb: a web interface to the cgDNA sequence-dependent coarse-grain model of double-stranded DNA. *Nucleic Acids Res.* **46**, W5–W10 (2018).
405. Walkey, C. D., Olsen, J. B., Guo, H., Emili, A. & Chan, W. C. W. Nanoparticle size and surface chemistry determine serum protein adsorption and macrophage uptake. *J. Am. Chem. Soc.* **134**, 2139–2147 (2012).



406. Angioletti-Uberti, S. Theory, simulations and the design of functionalized nanoparticles for biomedical applications: A Soft Matter Perspective. *npj Computational Materials* vol. 3 48 (2017).
407. Xia, Y., Xiong, Y., Lim, B. & Skrabalak, S. E. Shape-controlled synthesis of metal nanocrystals: Simple chemistry meets complex physics? *Angewandte Chemie - International Edition* vol. 48 60–103 (2009).
408. Abedini, A. *et al.* Recent Advances in Shape-Controlled Synthesis of Noble Metal Nanoparticles by Radiolysis Route. *Nanoscale Research Letters* vol. 11 287 (2016).
409. Ong, Q., Luo, Z. & Stellacci, F. Characterization of Ligand Shell for Mixed-Ligand Coated Gold Nanoparticles. *Acc. Chem. Res.* **50**, 1911–1919 (2017).
410. Prates Ramalho, J. P., Gkeka, P. & Sarkisov, L. Structure and phase transformations of DPPC lipid bilayers in the presence of nanoparticles: Insights from coarse-grained molecular dynamics simulations. *Langmuir* **27**, 3723–3730 (2011).
411. Nangia, S. & Sureshkumar, R. Effects of nanoparticle charge and shape anisotropy on translocation through cell membranes. *Langmuir* **28**, 17666–17671 (2012).
412. Skriver, H. L. & Rosengaard, N. M. Surface energy and work function of elemental metals. *Phys. Rev. B* **46**, 7157–7168 (1992).
413. Krpetić, Ž. *et al.* High-resolution sizing of monolayer-protected gold clusters by differential centrifugal sedimentation. *ACS Nano* **7**, 8881–8890 (2013).
414. Ghorai, P. K. & Glotzer, S. C. Molecular dynamics simulation study of self-assembled monolayers of alkanethiol surfactants on spherical gold nanoparticles. *J. Phys. Chem. C* **111**, 15857–15862 (2007).
415. Bennett, W. F. D., Shea, J. E. & Tieleman, D. P. Phospholipid Chain Interactions with Cholesterol Drive Domain Formation in Lipid Membranes. *Biophys. J.* **114**, 2595–2605 (2018).
416. Nalakarn, P., Boonnoy, P., Nisoh, N., Karttunen, M. & Wong-ekkabut, J. Dependence of fullerene aggregation on lipid saturation due to a balance between entropy and enthalpy. *Sci. Rep.* **9**, 1–11 (2019).

417. Herzog, F. A., Braun, L., Schoen, I. & Vogel, V. Improved Side Chain Dynamics in MARTINI Simulations of Protein-Lipid Interfaces. *J. Chem. Theory Comput.* **12**, 2446–2458 (2016).
418. Comenge, J. The Role of PEG Conformation in Mixed Layers: From Protein Corona Substrate to Steric Stabilization Avoiding Protein Adsorption. *Sci. Res.* 1–10 (2015) doi:10.14293/s2199-1006.1.sor-matsci.a0z6om.v1.
419. Smilgies, D.-M. & Folta-Stogniew, E. Molecular weight–gyration radius relation of globular proteins: a comparison of light scattering, small-angle X-ray scattering and structure-based data. *J. Appl. Crystallogr.* **48**, 1604–1606 (2015).
420. Salassi, S., Simonelli, F., Bochicchio, D., Ferrando, R. & Rossi, G. Au Nanoparticles in Lipid Bilayers: A Comparison between Atomistic and Coarse Grained Models. *J. Phys. Chem. C* acs.jpcc.6b12148 (2017) doi:10.1021/acs.jpcc.6b12148.
421. Samadi, A. *et al.* Platinum nanoparticles: A non-toxic, effective and thermally stable alternative plasmonic material for cancer therapy and bioengineering. *Nanoscale* **10**, 9097–9107 (2018).
422. Moglianetti, M. *et al.* Citrate-Coated, Size-Tunable Octahedral Platinum Nanocrystals: A Novel Route for Advanced Electrocatalysts. *ACS Appl. Mater. Interfaces* **10**, 41608–41617 (2018).
423. Maiorano, G. *et al.* Effects of cell culture media on the dynamic formation of protein-nanoparticle complexes and influence on the cellular response. *ACS Nano* **4**, 7481–7491 (2010).
424. Rizzello, L. & Pompa, P. P. Nanosilver-based antibacterial drugs and devices: Mechanisms, methodological drawbacks, and guidelines. *Chem. Soc. Rev.* **43**, 1501–1518 (2014).
425. Marsella, A., Valentini, P., Tarantino, P., Congedo, M. & Pompa, P. P. A gold nanoparticles-based colorimetric test to detect single nucleotide polymorphisms for improvement of personalized therapy of psoriasis. in *Biophotonics: Photonic Solutions for Better Health Care V* (eds. Popp, J., Tuchin, V. V., Matthews, D. L. & Pavone, F. S.) vol. 9887 98870P (2016).

426. Valentini, P. *et al.* DNA Barcoding Meets Nanotechnology: Development of a Universal Colorimetric Test for Food Authentication. *Angew. Chemie Int. Ed.* **56**, 8094–8098 (2017).
427. Kumar, S., Gandhi, K. S. & Kumar, R. Modeling of formation of gold nanoparticles by citrate method. *Ind. Eng. Chem. Res.* **46**, 3128–3136 (2007).
428. Goesmann, H. & Feldmann, C. Nanoparticulate Functional Materials. *Angew. Chemie Int. Ed.* **49**, 1362–1395 (2010).
429. Brandenberger, C. *et al.* Quantitative evaluation of cellular uptake and trafficking of plain and polyethylene glycol-coated gold nanoparticles. *Small* **6**, 1669–1678 (2010).
430. Bigall, N. C. & Eychmüller, A. Synthesis of noble metal nanoparticles and their non-ordered superstructures. *Philos. Trans. R. Soc. A Math. Phys. Eng. Sci.* **368**, 1385–1404 (2010).
431. Kister, T., Monego, D., Mulvaney, P., Widmer-Cooper, A. & Kraus, T. Colloidal Stability of Apolar Nanoparticles: The Role of Particle Size and Ligand Shell Structure. *ACS Nano* **12**, 5969–5977 (2018).
432. Morozova, T. I. *et al.* In Silico Design Enables the Rapid Production of Surface-Active Colloidal Amphiphiles. *ACS Cent. Sci.* **6**, 166–173 (2020).
433. Gisbert-González, J. M., Feliu, J. M., Ferre-Vilaplana, A. & Herrero, E. Why Citrate Shapes Tetrahedral and Octahedral Colloidal Platinum Nanoparticles in Water. *J. Phys. Chem. C* **122**, 19004–19014 (2018).
434. Al-Johani, H. *et al.* The structure and binding mode of citrate in the stabilization of gold nanoparticles. *Nat. Chem.* **9**, 890–895 (2017).
435. Park, J. W. & Shumaker-Parry, J. S. Structural study of citrate layers on gold nanoparticles: Role of intermolecular interactions in stabilizing nanoparticles. *J. Am. Chem. Soc.* **136**, 1907–1921 (2014).
436. Park, J.-W. W. & Shumaker-Parry, J. S. Strong resistance of citrate anions on metal nanoparticles to desorption under thiol functionalization. *ACS Nano* **9**, 1665–1682 (2015).

437. Lin, Y. *et al.* Study of Citrate Adsorbed on the Au(111) Surface by Scanning Probe Microscopy. *Langmuir* **19**, 10000–10003 (2003).
438. Brancolini, G. *et al.* Probing the influence of citrate-capped gold nanoparticles on an amyloidogenic protein. *ACS Nano* **9**, 2600–2613 (2015).
439. Dominguez, G. A. *et al.* Effects of charge and surface ligand properties of nanoparticles on oxidative stress and gene expression within the gut of *Daphnia magna*. *Aquat. Toxicol.* **162**, 1–9 (2015).
440. French, R. A. *et al.* Influence of ionic strength, pH, and cation valence on aggregation kinetics of titanium dioxide nanoparticles. *Environ. Sci. Technol.* **43**, 1354–1359 (2009).
441. Shukla, A. & Rehage, H. Zeta potentials and Debye screening lengths of aqueous, viscoelastic surfactant solutions (cetyltrimethylammonium bromide/sodium salicylate system). *Langmuir* **24**, 8507–8513 (2008).
442. Bhattacharjee, S. DLS and zeta potential – What they are and what they are not? *J. Control. Release* **235**, 337–351 (2016).
443. Dorobantu, L. S., Bhattacharjee, S., Foght, J. M. & Gray, M. R. Analysis of force interactions between AFM tips and hydrophobic bacteria using DLVO theory. *Langmuir* **25**, 6968–6976 (2009).
444. Ishikawa, Y., Katoh, Y. & Ohshima, H. Colloidal stability of aqueous polymeric dispersions: Effect of pH and salt concentration. *Colloids Surfaces B Biointerfaces* **42**, 53–58 (2005).
445. Pierre, A. . & Ma, K. DLVO Theory and Clay Aggregate Architectures Formed with AlCl<sub>3</sub>. *J. Eur. Ceram. Soc.* **19**, 1615–1622 (1999).
446. Ninham, B. W. On progress in forces since the DLVO theory. *Adv. Colloid Interface Sci.* **83**, 1–17 (1999).
447. Lyklema, J., van Leeuwen, H. P. & Minor, M. DLVO-theory, a dynamic re-interpretation. *Adv. Colloid Interface Sci.* **83**, 33–69 (1999).
448. Tavanti, F., Pedone, A. & Menziani, M. C. A closer look into the ubiquitin corona on

- gold nanoparticles by computational studies. *New J. Chem.* **39**, 2474–2482 (2015).
449. Chong, G. & Hernandez, R. Adsorption Dynamics and Structure of Polycations on Citrate-Coated Gold Nanoparticles. (2018) doi:10.1021/acs.jpcc.8b05202.
450. Kunze, J., Burgess, I., Nichols, R., Buess-Herman, C. & Lipkowski, J. Electrochemical evaluation of citrate adsorption on Au(111) and the stability of citrate-reduced gold colloids. *J. Electroanal. Chem.* **599**, 147–159 (2007).
451. Park, S. *et al.* Reversibly pH-responsive gold nanoparticles and their applications for photothermal cancer therapy. *Sci. Rep.* **9**, (2019).
452. Nam, J., Won, N., Jin, H., Chung, H. & Kim, S. pH-induced aggregation of gold nanoparticles for photothermal cancer therapy. *J. Am. Chem. Soc.* **131**, 13639–13645 (2009).
453. Shou, Q. *et al.* Effect of pH on the single-step synthesis of gold nanoparticles using PEO-PPO-PEO triblock copolymers in aqueous media. *J. Colloid Interface Sci.* **363**, 481–489 (2011).
454. Das, A., Chadha, R., Maiti, N. & Kapoor, S. Synthesis of pH sensitive gold nanoparticles for potential application in radiosensitization. *Mater. Sci. Eng. C* **55**, 34–41 (2015).
455. Park, J. W. Negative-Imaging of Citrate Layers on Gold Nanoparticles by Ligand-Templated Metal Deposition: Revealing Surface Heterogeneity. *Part. Part. Syst. Charact.* **36**, 1800329 (2019).
456. Note: The values used for comparison resulted from rescaling the published citrate surface densities to the dimensions of our test case which has a surface area of 21.2 nm<sup>2</sup>. in.
457. Hunt, S. T. & Román-Leshkov, Y. Principles and Methods for the Rational Design of Core-Shell Nanoparticle Catalysts with Ultralow Noble Metal Loadings. *Acc. Chem. Res.* **51**, 1054–1062 (2018).
458. Tavanti, F., Pedone, A. & Menziani, M. C. Multiscale Molecular Dynamics Simulation of Multiple Protein Adsorption on Gold Nanoparticles. *Int. J. Mol. Sci.* **20**, 3539 (2019).

459. Li, R. *et al.* Computational and experimental characterizations of silver nanoparticle-apolipoprotein biocorona. *J. Phys. Chem. B* **117**, 13451–13456 (2013).
460. Heikkilä, E. *et al.* Atomistic simulations of functional Au<sub>144</sub>(SR)<sub>60</sub> gold nanoparticles in aqueous environment. *J. Phys. Chem. C* **116**, 9805–9811 (2012).
461. Agrawal, Y. & Patel, V. Nanosuspension: An approach to enhance solubility of drugs. *J. Adv. Pharm. Technol. Res.* **2**, 81 (2011).
462. Jana, N. R. & Pal, T. Anisotropic metal nanoparticles for use as surface-enhanced raman substrates. *Adv. Mater.* **19**, 1761–1765 (2007).
463. Su, X. & Kanjanawarut, R. Control of metal nanoparticles aggregation and dispersion by PNA and PNA-DNA complexes, and its application for colorimetric DNA detection. *ACS Nano* **3**, 2751–2759 (2009).
464. Shipway, A. N., Lahav, M., Gabai, R. & Willner, I. Investigations into the electrostatically induced aggregation of Au nanoparticles. *Langmuir* **16**, 8789–8795 (2000).
465. Gkeka, P., Angelikopoulos, P., Sarkisov, L. & Cournia, Z. Membrane Partitioning of Anionic, Ligand-Coated Nanoparticles Is Accompanied by Ligand Snorkeling, Local Disordering, and Cholesterol Depletion. *PLoS Comput. Biol.* **10**, e1003917 (2014).
466. Gkeka, P., Angelikopoulos, P. & Cournia, Z. Study of Nanoparticle-Lipid Bilayer Interactions: Insights from Coarse-Grained Molecular Dynamics Simulations. *Biophys. J.* **104**, 426a (2013).
467. Pompa, P. P. *et al.* Physical assessment of toxicology at nanoscale: Nano dose-metrics and toxicity factor. *Nanoscale* **3**, 2889–2897 (2011).
468. Turkevich, J., Stevenson, P. C. & Hillier, J. A study of the nucleation and growth processes in the synthesis of colloidal gold. *Discuss. Faraday Soc.* **11**, 55 (1951).
469. Guarnieri, D. *et al.* Biotransformation and Biological Interaction of Graphene and Graphene Oxide during Simulated Oral Ingestion. *Small* **14**, 1800227 (2018).
470. Sitia, L., Catelani, T., Guarnieri, D. & Pompa, P. P. In Vitro Blood-Brain Barrier Models

- for Nanomedicine: Particle-Specific Effects and Methodological Drawbacks. *ACS Appl. Bio Mater.* **2**, 3279–3289 (2019).
471. Schubertová, V., Martinez-Veracoechea, F. J. & Vácha, R. Influence of ligand distribution on uptake efficiency. *Soft Matter* **11**, 2726–2730 (2015).
472. Guarnieri, D., Malvindi, M. A., Belli, V., Pompa, P. P. & Netti, P. Effect of silica nanoparticles with variable size and surface functionalization on human endothelial cell viability and angiogenic activity. *J. Nanoparticle Res.* **16**, 1–14 (2014).
473. Sun, J. *et al.* Tunable rigidity of (polymeric core)-(lipid shell) nanoparticles for regulated cellular uptake. *Adv. Mater.* **27**, 1402–1407 (2015).
474. Zorko, M. & Langel, Ü. Cell-penetrating peptides: Mechanism and kinetics of cargo delivery. *Advanced Drug Delivery Reviews* vol. 57 529–545 (2005).
475. Galdiero, S. *et al.* Fusogenic domains in herpes simplex virus type 1 glycoprotein H. *J. Biol. Chem.* **280**, 28632–28643 (2005).
476. Galdiero, S. *et al.* Analysis of a membrane interacting region of herpes simplex virus type 1 glycoprotein H. *J. Biol. Chem.* **283**, 29993–30009 (2008).
477. Carberry, T. P. *et al.* Dendrimer functionalization with a membrane-interacting domain of herpes simplex virus type 1: Towards intracellular delivery. *Chem. - A Eur. J.* **18**, 13678–13685 (2012).
478. Borchmann, D. E. *et al.* Membranotropic peptide-functionalized poly(lactide)- graft - poly(ethylene glycol) brush copolymers for intracellular delivery. *Macromolecules* **48**, 942–949 (2015).
479. Guarnieri, D. *et al.* Surface decoration with gH625-membranotropic peptides as a method to escape the endo-lysosomal compartment and reduce nanoparticle toxicity. *Nanotechnology* **26**, 1–11 (2015).
480. Falanga, A. *et al.* A peptide derived from herpes simplex virus type 1 glycoprotein H: Membrane translocation and applications to the delivery of quantum dots. *Nanomedicine Nanotechnology, Biol. Med.* **7**, 925–934 (2011).

481. Perillo, E. *et al.* Synthesis and in vitro evaluation of fluorescent and magnetic nanoparticles functionalized with a cell penetrating peptide for cancer theranosis. *J. Colloid Interface Sci.* **499**, 209–217 (2017).
482. Guarnieri, D. *et al.* Particle size affects the cytosolic delivery of membranotropic peptide-functionalized platinum nanozymes. *Nanoscale* **9**, 11288–11296 (2017).
483. Vitiello, G. *et al.* Fusion of raft-like lipid bilayers operated by a membranotropic domain of the HSV-type 1 glycoprotein gH occurs through a cholesterol-dependent mechanism. *Soft Matter* **11**, 3003–3016 (2015).
484. Galdiero, S. *et al.* Structure and orientation of the gH625-644 membrane interacting region of herpes simplex virus type 1 in a membrane mimetic system. *Biochemistry* **51**, 3121–3128 (2012).
485. Daily, M. D., Olsen, B. N., Schlesinger, P. H., Ory, D. S. & Baker, N. A. Improved coarse-grained modeling of cholesterol-containing lipid bilayers. *J. Chem. Theory Comput.* **10**, 2137–2150 (2014).
486. Bilayers, P. *et al.* A Critical Comparison of Biomembrane Force Fields: Structure and Dynamics of Model DMPC, POPC, and POPE Bilayers. *J. Phys. Chem. B* **120**, 3888–3903 (2016).
487. Galdiero, S., Falanga, A., Morelli, G. & Galdiero, M. GH625: A milestone in understanding the many roles of membranotropic peptides. *Biochimica et Biophysica Acta - Biomembranes* vol. 1848 16–25 (2015).
488. Jusufi, A., Devane, R. H., Shinoda, W. & Klein, M. L. Nanoscale carbon particles and the stability of lipid bilayers. *Soft Matter* **7**, 1139–1146 (2011).
489. Wong-Ekkabut, J. *et al.* Computer simulation study of fullerene translocation through lipid membranes. *Nat. Nanotechnol.* **3**, 363–368 (2008).
490. Wang, Z. W., Li, G. Z., Yi, X. Z., Guan, D. R. & Lou, A. J. An analytical solution to the electrical double layer potential for spherical particles: A functional theoretical approach. *J. Dispers. Sci. Technol.* **22**, 349–354 (2001).
491. Grahame, D. C. The electrical double layer and the theory of electrocapillarity. *Chem.*



- Rev.* **41**, 441–501 (1947).
492. Kotova, E. A., Kuzevanov, A. V., Pashkovskaya, A. A. & Antonenko, Y. N. Selective permeabilization of lipid membranes by photodynamic action via formation of hydrophobic defects or pre-pores. *Biochim. Biophys. Acta - Biomembr.* **1808**, 2252–2257 (2011).
493. Nawae, W., Hannongbua, S. & Ruengjitchatchawalya, M. Molecular dynamics exploration of poration and leaking caused by Kalata B1 in HIV-infected cell membrane compared to host and HIV membranes. *Sci. Rep.* **7**, 1–13 (2017).
494. Guha, S., Ghimire, J., Wu, E. & Wimley, W. C. Mechanistic Landscape of Membrane-Permeabilizing Peptides. *Chemical Reviews* vol. 119 6040–6085 (2019).
495. Vanni, S., Riccardi, L., Palermo, G. & De Vivo, M. Structure and Dynamics of the Acyl Chains in the Membrane Trafficking and Enzymatic Processing of Lipids. *Acc. Chem. Res.* **52**, 3087–3096 (2019).
496. Filippov, A., Orädd, G. & Lindblom, G. Influence of cholesterol and water content on phospholipid lateral diffusion in bilayers. *Langmuir* **19**, 6397–6400 (2003).
497. Allender, D. W., Sodt, A. J. & Schick, M. Cholesterol-Dependent Bending Energy Is Important in Cholesterol Distribution of the Plasma Membrane. *Biophys. J.* **116**, 2356–2366 (2019).
498. Wulandari, P. *et al.* Coordination of carboxylate on metal nanoparticles characterized by Fourier transform infrared spectroscopy. *Chem. Lett.* **37**, 888–889 (2008).
499. Chen, A. A. & Pappu, R. V. Parameters of monovalent ions in the AMBER-99 forcefield: Assessment of inaccuracies and proposed improvements. *J. Phys. Chem. B* **111**, 11884–11887 (2007).